

UC Merced

UC Merced Electronic Theses and Dissertations

Title

From experiments to models: Understanding the mechanisms of surface-assisted giant vesicle assembly

Permalink

<https://escholarship.org/uc/item/9fr554dh>

Author

Girish, Vaishnavi

Publication Date

2022

Peer reviewed|Thesis/dissertation

**From experiments to models: Understanding the mechanisms of  
surface-assisted giant vesicle assembly**

A dissertation submitted in partial satisfaction of the requirements for the  
degree Doctor of Philosophy

in

Bioengineering

by

Vaishnavi Girish

University of California, Merced

Committee in charge:

Professor Wei-Chun Chin, Chair

Professor Anand Bala Subramaniam

Professor Victor Muñoz

2022



The Dissertation of Vaishnavi Girish is approved, and it is acceptable in quality and form for publication on microfilm and electronically:

---

---

---

Chair

University of California, Merced

2022

## Table of Contents

List of tables .....	x
Funding and Contributions .....	xi
Acknowledgements .....	xii
Curriculum Vitae .....	xiv
Abstract .....	xv
Preface .....	xvi
Chapter 1: Introduction .....	1
1.1. Giant unilamellar vesicles and their applications .....	1
1.2. Lipid phases .....	2
1.3. Electrostatic and van der Waals forces between lipid bilayers .....	3
1.4. Current models and mechanisms for GUV assembly .....	5
1.4.1. GUVs form due to fluid shear and/or fluid flow between bilayers.....	5
1.4.2. GUVs form through bilayer phospholipid fragment (BPF) .....	5
1.4.3. GUVs form due to repulsive interbilayer interactions in bilayer stacks	6
1.4.4. GUVs form due to osmotic pressure gradients between bilayers .....	7
1.4.5. GUVs form due to electroosmosis .....	8
1.4.6. GUVs form due to substrate induced flux of water through bilayers ...	9
1.4.7. GUVs form via nanotube intermediates .....	9
1.4.8. Limitations of models in literature.....	9
1.5. Quantification of GUVs .....	10
1.6. Representing the yields and sizes distribution of GUVs .....	11
1.7. Summary of the Budding and Merging (BNM) model for GUV assembly .....	13
1.8. Bibliography .....	15
Chapter 2: Quantitative experiments of the yields of giant vesicles .....	22
2.1. Introduction .....	22
2.2. Materials and Methods .....	23
2.3. Results .....	25
2.3.1. Yields of zwitterionic lipid at varying surface concentrations .....	26

2.3.2. Yields of charged lipids at varying surface concentrations .....	30
2.3.3. Yields of mixtures of zwitterionic and charged lipids .....	32
2.4. Conclusions .....	38
2.5. Bibliography .....	38
Chapter 3: Model and Simulations of varying surface concentration of zwitterionic lipid.....	42
3.1. Introduction .....	42
3.2. Simulation set up .....	45
3.3. Simulating varying surface concentration.....	55
3.3.1. The molar yield is maximized when the fraction of sites with a negative budding energy is maximized.....	57
3.3.2. Effect of varying the fiber geometry on the molar yield and counts of GUVs.....	59
3.3.3. Molar yield is maximized when the fraction of sites with a negative budding energy is maximized for all fiber geometries with at least 1 bilayer that can bud spontaneously.....	61
3.3.3. Distributing bilayers evenly on fibers increases the maximum yields that can be obtained on all fiber geometries.....	62
3.3.4. The presence of external energy increases the yields and sizes of GUVs .....	65
3.3.5. Simulations of varying surface concentrations on a flat surface also show peaked molar yields .....	67
3.4. Conclusion.....	67
3.5. Bibliography .....	68
Chapter 4: Shear Induced Fragmentation.....	69
4.1. Introduction .....	69
4.2. Methods .....	69
4.3. Results .....	70
4.3.1. Images of the surface of paper coated with DOPG show the presence of an extended lipid mass that is not present for zwitterionic DOPC.....	70
4.3.2. The mass of lipid is consistent with a $L\alpha$ mesophase.....	73
4.3.3. Shear-induced fragmentation of the mesophase produces free-floating GUVs.....	75
4.3.4. The effect of salt on $L\alpha$ mesophase and GUV yields .....	78

4.3.5. Extended hydration time did not increase GUV yields .....	80
4.4. Conclusions .....	90
4.5. Bibliography .....	91
Chapter 5: Budding and merging with barriers to merging.....	92
5.1. Introduction .....	92
5.2. Budding and merging model with barriers explains the results .....	92
5.3. Conclusion.....	95
5.4. Bibliography .....	95
Chapter 6: Model and simulations of GUV assembly in salty solutions.....	96
6.1. Introduction .....	96
6.2. Simulation set up.....	97
6.3. Results of simulations of varying salt concentration.....	99
6.3.1. Effects of fiber geometry and salt concentration on the budding energy of each bilayer .....	99
6.3.2. Simulation results of varying salt concentrations .....	103
6.3.3. Budding time scales for cylindrical fibers compared to a flat geometry .....	104
6.3.4. Simulations of one-step modulation of salt .....	106
6.3.5. The molar yield is maximized at the salt concentration with the lowest budding energies.....	110
6.3.6. Effect of varying fiber geometry on the yields and sizes of GUVs at various salt concentrations .....	111
6.4. Limitations and scope of the simulation set-up.....	113
6.5. Bibliography .....	114
Appendix A: A comparison of different merging models.....	116
Appendix B: Assembly of GUVs on fabrics of diverse chemistries .....	127
Appendix C: Fluorescence dye has an effect on the assembly of GUVs .....	138
Appendix D: Impact of using buffers in solutions for GUV assembly .....	140

## List of figures

Figure 1.1: Different methods of representing the number of GUVs obtained. ....	12
Figure 1.2: Different methods of representing yield of GUVs. ....	13
Figure 2.1: Histograms of giant vesicle diameters obtained at varying surface lipid surface concentrations.....	27
Figure 2.2: Evolution of the yield of DOPC lipid at varying surface concentrations shows a peaked yield curve.....	28
Figure 2.3: Median and extreme diameters of GUVs composed of DOPC.....	29
Figure 2.4: Variation of molar yield with nominal surface concentration.....	31
Figure 2.5: Bar plots showing counts per microgram of lipid plotted for negatively charged lipids .....	32
Figure 2.6: Representative confocal images of varying mole fractions of negatively charged lipids DOPG and DOPS in mixtures of DOPC. ....	33
Figure 2.7: Plots showing the counts per microgram of lipid at varying mole fractions of negatively charged lipid DOPG and DOPS in zwitterionic lipid DOPC.....	34
Figure 2.8: Plot of the molar yield of the lipid mixture with varying mole fraction of charged lipid.....	36
Figure 2.9: Yields and distributions of varying surface concentrations of lipid mixtures composed of DOPC and DOPG.....	37
Figure 2.10: Histograms of diameters of GUVs obtained from lipid mixtures composed of mixtures containing 0 mol%, 5 mol%, 25 mol %, and 100 mol% of DOPG at the optimum surface concentration of each mixture.....	37
Figure 3.1: Schematic showing surface coverage and yields with increasing surface concentration of DOPC.....	42
Figure 3.2: Effect of increasing number of bilayers on fibers of varying geometries. ....	44
Figure 3.3: Simulation set up details.....	47
Figure 3.4: Flow of the simulation process on MATLAB for determining the number of nanobuds that bud. ....	50
Figure 3.5: Schematic of the merging template. ....	52
Figure 3.6: Histogram of diameters obtained at low salt (0.0032 mM) after different rounds of merging. ....	53
Figure 3.7: Configuration of lipids on the fibers at varying surface concentrations. ....	55
Figure 3.8: Simulation results for varying surface concentration of lipid on the substrate. .....	57
Figure 3.9: Fraction of bilayers with different budding energies. ....	58
Figure 3.10: Yields and size distributions of GUVs assembled on fibers of varying geometries. ....	59
Figure 3.11: a) Fraction of bilayers that can bud spontaneously (with a negative $\Delta E$ ) at varying nominal surface concentrations for different fiber geometries.....	61



Figure 3.12: Yields and size distributions of GUVs assembled on fibers with even numbers of bilayers distributed on all fibers.....	62
Figure 3.13: Yields and counts of GUVs obtained with external energy set to $1 k_B T$ . ....	65
Figure 3.14: Simulations of varying surface concentrations on a flat substrate. ....	67
Figure 4.1: Slices of 3D confocal images of DOPG on the surface of nanocellulose paper. ....	71
Figure 4.2: Slices of 3D confocal images of DOPC on the surface of nanocellulose paper.....	73
Figure 4.3: Plot of volume of the $L_\alpha$ smectic mesophase versus the nominal surface concentration.....	74
Figure 4.4: Slices of 3D confocal images of DOPS and on the surface of nanocellulose paper.....	75
Figure 4.5: Images of DOPG, DOPS and DOTAP harvested after 1 hour of hydration in 100 mM sucrose solution and sedimented in 100 mM glucose for 3 hours .....	76
Figure 4.6: Confocal images of x-y slices of the mesophase after transfer to an imaging chamber.....	76
Figure 4.7: Experiments on silanized glass showing that the $L_\alpha$ smectic mesophase can be sheared to produce GUVs. ....	77
Figure 4.8: 3D confocal images of $177 \text{ nmol/cm}^2$ DOPG on nanocellulose paper that is hydrated in PBS at short and long hydration times.....	79
Figure 4.9: 3D confocal images of $177 \text{ nmol/cm}^2$ DOPG on nanocellulose paper that is hydrated in 100 mM sucrose solution over long hydration periods.....	81
Figure 4.10: 3D confocal images of $174 \text{ nmol/cm}^2$ DOPS on nanocellulose paper that is hydrated 100 mM sucrose for 72 hours. ....	82
Figure 4.11: 3D confocal images of $202 \text{ nmol/cm}^2$ DOTAP on nanocellulose paper that is hydrated 100 mM sucrose for 72 hours. ....	83
Figure 4.12: 3D confocal images of $180 \text{ nmol/cm}^2$ DOPC on nanocellulose paper that is hydrated 100 mM sucrose for 72 hours. ....	84
Figure 4.13: Bar plots comparing molar yield of GUVs obtained from different lipid types after 1 versus 72 hours of hydration. ....	85
Figure 4.14: Slices of 3D confocal images of lipid mixtures composed of 95 mol% zwitterionic lipid DOPC and 5 mol% of charged lipid DOPG on the surface of nanocellulose paper.....	88
Figure 4.15: Schematic of the mechanism for shear-induced fragmentation. ....	89
Figure 5.1: Data from Figure 2.8 fit to the curve generated by Equation (20). The resulting fit has a SSE value of 0.0005765, showing a good fit. ....	94
Figure 6.1: Experimental results of molar yields and counts of zwitterionic lipid DOPC at assembled in varying concentrations of salt .....	97
Figure 6.2: Energy diagrams showing how fiber dimensions affect the energy of budding. ....	100
Figure 6.3: Variation of budding energy on glass.....	102

Figure 6.4: Results of simulation of GUV assembly on a flat surface and curved fibers at varying salt concentrations. ....	103
Figure 6.5: The budding timescales and counts are shown for different salt concentrations. ....	105
Figure 6.6: One-step modulation of the salt concentration produces high yields of GUVs in physiological salt solutions. ....	107
Figure 6.7: One-step modulation of the salt concentration produces high yields of GUVs in physiological salt solutions on glass. ....	109
Figure 6.8: Variation of budding energy on curved fibers compared to flat substrates..	110
Figure 6.9: Yields and size distributions of GUVs assembled on fibers of varying geometries. ....	112
Figure A.1: Comparison of histograms of diameters between experimental data and simulations for curved fibers. ....	116
Figure A.2: Histograms obtained using merging template 2 at the lowest and highest salt concentrations. ....	118
Figure A.3: Comparison of histograms of diameters between experimental data and simulations for a flat substrate. ....	119
A.4: Comparison of histograms of diameters between experimental data and simulations for curved fibers. ....	120
Figure A.5: Distributions of nanobuds and microbuds for different b values. ....	122
Figure A.6: Comparison of histograms of diameters between experimental data and simulations for curved fibers. ....	124
Figure A.7: Comparison of histograms of diameters between experimental data and simulations on curved fibers. ....	125
Figure A.8: Comparison of histograms of diameters between experimental data and simulations for a flat substrate. ....	126
Figure B.1: Scanning electron microscope images of the fabrics. ....	130
Figure B.2: Confocal microscope images of the surface of the hydrated fabrics after 1 hr. ....	132
Figure B.3: Confocal microscope images of giant polymersomes and giant lipid vesicles on the surface of silk fibers after 1 hr in aqueous buffer. ....	134
Figure B.4: Confocal microscope images of the surface of the hydrated fabrics after 1 h. ....	135
Figure B.5: Encapsulation of dye molecules after drying and rehydration on the substrate. ....	135
Figure C.1: Variation of molar yield at different mole fractions of dye. ....	138
Figure D.1: Molar yield and histogram of sizes obtained from GUV assembly in different buffers. ....	140

## List of tables

Table 2.1: Table showing the molecular structure, headgroup area, net charge and the phase transition temperature of zwitterionic lipid DOPC and charged lipids DOPG, DOPS and DOTAP. ....	26
Table 3.1: Table showing common parameters and their values used in the simulations	49
Table 6.1: Adhesion energy values for different salt concentrations calculated using Equation (24). ....	99
Table A.1: Table showing two options of merging templates, 1 and 2. ....	117
Table B.1: Properties of the fabrics. ....	131

## Funding and Contributions

### Contributions:

The budding and merging model was conceptualized and developed, and later expanded upon by Professor Anand Bala Subramaniam. The initial parameters of the simulation set-up for the model, including the concept of external energy, the use of debye lengths to vary adhesion energy were also proposed by Professor Subramaniam.

Experimental data at varying salt concentrations on tracing paper and glass were obtained by Joseph Pazzi.

### Grants:

The work in this dissertation have been largely possible due to the grants obtained from the National Science Foundation, NSF CBET-1512686 and NSF CAREER DMR-1848573. The data in this work was also collected, in part, with a confocal microscope acquired through the National Science Foundation MRI Award Number DMR- 1625733, and a scanning electron microscope acquired through NASA Grant NNX15AQ01A.

### Funding awards:

I would like to acknowledge UC Merced's Graduate Student Opportunity Program (GSOP) for enabling me to pursue my research through their funding from Fall 2020 to Summer 2021.

### Copyrighted material:

I would like to acknowledge the permission of the American Chemical Society (ACS) to reproduce figures from my publications in this dissertation.

Figures and text were reproduced with permission from: (1) Girish, V.; Pazzi, J.; Li, A.; Subramaniam, A. B. Fabrics of Diverse Chemistries Promote the Formation of Giant Vesicles from Phospholipids and Amphiphilic Block Copolymers. *Langmuir* **2019**, *35*, 9264–9273.

## Acknowledgements

I decided to pursue this PhD to learn how to do fundamental research. My 6 year stint in industry had been focused on very practical research. I worked on hair conditioners, a colloidal system that was dynamic, changing dramatically as it aged. It was sensitive to a range of processing conditions and new actives which is what often resulted in technical issues. However, in industry, one never has the time to delve into the science, particularly when there are simple ways to patch up the problems. I wanted to be able to think critically about technical questions, to be able to tap into the academic repository of journals and be able to come to the right conclusions. And I thought a PhD would be a challenge that would help me achieve those things.

At the end of this journey, I can say that it has been the most difficult and most rewarding challenge I have undertaken. I have learned to approach problems with a discerning eye, to think in a multifaced way, and to be able to understand and evaluate scientific work in a manner that can help me learn about various subjects. I have also learned to communicate my scientific work to a variety of audiences, which I think will benefit me throughout my career. And this journey would not have been possible without a number of people who have played a key role in supporting me.

First and foremost, I would like to acknowledge my advisor, Dr Anand Bala Subramaniam for your continual advice and input over the course of my PhD. Your guidance has been invaluable in the development of my research for this dissertation and your high standards and rigor have helped me achieve far more than I thought was possible.

I would also like to acknowledge my committee members, Dr Wei-chun Chin and Dr Victor Muñoz for their guidance and feedback in helping me sharpen my thinking.

A big thank you to my senior lab members, Joseph Pazzi and Alexander Li for showing me the ropes, answering all my questions, helping me troubleshoot as I learned, and for always being available to brainstorm ideas. I am also grateful for your company during those late night dinners and midnight lab sessions. I would also like to thank the newer members of my lab, Alexis Cooper, for organizing our lab bonding activities, Nimra Khurram and Vignesh Vijayananda for the youthful energy you bring to the lab. I have thoroughly enjoyed the expansion of our group and the wonderful camaraderie that you bring to the lab.

I would like to acknowledge Kennedy Nguyen from the IMF group for training me on the scanning electron microscope, for always being quick to help out with scheduling and any issues I've had over the years.

I would also like to acknowledge my parents for encouraging me to begin this journey. I doubt I would have had the courage to take on such a daunting task without your blessings and good wishes.

A special thank you to my husband Alexander Li who I met and married during the course of this PhD. Thank you for supporting me through the hard times, for being an incredible supply of joy and love. Your presence has been a source of light through this difficult journey.

Finally, I'd like to thank my sister Vasupradha Girish. Nothing in my life is ever complete without your participation. Thank you for always listening, always being there for me despite the oceans that lie between us.

## Curriculum Vitae

### **Education**

#### **UNIVERSITY OF CALIFORNIA, MERCED**

Bioengineering, Ph.D. student – Aug 2018 – Present (GPA 4.0)

Advisor: Anand Bala Subramaniam

#### **UNIVERSITY OF CAMBRIDGE, CAMBRIDGE, UK**

Bachelor of Arts/ Master of Engineering in Chemical Engineering - Oct 2008-June 2012

### **Work Experience**

#### **PROCTER AND GAMBLE**

Senior Process Engineer - Sept 2012-July 2018

Singapore

#### **ASTRA ZENECA**

Process Engineer Intern – July-Aug 2010

Bangalore, India

### **Fellowships and awards**

Graduate Student Opportunity Program Fellowship 2020-2021

Bioengineering Summer Fellowship 2020

NSF Innovation-Corps, UC Merced Venture labs 2019

## Abstract

**Title:** From experiments to models: Understanding the mechanisms of surface-assisted giant vesicle assembly

**Dissertation Advisor:** Anand Bala Subramaniam

**Author:** Vaishnavi Girish

**Degree:** Bioengineering

**University/Year:** University of California, Merced

**Committee chair:** Professor Wei-Chun Chin

Giant unilamellar vesicles (GUVs) are micrometer-sized compartments that can be assembled from amphiphilic lipid molecules in aqueous environments. The increasing interest in the use of cell-mimicking systems for therapeutics and drug delivery requires techniques that can enable the production of large numbers of GUVs at low costs. Despite the long history of producing GUVs, the mechanism of their assembly has not been understood. Furthermore, the impact of experimental factors such as surface concentration, and charge have also not been quantified due to a lack of available methods. Here, I report the quantitative impact of surface concentration, lipid headgroup charge, and salt in the hydration solutions on the yields and size distributions of GUVs using methods previously developed in the Subramaniam lab. I found that the evolution of yield of zwitterionic lipids with surface concentration is peaked while the yields of pure charged lipids as well as mixtures of zwitterionic and charged lipids increase with increasing surface concentration. I explain evolution of yields of zwitterionic lipids with increasing surface concentration and salt concentrations using the framework of the budding and merging (BNM) model. The BNM model describes GUV assembly as a process of nano-scale bud formation from bilayers followed by merging of the buds to form GUVs. I use MATLAB to simulate the process of coating sites on a substrate with lipid bilayers followed by budding and merging of bilayers. The results show that the impact of surface concentration and salt on the yields and size distributions can be predicted by the simulation. I also show that at high surface concentrations, charged lipids form GUVs via an alternative pathway which was named shear-induced fragmentation (SIF). The electrostatic repulsion between charged bilayers causes the bilayers to form an extended  $L\alpha$  mesophase which fragments and closes to form GUVs upon applying shear by pipetting. The quantification of yields has enabled us to systematically determine the effect of various experimental parameters. Furthermore, the ability to model and predict the impact of these parameters opens up avenues to large scale production, where the yields can be optimized depending on the required composition of lipids, hydration solutions, and substrates.



## Preface

Giant unilamellar vesicles (GUVs) have been of interest in the fields of synthetic biology, biophysics and bioengineering as well as in application such as therapeutics as minimal cell templates. Their ease of formation and visualization using optical microscopy techniques makes them ideal candidates for use in studying cellular processes in isolation. Their dimensions mimic that of cells and their versatility in incorporating a range of encapsulants makes them useful carriers in applications such as drug delivery. However, much of the large-scale applications of GUVs has been impeded by a lack of both, a mechanistic understanding underpinning their formation and a clear means of optimization via tunable parameters. In this dissertation, I address this lack of a comprehensive mechanism in the field and offer a means to understand the impact of different experimental parameters on GUV yields.

In chapter 1, I review the literature on GUVs, specifically focusing on what has been reported on their applications. I also review the current mechanisms in the field that describe GUV formation from thin-film hydration methods, highlighting the gaps and inconsistencies that need to be resolved. In previously published papers, the Subramaniam group determined a method of quantification that is statistically sound since it uses sample sizes of large populations of GUVs, between  $10^5$  and  $10^6$  orders of magnitude. This method of quantification was used to test various types of substrates and develop a thermodynamic model that describes the growth of GUVs using surface assisted assembly techniques. The model is the first in the field to explain the effect of different substrates. I briefly describe both, this method of quantification and the budding and merging (BNM) model that was proposed using the outcome of quantification of yield across different substrates. The model was used previously to explain the effect of nanoscale curvature on the yields and provide a qualitative understanding of the expected impact on the size distributions. Predictions on the numerical values of the yield and distribution of sizes was not provided.

In Chapter 2, I describe experimental results obtained using the quantification technique outlined in Chapter 1. The impact of surface concentration on GUV yield has not been studied in methodical, quantitative manner although certain studies in literature qualitatively demonstrate the need for higher surface concentrations when using charged lipids. Furthermore, there are no mechanistic explanations on the expected impact of surface concentration on the process of vesiculation in thin-film hydration methods. I describe the impact of surface concentration of zwitterionic lipid on the GUV yield using experiments. I find that the yield curve and vesicle counts peak at an optimal concentration beyond which point the yield drops with increasing surface concentration. Next, I expanded the study to include both positively and negatively charged lipids. Interestingly, I found the yield curves of charged lipids to increase with increasing concentration and plateau at high concentrations. Since many biological applications require mixtures of zwitterionic and negatively charged lipids to mimic cell membranes, I quantified the evolution of yields

of lipid mixtures composed of varying mole fractions of charged lipid doped into zwitterionic lipid at a fixed surface concentration. I found that the yield drops with increasing mole fractions of charged lipid. Similar to the results of pure charged lipid, I found that the yields could be largely recovered when the surface concentration was increased.

In Chapter 3, I extend the core budding and merging concept to consider the effect of multiple bilayers on the surface and its quantitative impact on the molar yield and the distribution of sizes of GUVs. The BNM model predicts the spontaneity of budding due to the fiber dimensions up to a certain critical concentration, beyond which bud formation is no longer spontaneous. High lipid concentrations result in larger numbers of fibers with bilayers assuming cylindrical geometries with radii above the critical radius, resulting in fewer buds. I wrote a MATLAB routine that considers 7 parameters which are fiber radius and length, bending energy, lipid concentration, salt concentration, energy input into the system, and the edge energy for the size distribution of nanobuds. I demonstrate that the model is versatile and that parameters listed above can be varied to determine the expected trends in GUV yields and size distributions. It allowed prediction of expected yields and distribution of sizes when parameters such as the geometry of the substrate, and adhesion energy are varied. These results show that the BNM model can be expanded to understand the role of concentration as a tunable parameter and that concentration is crucial to maximizing yield, a factor that has gone unnoticed in literature thus far.

In Chapter 4 I show that the evolution of charged lipids do not conform to the prediction of the BNM but instead follow an alternate mechanism of assembly. I report in Chapter 2, that while investigating charged lipids, I found experimentally that surfaces prepared with high surface concentrations and high mole fractions of charged lipids did not produce results consistent with zwitterionic lipid. Further investigations using high resolution confocal z-stack images of the surface of the paper after 1 hour of hydration revealed the presence of an  $L_{\alpha}$  mesophase for high concentrations of both positively and negatively charged lipids. Upon shear with a pipette, the mesophase fragments into GUVs. This method of producing GUVs is a bulk process termed shear-induced fragmentation (SIF) and was found to produce smaller vesicles (below 10  $\mu\text{m}$ ) than surface assisted assembly of GUVs. This nuanced behavior of lipids depending on their charge explains conflicting data in literature regarding the use of charged lipids to improve yields. While some papers report improvements in yields, others report diminished yields. In most cases, concentration has not been accounted for, which likely results in SIF being a pathway to vesicle formation in certain cases, thereby increasing yields in certain some experiments but not others. These results are described in Chapter 4.

In Chapter 5, I use the budding and merging model with barriers to merging to describe the mechanism for this reduction in yields. I show in Chapter 2 that at a fixed surface concentration the yield of GUVs produced drops with increasing charge. In chapter 5, I show that with increasing charge, the resulting nanobuds that are produced are likely

to face higher repulsion, increasing the barriers to merging which results in fewer micron-sized buds that contribute to GUV yields. I use the Grahame equation along with a simple partition function to reduce the probability of merging and determine the expected yields.

In Chapter 6, I simulate the yields and distributions of GUVs at varying concentrations of salt. The inability to obtain high GUV yields in ionic solutions using thin-film hydration techniques has been a long standing issue in the field. Since most physiological solutions have ions as a key component, the ability to produce and study GUVs in ionic conditions is crucial for most applications of GUVs. Certain modifications such as gel-assisted hydration using agarose have been shown to improve yields but with the drawback of having agarose in the GUV bilayers, resulting in altered physical properties of the vesicles. Furthermore, there is no mechanistic explanation in literature for the observed drop in yields. In chapter 6, I describe the impact of salt concentration on GUV yield. Here, the BNM model is used to explain the yield using variations in the adhesion energy term which is expressed as a function of the Debye length. The Debye length is a property of the growth solution and is directly linked to the concentration of ions present in the solution. I use the MATLAB routine from Chapter 3 with modifications to the adhesion energy to reproduce the variations in yields and sizes observed in experiments for cylindrical fibers as well as flat surfaces.

In Appendix A, I compare two different processes that were attempted to simulate the merging of nanobuds. The first is the merging template that is used in the simulations, and the second uses an exponential distribution with a varying exponential factor. I compare the histograms and yields of the two processes to show the differences in the two methods. In Appendix B, I report the results of GUV assembly on a variety of cylindrical fabrics, obtained from natural as well as synthetic sources. I show that we can produce GUVs on all the substrates, however, due to lipid entrapment between the pores of the fabric, the number of GUVs obtained was low compared to nanocellulose. In Appendix C, I report the variation of yields at varying concentrations of two dyes, Top-Fluor Cholesterol which is composed of the fluorescent bodipy group conjugated to a cholesterol molecule, and Rhodamine-PE which is composed of the fluorescent group rhodamine B sulfonyl conjugated to the 1,2-dioleoyl-*sn*-glycero-3-phosphoethanolamine (DOPE) headgroup. I show that the yields at varying concentrations of TopFluor Cholesterol remain steady compared to Rhodamine-PE which is more sensitive to concentration. In Appendix D, I report that using common buffers such as HEPES, PIPES and Tris with no additional salt results in a significant reduction of GUV yields.

## Chapter 1: Introduction

### 1.1. Giant unilamellar vesicles and their applications

Giant unilamellar vesicles (GUVs) are cell sized spherical compartments that are typically assembled from amphiphilic phospholipids in aqueous solutions. Vesicles that are over 1  $\mu\text{m}$  in diameter are classified as GUVs and their maximum diameter can be over 100  $\mu\text{m}$ . GUVs have been a subject of interest since they are large enough to probe using optical microscopy techniques<sup>1</sup>. Their compartmentalization properties mimic those of the plasma membrane on a basic level and so GUVs have been utilized as model membranes to study various membrane related properties such as rigidity<sup>2,3</sup>, protein interactions<sup>4,5</sup>, phase separation<sup>6,7</sup> and permeability<sup>8,9</sup>. Additional complexity such as proteins<sup>10,11</sup> or mixtures of charged lipids<sup>12</sup> can be introduced to GUVs to be studied in isolation, which is not possible in typical cells which are composed of a multiplicity of processes and factors, each of which can have an impact on the others. GUVs have also been used in synthetic biology as the smallest unit in building higher order structures such as prototissues<sup>13</sup> and vesicle networks<sup>14</sup>. GUVs can also function as picolitre-sized reactors, enabling small scale biochemical reactions such as polymerase chain reaction (PCR)<sup>15</sup> or enzymatic reactions<sup>16</sup> to be carried out. The low volume of GUVs compared to bulk reactions allows a higher contact rate between low concentrations of reactants enabling cost effective, small-scale studies.

GUVs have also shown potential for use in large scale applications such as drug delivery vehicles<sup>17-19</sup> and microreactors<sup>20,21</sup> for diagnostic purposes. The lumen of a GUV can encapsulate hydrophilic molecules<sup>22</sup> while the interior of the bilayers can encapsulate hydrophobic molecules<sup>23</sup>. Proteins or peptide chains embedded in the bilayer can be used for targeted release of cargo, for example, to regions with cancer cells<sup>24,25</sup>. While therapeutics have been largely dominated by nano-sized carriers such as liposomes with diameters between 50 to 300 nm<sup>26</sup>, delivery of actives to cancer sites is still low, with studies reporting only 0.7% of the nanoparticles reaching the target sites<sup>27,28</sup>. Barriers to delivery typically tend to be competitive interactions with tumor-associated macrophages<sup>27</sup> as well as the accumulation of the particles in the dense heterogenous vasculature surrounding the tumor cells<sup>29</sup>. GUVs have been used less often in therapeutics largely due to a lack of a comprehensive mechanism and an understanding of how to optimize GUV production for large scale use. However, GUVs between 3.5 to 4.5  $\mu\text{m}$  have been reported to show promising results in treating Alzheimer's using animal studies<sup>30</sup>. Dhand et al show that for pulmonary uptake, vesicles between 1 to 5  $\mu\text{m}$  are optimal, since smaller vesicles are lost via exhalation, while larger ones are trapped and cleared out by mucociliary systems<sup>18</sup>. GUVs also have a larger internal volume compared to nanoparticles. A 1  $\mu\text{m}$  GUV has an internal volume 1000 times higher than a 100 nm liposome. Thus, GUVs can encapsulate higher payloads and larger actives such as DNA complexes that have

applications in areas such as cancer therapy<sup>31</sup>. GUVs are also an optimal candidate for other therapeutic solutions such as artificial blood, since the average diameter of red blood cells is  $7 - 8 \mu\text{m}$ <sup>32</sup>, within the GUV size range. While a number of mechanisms have been proposed to explain various experimental observations, there is no single, comprehensive model that can be applied across different substrates and experimental conditions.

The key GUV production methods that I focus on are POPYRUS<sup>33,34</sup>, a method of thin-film hydration which utilizes nanocellulose as the substrate for GUV assembly and gentle hydration which utilizes glass as the substrate. In section 1.2, I discuss the existing models in literature and in section 1.4, I describe the budding and merging model that has been proposed by the Subramaniam Lab.

## 1.2. Lipid phases

In biological systems most lipids are organized into bilayers. Multiple oriented bilayers form a smectic phase<sup>35</sup> in which the length of the molecules are oriented along an axis and they are also organized into layers or lamellae<sup>36,37</sup>. The smectic phase can exist in a number of different states or phases. Pure lipids can exist in a gel-like  $L_\beta$  or  $S_o$  phase below a characteristic phase transition temperature  $T_m$  which is influenced by a number of factors such as temperature<sup>35,39</sup>, charge<sup>40,41</sup>, concentration<sup>39,42</sup>, and membrane composition<sup>43,44</sup>. Above the phase transition temperature, lipids exist in a fluid  $L_\alpha$  phase. Compared to the gel phase, the fluid phase is characterized by, lower bending rigidities, poorer packing since the lipid molecules occupy larger volumes, higher lateral diffusion, and higher permeability<sup>35,45</sup>. The phase transition temperature of lipids used in experiments in this dissertation are well below  $0^\circ\text{C}$ , in the range of  $-18^\circ\text{C}$  to  $-12^\circ\text{C}$ <sup>46,47</sup> and are in their fluid  $L_\alpha$  state at room temperature when they assemble into GUVs.

The addition of cholesterol to both the gel phase as well as to the fluid phase results in the liquid ordered phase,  $L_o$ <sup>48</sup>. This phase is midway between the gel and fluid phases and is characterized by a combination of properties of both phases. In the  $L_o$  phase, the lipid has a packed structure as in the gel phase but at the same time can undergo high lateral diffusion that is characteristic of the fluid phase<sup>35</sup>.

The structures that lipids assemble into depends on the shape of the molecule. The packing parameters, defined as  $v/a_0l_c$  where  $v$  is the chain volume,  $a_0$  is the area of the headgroup and  $l_c$  the chain length, determines the configurations that amphiphilic molecules can take when they aggregate in solution<sup>49</sup>. Molecules that have a packing parameter of  $\sim 1$  have a cylindrical shape and form bilayers in solution such as phosphatidylcholines. Molecules with a packing parameter less than 1 such as phosphatidylethanolamine are cone shaped and form an inverted hexagonal phase ( $H_{II}$ ) upon hydration<sup>35</sup>. Molecules with packing parameters greater than 1 have an inverted cone shape and form micelles in solution<sup>35</sup>. However, despite the variety of lipid molecules with

a range of packing parameters, most membranes in biological systems exist in the lamellar phase since only 20 – 50 % cylindrical lipids are required for the membrane to be organized into bilayers<sup>35</sup>. The role of non-lamellar phase forming lipids have been suggested to play important roles in forming intermediary phases in processes such as membrane fusion<sup>50</sup>.

### 1.3. Electrostatic and van der Waals forces between lipid bilayers

The forces between lipid bilayers are important in determining interactions between membranes in biological systems as well as in cases of thin film hydration, where they can influence the formation of vesicles. The surface of bilayers become charged either as a result of dissociation of groups from the lipid headgroups<sup>51</sup> or as a result of ions such as  $\text{Ca}^{2+}$  binding to neutral membranes<sup>52</sup>. The charges embedded in the surface of the bilayer or ions with the same charge as the surface are termed co-ions, while the ions that are released into solution or have the opposite charge as the surface are called counterions<sup>49</sup>. In the presence of a charged surface, the counterions in solution associate with the charges on the surface, forming the Stern layer<sup>53</sup>. Outside the Stern layer, is the diffuse layer, composed of a ‘cloud’ of counterions at a higher concentration than in the bulk solution<sup>49,53</sup>. Together, they form the electrical double layer. The counterions are driven to overcome attractive electrostatic interactions due to repulsive osmotic forces and dissociate from the surface to form this double layer to increase their configurational entropy<sup>49</sup>. As the surfaces are brought closer together, the repulsive pressure increases provided that the surface potential remains the same, that is, there is no additional counterion adsorption onto the surface with decreasing distance between the surfaces<sup>49</sup>.

Each ion follows a Boltzmann distribution in solution, given by the following equation<sup>49</sup>:

$$\rho = \rho_0 e^{-ze\psi/k_B T} \quad (1)$$

Here,  $\psi$  is the electric potential,  $\rho$  is the counterion density at any point  $x$  between the two surfaces,  $z$  is the valency of the ions in solution,  $e$  is the electronic charge,  $k_B$  is the Boltzmann constant and  $T$  is the temperature.

Combined with the Poisson equation, the Poisson-Boltzmann equation can be used to determine the electric potential, electric field and counterion density between two charged surfaces at varying separations given by equation 2:

$$\frac{d^2\psi}{dx^2} = -\left(\frac{ze\rho_0}{\epsilon_0\epsilon}\right) e^{-ze\psi/k_B T} \quad (2)$$

Here,  $\epsilon_0$  is the permittivity of free space,  $\epsilon$  is the dielectric constant, and  $x$  is the separation distance between two charged surfaces.

When no additional ions are added to pure water, the only ions in solution are counterions, dissociated from the lipid headgroups and ions that may be present as a result of dissolved carbon dioxide in water (described in section 2.3). The results of the Poisson-Boltzmann equation show that in low ionic solutions, the counterion concentration is highest close to the surfaces and reaches a minimum value at the mid-plane<sup>49</sup>.

In high ionic solutions including physiological buffers such as 1 × phosphate buffered saline (PBS), the presence of ions in the surrounding solution provides a bulk reservoir containing ions. Ions in solution can change the surface potential as a result of associating with the headgroup charges. For example, the Grahame equation can be used to determine that the surface potential of a surface with a charge density of  $-0.2 \text{ Cm}^{-2}$  drops from  $-477 \text{ mV}$  in pure water to  $-123 \text{ mV}$  in a 1:1 electrolyte solution containing  $10^{-1} \text{ M}$  of the electrolyte<sup>49</sup>. The solution to the Poisson Boltzmann equation in the presence of a high concentration of ions indicate that the electrostatic potential and surface charges are screened and decay exponentially away from the surface<sup>54</sup>. The characteristic decay length called the debye screening length, provides the distances over which the electric field of a charged particle or surface acts. The Debye screening length<sup>49</sup> is expressed as  $\kappa_D^{-1}$  in the following equation:

$$\kappa_D^{-1} = \sqrt{\frac{\epsilon_r \epsilon_0 k_B T}{2N_A e^2 [C]}} \quad (3)$$

Here  $\epsilon_0$  is the permittivity of free space,  $\epsilon_r$  is the dielectric constant,  $k_B$  is the Boltzmann constant,  $T$  is the absolute temperature,  $N_A$  is Avogadro's number,  $e$  is the elementary charge, and  $[C]$  is the ionic strength of the solution. In pure water at a pH of 7, the debye screening length is 960 nm and drops to 0.78 nm in 150 mM of sodium chloride. Thus, ions reduce the electrical double layer repulsion between surfaces.

While the dissociation of counterions leads to repulsive forces between bilayers, the van der Waals forces are attractive forces that can promote adhesion between bilayers. At small interbilayer distances, the van der Waals forces which vary as a power law with distance will exceed the repulsive double layer interactions which increase more slowly at small distances<sup>49</sup>. The DLVO theory (developed by Derjaguin, Landau, Verwey and Overbeek) proposes that the sum of the attractive and repulsive potentials gives the total interaction potential<sup>37</sup>.

Surfaces with a high charge density in low ionic solutions experience long range repulsion that results in an energy barrier at a critical separation which needs to be overcome for the surfaces to approach closer to each other<sup>49,55</sup>. For surfaces with low charge densities or for highly charged surfaces in concentrated ionic solutions, this long range repulsions are screened, and the energy barrier can be significantly lowered, enabling the surfaces to approach and adhere to each other<sup>49,55</sup>. If the surface charge is near zero, the

total interaction potential can be wholly attractive for a wider range of separation distances<sup>49</sup>. Therefore, the key parameter that can cause two charged surfaces to adhere to each other occurs as a result of lowering the surface potential or charge of the surfaces by inducing ion binding onto the surface or by adding salt to screen the double layer repulsion. Experiments using a surface force apparatus to measure the adhesion between zwitterionic lipids in monovalent salt solutions report an adhesion energy of  $1 \times 10^{-4} \text{ Jm}^{-2}$  in monovalent salt concentrations between 1 – 150 mM (the exact salt concentration was not reported)<sup>49</sup>. The adhesion was accounted for by the van der Waals attraction.

## **1.4. Current models and mechanisms for GUV assembly**

### **1.4.1. GUVs form due to fluid shear and/or fluid flow between bilayers**

Reeves and Dowben who were the first to establish a protocol for GUV assembly note that the conditions for vesicle formation required that the lipids are spread thinly, the stacks are well-hydrated, and the buffer is absent of salt<sup>56</sup>. In their procedure, the dried lipid films spread on the surface of glass flasks are exposed to water-saturated nitrogen for 15 minutes and allowed to equilibrate. During this time, the lipids self-assemble into stacks of bilayers on the surface. An aqueous solution is then poured into the flask coated with lipids. They propose that the moisture in the nitrogen causes the lamellae to swell. The aqueous solution then ‘runs’ between the bilayers, causing them to detach from their points of attachment and form vesicles<sup>56</sup>. They also suggest that salt or proteins in solution might act as ionic bridges between lamellae, preventing their separation and thus reducing yields.

This mechanism does not explain the reason for the polydisperse size distribution that is characteristic of vesicles obtained from thin-film hydration techniques. It also does not explain how or why this process of swelling and detachment of bilayers changes in the presence of charged lipids or different substrates, both of which affect the yield significantly.

### **1.4.2. GUVs form through bilayer phospholipid fragment (BPF)**

This category of models has been influenced by models for small unilamellar vesicle (SUV) formation and the resultant size distribution. Lasic proposed a generalized mechanism for vesicle formation from a variety of methods (including thin film hydration) using the detergent depletion technique as the basis<sup>57</sup>. The formation of an intermediary structure, termed a bilayered phospholipid fragment (BPF) is hypothesized, which is unstable due to its exposed edges. The BPFs merge with each other to lower the energy of the exposed edges by lowering the total circumference of the fragments in solution. Due to the exposed edges however, the energy of the BPF is not at its minimum and can be reduced



further by curving into a vesicle. This process increases the curvature elastic energy of the bilayer<sup>58</sup>. Hence, bilayers form vesicles if the curvature elastic energy is less than the edge energy of the exposed hydrophobic edges, determined by a critical radius  $r_c$ . Vesicle will not form if their radius is below  $r_c$ <sup>57</sup>. This critical radius was measured to be  $\sim 10$  nm for egg PC vesicles<sup>59</sup>. The elastic curvature energy of the bilayer increases when the bilayer closes in on itself to form a vesicle.

The key gap in this proposed mechanism is the elucidation of how the lipid configuration is affected by the substrate that is employed and its impact on the yields of GUVs. It also does not explain how other variables such as the presence of ions or charged lipids affect the formation of GUVs, both of which are important problems in the field.

### 1.4.3. GUVs form due to repulsive interbilayer interactions in bilayer stacks

This general class of proposed mechanisms is significantly influenced by measurements of changes in equilibrium interlamellar spacing of bilayers using neutron and x-ray spectroscopy in the late 1960s to the 1980s<sup>60</sup>. These measurements were performed through x-ray diffraction<sup>60-64</sup> or scattering<sup>65</sup> techniques and small angle neutron scattering<sup>66</sup>. Typical model systems for measuring these interactions are either multilamellar vesicles (MLVs)<sup>60-64</sup> or multibilayer stacks on the surface of a silicone substrate<sup>65</sup> or glass capillaries<sup>67,68</sup>. These experiments reveal the presence of interbilayer forces composed of the attractive van der Waals force<sup>9</sup> and repulsive forces that arise from the water molecules intercalating between the bilayers (hydration force)<sup>69</sup>, steric forces arising from undulations of the bilayer and electrostatic repulsion<sup>70</sup>. The differences in these forces determine the interbilayer spacing. Upon exposure to saturated water, they separate to achieve equilibrium interlamellar spacing that corresponds to a minimum in interaction energy<sup>61</sup>. The spacing can range between 3 nm and 7 nm<sup>68</sup> and can be modified using a different experimental parameters such as the presence of salt, which has been suggested to reduce interbilayer distances while charged lipids<sup>71,72</sup> and dissolved osmolytes<sup>73</sup> between bilayers have been suggested to increase interbilayer distances.

Hishida et al suggest that it is the steric forces that drive the formation of GUVs<sup>67</sup>. Their experiments using time resolved small angle X-ray scattering (TR-SAXS) suggest that GUVs form via water molecules intercalating between the bilayers and causing them to swell<sup>67</sup>. They carry out x-ray diffraction on bilayer stacks prepared by depositing lipids into a capillary glass tube with an outer diameter of 1.5 mm. The glass tube was placed in a window coated with a polyimide film for the x-ray experiments. Ultrapure water was added into the glass tube to immerse the entire lipid film. The repeat distance of the bilayers appears to increase from 51 to 64 Å in the first 170 seconds after hydration after which it appears to remain unchanged. Beyond this time point, the diffraction peak intensity decreased while the repeat distance appeared constant. They suggest that since

the peak intensity is expected to correspond to the number of bilayers present, the drop in intensity can be explained as the ‘peeling off’ of bilayer from the stack to form GUVs<sup>67</sup>, a phenomenon they relate to the unbinding transition of lipid bilayers. The unbinding is proposed to be a result of Helfrich repulsion, which was proposed by Helfrich to occur as a result of undulations of fluid bilayers, causing steric repulsion between the bilayers<sup>74</sup>.

No evidence is provided that connects the interbilayer energy with the formation of GUVs, however potential high energy exposed edges of the fragments can be considered as driving forces for self-closure. Helfrich repulsion is a function of the bending rigidity and the temperature, both of which have been held constant in experiments conducted at room temperature with identical lipid compositions. If the Helfrich repulsion is the driving force for vesicle formation, it is unclear why experimental factors such as salt concentration, lipid charge or substrate type affect the yield and size distributions. Other experimental inconsistencies include that the buds remain attached to the surface, which cannot occur if the bilayers ‘peel off’. Furthermore, while the presence of a repulsive force can enable bilayer separation, it does not account for the difference in sizes and the changes in size distributions under different experimental conditions.

A direct modification of this measured interbilayer interaction has also proposed to result in the formation of GUVs. An increase in the electrostatic repulsion by incorporating charged lipids was proposed by Akashi et al as a solution to improve GUV yields since separation of the bilayer stacks from each other has been suggested as a prerequisite for GUV formation<sup>74,52</sup>. The presence of salts in the hydration solutions are expected to screen the charges of counterions in solution, reducing the distances between bilayers to scales where van der Waals forces dominate. While charged lipids have been used in multiple papers to mitigate the effect of salts in solution, they introduce defects and reduce yields compared to zwitterionic lipids<sup>75–77</sup>. As I show later in the dissertation, these contradictory results can be explained by two different mechanisms that occur depending on the concentration and charge of the lipids. The repulsive interaction controls the formation of an expanded layer which I find has no driving force to self-close and in fact remains relatively stable until sheared.

#### **1.4.4. GUVs form due to osmotic pressure gradients between bilayers**

In this class of mechanisms, osmotic pressure between the bilayers is proposed to drive the formation of GUVs. Osmotic pressure gradients induced by adding sugars<sup>78,79</sup>, salts<sup>80</sup>, or polymers<sup>73</sup>. Water enters in between the stacks in order to balance the osmotic pressure. This causes the stacks to separate since there is a net transport of water. Bilayers can lyse if the expansion is sufficiently large and these could self-close to form GUVs.

Methods that have used gel-assisted hydration have shown that GUVs can be produced in high salt. As described earlier, high salt solutions have typically inhibited the

assembly of GUVs which has been hypothesized to occur due to higher adhesion of the bilayers as a result of screening of the counterions in the electric double layer that forms on the surface of the bilayers. The osmotic pressure generated by the dissolution of agarose gels into the surrounding solution is hypothesized to cause a significant influx of water into the lamellae<sup>73</sup>, thus compensating for the added adhesion in the presence of salt. We have found similar effects when using polymers to coat substrates.

#### 1.4.5. GUVs form due to electroosmosis

This set of mechanisms are specific to the electroformation technique. Electroformation involves using metal electrodes or glass surfaces coated with conductive material such as indium tin oxide and running a current across the glass coated with lipid<sup>81,82</sup>. Angelova and Dimitrov who conducted early experiments on electroformation in the 1980s describe the forces acting on the bilayers as a combination of attractive van der Waals forces between the lipid bilayers as well as the forces between the bilayers and the metal electrode, and repulsive electrostatic forces between the membranes<sup>83</sup>. They also describe the forces between the electric field that is applied and the membranes, which can be either attractive or repulsive depending on the charge of the membrane and the electrode. Similar to other papers described above, they also list undulation and hydration forces and osmotic pressure as the other repulsive forces. Undulation forces are understood to be a function of temperature while osmotic pressure a function of the osmolarity of a solution.

Electroosmosis which is the flow of fluid due in the presence of applied electric potential, has been considered to be a key driving force in the formation of GUVs via electroformation<sup>84,85</sup>. Charged counterions in solution migrate due to the electric field, carrying with them a solvation shell composed of water molecules<sup>86</sup>. This effect has been measured as vibrations of the lipid film at the same frequency as the applied AC field which has been suggested to cause the bilayers to lift off and bud, and form GUVs when detached from the surface of the electrode or glass<sup>85,87</sup>. Micheletto et al. show that the buds on the surface of the glass merge to form larger buds as long as they are connected to the lipid film on the surface<sup>19</sup>.

The interaction of electric fields with the lipid membrane however is unique to the method of electroformation. The electro-osmotic oscillations which enable bilayer separation to a distance that enables budding are not present for methods such as gentle hydration or POPYRUS. Furthermore, the separation of the membranes alone that the applied electric field induces does not appear to be sufficient in all cases of electroformation. For example, the presence of charged lipids also induces separation due to electrostatic repulsion between bilayers, however, they have been reported to be problematic in obtaining high yields<sup>77</sup> despite their ability to increase interbilayer separation<sup>70</sup>.

#### **1.4.6. GUVs form due to substrate induced flux of water through bilayers**

The flux of water through the substrate due to its porosity has been suggested as a potential mechanism for GUV yields using gel-assisted hydration<sup>88</sup>. Weinberger et al. attribute the ability to assemble GUVs on PVA gels due to additional pathways for water penetration into the bilayer stacks which include pathways through the gel. Thus, the permeability of the substrate is proposed as a crucial factor to maximize yields. We find however that while the membranes require hydration for GUVs to form, an increase of water flux alone is not sufficient to maximize yield. Pazzi and Subramaniam show there is no statistical difference between yields of GUVs grown on glass and porous regenerated cellulose<sup>33</sup>.

#### **1.4.7. GUVs form via nanotube intermediates**

A recently proposed model suggests that GUVs form via intermediary nanotubes<sup>89</sup>. The experiments involve depositing MLVs of various sizes and lamellarities onto glass coated with SiO<sub>2</sub>. The MLVs break on the substrate and form multibilayer stacks. While the bilayer coating the substrate surface remains attached through strong adhesion forces, subsequent bilayers de-wet and curve into nanotubes. Confocal micrographs show the upper bilayer retracting and leaving behind a network of nanotubes attached to the bilayer below following which spherical vesicles emerge from the nanotubes<sup>89</sup>. The driving force behind the transformation of nanotubes into GUVs is proposed to be a reduction of free energy through the reduction of curvature in the formation of spherical GUVs from cylindrical tubes. Similar reports of myelin figures have been seen during the course of GUV growth<sup>56,90</sup>. However, this pathway appears to only work for lipid mixtures that have negatively charged lipids. POPC, the only composition with purely zwitterionic lipid did not form vesicles through this method<sup>89</sup>.

#### **1.4.8. Limitations of models in literature**

One of the significant limitations of testing these various models for the mechanism of formation is that there is inadequate quantitative data in literature. Yields are often qualitative, include vesicles only over a certain size cut-off or contain too few vesicles for a rigorous statistical analysis. Pazzi and Subramaniam reported a method for quantifying the distribution of sizes and the molar yield which grew from a body of work of trying to understand the effect of cellulose fibers on the formation of GUVs<sup>33,91</sup>. This quantitative metric is the basis for the experimental data in this dissertation. I show that the budding and merging model is the only model that can be extended to produce predictions that match quantitative data on the distribution of sizes and yields due to the effect of substrate geometry, lipid concentration, and lipid charge. I also show that the data reveals an alternate pathway for high surface concentration of mixtures containing charged lipids.

## 1.5. Quantification of GUVs

PAPYRUS is a method of thin film hydration developed by the Subramaniam Lab that uses cellulose substrates, of which nanocellulose was found to be the highest yielding substrate<sup>33,34</sup>. As in all thin-film hydration methods, lipids are dissolved in chloroform and applied on a substrate, which in this case was a circular disk of nanopaper. After driving off excess solvent under vacuum, the lipid coated paper was placed in a well-plate and hydrated with a 100 mM sucrose solution for an hour. The GUVs that form on the surface were harvested by aspirating with a pipette and then stored in an Eppendorf tube. The quantification of the GUVs involved sedimenting an aliquot of the solution in an equimolar solution of glucose. The higher density of the sucrose-filled vesicles caused them to sink to the bottom of the chamber. After 3 hours of sedimentation, the entire bottom of the imaging chamber was imaged using a confocal microscope. All lipid solutions contained 0.5 mol% of Top-fluor Cholesterol. The images were processed using a custom routine in MATLAB, which identified the diameter and intensity of each GUV and output a list of all the GUVs and their diameters. Thus, all vesicles in an aliquot were imaged, processed and analyzed, allowing the quantification of yields with a high confidence level<sup>33</sup>. Coupled with the concept of a molar yield, the fraction of moles deposited that are present in GUVs allowed the probing of subtler aspects of lipid utilization that are lost when analyzing only the GUV counts since the populations are polydisperse.

It should be noted that experimental factors such as the age of the lipid solution, the choice of lipid dye, technique for application of lipid on the substrate, and harvesting technique can affect the yield of GUVs. Variations in imaging such as time for the vesicles to sediment, the pinhole diameter, the laser power and gain of the microscope can affect the measurement of the yield<sup>92</sup>. These variations were minimized by standardizing how I conducted the experiments and how I measured the yield.

To control for lipid aging I ensured that the working solutions of lipid mixtures were always made and used within a week. Fresh batches were made on a weekly basis from stock solutions. The dye used was kept constant, which is TopFluor-cholesterol at 0.5 mol %. The volume of the lipid applied on the substrate was always kept constant, changing only the concentration of the lipid solution when required. This was done to ensure that the application of lipid on the substrate did not vary when varying the surface concentration. Harvesting techniques were standardized to pipetting exactly 6 times to minimize variations between experiments.

Imaging parameters were kept constant as described in section 2.2. Sedimentation time was kept constant at 3 hours by timing repeats at intervals of 50 minutes, the time taken to image one sample, so that each repeat was ready to be imaged at 3 hours. Further, all experiments were performed 3 independent times for each data point to account for

potential experimental variations. The results are plotted as a mean yield with error bars corresponding to the standard deviation.

### 1.6. Representing the yields and sizes distribution of GUVs

The size distributions and yields of GUVs can be represented in a number of different ways. **Figure 1.1** shows various representations of a population of GUVs that is typically obtained from a single experiment. **Figure 1.1 a)** shows a histogram of diameters normalized by the mass of lipid deposited while **Figure 1.1 b)** represents the number of GUVs per microliter of harvested solution, in other words, the final concentration of GUVs in solution. **Figure 1.1 c)**, the number of GUVs obtained were plotted as relative frequency, normalized with the total number of GUVs obtained. In **Figure 1.1 d)**, the number of moles in the GUVs in each bin is plotted as a function of diameter. Most data in literature determining GUV yields typically represents the data as a histogram. Furthermore, while normalizing against the volume of the harvested solution or the total number of GUVs can also be useful, we found that normalizing against the amount of lipid deposited allows us to gain a quick idea of the relationship between the mass of lipid deposited and the GUV counts. This is useful for determining the cost of generating a given number of GUV at larger scales.

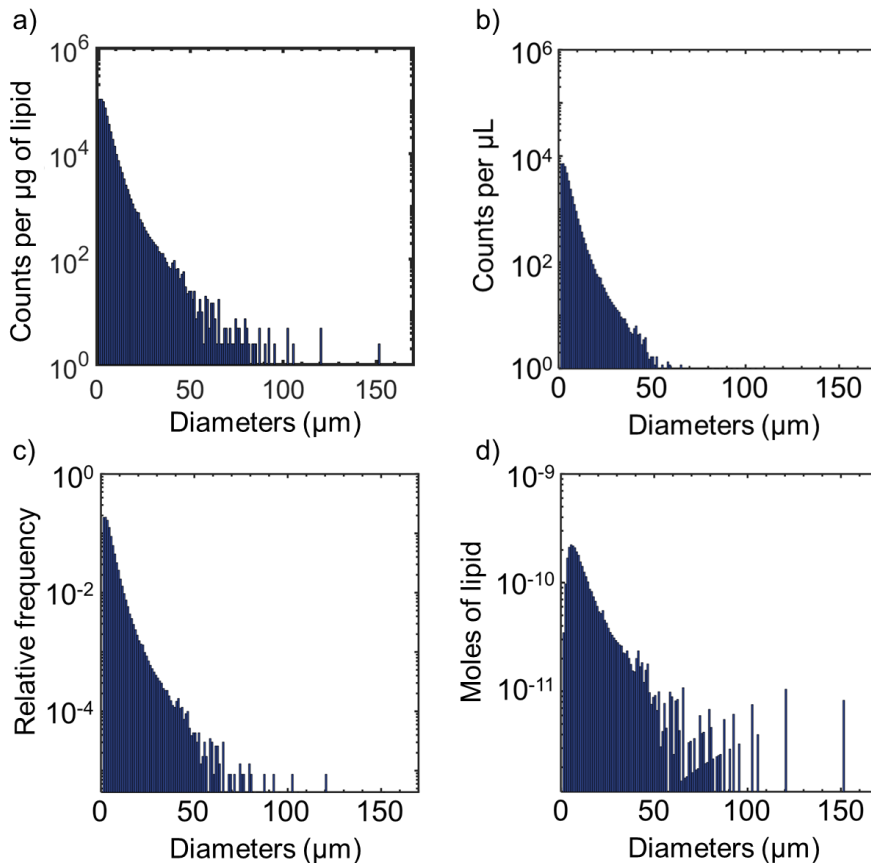


**Figure 1.1:** Different methods of representing the number of GUVs obtained. a) Histogram of GUVs showing the counts of GUVs normalized by the mass of lipid deposited at different diameters. b) The concentration of GUVs in solution, represented as the counts of GUVs per microliter of harvested solution. c) The number of GUVs obtained for each diameter normalized by the total number of GUVs obtained. d) The moles of lipid present in GUVs of each diameter. All bin widths in the plots are 1  $\mu\text{m}$ .

The polydispersity of the distribution makes it difficult to directly compare lipid utilization from the number of GUVs between samples. For this reason, we use the concept of a molar yield which considers the polydispersity of the samples. The molar yield is calculated as the moles of lipid in the GUVs as a fraction of the moles deposited given by the following equation<sup>33</sup>:

$$\left( \frac{2\pi m V_h}{N_A A_{hg} M V_{al}} \sum_{i=1}^n d_i^2 \right) \times 100$$

Here,  $m$  is the molecular weight of the lipid,  $V_h$  is the volume of solution harvested,  $N_A$  is Avogadro's number,  $A_{hg}$  is the headgroup area,  $M$  is the mass of lipid deposited,  $V_{al}$  is the volume of the aliquot in the imaging chamber,  $d_i$  is the diameter of vesicle  $i$  and  $n$  is the total number of GUVs in the aliquot.

**Figure 1.2** shows two ways of representing yields, using the results from this dissertation as examples. **Figure 1.2 a)** shows the molar yield, while **Figure 1.2 b)** shows the absolute yield, or the total moles of lipid in all GUVs without normalizing for the lipid applied. While the molar yield is useful to represent the lipid losses we can expect and the fraction of lipid that is converted into useful GUVs, the absolute yield shows the total moles obtained in GUVs.

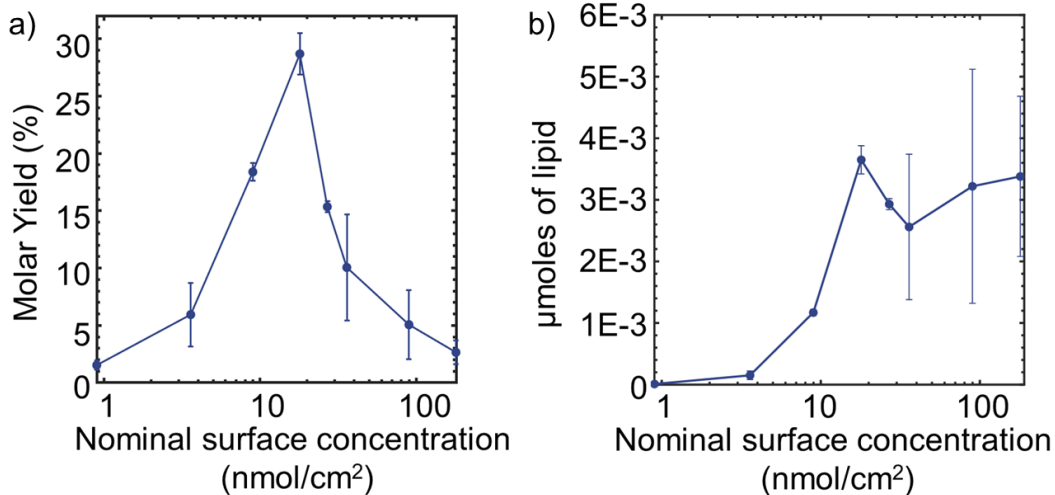


**Figure 1.2:** Different methods of representing yield of GUVs. a) The molar yield of GUVs showing the moles of lipid in GUVs as a fraction of the moles deposited. b) The absolute yield or the total moles in the GUVs obtained for a sample.

### 1.7. Summary of the Budding and Merging (BNM) model for GUV assembly

The budding and merging (BNM) model proposed by the Subramaniam Lab attempts to bridge the gap in literature related to the GUV formation mechanism. The ability to propose the model was in a large part due to the quantification method developed in the lab that enabled statistical comparisons between different substrates. A study of the differences enabled the proposal of the BNM model. The BNM model describes vesicle formation via the formation of nanometer sized buds that merge to form micron sized buds. The micron sized buds themselves can merge to grow larger in certain cases while they remain attached to the lipid pool on the surface. The buds can be detached from the surface via aspiration with a pipette which causes them to close in on themselves and form GUVs. The change in energy for bud formation is given by the following equation:

$$\Delta E = \int_{S_2} dS\{2\kappa_b H^2\} - \int_{S_1} dS\{2\kappa_b H^2\} - \int_{S_1} dS\{\xi\} + \int_{C_1} dr\{\lambda\} \quad (4)$$

Formation of GUVs on fibers:



$$\Delta E_{R_{B,c}} = \pi\kappa_B \left(8 - \frac{L_C}{R_C}\right) + 4\pi R_c \lambda - 2\pi R_c L_c \xi \quad (5)$$

Formation of GUVs on glass:

$$\Delta E_{R_{B,c}} = 8\pi\kappa_B + 2\pi R_d \lambda - \pi R_d^2 \xi \quad (6)$$

Here,  $\kappa_b$  is the bending modulus,  $H$  is the mean curvature,  $L_C$  is the length of the fiber,  $R_C$  is the radius of the fiber,  $\lambda$  represents the edge energy,  $\xi$  represents adhesion energy, represented by zero or negative values, denoting an attractive force. On glass, the curvature, edge energy term and adhesion energy will be positive across all values of the variables listed. Thus, bud formation on glass is always endergonic, requiring energy input. On nanocellulose however, the curvature term is negative when  $\frac{L_C}{R_C} > 8$ . Thus, at certain values of  $\frac{L_C}{R_C}$ , the energy for budding can be negative, indicating that budding on fibers can be spontaneous. The incorporation of the topology of the substrate allows us to explain the results obtained on different surfaces and elucidates the importance of surface geometry on yield.

The surface of nanopaper was observed to consist of a range of fiber lengths and diameters. Using a fiber radius of 12 nm and a length of 2000 nm, the bud radius was calculated to be 62 nm, far smaller than the size of a GUV. Vesicles obtained from thin-film hydration methods show a right skewed distribution of diameters across all substrates. Observations of the surface of the substrate immediately after hydration shows the presence of micron sized buds within 4 minutes of hydration. Some of the buds can be seen to undergo multiple merging events to form a single large bud. The model suggests that a similar phenomenon occurs at the nanobud scale as multiple nanobuds merge to form buds in the size range of GUVs. The elastic energy of a spherical bud is  $8\pi\kappa_B$ , unaffected by the radius of the bud. Therefore, merging of multiple buds into a single large bud is more energetically favorable and is the driving force for merging. The number of buds required to merge increases with the size of the final bud. A 100  $\mu\text{m}$  GUV will require 650,000 nanobuds of radius 62 nm to merge, 100 times that of a 10  $\mu\text{m}$  GUV which will require only 6500 nanobuds to merge. GUVs of smaller sizes, are likely to be far more prevalent than GUVs of larger sizes.

The BNM model was used to describe the yields obtained from 6 different surfaces with a mixture of flat and curved geometries, a mix of hydrophobic and hydrophilic surfaces and the presence and absence of pores. The results show that hydrophilic surfaces are necessary for the assembly of lipid bilayers, and the porosity of the substrate alone does not increase yields. The model also explains the size distribution of the GUVs, with a large number of vesicles between 1 – 5  $\mu\text{m}$  that tapers off rapidly towards the larger diameters. The ability to characterize large populations of vesicles has allowed us to compare electroformation, PAPYRUS, gentle hydration, allowing the identification of the most desirable substrate based on the application. For membranes templated on cylindrical fibers, the formation of nanoscale buds from nanofibers is exergonic, providing a

spontaneous pathway to forming GUVs. A similar pathway does not exist for membranes templated on flat and spherical surfaces.

## 1.8. Bibliography

- (1) Dimova, R.; Aranda, S.; Bezlyepkina, N.; Nikolov, V.; Riske, K. a; Lipowsky, R. A practical guide to giant vesicles. Probing the membrane nanoregime via optical microscopy. *J. Phys. Condens. Matter* **2006**, *18*, S1151–S1176.
- (2) Rawicz, W.; Olbrich, K. C.; McIntosh, T.; Needham, D.; Evans, E. A. Effect of chain length and unsaturation on elasticity of lipid bilayers. *Biophys. J.* **2000**, *79*, 328–339.
- (3) Faizi, H. A.; Frey, S. L.; Steinkühler, J.; Dimova, R.; Vlahovska, P. M. Bending rigidity of charged lipid bilayer membranes. *Soft Matter* **2019**, *15*, 6006–6013.
- (4) Alsaadi, E. A. J.; Neuman, B. W.; Jones, I. M. Identification of a membrane binding peptide in the envelope protein of MHV coronavirus. *Viruses* **2020**, *12*, 1–13.
- (5) Sorre, B.; Callan-Jones, A.; Manzi, J.; Goud, B.; Prost, J.; Bassereau, P.; Roux, A. Nature of curvature coupling of amphiphysin with membranes depends on its bound density. *Proc. Natl. Acad. Sci. U. S. A.* **2012**, *109*, 173–178.
- (6) Morales-Pennington, N. F.; Wu, J.; Farkas, E. R.; Goh, S. L.; Konyakhina, T. M.; Zheng, J. Y.; Webb, W. W.; Feigenson, G. W. GUV preparation and imaging: Minimizing artifacts. *Biochim. Biophys. Acta - Biomembr.* **2010**, *1798*, 1324–1332.
- (7) Scheve, C. S.; Gonzales, P. A.; Momin, N.; Stachowiak, J. C. Steric pressure between membrane-bound proteins opposes lipid phase separation. *J. Am. Chem. Soc.* **2013**, *135*, 1185–1188.
- (8) Bhatia, T.; Robinson, T.; Dimova, R. Membrane permeability to water measured by microfluidic trapping of giant vesicles. *Soft Matter* **2020**, *16*, 7359–7369.
- (9) Nishimura, K.; Matsuura, T.; Sunami, T.; Fujii, S.; Nishimura, K.; Suzuki, H.; Yomo, T. Identification of giant unilamellar vesicles with permeability to small charged molecules. *RSC Adv.* **2014**, *4*, 35224–35232.
- (10) Witkowska, A.; Jablonski, L.; Jahn, R. A convenient protocol for generating giant unilamellar vesicles containing SNARE proteins using electroformation. *Sci. Rep.* **2018**, *8*, 1–8.
- (11) Litschel, T.; Schwille, P. Protein Reconstitution Inside Giant Unilamellar Vesicles. *Annu. Rev. Biophys.* **2021**, *50*, 525–548.
- (12) Steinkühler, J.; De Tillieux, P.; Knorr, R. L.; Lipowsky, R.; Dimova, R. Charged giant unilamellar vesicles prepared by electroformation exhibit nanotubes and transbilayer lipid asymmetry. *Sci. Rep.* **2018**, *8*, 1–9.

- (13) Li, Q.; Li, S.; Zhang, X.; Xu, W.; Han, X. Programmed magnetic manipulation of vesicles into spatially coded prototissue architectures arrays. *Nat. Commun.* **2020**, *11*, 1–9.
- (14) Bolognesi, G.; Friddin, M. S.; Salehi-Reyhani, A.; Barlow, N. E.; Brooks, N. J.; Ces, O.; Elani, Y. Sculpting and fusing biomimetic vesicle networks using optical tweezers. *Nat. Commun.* **2018**, *9*, 1–11.
- (15) Sato, Y.; Komiya, K.; Kawamata, I.; Murata, S.; Nomura, S. I. M. Isothermal amplification of specific DNA molecules inside giant unilamellar vesicles. *Chem. Commun.* **2019**, *55*, 9084–9087.
- (16) Lefrançois, P.; Goudeau, B.; Arbault, S. Dynamic monitoring of a bi-enzymatic reaction at a single biomimetic giant vesicle. *Analyst* **2020**, *145*, 7922–7931.
- (17) Lengyel, M.; Kállai-Szabó, N.; Antal, V.; Laki, A. J.; Antal, I. Microparticles, microspheres, and microcapsules for advanced drug delivery. *Sci. Pharm.* **2019**, *87*.
- (18) Dhand, C.; Prabhakaran, M. P.; Beuerman, R. W.; Lakshminarayanan, R.; Dwivedi, N.; Ramakrishna, S. Role of size of drug delivery carriers for pulmonary and intravenous administration with emphasis on cancer therapeutics and lung-targeted drug delivery. *RSC Adv.* **2014**, *4*, 32673–32689.
- (19) Lussier, F.; Staufer, O.; Platzman, I.; Spatz, J. P. Can Bottom-Up Synthetic Biology Generate Advanced Drug-Delivery Systems? *Trends Biotechnol.* **2021**, *39*, 445–459.
- (20) Tsugane, M.; Suzuki, H. Reverse Transcription Polymerase Chain Reaction in Giant Unilamellar Vesicles. *Sci. Rep.* **2018**, *8*, 1–11.
- (21) Soga, H.; Fujii, S.; Yomo, T.; Kato, Y.; Watanabe, H.; Matsuura, T. In vitro membrane protein synthesis inside cell-sized vesicles reveals the dependence of membrane protein integration on vesicle volume. *ACS Synth. Biol.* **2014**, *3*, 372–379.
- (22) York-Duran, M. J.; Godoy-Gallardo, M.; Labay, C.; Urquhart, A. J.; Andresen, T. L.; Hosta-Rigau, L. Recent advances in compartmentalized synthetic architectures as drug carriers, cell mimics and artificial organelles. *Colloids Surfaces B Biointerfaces* **2017**, *152*, 199–213.
- (23) Barenholz, Y. Doxil® - The first FDA-approved nano-drug: Lessons learned. *J. Control. Release* **2012**, *160*, 117–134.
- (24) Staufer, O.; Antona, S.; Zhang, D.; Csatári, J.; Schröter, M.; Janiesch, J. W.; Fabritz, S.; Berger, I.; Platzman, I.; Spatz, J. P. Microfluidic production and characterization of biofunctionalized giant unilamellar vesicles for targeted intracellular cargo delivery. *Biomaterials* **2021**, *264*, 120203.
- (25) Wang, J.; Zhu, M.; Nie, G. Biomembrane-based nanostructures for cancer targeting and therapy: From synthetic liposomes to natural biomembranes and membrane-

- vesicles. *Adv. Drug Deliv. Rev.* **2021**, *178*, 113974.
- (26) Liu, P.; Chen, G.; Zhang, J. A Review of Liposomes as a Drug Delivery System: Current Status of Approved Products, Regulatory Environments, and Future Perspectives. *Molecules* **2022**, *27*.
- (27) Dai, Q.; Wilhelm, S.; Ding, D.; Syed, A. M.; Sindhvani, S.; Zhang, Y.; Chen, Y. Y.; Macmillan, P.; Chan, W. C. W. Quantifying the Ligand-Coated Nanoparticle Delivery to Cancer Cells in Solid Tumors. *ACS Nano* **2018**, *12*, 8423–8435.
- (28) Wilhelm, S.; Tavares, A. J.; Dai, Q.; Ohta, S.; Audet, J.; Dvorak, H. F.; Chan, W. C. W. Analysis of nanoparticle delivery to tumours. *Nat. Rev. Mater.* **2016**, *1*, 16014.
- (29) Jain, R. K.; Stylianopoulos, T. Delivering nanomedicine to solid tumors. *Nat. Rev. Clin. Oncol.* **2010**, *7*, 653–664.
- (30) Mutlu, N. B.; Değim, Z.; Yilmaz, Ş.; Eiz, D.; Nacar, A. New perspective for the treatment of Alzheimer diseases: Liposomal rivastigmine formulations. *Drug Dev. Ind. Pharm.* **2011**, *37*, 775–789.
- (31) Udomprasert, A.; Kangsamaksin, T. DNA origami applications in cancer therapy. *Cancer Sci.* **2017**, *108*, 1535–1543.
- (32) Jay, A. W. Geometry of the human erythrocyte. I. Effect of albumin on cell geometry. *Biophys. J.* **1975**, *15*, 205–222.
- (33) Pazzi, J.; Subramaniam, A. B. Nanoscale Curvature Promotes High Yield Spontaneous Formation of Cell-Mimetic Giant Vesicles on Nanocellulose Paper. *ACS Appl. Mater. Interfaces* **2020**, *12*, 56549–56561.
- (34) Pazzi, J.; Xu, M.; Subramaniam, A. B. Size distributions and yields of giant vesicles assembled on cellulose papers and cotton fabric. *Langmuir* **2018**, ASAP Artic, <https://doi.org/10.1021/acs.langmuir.8b03076>.
- (35) Stillwell, W. Chapter 10 - Lipid Membrane Properties. In *An Introduction to Biological Membranes*; Stillwell, W. B. T.-A. I. to B. M. (Second E., Ed.; Elsevier, 2016; pp 181–220.
- (36) Hanson, J. M.; Gettel, D. L.; Tabaei, S. R.; Jackman, J.; Kim, M. C.; Sasaki, D. Y.; Groves, J. T.; Liedberg, B.; Cho, N. J.; Parikh, A. N. Cholesterol-Enriched Domain Formation Induced by Viral-Encoded, Membrane-Active Amphipathic Peptide. *Biophys. J.* **2016**, *110*, 176–187.
- (37) Hirst, L. S. *Fundamentals of Soft Matter Science (2nd ed.)*; CRC Press, 2019.
- (38) Inoko, Y.; Mitsui, T. Structural Parameters of Dipalmitoyl Phosphatidylcholine Lamellar Phases and Bilayer Phase Transitions. *J. Phys. Soc. Japan* **1978**, *44*, 1918–1924.
- (39) Luzzati, V.; Tardieu, A. Lipid Phases: Structure and Structural Transitions. *Annu. Rev. Phys. Chem.* **1974**, *25*, 79–94.

- (40) Fisher, K. A.; Stoeckenius, W.; Sackmann, E.; Neumcke, B.; Weisenseel, M. H.; Fromter, E.; Thews, G.; Hutten, H. Physical Foundations of the Molecular Organization and Dynamics of Membranes. In *Biophysics*; Hoppe, W., Lohmann, W., Markl, H., Ziegler, H., Eds.; Springer Berlin Heidelberg: Berlin, Heidelberg, 1983; pp 425–457.
- (41) Himeno, H.; Shimokawa, N.; Komura, S.; Andelman, D.; Hamada, T.; Takagi, M. Charge-induced phase separation in lipid membranes. *Soft Matter* **2014**, *10*, 7959–7967.
- (42) Guldbrand, L.; Jönsson, B.; Wennerström, H. Hydration forces and phase equilibria in the dipalmitoyl phosphatidylcholine-water system. *J. Colloid Interface Sci.* **1982**, *89*, 532–541.
- (43) Zhao, J.; Wu, J.; Heberle, F. A.; Mills, T. T.; Klawitter, P.; Huang, G.; Costanza, G.; Feigenson, G. W. Phase studies of model biomembranes: Complex behavior of DSPC/DOPC/Cholesterol. *Biochim. Biophys. Acta - Biomembr.* **2007**, *1768*, 2764–2776.
- (44) Imam, Z. I.; Kenyon, L. E.; Ashby, G.; Nagib, F.; Mendicino, M.; Zhao, C.; Gadok, A. K.; Stachowiak, J. C. Phase-Separated Liposomes Enhance the Efficiency of Macromolecular Delivery to the Cellular Cytoplasm. *Cell. Mol. Bioeng.* **2017**, *10*, 387–403.
- (45) Lee, C. H.; Lin, W. C.; Wang, J. All-optical measurements of the bending rigidity of lipid-vesicle membranes across structural phase transitions. *Phys. Rev. E - Stat. Physics, Plasmas, Fluids, Relat. Interdiscip. Top.* **2001**, *64*, 4.
- (46) Caffrey, M. *Lipid Thermotropic Phase Transition Database (LIPIDAT)*; NIST standard reference database; U.S. Department of Commerce, National Institute of Standards and Technology, Standard Reference Data Program, 1993.
- (47) Hirsch-Lerner, D.; Barenholz, Y. Probing DNA-cationic lipid interactions with the fluorophore trimethylammonium diphenyl-hexatriene (TMADPH). *Biochim. Biophys. Acta - Biomembr.* **1998**, *1370*, 17–30.
- (48) Sankaram, M. B.; Thompson, T. E. Cholesterol-induced fluid-phase immiscibility in membranes. *Proc. Natl. Acad. Sci. U. S. A.* **1991**, *88*, 8686–8690.
- (49) Israelachvili, J. N. *Intermolecular and Surface Forces: Third Edition*; 2011.
- (50) Cullis, P. R.; Hope, M. J.; Tilcock, C. P. S. Lipid polymorphism and the roles of lipids in membranes. *Chem. Phys. Lipids* **1986**, *40*, 127–144.
- (51) Cowley, A. C.; Fuller, N. L.; Parsegian, V. A. Measurement of Repulsive Forces between Charged Phospholipid Bilayers. *Biochemistry* **1978**, *17*, 3163–3168.
- (52) Akashi, K. I.; Miyata, H.; Itoh, H.; Kinoshita, K. Formation of giant liposomes promoted by divalent cations: Critical role of electrostatic repulsion. *Biophys. J.* **1998**, *74*, 2973–2982.

- (53) Park, S.-J.; Seo, M.-K. Chapter 1 - Intermolecular Force. In *Interface Science and Composites*; Park, S.-J., Seo, M.-K. B. T.-I. S. and T., Eds.; Elsevier, 2011; Vol. 18, pp 1–57.
- (54) Andelman, D. CHAPTER 12 - Electrostatic Properties of Membranes: The Poisson-Boltzmann Theory. In *Structure and Dynamics of Membranes*; Lipowsky, R., Sackmann, E. B. T.-H. of B. P., Eds.; North-Holland, 1995; Vol. 1, pp 603–642.
- (55) Matter, F.; Luna, A. L.; Niederberger, M. From colloidal dispersions to aerogels: How to master nanoparticle gelation. *Nano Today* **2020**, *30*.
- (56) Reeves, J. P.; Dowben, R. M. Formation and properties of thin-walled phospholipid vesicles. *J. Cell. Physiol.* **1969**, *73*, 49–60.
- (57) Lasic, D. D. On the mechanism of vesicle formation. *J. Memb. Sci.* **1990**, *50*, 215–222.
- (58) Lasic, D. D. A molecular model for vesicle formation. *Biochim. Biophys. Acta* **1982**, *692*, 501–502.
- (59) Israelachvili, J. N.; Mitchell, D. J.; Ninham, B. W. Theory of self-assembly of hydrocarbon amphiphiles into micelles and bilayers. *J. Chem. Soc. Faraday Trans. 2 Mol. Chem. Phys.* **1976**, *72*, 1525–1568.
- (60) Rand, R. P. Interacting phospholipid bilayers: measured forces and induced structural changes. *Annu. Rev. Biophys. Bioeng.* **1981**, *10*, 277–314.
- (61) Lis, L. J.; McAlister, M.; Fuller, N.; Rand, R. P.; Parsegian, V. A. Interactions between neutral phospholipid bilayer membranes. *Biophys. J.* **1982**, *37*, 657–665.
- (62) Cowley, A. C.; Fuller, N. L.; Parsegian, V. A. Measurement of Repulsive Forces between Charged Phospholipid Bilayers. *Biochemistry* **1978**, *17*, 3163–3168.
- (63) Gulik-krzywicki, T.; Tardieu, A.; Luzzati, V. The Smectic Phase of Lipid-Water Systems: Properties Related to the Nature of the Lipid and to the Presence of Net Electrical Charges. *Mol. Cryst.* **1969**, *8*, 285–291.
- (64) LeNeveu, D. M.; Rand, R. P.; Parsegian, V. A.; Gingell, D. Measurement and modification of forces between lecithin bilayers. *Biophys. J.* **1977**, *18*, 209–230.
- (65) Hemmerle, A.; Malaquin, L.; Charitat, T.; Lecuyer, S.; Fragneto, G.; Daillant, J. Controlling interactions in supported bilayers from weak electrostatic repulsion to high osmotic pressure. *Proc. Natl. Acad. Sci. U. S. A.* **2012**, *109*, 19938–19942.
- (66) Lemmich, J.; Mortensen, K.; Ipsen, J. H.; Hønger, T.; Bauer, R.; Mouritsen, O. G. Small-angle neutron scattering from multilamellar lipid bilayers: Theory, model, and experiment. *Phys. Rev. E - Stat. Physics, Plasmas, Fluids, Relat. Interdiscip. Top.* **1996**, *53*, 5169–5180.
- (67) Hishida, M.; Seto, H.; Yamada, N. L.; Yoshikawa, K. Hydration process of multi-stacked phospholipid bilayers to form giant vesicles. *Chem. Phys. Lett.* **2008**, *455*,

297–302.

- (68) Hartung, J.; Helfrich, W.; Klösgen, B. Transformation of phosphatidylcholine multilayer systems in a large excess of water. *Biophys. Chem.* **1994**, *49*, 77–81.
- (69) Leikin, S.; Parsegian, V. A.; Rau, D. C.; Rand, R. P. Hydration forces. *Annu. Rev. Phys. Chem.* **1993**, *44*, 369–395.
- (70) Cowley, A. C.; Fuller, N. L.; Rand, R. P.; Parsegian, V. A. Measurement of repulsive forces between charged phospholipid bilayers. *Biochemistry* **1978**, *17*, 3163–3168.
- (71) Stein, H.; Spindler, S.; Bonakdar, N.; Wang, C.; Sandoghdar, V. Production of isolated giant unilamellar vesicles under high salt concentrations. *Front. Physiol.* **2017**, *8*, 1–16.
- (72) Akashi, K.; Miyata, H.; Itoh, H.; Kinoshita, K. Preparation of giant liposomes in physiological saline and characterization under an optical microscope. *Prog. Biophys. Mol. Biol.* **1996**, *65*, PMI21–PMI21.
- (73) Horger, K. S.; Estes, D. J.; Capone, R.; Mayer, M. Films of agarose enable rapid formation of giant liposomes in solutions of physiologic ionic strength. *J. Am. Chem. Soc.* **2009**, *131*, 1810–1819.
- (74) Helfrich, W. Steric Interaction of Fluid Membranes in Multilayer Systems. *Zeitschrift für Naturforsch. - Sect. A J. Phys. Sci.* **1978**, *33*, 305–315.
- (75) Estes, D. J.; Mayer, M. Electroformation of giant liposomes from spin-coated films of lipids. *Colloids Surfaces B Biointerfaces* **2005**, *42*, 115–123.
- (76) Li, Q.; Wang, X.; Ma, S.; Zhang, Y.; Han, X. Electroformation of giant unilamellar vesicles in saline solution. *Colloids Surfaces B Biointerfaces* **2016**, *147*, 368–375.
- (77) Rodriguez, N.; Pincet, F.; Cribier, S. Giant vesicles formed by gentle hydration and electroformation: A comparison by fluorescence microscopy. *Colloids Surfaces B Biointerfaces* **2005**, *42*, 125–130.
- (78) Tsumoto, K.; Matsuo, H.; Tomita, M.; Yoshimura, T. Efficient formation of giant liposomes through the gentle hydration of phosphatidylcholine films doped with sugar. *Colloids Surfaces B Biointerfaces* **2009**, *68*, 98–105.
- (79) Shohda, K.; Takahashi, K.; Suyama, A. A method of gentle hydration to prepare oil-free giant unilamellar vesicles that can confine enzymatic reactions. *Biochem. Biophys. Reports* **2015**, *3*, 76–82.
- (80) Yamada, N. L.; Hishida, M.; Seto, H.; Tsumoto, K.; Yoshimura, T. Unbinding of lipid bilayers induced by osmotic pressure in relation to unilamellar vesicle formation. *EPL* **2007**, *80*, 48002.
- (81) Herold, C.; Chwastek, G.; Schwille, P.; Petrov, E. P. Efficient electroformation of supergiant unilamellar vesicles containing cationic lipids on ITO-coated electrodes. *Langmuir* **2012**, *28*, 5518–5521.

- (82) Méléard, P.; Bagatolli, L. A.; Pott, T. Giant Unilamellar Vesicle Electroformation. **2009**, *465*, 161–176.
- (83) Angelova, M.; Dimitrov, D. S. A mechanism of liposome electroformation. *Trends Colloid Interface Sci. II* **1988**, *67*, 59–67.
- (84) Angelova, M. I.; Dimitrov, D. S. Liposome electroformation. *Faraday Discuss. Chem. Soc.* **1986**, *81*, 303–311.
- (85) Dimitrov, D. S.; Angelova, M. I. Progress in Colloid & Polymer Science Lipid swelling and liposome formation on solid surfaces in external electric fields. *Colloid Polym. Sci* **1987**, *73*, 48–56.
- (86) Kamiya, H.; Otani, Y.; Fuji, M.; Miyahara, M. *Characteristics and Behavior of Nanoparticles and Its Dispersion Systems*; 2018.
- (87) Micheletto, Y. M. S.; Marques, C. M.; Silveira, N. P. Da; Schroder, A. P. Electroformation of Giant Unilamellar Vesicles: Investigating Vesicle Fusion versus Bulge Merging. *Langmuir* **2016**, *32*, 8123–8130.
- (88) Weinberger, A.; Tsai, F. C.; Koenderink, G. H.; Schmidt, T. F.; Itri, R.; Meier, W.; Schmatko, T.; Schröder, A.; Marques, C. Gel-assisted formation of giant unilamellar vesicles. *Biophys. J.* **2013**, *105*, 154–164.
- (89) Köksal, E. S.; Liese, S.; Kantarci, I.; Olsson, R.; Carlson, A.; Gözen, I. Nanotube-Mediated Path to Protocell Formation. *ACS Nano* **2019**.
- (90) Harbich, W. Helfrich, W. THE SWELLING OF EGG LECITHIN IN WATER. *Chem. Phys. Lipids* **1984**, *36*, 39–63.
- (91) Kresse, K. M.; Xu, M.; Pazzi, J.; García-Ojeda, M.; Subramaniam, A. B. Novel Application of Cellulose Paper As a Platform for the Macromolecular Self-Assembly of Biomimetic Giant Liposomes. *ACS Appl. Mater. Interfaces* **2016**, *8*, 32102–32107.
- (92) Pazzi, J. E. A Comprehensive Characterization of Surface-Assembled Populations of Giant Liposomes using Novel Confocal Microscopy-Based Methods, University of California, Merced, 2021.



## Chapter 2: Quantitative experiments of the yields of giant vesicles

### 2.1. Introduction

In this chapter, I report systematic quantitative experiments to evaluate the impact of the surface concentration of lipid and the headgroup charge of the lipid on the yield of GUVs. Studies of these experimental factors in literature are extremely limited and only qualitative. However, applications of GUVs in therapeutics or biomimetics require the ability to assemble GUVs in larger number and composed of a range of lipid types, depending on the use. Systematic, quantitative studies of surface concentration and headgroup charge will not only enable optimization of yield in various applications but will also provide a fundamental understanding which we can use to build models.

Studies on the effect of concentration on the yield have been very limited in literature. Angelova and Dimitrov qualitatively show that zwitterionic lipids deposited on electrodes do not form many GUVs from 2 – 3 bilayers when using the electroformation methods for zwitterionic egg PC lipid in distilled water<sup>1</sup>. They find that increasing the bilayers to a minimum of 5 bilayers is necessary to obtain GUVs. Estes and Meyer also determine the effects of varying concentration for lipid mixtures with neutral and negatively charged lipids on yield using electroformation<sup>2</sup>. They use qualitative methods to report that mixtures with negatively charged lipid doped into zwitterionic lipid produce higher yields at higher surface concentrations. However, the absence of quantitative data and the use of relatively narrow concentration ranges make it difficult to draw definitive conclusions about the relationship between the surface concentration of pure zwitterionic lipid and the GUV yields. In section 2.3.1, I report results on the effect of surface concentration of zwitterionic lipid 1,2-dioleoyl-*sn*-glycero-3-phosphocholine (DOPC) on the yield and size distribution of GUVs when assembled on nanocellulose. I varied the surface concentration systematically from 0.90 nmol/cm<sup>2</sup> to 180 nmol/cm<sup>2</sup>. The yields changed non-monotonically, peaking at an optimal concentration of 18 nmol/cm<sup>2</sup>.

Charged lipids play crucial roles in cellular activity. Negatively charged lipids are a key component of most plasma membranes. Mammalian plasma membrane can have between 16% and 30% of charged lipids, namely phosphatidylserine, phosphatidylinositol, cardiolipin and phosphatidic acid<sup>3,4</sup> while bacteria can up to have from 11% up to 100% of charged lipids namely phosphatidylglycerol and cardiolipin<sup>5,6</sup>. Phosphatidylserine is present exclusively in the inner leaflet and their transport to the outer leaflet has been implicated as a signaling mechanism in apoptotic cells for phagocytosis<sup>7,8</sup>. After phosphatidylcholine, phosphatidylglycerol is the most abundant lipid in pulmonary surfactant<sup>9</sup>. Therefore, for biophysical experiments, the ability to produce vesicles with charged lipids is important.

On the other hand, the presence of charged lipids has been reported to negatively impact drug delivery systems. Vesicles with negatively charged lipids were found to have lower circulation times compared to vesicles composed of neutral lipids<sup>10,11</sup>. Negatively

charged liposomes were found to be tagged more frequently by proteins that induce phagocytosis, a process that removes foreign particles from the system<sup>11,12</sup>.

In section 2.3.2, I report the yield and distributions of GUVs that are obtained at various surface concentrations of the charged lipids 1,2-dioleoyl-*sn*-glycero-3-phospho-(1'-*rac*-glycerol) (DOPG), 1,2-dioleoyl-*sn*-glycero-3-phospho-L-serine (DOPS) and 1,2-dioleoyl-3-trimethylammonium-propane (DOTAP). I varied the surface concentration between 2 nmol/cm<sup>2</sup> and 202 nmol/cm<sup>2</sup>. Salient properties of the lipids that were used are shown in Table 2.1. I found that the evolution of molar yields of negatively charged lipid was in stark contrast with zwitterionic DOPC. The yields increased monotonically with concentration, with the rate of increase slowing down at higher surface concentrations.

In literature, the ability to grow vesicles using mixtures of charged lipids and zwitterionic lipids is mixed. Akashi et. al propose doping charged lipids into mixtures of zwitterionic lipids to increase GUV yield in low and high salt conditions<sup>13,14</sup>. They only considered giant vesicles over 25  $\mu\text{m}$  for the purpose of determining relative yields. They report an absence of GUVs using the gentle hydration technique when using purely zwitterionic lipid even in low salt conditions. Using a ratio of 9:1 phosphatidylcholine: phosphatidylglycerol produced yields in low salt as well as in solutions containing monovalent salt at concentrations up to 100 mM. Many papers follow Akashi's method of doping in a small amount of negatively charged lipids to increase yields specifically in high salt conditions<sup>15,16</sup>. Conversely, the use of charged lipids in electroformation and gentle hydration have been reported to reduce yields and increase the number of GUVs with other defects, such as nested vesicles, aggregates or nanotubes within the vesicles or associated with the outer membrane<sup>17</sup>. Compared to zwitterionic lipids, charged lipids have also been associated with requiring higher lipid quantities or in the case of electroformation, higher voltage compared to produce GUVs<sup>2,18</sup>.

In section 2.3.3, I present results from experiments in which I assemble GUVs from mixtures of zwitterionic and charged lipids. I fixed the surface concentration of lipids at the optimum concentration of pure DOPC (18 nmol/cm<sup>2</sup>) and varied the mole fraction of DOPG from 0 mol% to 100 mol%. I found with increasing mole fraction of charged lipid, the yields of the vesicles drop from 29% for mixtures with 0.5% DOPG to 8% with 50% DOPG in the mixture. Experiments that replaced DOPG with DOPS, which also has a net charge of -1, showed similar results. I also found that most of the yield could be recovered by increasing the surface concentration of charged mixtures.

## 2.2. Materials and Methods

**Chemicals.** We purchased 1,2-dioleoyl-*sn*-glycero-3-phosphocholine (DOPC), 23-(dipyrrrometheneboron difluoride)-24-norcholesterol (TopFluor-Cholesterol), 1,2-dioleoyl-*sn*-glycero-3-phospho-(1'-*rac*-glycerol) (DOPG), 1,2-dioleoyl-3-trimethylammonium-propane (DOTAP), and 1,2-dioleoyl-*sn*-glycero-3-phospho-L-serine

(DOPS) from Avanti Polar Lipids. We purchased sucrose (BioXtra grade, purity  $\geq 99.5\%$ ) glucose (BioXtra grade, purity  $\geq 99.5\%$ ), casein from bovine milk (BioReagent grade). We obtain ultrapure water (resistivity  $\geq 18.2 \text{ M}\Omega$ ) from an ELGA Pure-lab Ultra water purification system (Woodridge, IL). We purchased chloroform (ACS grade, purity  $\geq 99.8\%$  with 0.75% ethanol as preservative) from Thermo Fisher Scientific (Waltham, MA). We purchase poly(dimethyl)siloxane (Sylgard 184 silicone elastomer kit) from Krayden.

**Materials.** We purchased artist grade tracing paper from Jack Richeson and Co. Inc, circular hole punches (EK Tools Circle Punch, 3/8 in), square hollow punch (Amon Tech) and Quick-set Epoxy (Loctite) on Amazon. We purchased glass coverslips (Gold Seal, 22 mm  $\times$  22 mm), premium plain glass microscope slides (75 mm  $\times$  25 mm), 48-well plates (Corning™ Costar™ Flat bottom cell culture plates) and polystyrene petri dishes from Thermo Fisher Scientific (Waltham, MA).

**Assembly of GUVs.** We deposit 10  $\mu\text{L}$  of lipid solution of the required concentration onto tracing paper cut out into 9.5 mm diameter circles. The lipid was spread on the paper using a Hamilton syringe. All work with chloroform was conducted in a chemical-safety fume hood. After the excess chloroform evaporated from the surface of the substrates, I placed the lipid-coated paper in a vacuum chamber for at least 1 hour to drive off any residual solvent. To assemble GUVs, I placed the dry lipid-coated paper in a 48-well plate and added 150  $\mu\text{L}$  of a 100 mM solution of sucrose into the well. I allowed the sample to hydrate for 1 hour. I then harvested the GUVs by using a pipette with its tip cut off by aspirating gently 6 times along the surface of the paper. The solution was stored in an Eppendorf tube for use in imaging and analysis.

**Imaging GUVs.** The harvested vesicles were imaged in custom poly(dimethylsiloxane) square chambers with dimensions width  $\times$  length  $\times$  height = 6 mm  $\times$  6 mm  $\times$  1 mm that was covalently bonded to a microscope slide. The chambers were passivated with 1 mg/mL casein dissolved in 1 $\times$  PBS. We added an aliquot of the GUV solution into the imaging chamber, adjusting the volume to obtain between 100,000 to 150,000 objects in the imaging plane. We then added an isomolar solution of 100 mM glucose to bring the total volume of solution in the chamber to 60  $\mu\text{L}$ . The denser sucrose-filled vesicles sink to the bottom of the chamber. The vesicles were allowed to sediment for 3 hours, following which they were imaged using a confocal laser scanning microscope (LSM 880 with Airyscan+FAST, Axio Imager.Z2m, Zeiss, Germany, Objective: Plan-Apochromat 10 $\times$ /0.45 NA M27). Images were collected with the pinhole fully open, with a diameter of 599  $\mu\text{m}$ . The laser power and gain were kept constant between all experiments. We imaged the bottom of the entire chamber using an automated tilescan routine and capture 64 images (850.19  $\mu\text{m}$   $\times$  850.19  $\mu\text{m}$ , 3212  $\times$  3212 pixels per image).

**Image processing.** We used a custom MATLAB (Mathworks Inc., Natick, MA) routine that uses intensity thresholding followed by watershed segmentation. GUVs are distinguished from structures such as MLVs using the intensity of the objects detected.

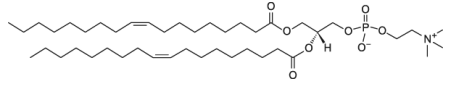
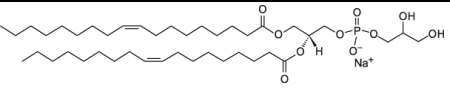
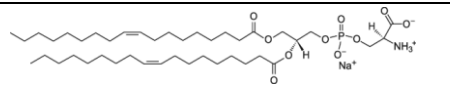
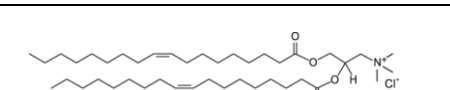
**Surface concentrations of zwitterionic lipid used:** Working in a chemical fume hood, I deposited 10  $\mu\text{L}$  lipids dissolved in chloroform at a concentration of 0.05 mg/mL, 0.2 mg/mL, 0.5 mg/mL, 1 mg/mL, 1.5 mg/mL, 2 mg/mL, 5 mg/mL, and 10 mg/mL on 0.95 cm diameter (area of 0.7  $\text{cm}^2$ ) circular pieces of tracing paper to obtain nominal surface concentrations of 0.9  $\text{nmol}/\text{cm}^2$ , 3.6  $\text{nmol}/\text{cm}^2$ , 9  $\text{nmol}/\text{cm}^2$ , 18  $\text{nmol}/\text{cm}^2$ , 27  $\text{nmol}/\text{cm}^2$ , 36  $\text{nmol}/\text{cm}^2$ , 90  $\text{nmol}/\text{cm}^2$ , and 180  $\text{nmol}/\text{cm}^2$  respectively. Experiments at each nominal surface concentration were performed three times with independent pieces of paper. All other steps were carried out as described in section 2.2.

**Surface concentrations of charged lipids used:** I deposited 10  $\mu\text{L}$  lipids dissolved in chloroform at the desired concentrations. Surface concentrations of 2  $\text{nmol}/\text{cm}^2$ , 9  $\text{nmol}/\text{cm}^2$ , 18  $\text{nmol}/\text{cm}^2$ , 35  $\text{nmol}/\text{cm}^2$ , 89  $\text{nmol}/\text{cm}^2$ , and 177  $\text{nmol}/\text{cm}^2$  of 1,2-dioleoyl-*sn*-glycero-3-phospho-(1'-*rac*-glycerol) (DOPG), correspond to 0.1 mg/mL, 0.5 mg/mL, 1 mg/mL, 2 mg/mL, 5 mg/mL and 10mg/mL of lipid in chloroform solution. We used 1 mg/mL, 5 mg/mL and 10 mg/mL of 1,2-dioleoyl-*sn*-glycero-3-phospho-L-serine (DOPS), corresponding to surface concentrations of 2  $\text{nmol}/\text{cm}^2$ , 17  $\text{nmol}/\text{cm}^2$ , 87  $\text{nmol}/\text{cm}^2$ , and 174  $\text{nmol}/\text{cm}^2$ . Similarly, we used 0.5 mg/mL, 1 mg/mL, 2.5 mg/mL 5 mg/mL and 10 mg/mL of 1,2-dioleoyl-3-trimethylammonium-propane (DOTAP) in chloroform which corresponds to surface concentrations of 10  $\text{nmol}/\text{cm}^2$ , 20  $\text{nmol}/\text{cm}^2$ , 50  $\text{nmol}/\text{cm}^2$ , 100  $\text{nmol}/\text{cm}^2$  and 202  $\text{nmol}/\text{cm}^2$ . Experiments at each nominal surface concentration were performed three times with independent pieces of paper.

### 2.3. Results

The structures and physical properties of the lipids that were chosen are listed in **Table 2.1**. All the lipids have two oleoyl chains consisting of 18 carbon atoms with one unsaturated bond at the C9 position and have chain melting temperatures well below room temperature. DOPC is zwitterionic with a net charge of zero. The  $\text{pK}_a$  of the phosphate group in DOPC is 0.8<sup>19</sup>. The choices of charged lipids were made so that there was no variation in alkyl chain lengths compared to DOPC which allows a direct comparison of the effect of headgroup charges to DOPC as well as results in the literature<sup>14,17,18,20–22</sup>. The chosen headgroups were phosphatidylglycerol (DOPG), phosphatidylserine (DOPS), and trimethyl ammonium propane (DOTAP). The  $\text{pK}_a$  of the phosphate group of DOPG is 2.6, the carboxylate group and phosphate group of DOPS is 5.5 and 3.5 respectively, and the ammonium group of DOPS is 11.5<sup>23</sup>. The solutions used for hydration, 100 mM sucrose in ultrapure water, had a pH of 5.6. This pH is consistent with ultrapure water in equilibrium with atmospheric carbon dioxide<sup>24</sup>. I also perform experiments with phosphate buffered saline (PBS) in sucrose which is buffered at a pH of 7.4. In both solutions, the net charge of the headgroups of DOPG<sup>25</sup>, DOPS<sup>26</sup>, and DOTAP<sup>27</sup> are -1, -1, and +1. Cellulose has carboxyl groups dispersed in its molecular structure<sup>28</sup>. The carboxyl groups have  $\text{pK}_a$

values between 4.0 and 4.1<sup>29</sup>. Thus, the cellulose nanofibers have a net negative charge in ultrapure water and in PBS.

Lipid	Molecular Structure	Headgroup Area	Net Charge, z	Phase-Transition Temperature
DOPC		72.4 <sup>30</sup>	0	-17 <sup>31</sup>
DOPG		70.8 <sup>32</sup>	-1	-18 <sup>31</sup>
DOPS		64.1 <sup>33</sup>	-1	-11 <sup>31</sup>
DOTAP		70 <sup>34</sup>	+1	-11.9 <sup>35</sup>

**Table 2.1:** Table showing the molecular structure, headgroup area, net charge and the phase transition temperature of zwitterionic lipid DOPC and charged lipids DOPG, DOPS and DOTAP.

### 2.3.1. Yields of zwitterionic lipid at varying surface concentrations

Using zwitterionic lipid 1,2-dioleoyl-*sn*-glycero-3-phosphocholine (DOPC), I varied the surface concentration of lipid from 0.9 nmol/cm<sup>2</sup> to 180 nmol/cm<sup>2</sup>, to cover 3 orders of magnitude. All mixtures were doped with 0.5 mol% of TopFluor-Cholesterol. The size of the nanocellulose substrate was fixed at 0.7 cm<sup>2</sup>. I added 10  $\mu$ L of varying concentrations of lipid solution on the surface to keep the volume of the solution identical across all concentrations. This was done to minimize variations in spreading the lipid on the surface of the substrate. I place the lipid-coated substrate in the vacuum for 1 hour to drive off any residual solvent and then hydrated in 100 mM sucrose solution for 1 hour. The GUVs were harvested, imaged and quantified as described in section 2.2. The number of GUVs obtained and their diameters are shown in the histograms in **Figure 2.1**. The histograms illustrate the variations in the size distributions at different lipid concentrations. The distributions broadened from 0.9 nmol/cm<sup>2</sup> to 18 nmol/cm<sup>2</sup> and the total number of vesicles formed increased from  $0.53 \pm 0.04 \times 10^5$  to  $5.75 \pm 1.47 \times 10^5$ . At concentrations greater

than  $18 \text{ nmol/cm}^2$ , the distribution consistently narrowed until the highest concentration that was tested. The number of vesicles also dropped to  $0.97 \pm 0.29 \times 10^5$ .

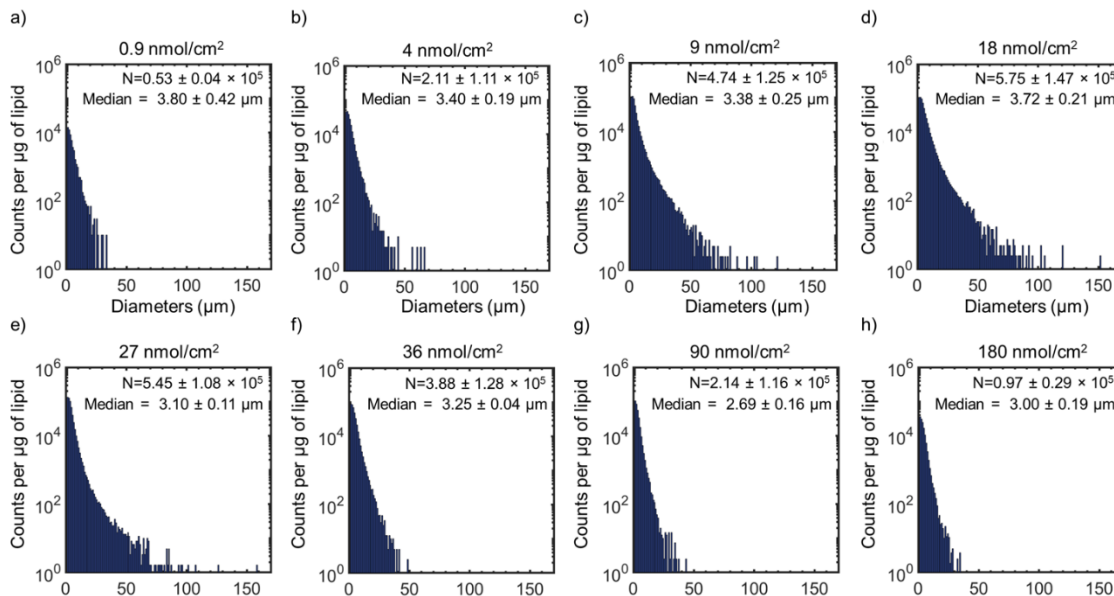


**Figure 2.1:** Histograms of giant vesicle diameters obtained at varying surface lipid surface concentrations. Normalized histograms of diameters obtained from assembly in 100 mM sucrose at a nominal surface concentration of a)  $0.9 \text{ nmol/cm}^2$ , b)  $4 \text{ nmol/cm}^2$ , c)  $9 \text{ nmol/cm}^2$ , d),  $18 \text{ nmol/cm}^2$ , e)  $27 \text{ nmol/cm}^2$ , f)  $36 \text{ nmol/cm}^2$ , g)  $90 \text{ nmol/cm}^2$  h)  $180 \text{ nmol/cm}^2$ . Bin widths are  $1 \mu\text{m}$ . Each histogram is an average from 3 independent repeats. Inset values are the average  $\pm$  standard deviation of the total counts and median diameter of the three repeats. The total number of vesicles and the number of vesicles with larger diameters peaked at the optimal concentration of  $18 \text{ nmol/cm}^2$ .

The resulting molar yields and GUV counts were compiled and plotted in **Figure 2.2**. Qualitative analysis of the confocal images in **Figure 2.2** a, iii) show that at a concentration of  $18 \text{ nmol/cm}^2$  the vesicles were most abundant and were larger in size while concentrations both higher and lower than the optimal had smaller and fewer vesicles. At  $18 \text{ nmol/cm}^2$  (iii), the largest vesicle has a diameter of  $\sim 80 \mu\text{m}$ . At a concentration of  $9 \text{ nmol/cm}^2$ , the largest diameter is  $\sim 50 \mu\text{m}$  while in all other images, there are no vesicles over  $20 \mu\text{m}$ . **Figure 2.2** b) shows the variation in molar yield with increasing surface concentration of lipid. Increasing surface concentration from  $0.9 \text{ nmol/cm}^2$  to  $18 \text{ nmol/cm}^2$  resulted in an increase in the molar yield of DOPC from 1.5% to a maximum value of 30%. Further increases in the surface concentration led to a decrease in the molar yield. I find, therefore, that there is a narrow range of surface concentrations where the

yield is close to 30%. I also note that the rise in the molar yield to its maximum was steeper than the fall after the peak.

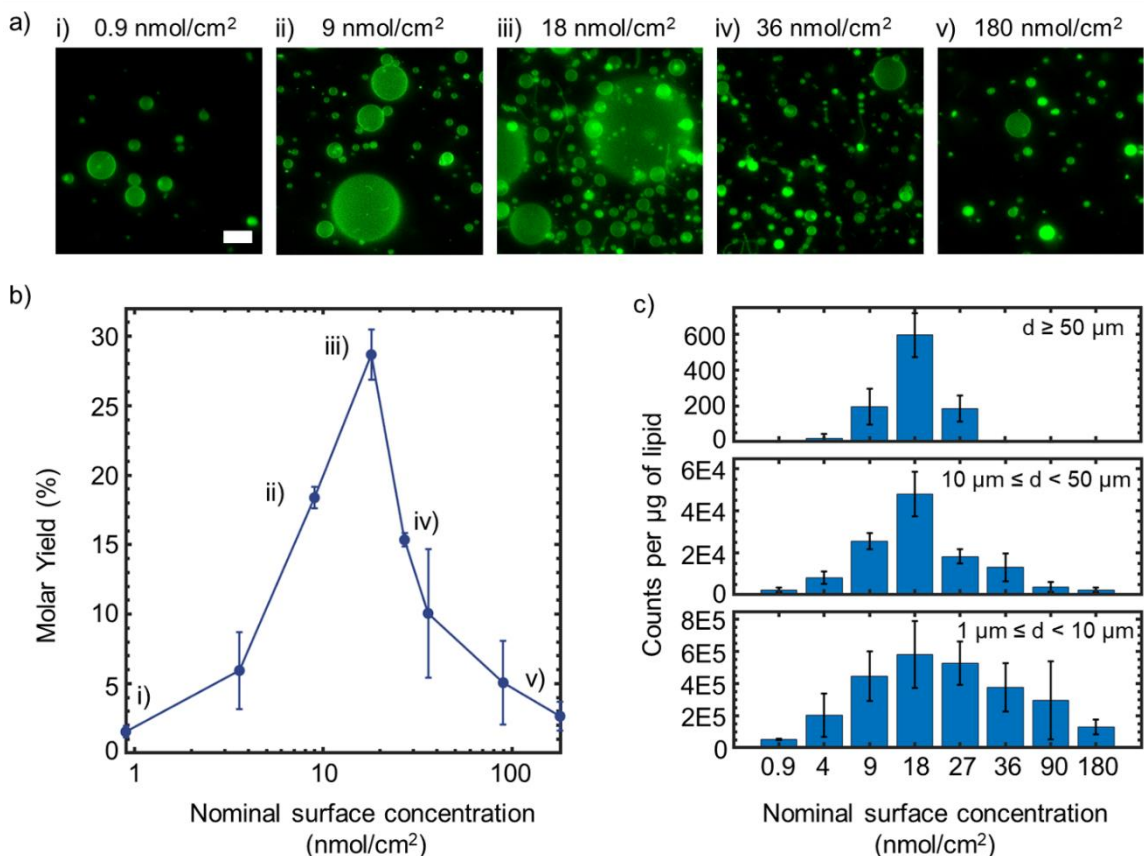


**Figure 2.2:** Evolution of the yield of DOPC lipid at varying surface concentrations shows a peaked yield curve. a) Representative confocal images of harvested giant unilamellar vesicles for 5 nominal surface concentrations of lipid on nanocellulose, with the concentration values shown above the images. The roman numerals correspond to surface concentration points in b). b) Molar yield at varying surface concentrations plotted with error bars showing the standard deviation. c) Counts per microgram of lipid at varying surface concentrations, shown in 3 different size categories. Both the molar yield and the counts per microgram of lipid peak at the same nominal surface concentration of 18 nmol/cm<sup>2</sup>. Scale bar: 20 μm.

To better visualize the impact of surface concentration on the sizes of the vesicles, the histograms in **Figure 2.1** were replotted in **Figure 2.2 c)**, with the counts sub-divided into 3 size classes, small vesicles between 1 to 10 μm, medium sized vesicles between 10 to 50 μm and large vesicles which included all vesicles over 50 μm. This method of plotting sizes enables a clearer comparison between concentration while highlighting the variations in the effect of surface concentration on the different size classes. The counts of all three

size categories are peaked, and the maximum value corresponds to the surface concentration at which the molar yield was also maximized. I only obtained GUVs over 50  $\mu\text{m}$  for a few concentrations close to the optimum concentration. Approximately 600 GUVs per microgram of lipid over 50  $\mu\text{m}$  were produced at the optimal concentration of 18  $\text{nmol}/\text{cm}^2$  and 185 and 195 GUVs per microgram of lipid at 27  $\text{nmol}/\text{cm}^2$  and 9  $\text{nmol}/\text{cm}^2$  respectively and just 2 GUVs per microgram of lipid for a concentration of 4  $\text{nmol}/\text{cm}^2$ . No vesicles over 50  $\mu\text{m}$  were produced for other nominal surface concentrations.

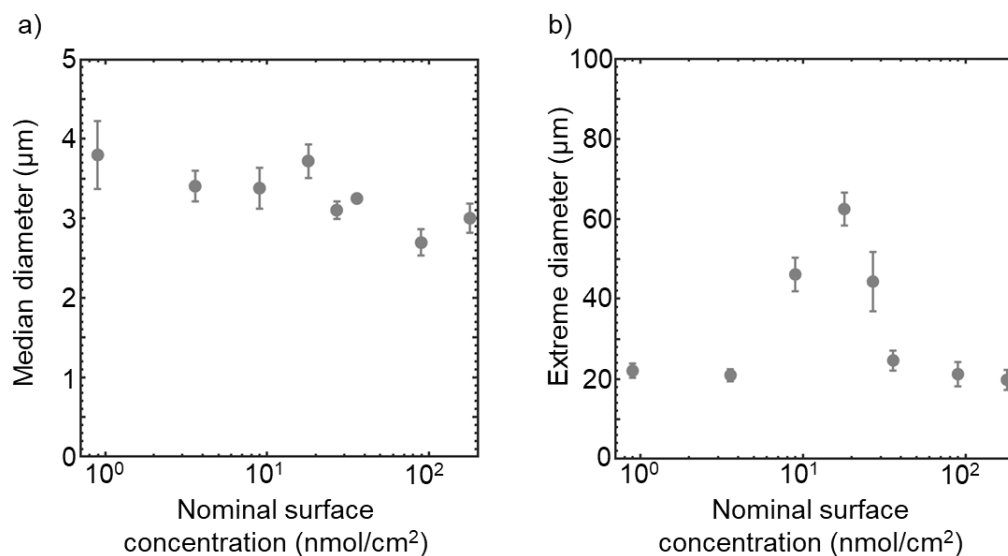


**Figure 2.3:** Median and extreme diameters of GUVs composed of DOPC. Plot of a) the median diameter and b) extreme diameters for each nominal surface concentration averaged over 3 independent runs. The error bars are the standard deviations from the 3 runs.

I also note that the fraction of large vesicles was closely correlated with maximizing the molar yield and fell rapidly as the molar yield dropped below 15%. This can be seen in **Figure 2.3**, which shows the variation of the median diameters and the extreme diameter for each nominal surface concentration. The median diameter did not vary significantly for the first four points until a nominal surface concentration of 18  $\text{nmol}/\text{cm}^2$  following which it dropped from 3.7  $\mu\text{m}$  to a minimum value of 2.7  $\mu\text{m}$  at a concentration of 90  $\text{nmol}/\text{cm}^2$ . The extreme diameter<sup>36</sup> was calculated as the average diameter of the 100 largest GUVs in each sample. I note that the variation of extreme diameters mimics the peaked shape of the molar yield curve, with its maximum value occurring at the same concentration at which the molar yield peaks, 18  $\text{nmol}/\text{cm}^2$ .



### 2.3.2. Yields of charged lipids at varying surface concentrations

To determine the impact of charge on yields, I varied the surface concentration of negatively charged lipids DOPG, DOPS and DOTAP on nanocellulose. Each lipid type was doped with 0.5 mol% Top-Fluor Cholesterol for imaging using confocal microscopy but was otherwise composed of a single lipid type. **Figure 2.4** compares the plots of the molar yield at varying nominal surface concentrations of zwitterionic lipid DOPC and charged lipids DOPG, DOPS and DOTAP. The plots show a clear distinction in the evolution of molar yield between lipids with a net neutral headgroup charge (DOPC) and those with a net positive (DOTAP) or negative charge (DOPG, DOPS). The peaked yield of DOPC shown in **Figure 2.4 a)** is in clear contrast with the molar yields for charged lipids which appear in general to rise monotonically with increasing surface concentration, with the rise being steeper at the initial stages and decreasing at the higher concentrations. Note, **Figure 2.4 a)** is a reproduction of the data from Fig 2.1.b) plotted on a linear scale and divided into molar yield of diameters,  $d$ , from 3 size classes,  $1 \mu\text{m} \leq d < 10 \mu\text{m}$ ,  $10 \mu\text{m} \leq d < 50 \mu\text{m}$ , and  $d \geq 50 \mu\text{m}$ . The maximum molar yield is  $21.9 \pm 1.1\%$  for DOPG,  $17.3 \pm 2.6\%$  for DOPS and  $9.7 \pm 1.6\%$  for DOTAP. As noted in the previous section zwitterionic DOPC has an optimum molar yield of 30%. Note that the yield of DOPC is maximized at a nominal surface concentration of  $18 \text{ nmol/cm}^2$  while for DOPG, DOPS and DOTAP, it is at  $177 \text{ nmol/cm}^2$ ,  $174 \text{ nmol/cm}^2$  and  $101 \text{ nmol/cm}^2$  respectively.

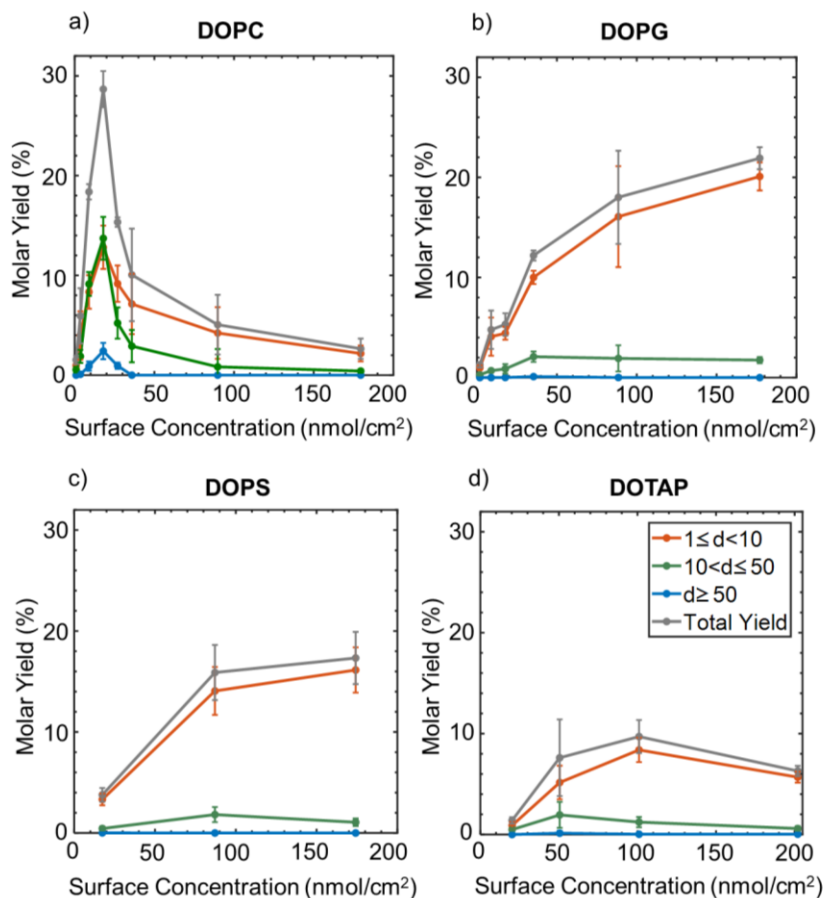


**Figure 2.4:** Variation of molar yield with nominal surface concentration. Different lipid compositions include a) zwitterionic lipid DOPC, b) negatively charged lipid DOPG and c) DOPS, d) positively charged lipid DOTAP. DOPC data was reproduced for comparison purposes from **Figure 2.2**, plotted on a linear scale. The red points represent GUVs with diameter,  $d$ , between  $1 \mu\text{m} \leq d < 10 \mu\text{m}$  (small GUVs), the green points represent GUVs between  $10 \mu\text{m} \leq d < 50 \mu\text{m}$  (large GUVs), and the blue points represent GUVs  $d \geq 50 \mu\text{m}$  (very large GUVs). The gray points are the total molar yield of all GUVs. The lines connecting the points are guides to the eye.

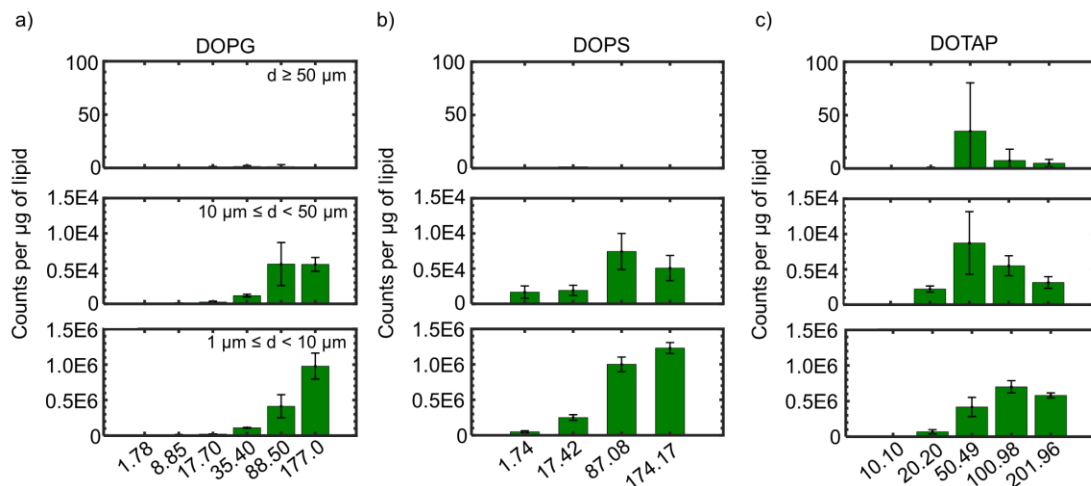


**Figure 2.5:** Bar plots showing counts per microgram of lipid plotted for negatively charged lipids a) DOPG, b) DOPS and c) positively charged lipid DOTAP. The counts are divided into 3 size categories of diameters,  $d$ , between  $1 \leq d < 10 \mu\text{m}$ ,  $10 \leq d < 50 \mu\text{m}$ ,  $d \geq 50 \mu\text{m}$ .

Another important difference between the zwitterionic yields and the yields of charged lipids is the number of large vesicles that are produced. The molar yield of medium-sized vesicles composed of DOPC with diameters between 10 to 50  $\mu\text{m}$  had a maximum value of  $13.7 \pm 2.1\%$  when the total molar yield peaks whereas, the maximum value for DOPG, DOPS and DOTAP are  $2.1 \pm 0.5\%$ ,  $1.8 \pm 0.7\%$  and  $1.9 \pm 1.3\%$  respectively. The molar yield of vesicles composed of DOPC with diameters over 50  $\mu\text{m}$  is  $12.8 \pm 2.2\%$ , almost as high as the molar yield of medium-sized vesicles. For DOPG, DOPS and DOTAP, the maximum value molar yield of vesicles over 50  $\mu\text{m}$  is very small,  $0.013 \pm 0.013\%$  and  $0.013 \pm 0.02\%$  and  $0.13 \pm 0.2\%$  respectively. Note that the errors are large due to sparse presence of very large vesicles and a large sample to sample variation. This is further highlighted in **Figure 2.5** which shows the bar plots of GUVs obtained from the charged lipids divided into 3 size classes. DOPG and DOPS have less than 5 GUVs per microgram of lipid (too low to be seen on the plots) while DOTAP has a maximum of 35 GUVs per microgram of lipid at a concentration of 50  $\text{nmol}/\text{cm}^2$  and drops to 5 GUVs per microgram of lipid at 202  $\text{nmol}/\text{cm}^2$ . These values are consistently lower than the value of 600 GUVs per microgram of lipid for zwitterionic DOPC (**Figure 2.2 c**). Thus, charged lipids form GUVs with much smaller diameters compared to zwitterionic lipids.

### 2.3.3. Yields of mixtures of zwitterionic and charged lipids

I present results from experiments in which charged lipids DOPG, and DOPS were doped into mixtures containing zwitterionic DOPC at varying molar ratios. The mole fraction of DOPG and DOPS were varied between 0 mol% to 100 mol%. I carried out 3 independent runs for each lipid mixture and tested DOPG:DOPC molar ratios of 0:1, 0.005:0.995,

0.05:0.95, 0.25:0.75, 0.5:0.5 and 1:0 mol as well as DOPS:DOPC molar ratios of 0.05:0.95, 0.1:0.9, 0.25:0.75 and 1:0. **Figure 2.6** shows confocal images of harvested vesicles from lipid mixtures composed of varying mole fractions of DOPG and DOPS. Pure DOPC (0 mol% DOPG and 0 mol% DOPS) has the highest density of vesicles as well as a large number of vesicles over 10  $\mu\text{m}$ . Visually, 0.5% DOPG appears to have a slightly lower density of vesicles but has several medium to large vesicles (diameters over 10  $\mu\text{m}$ ). At 5 mol% DOPG, there is a clear reduction in the density and sizes of vesicles, with most of them below 10  $\mu\text{m}$ . The images show qualitatively that this trend continues up to 100 mol% DOPG, which has the lowest number of vesicles across all size ranges with no large vesicles (over 50  $\mu\text{m}$ ) in the image. Confocal images of DOPS mixtures (**Figure 2.6 g** - **j**)) show the same trends as DOPG.

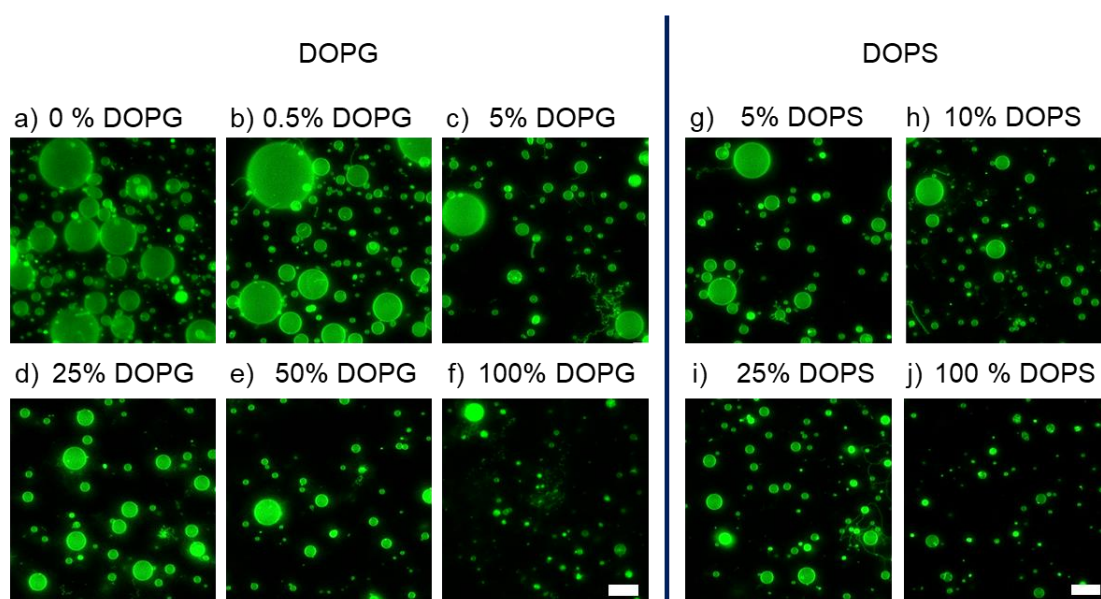


**Figure 2.6:** Representative confocal images of varying mole fractions of negatively charged lipids DOPG and DOPS in mixtures of DOPC. a)-f) show GUVs from mixtures of DOPC and DOPG after harvesting and sedimentation in 100 mM glucose solution. The corresponding mole fractions of DOPG in the mixture is shown above each image. g)-j) show GUVs from mixtures of DOPC and DOPS after harvesting and sedimentation in 100 mM glucose solution. The corresponding mole fractions of DOPS in the mixture is shown above each image. Scale bar: 25  $\mu\text{m}$ .

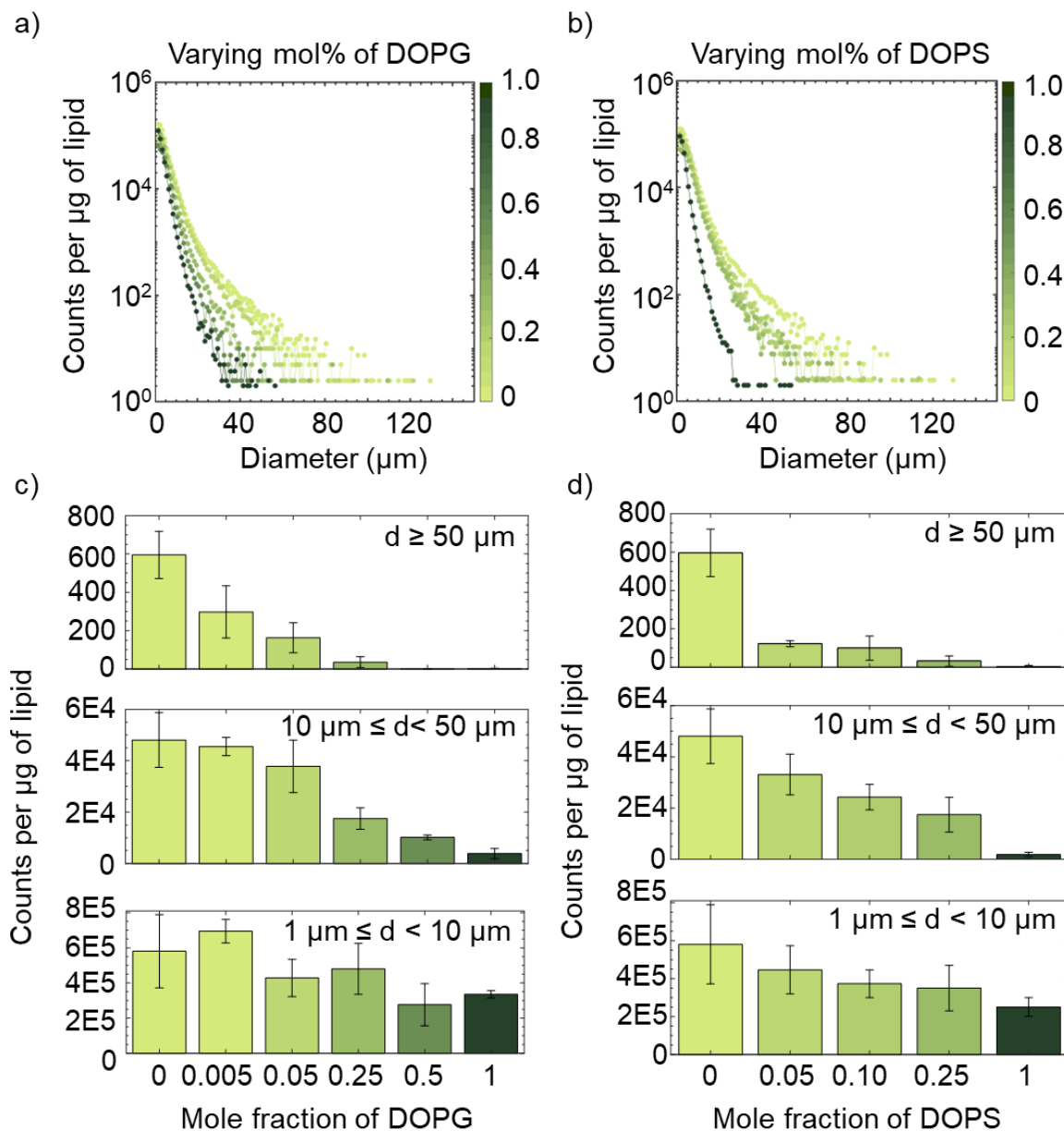


**Figure 2.7:** Plots showing the counts per microgram of lipid at varying mole fractions of negatively charged lipid DOPG and DOPS in zwitterionic lipid DOPC. Histogram of the counts per microgram of lipid at different mole fractions of a) DOPG and b) DOPS. Bin widths are  $1 \mu\text{m}$ . The colour bar on the right shows the colours at different mole fractions of the respective charged lipid. Bar plots of the counts per microgram of lipid divided into 3 size classes at varying mole fractions of c) DOPG and d) DOPS. The 3 size classes show the GUV counts for diameters,  $d$  between  $1 \leq d < 10 \mu\text{m}$ ,  $10 \leq d < 50 \mu\text{m}$  and  $d \geq 50 \mu\text{m}$ . Each point is an average of 3 independent runs. The error bars show the standard deviation. For all the plots, darker colour shades correspond to higher fractions of charged lipids in the mixture.

To quantitatively analyze the differences, I plot the diameters in a histogram and in bar plots that show the vesicle count across different size classes. **Figure 2.7**, a) and b) show the histograms for varying mole fractions of DOPG and DOPS respectively. The size distribution at all mole fractions skews to the right, similar to the histograms shown in sections 2.3 and 2.4. The darker tones in the histogram show a higher mole fraction of charged lipid. With increasing fractions of charged lipid, the histograms show a clear narrowing of the size distributions as well as a steeper drop in counts with increasing diameters.

The bar plots show the effect of charge on small ( $1 \mu\text{m} \leq d < 10 \mu\text{m}$ ), medium ( $10 \mu\text{m} \leq d < 50$ ) and large vesicles ( $d \geq 50 \mu\text{m}$ ) more clearly. For both DOPG as well as DOPS mixtures, the counts decrease with increasing mole fractions of charged lipid across all three size classes (with the exception of 0.005 mole fraction of DOPG), indicating that the total number of vesicles in general drops as with an increase the membrane charge. Vesicles with diameters over  $50 \mu\text{m}$  dropped most steeply. Introducing a mole fraction of 0.005 of DOPG into DOPC, halved the number of large vesicles from  $595 \pm 123$  to  $298 \pm 136$ . The number of vesicles below  $10 \mu\text{m}$  were larger for this lipid mixture, indicating a reduction in merging of micron-scale GUV buds with increasing surface charge. At 0.25 mole fraction of charged lipid, the number of vesicles over  $50 \mu\text{m}$  dropped to  $35 \pm 28$  for DOPG, and  $33 \pm 26$  for DOPS, approximately twenty times lower than for pure DOPC. This trend continued with increasing charge and pure DOPG and DOPS had only  $1 \pm 2$  and  $3 \pm 6$  vesicles respectively. Medium sized vesicles dropped more gradually, ( $10 \mu\text{m} \leq d < 50$ ) from 48,000 vesicles per microgram of lipid for mixtures without charged lipid to 1900 – 3800 vesicles per microgram of lipid for pure charged lipid, which is a drop by a factor of 25 for DOPG and 12 for DOPS. Small vesicles reduced by a factor of 1.7 for DOPG and 2.3 for DOPS.

The effect of charge on the molar yield at a fixed surface concentration is shown in **Figure 2.8**. The plot shows the molar yield decreased continuously but the rate at which it falls slowed down with increasing mole fraction of charged lipid. The molar yield of vesicles across all three size classes decreased as the amount of charged lipid increased. Pure DOPC had the highest molar yield at  $31 \pm 8\%$  and pure DOPG and DOPS have the lowest at  $5 \pm 1\%$  and  $4 \pm 1\%$  respectively. The yield drops to half the maximum value at 0.25 mole fraction for DOPG and DOPS with yields of  $14 \pm 3\%$  and  $13 \pm 1\%$  respectively. The results indicate that with increasing membrane charge, GUVs form less efficiently. This trend is reproduced with two negatively charged lipids with different headgroups.

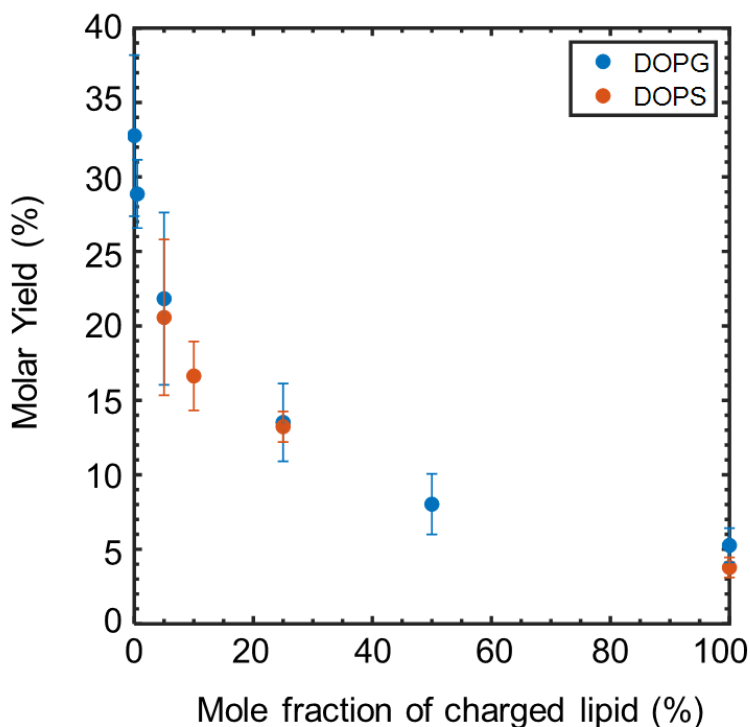


**Figure 2.8:** Plot of the molar yield of the lipid mixture with varying mole fraction of charged lipid. The nominal surface concentration was fixed at  $18 \text{ nmol/cm}^2$ . The blue points show the mole fraction of DOPG, and the red point show the fraction of DOPS in the lipid mixture. Each point is an average of 3 individual runs. The error bars are the standard deviation.

Since surface concentration was an important factor in optimizing yields of both pure zwitterionic as well as charged lipids, I varied the surface concentration of lipid mixtures with 5 mol% DOPG and 25 mol% DOPG. **Figure 2.9** a) and b) show the results of increasing the surface concentration. Interestingly, the yields appear to be peaked, similar to the yields of zwitterionic DOPC, however, the peaks occur at a different nominal surface concentration, depending on the mole fraction of charged lipid. For the lipid mixture containing 5 mol% DOPG, the yields increased from  $18.4 \pm 4.8\%$  at a nominal surface concentration of  $9.0 \text{ nmol/cm}^2$  to a maximum value of  $27.3 \pm 3.6\%$  at  $36 \text{ nmol/cm}^2$ . When the nominal surface concentration was increased further, the yields dropped initially to  $18.8 \pm 3.3$  and then increased to  $22.9 \pm 1.2\%$ . For the lipid mixture containing 25 mol% DOPG, the yields increased from  $12.1 \pm 5.1\%$  at a nominal surface concentration of  $9.0 \text{ nmol/cm}^2$  to a peak value of  $28.8 \pm 4.3\%$  at  $90 \text{ nmol/cm}^2$ . When the nominal surface concentration was further increased to  $179 \text{ nmol/cm}^2$ , the yield dropped to  $21.5 \pm 6.9\%$ . Comparing the highest yields of the lipid mixtures, I note that most of the yield was recovered when the surface concentration is increased to the optimum value.

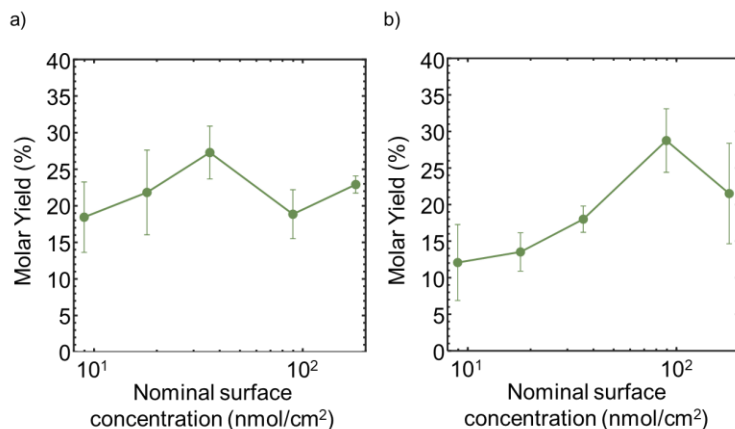


**Figure 2.9:** Yields and distributions of varying surface concentrations of lipid mixtures composed of DOPC and DOPG. Plots showing evolution of the molar yield with surface concentrations for lipid mixtures composed of DOPC and a) 5 mol% DOPG and b) 25 mol% DOPG.

Since the optimal yields of DOPG at 5 mol%, 25 mol% and 100 mol% are comparable to the yield of pure DOPC, I compare the histogram of sizes in **Figure 2.10** to determine whether there were differences in sizes. I note here that the GUV size distribution narrows with increasing charge, indicating that even though the yields of charged lipids were recovered by increasing the surface concentration, the presence of charged headgroups reduces the number of large vesicles. The largest vesicles for 0 and 5 mol% DOPG was over 100  $\mu\text{m}$  in diameter. This dropped to 74  $\mu\text{m}$  for 25 mol% DOPG and 36  $\mu\text{m}$  for 100 mol% DOPG.

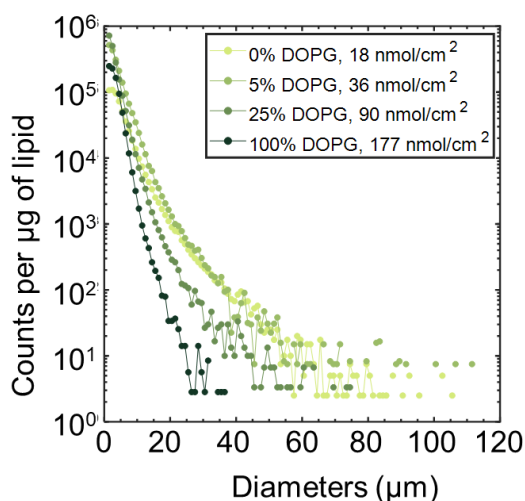


**Figure 2.10:** Histograms of diameters of GUVs obtained from lipid mixtures composed of mixtures containing 0 mol%, 5 mol%, 25 mol %, and 100 mol% of DOPG at the optimum surface concentration of each mixture. Bin widths are 1  $\mu\text{m}$ .



## 2.4. Conclusions

I showed that the evolution of the yields of DOPC is non-monotonic with surface concentration. The yield was optimized at a maximum value of 30% at narrow concentration range close to 18 nmol/cm<sup>2</sup> and was closely correlated to the number of large vesicles particularly vesicles with diameters over 50 μm. On the other hand, the yields of anionic lipids DOPG and DOPS and cationic lipid DOTAP varied dramatically in comparison to zwitterionic lipid DOPC across different surface concentrations. The yields of all the charged lipids were low at a surface concentration of 18 nmol/cm<sup>2</sup> but increased with increasing surface concentrations, plateauing at a yield of 25% for DOPS and DOPG and at 10% for DOTAP. I also showed that when the concentration is fixed at 18 nmol/cm<sup>2</sup>, the optimum concentration of pure DOPC, both the molar yield and the sizes of GUVs composed of lipid mixtures of zwitterionic and charged lipids fell systematically with increasing mole fraction of the anionic charged lipids DOPG and DOPS. The molar yields were mostly recovered when the surface concentrations of mixtures containing 5 mol% and 25 mol% of charged lipid were increased. This detailed quantitative data is the first of its kind collected in the field. These results enables the optimization of the yields of lipids, depending on the lipid type. This is particularly useful to open up avenues into larger-scale production for applications that require cell mimics. The quantitative evolution of yields has important implications for the building mechanistic models of GUV assembly which are discussed in the next chapters.

## 2.5. Bibliography

- (1) Angelava, M. I.; Dimitrov, D. S. Swelling of Charged Lipids and Formation of Liposomes on Electrode Surfaces. *Mol. Cryst. Liq. Cryst. Inc. Nonlinear Opt.* **1987**, *152*, 89–104.
- (2) Estes, D. J.; Mayer, M. Electroformation of giant liposomes from spin-coated films of lipids. *Colloids Surfaces B Biointerfaces* **2005**, *42*, 115–123.
- (3) Vance, J. E. Phospholipid Synthesis and Transport in Mammalian Cells. *Traffic* **2015**, *16*, 1–18.
- (4) Nelson, G. J. Lipid composition of erythrocytes in various mammalian species. *Biochim. Biophys. Acta* **1967**, *144*, 221–232.
- (5) Malanovic, N.; Lohner, K. *Antimicrobial peptides targeting Gram-positive bacteria*; 2016; 9, 59.
- (6) Epanand, R. M.; Epanand, R. F. Lipid domains in bacterial membranes and the action of antimicrobial agents. *Biochim. Biophys. Acta - Biomembr.* **2009**, *1788*, 289–294.

- (7) Mariño, G.; Kroemer, G. Mechanisms of apoptotic phosphatidylserine exposure. *Cell Res.* **2013**, *23*, 1247–1248.
- (8) Fadok, V. A.; Bratton, D. L.; Rose, D. M.; Pearson, A.; Ezekewitz, R. A. B.; Henson, P. M. A receptor for phosphatidylserine-specific clearance of apoptotic cells. *Nature* **2000**, *405*, 85–90.
- (9) Agassandian, M.; Mallampalli, R. K. Surfactant phospholipid metabolism. *Biochim. Biophys. Acta - Mol. Cell Biol. Lipids* **2013**, *1831*, 612–625.
- (10) Levchenko, T. S.; Rammohan, R.; Lukyanov, A. N.; Whiteman, K. R.; Torchilin, V. P. Liposome clearance in mice: The effect of a separate and combined presence of surface charge and polymer coating. *Int. J. Pharm.* **2002**, *240*, 95–102.
- (11) Lee, J. S.; Ankone, M.; Pieters, E.; Schiffelers, R. M.; Hennink, W. E.; Feijen, J. Circulation kinetics and biodistribution of dual-labeled polymersomes with modulated surface charge in tumor-bearing mice: Comparison with stealth liposomes. *J. Control. Release* **2011**, *155*, 282–288.
- (12) Owens, D. E.; Peppas, N. A. Opsonization, biodistribution, and pharmacokinetics of polymeric nanoparticles. *Int. J. Pharm.* **2006**, *307*, 93–102.
- (13) Akashi, K. I.; Miyata, H.; Itoh, H.; Kinoshita, K. Preparation of giant liposomes in physiological conditions and their characterization under an optical microscope. *Biophys. J.* **1996**, *71*, 3242–3250.
- (14) Akashi, K. I.; Miyata, H.; Itoh, H.; Kinoshita, K. Formation of giant liposomes promoted by divalent cations: Critical role of electrostatic repulsion. *Biophys. J.* **1998**, *74*, 2973–2982.
- (15) D’Onofrio, T. G.; Hatzor, A.; Counterman, A. E.; Heetderks, J. J.; Sandel, M. J.; Weiss, P. S. Controlling and measuring the interdependence of local properties in biomembranes. *Langmuir* **2003**, *19*, 1618–1623.
- (16) Stein, H.; Spindler, S.; Bonakdar, N.; Wang, C.; Sandoghdar, V. Production of isolated giant unilamellar vesicles under high salt concentrations. *Front. Physiol.* **2017**, *8*, 1–16.
- (17) Rodriguez, N.; Pincet, F.; Cribier, S. Giant vesicles formed by gentle hydration and electroformation: A comparison by fluorescence microscopy. *Colloids Surfaces B Biointerfaces* **2005**, *42*, 125–130.
- (18) Li, Q.; Wang, X.; Ma, S.; Zhang, Y.; Han, X. Electroformation of giant unilamellar vesicles in saline solution. *Colloids Surfaces B Biointerfaces* **2016**, *147*, 368–375.
- (19) Moncelli, M. R.; Becucci, L.; Guidelli, R. The intrinsic pK<sub>a</sub> values for phosphatidylcholine, phosphatidylethanolamine, and phosphatidylserine in monolayers deposited on mercury electrodes. *Biophys. J.* **1994**, *66*, 1969–1980.
- (20) Akashi, K. I.; Miyata, H.; Itoh, H.; Kinoshita, K. Preparation of giant liposomes in physiological conditions and their characterization under an optical microscope.

*Biophys. J.* **1996**, *71*, 3242–3250.

- (21) Magome, N.; Takemura, T.; Yoshikawa, K. Spontaneous formation of giant liposomes from neutral phospholipids. *Chem. Lett.* **1997**, No. 3, 205–206.
- (22) Walde, P.; Cosentino, K.; Engel, H.; Stano, P. Giant Vesicles: Preparations and Applications. *ChemBioChem* **2010**, *11*, 848–865.
- (23) Gilbale, D.; Docto, D.; Kingi, D. T.; Kurniawan, J.; Monahan, D.; Tang, A.; Kuhl, T. L. How Well Can You Tailor the Charge of Lipid Vesicles? *Langmuir* **2019**, *35*, 15960–15969.
- (24) Mahnke, J.; Stearnes, J.; Hayes, R. A.; Fornasiero, D.; Ralston, J. The influence of dissolved gas on the interactions between surfaces of different hydrophobicity in aqueous media. Part I. Measurement of interaction forces. *Phys. Chem. Chem. Phys.* **1999**, *1*, 2793–2798.
- (25) Suleiman, E.; Damm, D.; Batzoni, M.; Temchura, V.; Wagner, A.; Überla, K.; Vorauer-Uhl, K. Electrostatically driven encapsulation of hydrophilic, non-conformational peptide epitopes into liposomes. *Pharmaceutics* **2019**, *11*, 619.
- (26) Lütgebaucks, C.; Macias-Romero, C.; Roke, S. Characterization of the interface of binary mixed DOPC:DOPS liposomes in water: The impact of charge condensation. *J. Chem. Phys.* **2017**, *146*.
- (27) Aliu, H.; Rask, C.; Brimnes, J.; Andresen, T. L. Enhanced efficacy of sublingual immunotherapy by liposome-mediated delivery of allergen. *Int. J. Nanomedicine* **2017**, *12*, 8377–8388.
- (28) Herrington, T. M.; Midmore, B. R. Adsorption of Ions at the Cellulose / Aqueous Electrolyte Interface. *J. Chem. SOC., Faraday Trans. 1* **1984**, *80*, 1525–1537.
- (29) Edelson, M. R.; Hermans, J. Flow of gels of cellulose microcrystals. II. Effect of added electrolyte. *J. Polym. Sci. Part C Polym. Symp.* **2007**, *2*, 145–152.
- (30) Kučerka, N.; Tristram-Nagle, S.; Nagle, J. F. Structure of fully hydrated fluid phase lipid bilayers with monounsaturated chains. *J. Membr. Biol.* **2006**, *208*, 193–202.
- (31) Caffrey, M. *Lipid Thermotropic Phase Transition Database (LIPIDAT)*; NIST standard reference database; U.S. Department of Commerce, National Institute of Standards and Technology, Standard Reference Data Program, 1993.
- (32) Pan, J.; Herberle, F. A.; Tristram-Nagle, S.; Szymanski, M.; Koepfinger, M.; Katsaras, J.; Kucerka, N. Molecular structures of fluid phase phosphatidylglycerol bilayers as determined by small angle neutron and X-ray scattering. *BBA - Biomembr.* **2013**, *1818*, 2135–2148.
- (33) Petrache, H. I.; Tristram-Nagle, S.; Gawrisch, K.; Harries, D.; Parsegian, V. A.; Nagle, J. F. Structure and Fluctuations of Charged Phosphatidylserine Bilayers in the Absence of Salt. *Biophys. J.* **2004**, *86*, 1574–1586.

- (34) Koltover, I.; Salditt, T.; Safinya, C. R. Phase diagram, stability, and overcharging of lamellar cationic lipid- DNA self-assembled complexes. *Biophys. J.* **1999**, *77*, 915–924.
- (35) Hirsch-Lerner, D.; Barenholz, Y. Probing DNA-cationic lipid interactions with the fluorophore trimethylammonium diphenyl-hexatriene (TMADPH). *Biochim. Biophys. Acta - Biomembr.* **1998**, *1370*, 17–30.
- (36) Pazzi, J.; Subramaniam, A. B. Nanoscale Curvature Promotes High Yield Spontaneous Formation of Cell-Mimetic Giant Vesicles on Nanocellulose Paper. *ACS Appl. Mater. Interfaces* **2020**, *12*, 56549–56561.

## Chapter 3: Model and Simulations of varying surface concentration of zwitterionic lipid

### 3.1. Introduction

In the previous chapter, I reported quantitative data that showed the effect surface concentration on the yields and distributions of GUVs. Here I carry out simulations on MATLAB in which I vary the surface concentration of zwitterionic lipid using the budding and merging model as a framework. In section 3.2, I describe the set-up of the simulation. In section 3.3, I describe results from simulations.

The yields of zwitterionic lipid can be summarized using the schematic in **Figure 3.1**. At lower lipid concentrations, I expect the fibers to be coated with fewer bilayers while at higher lipid concentrations, fibers will be templated with more bilayers. The schematic shows the configuration of the surfaces before and after hydration at varying lipid concentrations. The sparse coverage of the lipid at lower concentrations, results in a low number of buds. I also expect the first bilayer to exhibit strong adhesion to the cellulose fibers, preventing budding of single or partial bilayers. As the lipid concentration on the surface is increased, more bilayers are available to bud, resulting in a larger number of nanobuds. This explains the increase in yield up to a peak concentration of  $18 \text{ nmol/cm}^2$ . However, increasing the surface concentration further resulted in a reduction of yields, with yield of  $2.67 \pm 1.02$  for a concentration of  $179 \text{ nmol/cm}^2$ . This decrease in yield can be explained using the budding and merging model.

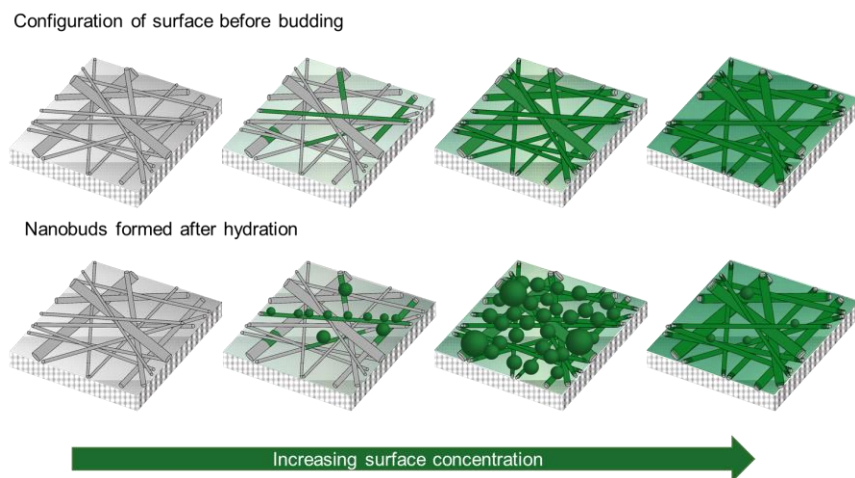


**Figure 3.1:** Schematic showing surface coverage and yields with increasing surface concentration of DOPC. As the nominal surface concentration increases, more of the fibers are coated with increasing number of fibers forming multilayers. For higher nominal surface concentrations most fibers are coated with multilayers. Fibers are coated sufficiently that budding is no longer spontaneous and any buds that form do so due to

external energy. In this scenario the number of GUVs and their sizes will increase and then decrease with increasing nominal surface concentrations.

The budding and merging model has previously shown that the substrate on which lipids are templated affects the energy pathways available for nanobud formation<sup>1</sup>. The energy of budding of membranes templated on cylindrical fibers is given by Equation (5). Building on the previously published model, the contributions of each concentric bilayer  $n$  with thickness,  $d$ , were explicitly considered, which results in  $R_c = R_f + nd$ . Performing this substitution into Equation (5), we obtain the following equation:

$$\Delta E_{RB} = \pi\kappa_B \left( 8 - \frac{L_f}{R_f + nd} \right) + 4\pi(R_f + nd)\gamma - 2\pi(R_f + nd)L_c\xi \quad (7)$$

Here,  $\kappa_B$  is the bending rigidity,  $\gamma$  is the edge energy, and  $\xi$  is the adhesion energy.  $R_f$  is the radius of the fiber. The variable  $L_c$  in equation (5) is the critical length, which refers to the length of the membrane section that results in a single bud. A bilayer can bud either in its entirety, forming a single bud or as multiple segments, forming multiple buds<sup>1</sup>. For simplicity, we assume that the critical length is equivalent to the length of the fiber  $L_f$ , and so each bilayer forms one bud. **Figure 3.2 a)** shows a transverse schematic of different numbers of bilayers templated on a fiber of radius 20 nm. With increasing numbers of bilayers, the radius of the outermost bilayer increases, thus reducing the curvature of the of bilayer. Solving for  $\Delta E \leq 0$ , we obtain that the following equation:

$$n^* \leq \frac{1}{d} \left( \frac{4\kappa_B - \left( 2\kappa_B(8\kappa_B + 2\lambda L_f - \xi L_f^2) \right)^{\frac{1}{2}}}{2\xi L_f - 4\lambda} - R_f \right) \quad (8)$$

Here,  $n^*$  is the critical number of bilayers above which the net energy of budding is positive, causing the budding process to become non-spontaneous. Bilayers with  $n \leq n^*$  can bud spontaneously while bilayers with  $n \geq n^*$  will require energy input to bud.

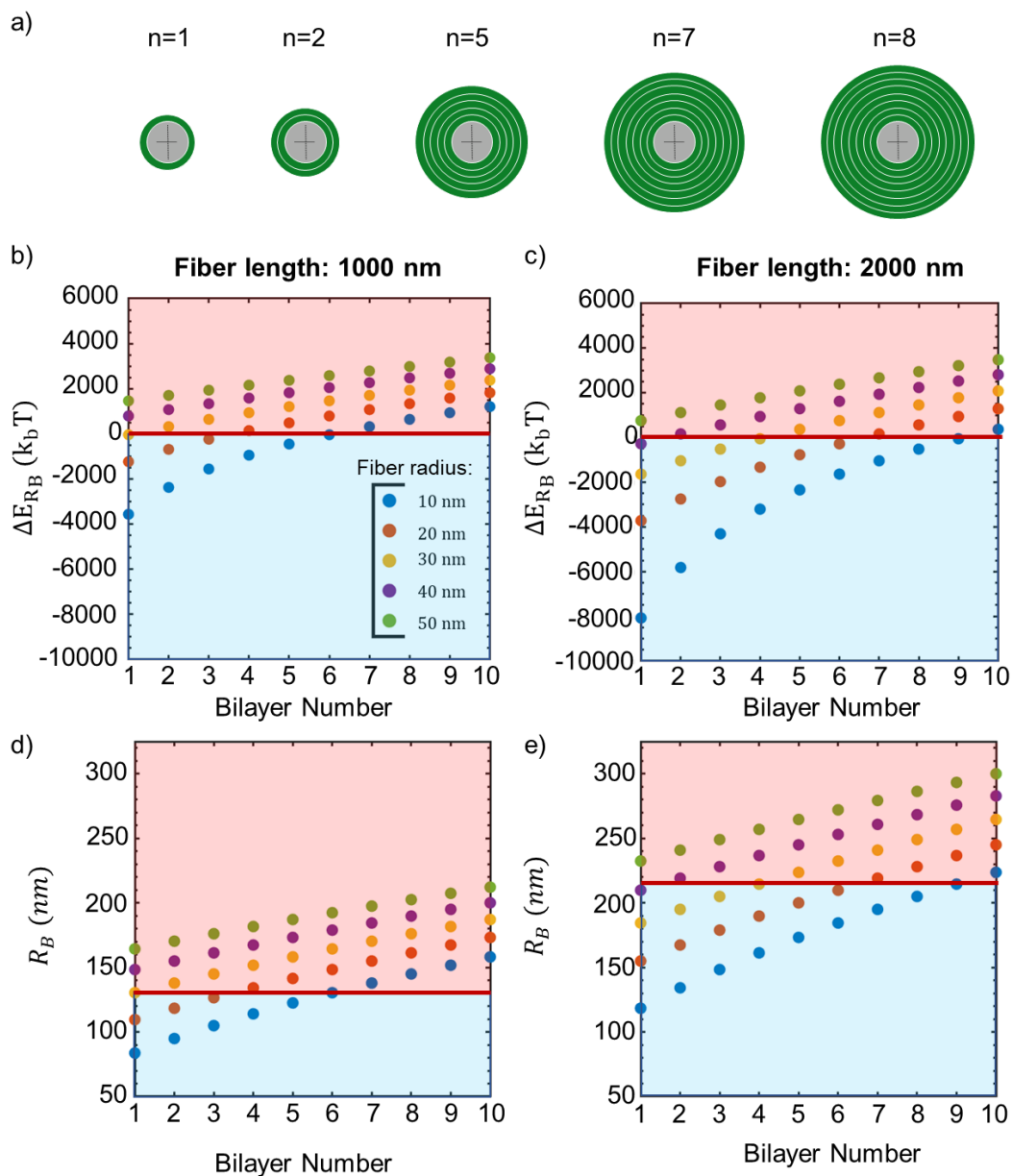


**Figure 3.2:** Effect of increasing number of bilayers on fibers of varying geometries. a) Transverse schematic showing a fiber (gray filled circles) covered with increasing numbers,  $n$  of concentric bilayers (green lines). The radius of the outermost bilayer increases with each progressive bilayer. Plots of the budding energy vs the number of bilayers and the on the surface for five fibers with radii indicated in the legend for fiber length of b) 1000 nm and c) 2000 nm. The y-axis is the budding energy normalized by  $k_B T$ . The red shaded area indicates positive changes in free energy for budding, the blue area indicated negative changes in free energy for budding. For a given fiber diameter, increasing concentric bilayers causes the budding energy to increase, eventually resulting in positive budding energy. Larger fiber lengths can support larger number of bilayers with a negative budding energy. At this point, budding is no longer spontaneous. The bud radius

$R_B$  obtained from d) 1000 nm fibers and e) 2000 nm fibers. With increasing numbers of bilayers the bud radius obtained increases. Larger fibers have larger bud sizes. The red shaded area indicates configurations where buds do not form spontaneously.

**Figure 3.2** b) and c) show the relationship between the bilayer number  $n$  and the budding energy  $\Delta E$ . The radius of the fiber  $R_f$  and the length  $L_f$  play a crucial role in determining the energy of budding. The budding energy always becomes more positive with increasing  $n$ . In all cases, the second bilayer for example, will have a more favorable energy of budding compared to the 8<sup>th</sup> bilayer. Mathematically, higher values of  $n$  result in the first term of equation (7) becoming more positive. Conceptually, at higher values of  $n$ , the curvature of the bilayer templated on the fiber is reduced. A negative energy of budding entails that the configuration of lipid in a spherical bud is more favorable than the configuration of lipids as a cylinder. As  $n$  increases in value, the curvature of the bilayer templated on the fiber is reduced, resulting in a lower energy cost in remaining in its current state. When  $n > n^*$ , the process of budding does not release energy but instead requires an energy penalty in the absence of which budding cannot occur. Lower fiber radii can support more bilayers before  $n$  exceeds the critical value of  $n^*$  due to their larger curvature. For example, a fiber of radius 20 nm radius and 2000 nm fiber length can support 6 concentric bilayers before the budding of the outermost bilayer becomes non-spontaneous. On the other hand, none of the bilayers on a fiber 50 nm in radius on either fiber length can bud spontaneously. Aside from curvature, the aspect ratio of the fiber, varied by changing the length of a fiber for a given radius also impacts the number of bilayers that can bud spontaneously on the fibers. Higher values of  $L_f$  cause in the first term in equation (7) to become more negative. Comparisons of b) and c) illustrate that longer fibers have a higher  $n^*$  value. For a given radius of 10 nm, fibers that are 1000 nm has an  $n^*$  value of 6 bilayers whereas fibers that are 2000 nm long have an  $n^*$  value of 9 bilayers. **Figure 3.2** d) and e) show the impact of changing fiber geometry as well as the bilayer number. Bilayers with larger  $n$  value have more surface area, and a result more lipid molecules, forming larger nanobuds. Similarly, fibers with larger lengths and radii result in larger buds.

### 3.2. Simulation set up

The simulation was set up and carried out on MATLAB as described in this section. The overall concept of the simulation is to calculate the number of nanobuds that form using the equations of the budding and merging model, given values for 7 parameters followed by merging the nanobuds to form GUVs.

#### Budding

I set the number of sites  $N$  to be 1000. Each of these sites was a single cylindrical fiber with a radius,  $R_f$  and length  $L_f$ . The first step in simulating the assembly of GUVs was to ‘coat’ the fibers with lipid. This was done by assigning bilayers to each site, assuming each



bilayer had a thickness of 4 nm and was wrapped around the fiber in concentric cylinders. In experiments, I used a Hamilton syringe to spread 10  $\mu\text{L}$  of lipid dissolved in chloroform at the appropriate concentration to deposit lipid on a fixed area of substrate. This manual application results in local variations in concentration which I mimic in the simulations by randomizing the distribution of bilayers on the fibers. Since the assignment of bilayers to each fiber is independent of all other fibers, I use a Poisson distribution to determine the distribution of bilayers on the fibers. I use the *poisspdf* function on MATLAB which produces a Poisson probability mass function with the form:  $f(n|\lambda) = \frac{\lambda^n}{n!} e^{-\lambda}$ . In this equation,  $\lambda$  is the average number of bilayers on the sites and  $n = \{0,1,2, \dots, 40\}$  is the number of bilayers at a given site. I use two cylindrical geometries  $R_f \times L_f$ : 20 nm  $\times$  1000 nm and 20 nm  $\times$  2000 nm at a 2:1 ratio of surface area of nanocellulose paper. I obtain the number of fibers with a given bilayer using the following Equation (9):

$$N_{bilayers} = Nf(n|\lambda) \quad (9)$$

**Figure 3.3** shows the resulting distributions for two different values of  $\lambda$ , the mean value of the Poisson distribution. With increasing  $\lambda$ , a larger number of sites have more bilayers. The number of empty sites is higher at lower values of  $\lambda$  and drops as  $\lambda$  increased. The function  $f(n|\lambda)$  produces a matrix of probabilities for discrete values of  $n$ . Using Equation (9) produces a matrix containing the number of sites with  $n$  bilayers for  $n = \{0,1,2, \dots, 40\}$ .

The nominal surface concentration was calculated by determining the moles of lipid in the bilayers coating the fibers. The area of the surface was calculated as the two dimensional area occupied by the 1000 fibers as shown in **Figure 3.3** b), similar to how the area of the nanocellulose substrate was calculated as the area of the circular disk. The moles of lipid on each fiber,  $m_s(i)$ , given  $n(i)$  conformal bilayers with thickness  $d$  coating it is given by Equation (10).

$$m_s(i) = \frac{4\pi}{A_{hg}N_a} \sum_{n(i)=1}^{n(i)} (R_f + n(i)d)L_f(i) \quad (10)$$

$$M_s = \sum_{i=1}^N m_s(i) \quad (11)$$

The nominal surface concentration is thus,

$$NSC = \frac{M_s}{A_s} \quad (12)$$

Where area of the surface  $A_s$  for 1000 fibers with geometries specified is  $5.32 \times 10^{-7} \text{ cm}^2$ .

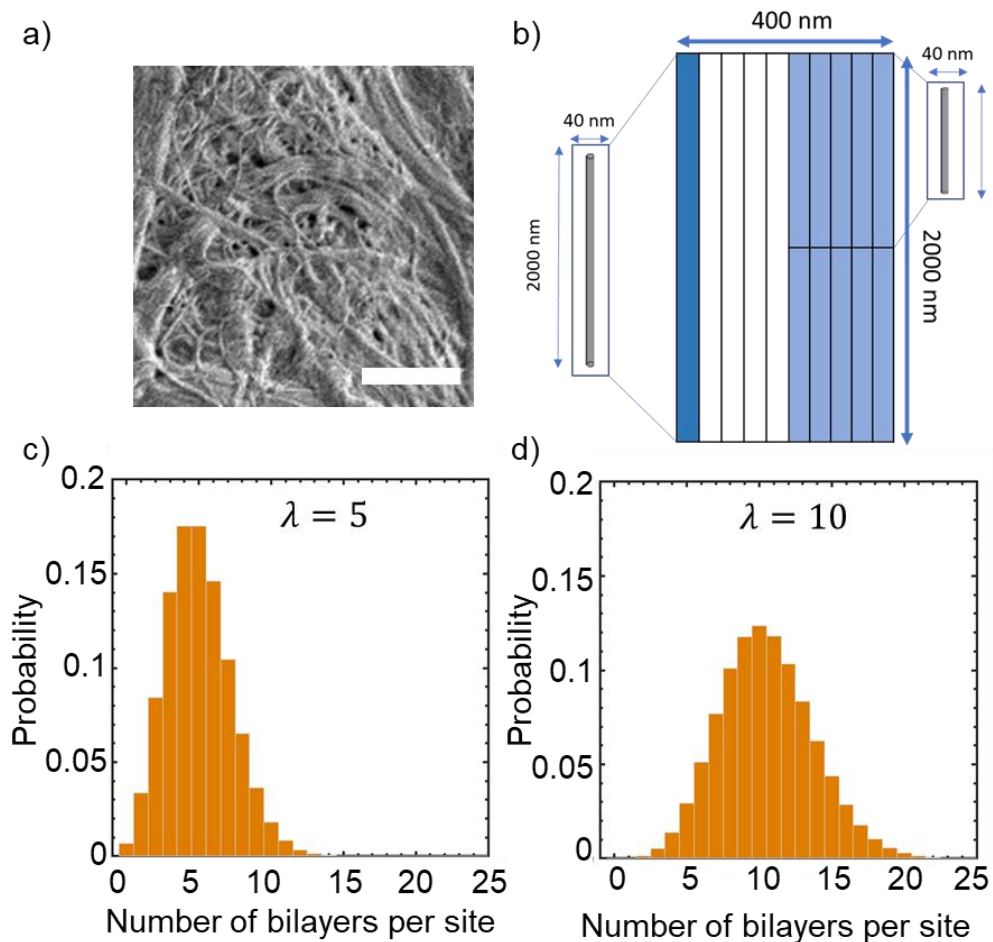


**Figure 3.3:** Simulation set up details. a) Scanning electron microscope image of nanocellulose showing a network of fibers. b) Simplified model of fibers used in the simulation. Two fiber sizes,  $R_f = 20$  nm,  $L_f = 1000$  nm and  $R_f = 20$  nm,  $L_f = 2000$  nm. The simulated area was calculated as the 2-D area shown. Poisson probability distributions for two different mean values of c) 5 and d) 10.

Each bilayer has an area that is a function of the geometry of the fiber and its sequence number  $n(i)$  with  $n(i) = 1$  being the bilayer closest to the fiber. Equations 10 to 12 were implemented on MATLAB by first generating a matrix containing the number of bilayers with a given  $n(i)$  on each fiber type. Equation 10 was applied to calculate the moles in all bilayers with a given  $n(i)$ . The resulting matrix was summed to determine the total moles of lipid for all  $n(i)$  on all fibers. The resulting value was divided by the area of the simulation  $A_S$  to determine the nominal surface concentration.

Once the lipid has been distributed across the fibers, the next stage of the simulation determined which bilayers form buds. The first assumption we make regarding the process of budding is that the bilayers bud sequentially from the outer bilayers. Therefore, on a fiber with five bilayers, the fifth and outermost bilayer buds first, exposing the fourth

bilayer which then buds, followed by the third bilayer and then the second bilayer. The second assumption we make is that the first bilayer which is the bilayer in contact with the substrate experiences high adhesion to the substrate and therefore does not bud even when exposed to the hydrating solution. Although it is possible for a single bilayer to form breaks in the membrane and form multiple nanobuds, for the sake of simplicity, in the simulation, each bilayer corresponds to a single nanobud. Outer bilayers have a larger area, since they have a larger radius and therefore form larger nanobuds.

In experiments, the act of pipetting the growth solution into the chamber is expected to introduce energy into the system as a result of the hydrodynamic flows and hydration of the lipid headgroups. To account for this energy, we added an impulse of external energy as a parameter in my simulation which was present only at the initial stage as a sharp impulse with no decay time. Thus, buds can form via two pathways, external energy, and spontaneous budding.

I determined the fraction of sites that bud due to the impulse of energy using the generic partition function in Equation (13):

$$\Phi = \Phi_0 \exp\left(-\frac{\Delta E_{R_B}}{W(\Delta t_i)}\right) \quad (13)$$

Here,  $\Phi_0 = 1$ ,  $\Delta E_{R_B}$  is the energy for forming a bud of radius  $R_B$ , and  $W$  is the energy available to perform work on the site at the point of hydration set to  $20,000 k_b T$  ( $8.2 \times 10^{-17}$  J). The number of bilayers that bud due to external energy ( $B_{ext}$ ) were calculated using Equation (14):

$$B_{ext} = \Phi N_{bilayers} \quad (14)$$

Once we determine which bilayers bud due to external energy, we determined the energy of budding of the bilayers which were exposed. The budding energy was calculated using Equation (7), which determines whether the budding of a certain bilayer is spontaneous. As described in section 3.1, if the energy is negative, bud formation is exergonic and therefore favorable. All bilayers with a negative budding energy were allowed to bud in the simulation. Outermost bilayers with a positive energy were allowed to bud via the external energy pathway in the initial stage. Any other bilayers with a positive budding energy were not allowed to bud. **Table 3.1** shows the parameters that were used in the simulations. The radius and lengths,  $R_f$  and  $L_f$  were set at the values shown below but were altered subsequently to determine their effect on yields.

Parameter	Symbol	Value	Unit
Fiber radius	$R_f$	20	nm
Fiber length	$L_f$	1000, 2000	nm
Number of sites	-	1000	-
Bilayer thickness	$d$	$4^2$	nm
Headgroup area	$A_{hg}$	$0.724^3$	$\text{nm}^2$
Edge energy	$\gamma$	$1 \times 10^{-11}$	J/m
Bending rigidity	$\kappa_B$	$8.5 \times 10^{-20}$	J
Adhesion energy	$\xi$	$6 \times 10^{-6}$	$\text{J/m}^2$

**Table 3.1:** Table showing common parameters and their values used in the simulations.

**Figure 3.4** shows the process used to determine the number of buds that form. Using the calculations from Equations 13 and 14 an array was produced containing the number of outer bilayers of each  $n(i)$  that bud due to external energy (**Figure 3.4 c**). All values were rounded down and only whole bilayers were considered. The first bilayer was assumed to adhere strongly to the substrate and was not allowed to bud under any circumstance. Next, the largest bilayer number with a negative budding energy as identified as shown in **Figure 3.4 d**). This is the 3<sup>rd</sup> bilayer on 1000 nm fibers. All subsequent rounds of budding were set to occur without any external energy, therefore only bilayers that can bud spontaneously will do so. **Figure 3.4 e**) shows **Figure 3.4 c**) reproduced, highlighted with sites that will have 3 or fewer bilayers after budding due to external energy. Sites that initially had 4 bilayers will now have 3 bilayers, of which both the 3<sup>rd</sup> and the 2<sup>nd</sup> bilayer will be able to bud. Similarly, sites that had 3 bilayers will now have 2 bilayers of which just the 2<sup>nd</sup> bilayer can bud. Sites that had 2 bilayers, however, will now have only 1 bilayer which cannot bud. **Figure 3.4 f**) shows the sum of the bilayers that bud spontaneously as well as due to external energy.

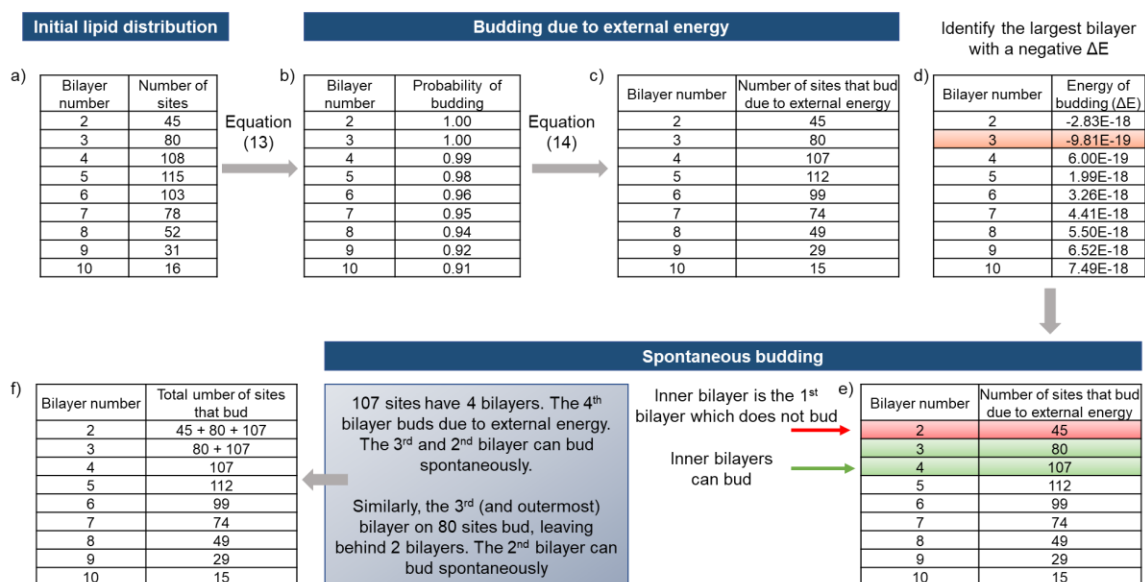


**Figure 3.4:** Flow of the simulation process on MATLAB for determining the number of nanobuds that bud. The tables show the samples of arrays for fibers with a length of 1000 nm. Arrays show a) the number of sites with 2 – 10 bilayers b) probability of budding of each bilayer calculated using equation 13, c) the number of sites with 2 – 10 bilayers that bud due to external energy calculated using equation 14, d) The energy of budding for each bilayer calculated using equations 5 or 6 depending on the substrate type. e) is the array in c) replicated to highlight the number of sites that have exposed inner bilayers that can bud spontaneously. f) shows the total number of bilayers that can bud either spontaneously or via external energy.

All bilayer larger than the 3<sup>rd</sup> bilayer cannot bud since subsequent rounds of budding will not have external energy from the remaining bilayers, all bilayers with a positive energy of budding were excluded since subsequent rounds of budding were set to occur without any external energy. Only sites with a negative energy of budding of the outer bilayers were considered for the next step. A matrix of all the bilayers with a negative energy of budding including the inner bilayers was generated. This was combined with the bilayers that budded as a result of external energy to produce a matrix of all bilayers that could bud. The bilayer counts were converted to areas and a list of nanobud diameters was calculated.

### Simulation set up on glass

On glass or geometries where the surface does not have features which can be defined as sites, buds are expected to form by forming breaks in the lipid layering the substrate<sup>1</sup>. It is likely that these breaks are of varying areas, resulting in buds of different sizes. Here, for simplicity, I use a single size, a disk of radius  $R_d = 335$  nm. The number of sites is also set

to 1000 for consistency. I use a Poisson distribution to determine the number of bilayers per site. The moles deposited on the surface is calculated using the following Equation:

$$M_s = \sum_{i=1}^N \frac{2\pi R_d^2 n}{A_{hg} N_a} (i) \quad (15)$$

The nominal surface concentration is calculated using the Equation (16):

$$NSC = \frac{M_s}{\pi R_d^2 N} \quad (16)$$

The energy of budding on a flat surface such as glass is given by the following equation:

$$\Delta E_{flat} = 8\pi\kappa_B + 2\pi R_d \gamma - \pi R_d^2 \xi \quad (17)$$

All other simulation steps were identical between cylindrical and flat geometries.

## Merging

### Merging strategy using a template to carry out recursive merging

Merging of spherical buds, which occurs by rearranging the membrane, is favored because it decreases the total elastic free energy of the surface<sup>1</sup>. On the surface of the nanopaper in experiments, the micrometer-sized buds span many fibers. Confocal images of microbud merging can be seen within minutes of hydration nanocellulose coated with lipid<sup>1</sup>. Microbud merging occurs primarily in regions with a high density of buds when they are in close proximity to each other. Fewer instances of merging are seen in regions where buds are sparser and spaced farther apart. We assume that nanobud merging is based on similar principles. Given a fixed substrate area, a higher density of nanobuds will result in a larger number of merging events. we use the concept of a merging ‘template’, which is a set of cluster sizes. Each cluster represents the number of nanobuds chosen to merge into a single larger bud. To model this process, I implement an iterative algorithm that selects and merges point-like buds **Figure 3.5** that are organized randomly on lattice sites.

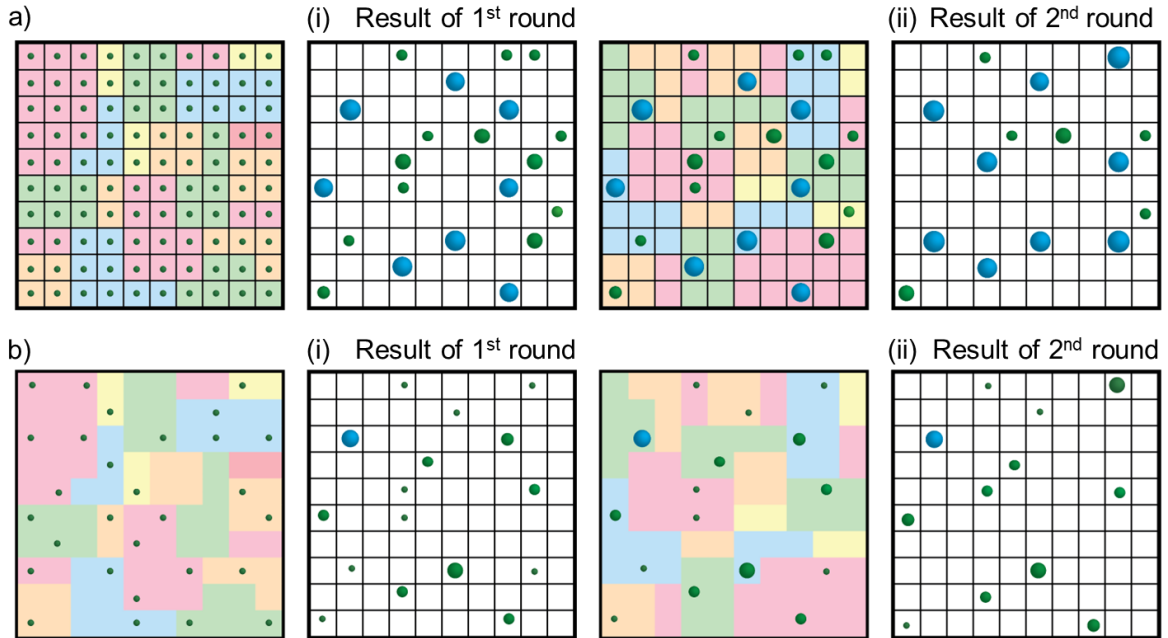


**Figure 3.5:** Schematic of the merging template. Two rounds of recursive merging shown starting with a) a high density of nanobuds and b) a low density of nanobuds distributed randomly across the sites. Different blocks of colour show different cluster sizes. Buds within a block of colour will merge into a single bud. The sites present in each cluster are chosen randomly. The green buds are nanometer-sized buds, and the blue buds are micrometer sized buds. Only the blue micrometer buds contribute to the yield.

The following equation is used to assign to assign the number of lattice sites in bins  $x(i)$ :

$$N(i) = 5 \times 10^8 x(i)^{-1.5} \quad (18)$$

The value of  $i$  ranges from 1 to 10 and maps one-to-one to the sizes of the clusters,  $x(i) = \{10, 25, 50, 100, 500, 1000, 5000, 10000, 20000, 50000\}$ . The total number of sites,  $N_{tot}$  is calculated using the following equation:

$$N_{tot} = \sum_{i=1}^{10} x(i)N(i) \quad (19)$$

I use the nominal surface concentration with the highest number of nanobuds as our lattice size,  $N_{tot}$  (**Figure 3.5** a). For concentrations with lower nominal surface concentration, we leave blank sites (Fig 3 b (i)). We then select clusters of lattice sites randomly (colored squares) and merge all the buds that fall within a cluster (Fig 3a,b (ii)).

The number of clusters is set such that all sites are chosen. We repeat the process, rearranging the selected lattice sites while keeping the total number of sites of a given number selected for each round the same. The concept of nanobud density affecting the merging was incorporated by adding zeros (empty sites in **Figure 3.5**) so that the total sites was constant. Increasing the number of zeros while maintaining the template keeps the number of buds chosen per cluster the same, however, the effective cluster size decreases since the number of non-zero buds in each cluster decreases. I allowed 5 rounds of recursive merging to occur for each concentration. For the first round, the merging template was applied to the initial nanobud distribution. After merging, I added zeros to keep the total number of sites constant and applied the same merging template for the second time. I repeated this process 5 times for each concentration.

Examples of how the distributions vary with increasing rounds of merging are shown in **Figure 3.6**. After the first round of merging, the number of GUVs is sparse, the number of merging events is not sufficient to convert nanobuds into microbuds. After the second round of merging, the distribution appears to look similar to the histograms obtained from experiments – the distributions are right tailed, with significantly more small vesicles than large ones. This is expected since smaller vesicles require fewer merging events compared to larger vesicles which results in a higher probability of obtaining a small vesicle. With further rounds of merging, the number of small vesicles decreases while the number of larger vesicles increase. **Figure 3.6 d**) shows the variation of molar yields with each round of simulations. The number of rounds of merging was limited to 5 since the molar yield stabilizes within 5 rounds. Further details about the types of merging routines and a detailed comparison of histograms are provided in Appendix A.

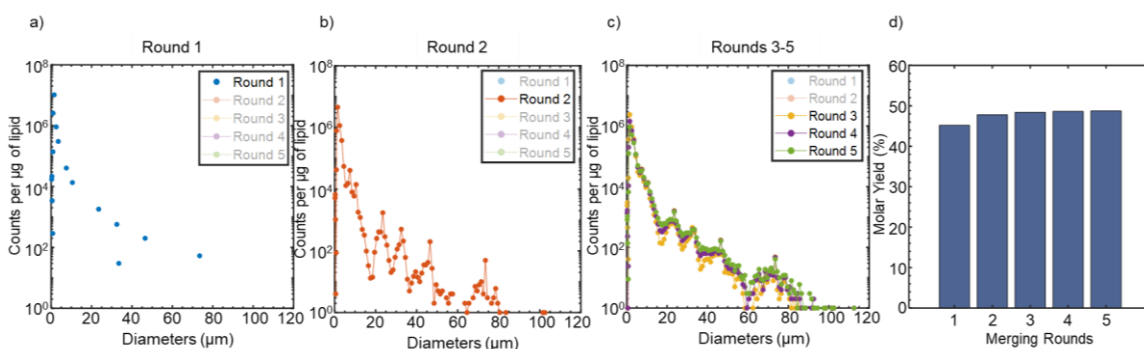


**Figure 3.6:** Histogram of diameters obtained at low salt (0.0032 mM) after different rounds of merging. a) 1 round of merging b) 2 rounds of merging and c) 3 – 5 rounds of merging. With increasing rounds of merging, the number of large vesicles increase while the number of small vesicles decrease. d) Bar plots showing the molar yield after each round of merging.



### Yield calculations

I obtain a list of GUV produced upon merging of the nanobuds for each salt concentration. The molar yield is calculated using the following equation:

$$MY = 100 \left( \frac{2\pi}{A_{hg} N_a M_S} \sum_{j=1}^n (d_j)^2 \right) \quad (20)$$

In this equation,  $A_{hg}$  is the headgroup area,  $N_a$  is Avogadro's constant,  $N, d_j$  is the diameters of the GUVs and  $n$  is the total number of GUVs. The counts per  $\mu\text{g}$  lipid were calculated using the following equation:

$$N_{\mu g} = \frac{1}{M_S M_W} \sum_{i=1}^n N_{GUV(i)} \quad (21)$$

In equation (21),  $N_{\mu g}$  is the GUV counts per bin,  $N_{GUV(i)}$  is the number of GUVs in each bin and  $M_w$  is the molecular weight of the lipid molecule.

### 3.3. Simulating varying surface concentration

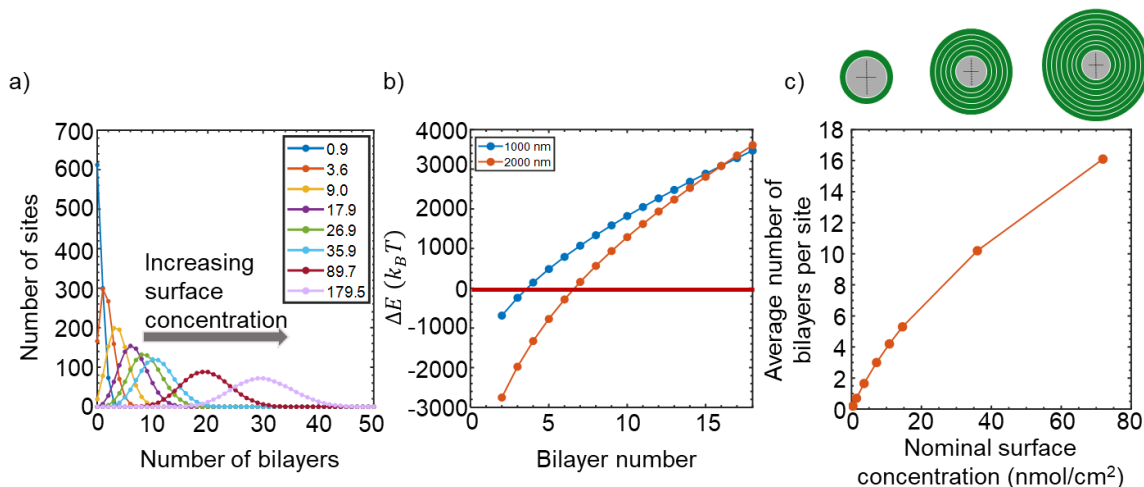


**Figure 3.7:** Configuration of lipids on the fibers at varying surface concentrations. a) Poisson distribution with different values of  $\lambda$ . Legend shows the nominal surface concentration corresponding to each curve. b) Budding energy of each bilayer templated on fibers that have a radius of 20 nm and a length of either 1000 nm (blue) or 2000 nm (red). c) Above the plot: schematic of fibers templated with 1, 5 and 8 bilayers. Plot shows the average number of bilayers per site at different nominal surface concentrations.

The simulations to vary surface concentration were carried out using the parameters in

**Table 3.1** and the merging template as described in section 3.2. I tested a range of nominal surface concentrations from 0.45 nmol/cm<sup>2</sup> to 354.75 nmol/cm<sup>2</sup> which corresponded to a mean value of the Poisson distribution from 0.25 to 44.7 bilayers. **Figure 3.7** shows how the configuration of bilayers changes with at different nominal surface concentrations. **Figure 3.7 a)** shows the number of sites with a certain number of bilayers for concentrations that match the experimental values. At the lowest surface concentration of 0.45 nmol/cm<sup>2</sup>, 78% of the sites were empty. With increasing surface concentration, the number of empty sites decreased to zero as the curves shifted towards a larger number of bilayers. At high concentrations such as 179.5 nmol/cm<sup>2</sup>, all sites are filled, and the mean number of bilayers is approximately 30. The energy of budding of each bilayer is shown in **Figure 3.7 b)** for fibers with radii of 20 nm and lengths of either 1000 nm (blue) or 2000 nm (red). Bilayers with negative budding energies were able to bud spontaneously while bilayers with positive budding energies could only bud using external energy. Fibers with lower aspect ratios support fewer bilayers that can spontaneously bud. Only the second and third bilayers could bud spontaneously on 1000 nm fibers which had a 50% lower aspect ratio compared to 2000 nm fibers of the same radius on which bilayers 2 – 6 could bud spontaneously. **Figure 3.7 c)** shows the variation of average number of bilayers per site

with nominal surface concentration. With increasing surface concentrations, the average number of bilayers increased as expected. The panel above the plot shows a cross section of fibers of 20 nm radius templated with 1, 5 and 8 bilayers. The radius of the bilayer templating the fiber increased with an increasing number of bilayers.

The simulation results are shown in **Figure 3.8**. The budding and merging model remarkably reproduced the peaked behavior of the molar yield curve that was seen in the experimental results. The highest value of the molar yield is 60% and occurred at a nominal surface concentration of 5.78 nmol/cm<sup>2</sup>. The molar yield curve is also asymmetric about the peak value, the rise to the peak concentration being steeper than the fall to lower molar yields. The counts per microgram of lipid show that the counts for the two larger size classes peaks at the same nominal surface concentration as the molar yield, indicating that like in the experiments, the number of large vesicles obtained is highly correlated with molar yield. The results demonstrate that the principles of the budding and merging model with respect to surface concentration is the key factor in affecting yields. At very low surface concentrations, many sites only have a single bilayer, which cannot bud due to its affinity to the cellulose fibers. As the concentration is increased, additional bilayers are templated onto the fibers that can bud spontaneously. At high concentrations, most of the bilayers cannot bud spontaneously, and therefore do not bud, resulting in a lower molar yield. I note that the highest molar yield obtained from simulations was 60%, twice the molar yield obtained from experiments. Since the simulation are an idealized form of the process, this is not unexpected. In reality, nanopaper is porous, which likely results in lipids penetrating and getting trapped in the inner layers of the substrate. There can also be other source of losses in experiments that are not accounted for in the simulations such as losses during harvesting, transfer, and imaging. Another key difference is that the fibers of nanocellulose are polydisperse, with a range of radii and lengths. Fibers of larger radii and shorter lengths will enable fewer bilayers to bud whereas longer and thinner fibers will enable larger numbers of bilayers to bud.

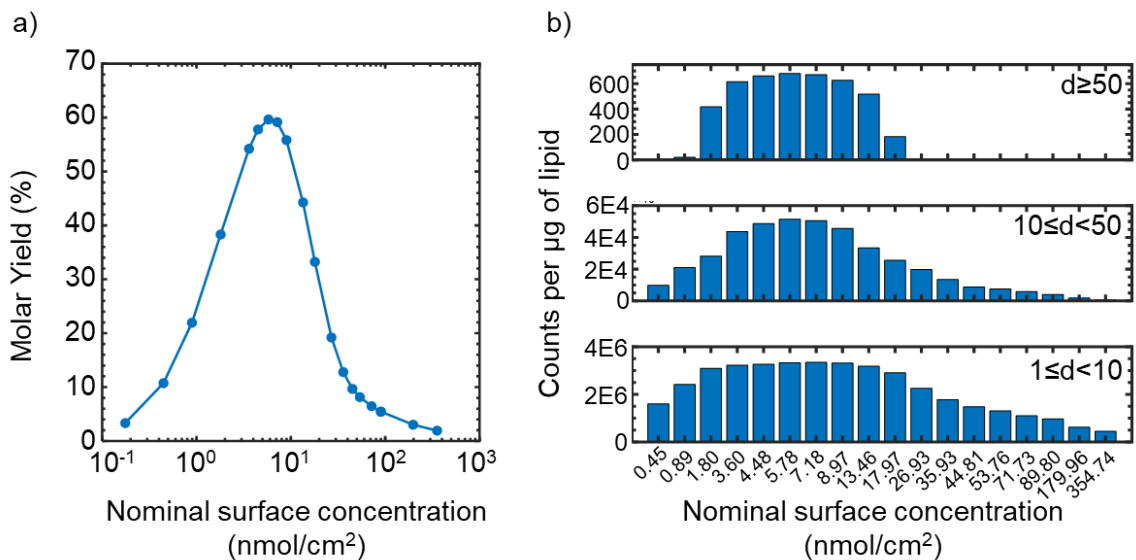


**Figure 3.8:** Simulation results for varying surface concentration of lipid on the substrate. a) Molar yield of GUVs obtained from the simulation at different nominal surface concentrations shows a peaked yield. b) Counts per microgram of lipid for different nominal surface concentrations divided into 3 size classes with diameters,  $d$  between  $1 \leq d < 10 \mu\text{m}$ ,  $10 \leq d < 50 \mu\text{m}$ ,  $d \geq 50 \mu\text{m}$ . Counts for diameters larger than  $10 \mu\text{m}$  are also peaked.

### 3.3.1. The molar yield is maximized when the fraction of sites with a negative budding energy is maximized

Since the simulations were able to mimic the yield curve and the size distributions seen in the experiments, I investigated further to determine the factor(s) that were critical to maximizing molar yield. **Figure 3.9** shows a plot of the fraction of sites for which the outermost bilayer has a positive budding energy (red curve) or negative budding energy (blue curve). The gray curve represents sites that have zero bilayers and therefore do not contribute to the molar yield. The fraction of zero bilayers was highest for the lowest nominal surface concentration of  $0.45 \text{ nmol/cm}^2$  and decreased with increasing surface concentration. There were no empty sites above a concentration of  $13.44 \text{ nmol/cm}^2$ . The fraction of sites with an outer bilayer that has a positive energy of budding is zero for concentrations up to  $0.89 \text{ nmol/cm}^2$  but increases as more bilayers are added to the sites with increasing surface concentration. Above nominal surface concentrations of  $53.63 \text{ nmol/cm}^2$ , all sites have outer bilayers with a positive energy of budding and any budding can only occur in the presence of external energy. The fraction of sites with a negative budding energy has a peaked curve, similar to the molar yield curve. I found that the molar yield peaks at the nominal surface concentration that has the highest fraction of sites with outer bilayers that have a negative budding energy. This can be explained using the

schematic of fibers in **Figure 3.9**. The gray in the center represents a cross section of a fiber. The first bilayer is colored in red and does not bud under any circumstance. Green bilayers can bud spontaneously, and orange bilayers have a positive energy of budding and can only bud due to external energy. When 5 bilayers are templated onto the surface, bilayers 2-5 will bud. However, when 8 bilayers are templated onto the fiber, even if the outer bilayer can bud due to external energy, the bilayer below cannot do so since it also has a positive energy of budding. Since it cannot bud, it prevents the bilayers below from budding despite their ability to bud spontaneously. Thus, the energy of the outermost bilayer is crucial to determining whether any of the bilayers templated on a fiber can bud. When the fibers are templated with the maximum number of bilayers that can bud spontaneously, the molar yield is maximized.

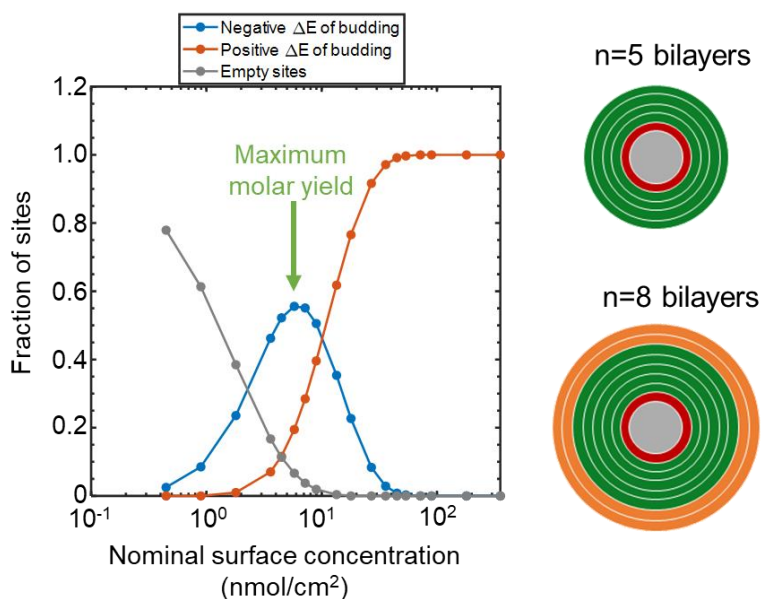


**Figure 3.9:** Fraction of bilayers with different budding energies. The simulation templated bilayers on fibers with radii of 20 nm and lengths of 1000 nm and 2000 nm distributed in a 1:1 ratio by area.. Fraction of bilayers that have a positive (red) or negative (blue) energy of budding or are empty (gray) at different nominal surface concentrations. The molar yield peaks at the concentration with the highest fraction of sites that have an outer bilayer with a negative energy of budding and can bud spontaneously.

### 3.3.2. Effect of varying the fiber geometry on the molar yield and counts of GUVs

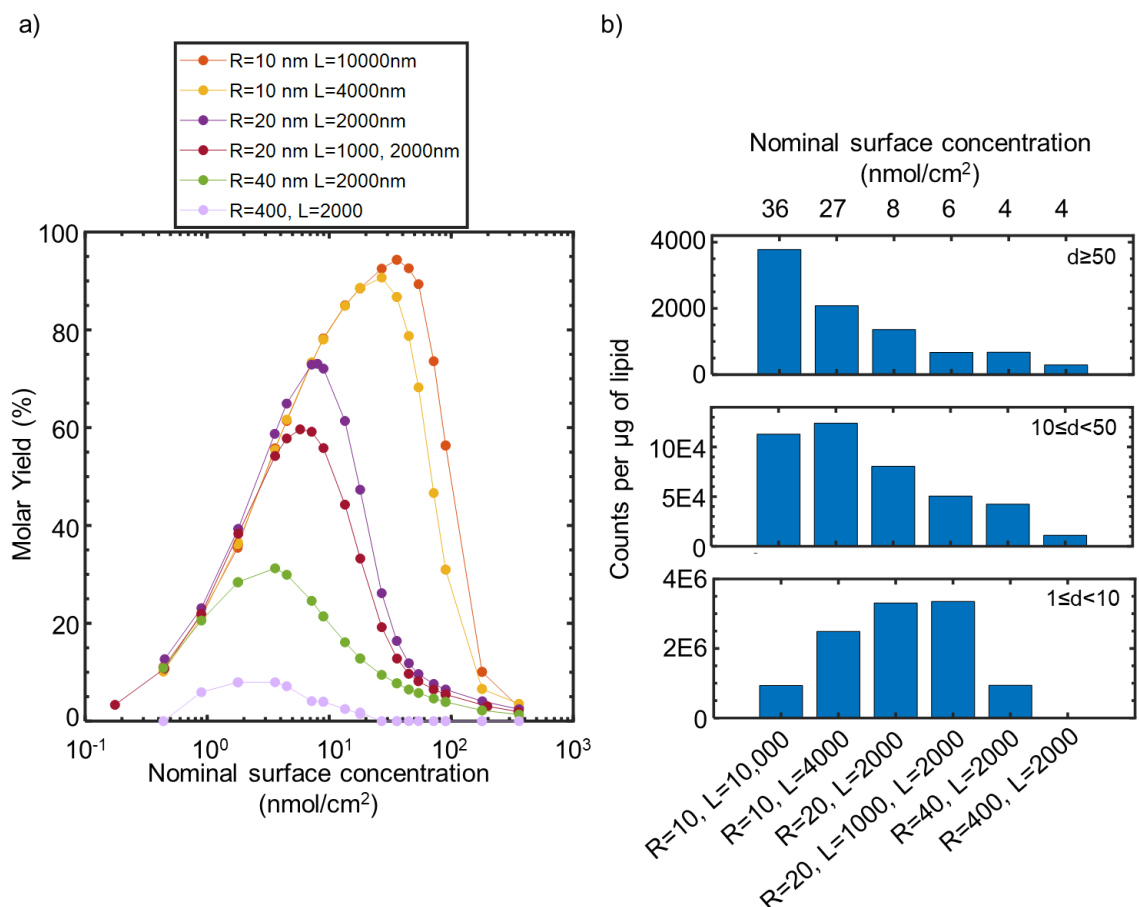


**Figure 3.10:** Yields and size distributions of GUVs assembled on fibers of varying geometries. a) Evolution of molar yields with varying surface concentrations on different fiber geometries. The legend shows fiber dimensions with radius,  $R$  and length,  $L$ . The molar yield of GUVs on a fibers shows a peaked behavior. b) Counts per microgram of lipid for the nominal concentrations at which the molar yield peaks. The x-axis at the bottom shows the fiber geometries and the x-axis at the top shows the nominal surface concentration at which the molar yield is maximized. The counts are divided into 3 size classes with diameters,  $d$  between  $1 \leq d < 10 \mu\text{m}$ ,  $10 \leq d < 50 \mu\text{m}$ ,  $d \geq 50 \mu\text{m}$ .

In section 3.1, I noted that the fiber geometry is an important factor in determining the budding energy of the bilayers templated on the substrate. Here, I use the simulations to show the effect of fiber geometry on GUV yields. In **Figure 3.10 a)**, I compare the evolution of molar yields with increasing surface concentration on fibers of different geometries. I note that the yields are peaked for all fiber geometries but the maximum yield that can be obtained varies depending on the fiber dimensions. Increasing the radius of the fiber reduces its curvature, which results in a decrease in the maximum molar yield.

Conversely, increasing the aspect ratio of the fibers by increasing the length, or decreasing the radius increases the molar yield. I previously showed that fibers with a mixed geometry of lengths of 1000 nm and 2000 nm and fixed radius of 20 nm produced a maximum yield of 60%. When the substrate was simulated with monodisperse fibers that were 2000 nm length with the radius fixed at 20 nm, the yield increased to 70%. An increase in the curvature by lowering the radius to 10 nm, as well as an increase the aspect ratio by increasing the length to 4000 nm raised the maximum yield to 91%. A further increase in the aspect ratio by increasing the fiber length to 10,000 nm while maintaining the radius at 10 nm increased the yield slightly more to a value of 94%. Conversely, a reduction in curvature by increasing the radius from 20 nm to 35 nm while keeping the length constant at 2000 nm reduced the yield by a factor of 2.25 to 31%. A large decrease in curvature was introduced by increasing the radius to 400 nm while maintaining the length at 2000 nm which caused the maximum yield to drop to 8%.

I note that the nominal surface concentration at which the molar yield is maximized also increases with increasing curvature and aspect ratio. For the two lowest yielding fiber dimensions tested which were fibers of radius 400 nm and 35 nm and constant lengths of 2000 nm, the yield was maximized at a nominal surface concentration of 4 nmol/cm<sup>2</sup>. Fibers of the same length but with radii of 20 nm caused the molar yield peak to occur at surface concentrations of 8 nmol/cm<sup>2</sup>. For fibers with radii of 10 nm and lengths of 4000 nm and 10,000 nm, the molar yield peaked at 27 nmol/cm<sup>2</sup> and 36 nmol/cm<sup>2</sup> respectively.

**Figure 3.10** b) shows the counts per microgram of lipid for the surface concentrations at which the molar yield is maximized for each fiber geometry. Vesicles with diameters over 50 μm decreased in number with decreasing curvature and aspect ratio. Vesicles with diameters between 10 μm and 50 μm largely followed the same trend with the exception of an increase when fibers with a radius of 10 nm and length of 10000 nm are reduced to a length of 4000 nm. The small vesicles (diameters below 10 μm) peak for fibers with a radius of 20 nm and length of 2000 nm. I also determined that the reason for the GUV counts in different size classes peaking at different fiber is largely due to an increase in the mean diameter of the nanobuds, which results in larger GUVs after merging. The mean diameter of the nanobuds is 0.79 μm, 0.48 μm and 0.36 μm for fibers with  $R_f \times L_f = 10 \text{ nm} \times 10000 \text{ nm}$ ,  $10 \text{ nm} \times 4000 \text{ nm}$  and  $20 \text{ nm} \times 2000 \text{ nm}$  respectively. Merging of clusters  $\geq 5000$  buds produced vesicles over 50 μm in diameter for nanobuds produced on fibers with  $R_f \times L_f = 10 \text{ nm} \times 10000 \text{ nm}$  whereas only clusters  $\geq 20,000$  produced large GUVs from nanobuds produced on 20 nm fibers. Though fibers that are 40 nm and 400 nm in diameter also have higher mean diameters (0.45 μm and 1.28 μm respectively), they have significantly fewer nanobuds, which results in lower counts across all size classes. 40 nm fibers produce 3.7 times fewer nanobuds than 20 nm fibers, and the increase in nanobud diameter by a factor of 1.2 does not offset this reduction in nanobud counts. Fibers with dimensions  $R_f \times L_f = 10 \text{ nm} \times 10000 \text{ nm}$  produce 3.8 times fewer nanobuds than 20 nm fiber as well. However, since the mean diameters of the nanobuds

produced is 2 times higher, resulting in an increase in 4.7 times more moles of lipid per nanobud, the yield of the nanobuds produced on fibers with  $R_f \times L_f = 10 \text{ nm} \times 10000 \text{ nm}$  is 1.3 times higher than the yield on 20 nm fibers.

### 3.3.3. Molar yield is maximized when the fraction of sites with a negative budding energy is maximized for all fiber geometries with at least 1 bilayer that can bud spontaneously

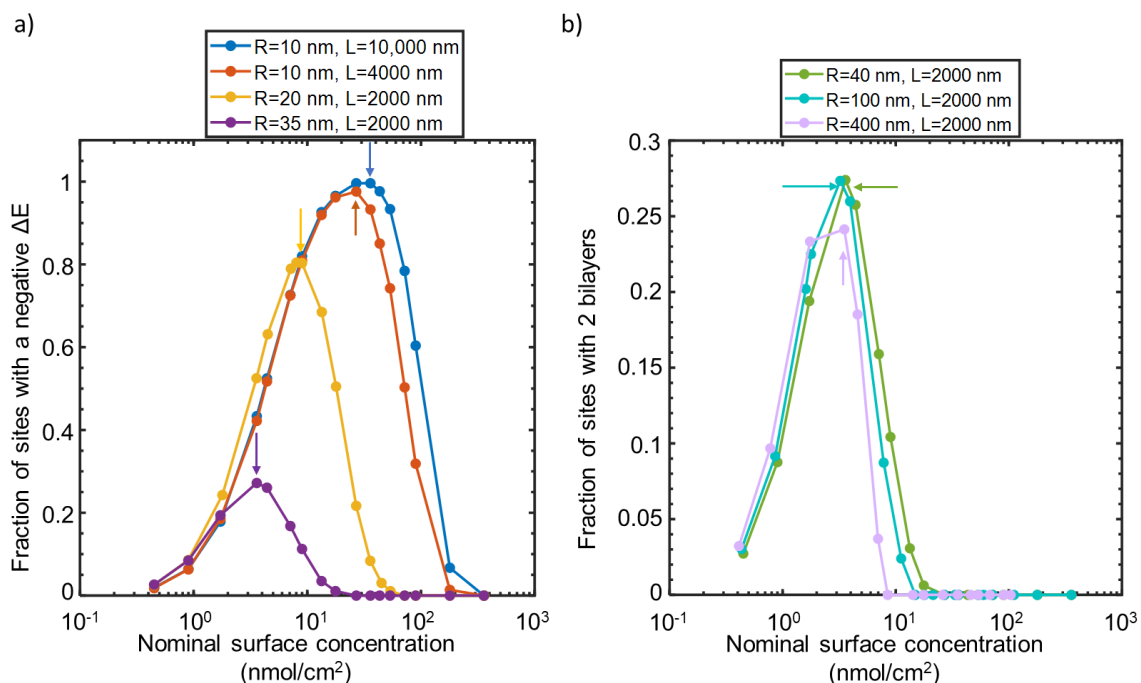


**Figure 3.11:** a) Fraction of bilayers that can bud spontaneously (with a negative  $\Delta E$ ) at varying nominal surface concentrations for different fiber geometries. The colored arrows show the nominal surface concentrations at which the molar yield peaks for each fiber geometry. For all fiber geometries, the molar yield peaks when the fraction of bilayers with a negative  $\Delta E$  is maximized. b) Fraction of sites with two bilayers for fibers that do not support any bilayers that can bud spontaneously. Colored arrows show the nominal surface concentrations at which the molar yield peaks for each fiber geometry. The molar yield peaks when the fraction of sites with two bilayers is maximized. Legends show fiber dimensions with radius, R and length, L.

Using **Figure 3.9**, I determined earlier that the molar yield peaks at the surface concentration at which the fraction of sites with an outer bilayer that has a negative budding energy is maximized. In **Figure 3.11**, I show that this holds true for other fiber dimensions that I tested. **Figure 3.11** a) shows the results for different fiber geometries that have at



least one bilayer that can bud spontaneously. The arrows show the nominal surface concentration at which the molar yield is maximized. Consistent with what was seen in **Figure 3.9**, the molar yield does indeed peak when the fraction of sites with a negative  $\Delta E$  of budding is maximized. Both fiber geometries with radii of 10 nm, have yields above 90%. On fibers with lengths of 4000 nm and 10,000 nm, 97.6% and 99.6% of the sites respectively have outer bilayers that have a negative energy of budding. In comparison, for fibers with a radius of 20 nm, 80.0% of the sites have a negative budding energy and this number falls to 27.2% when the fiber radius is increased to 35 nm.

**Figure 3.11** b) shows plots of fibers that cannot support any spontaneous budding. The molar yield is maximized at the nominal surface concentration which has the highest fraction of sites with 2 bilayers. All budding occurs due to external energy at the initial time point, and so only the outermost bilayer can bud. The wasted lipid is therefore minimized when there are only 2 bilayers on the site, which allows  $\sim 50\%$  of the lipid on a fiber to form a nanobud. This is consistent across all fiber geometries that cannot support any spontaneous budding.

### 3.3.3. Distributing bilayers evenly on fibers increases the maximum yields that can be obtained on all fiber geometries

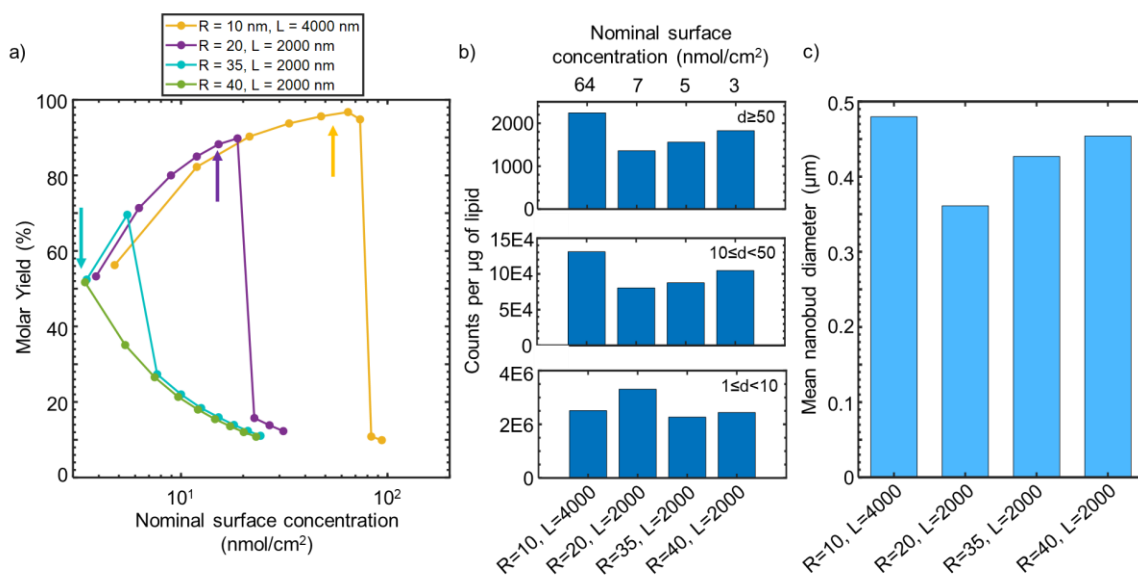


**Figure 3.12:** Yields and size distributions of GUVs assembled on fibers with even numbers of bilayers distributed on all fibers. a) Evolution of molar yields with varying surface concentrations on different fiber geometries with bilayers ranging from 2 to 10 bilayers. The legend shows fiber dimensions with radius, R and length, L. b) Counts per microgram of lipid for the nominal concentrations at which the molar yield peaks. The x-axis at the bottom shows the fiber geometries and the x-axis at the top shows the nominal surface

concentration at which the molar yield is maximized. The counts are divided into 3 size classes with diameters,  $d$  between  $1 \leq d < 10 \mu\text{m}$ ,  $10 \leq d < 50 \mu\text{m}$ ,  $d \geq 50 \mu\text{m}$ .

I showed previously that one way to optimize molar yield is to tailor the fiber geometry to have high curvatures and aspect ratios. Since the Poisson distribution results in sites with a range of bilayers, it is impossible to avoid sites with too many bilayers or fewer bilayers than the optimal number. Here, I test the effect of evenly distributed bilayers on the yields and distributions of GUVs. **Figure 3.12** shows the results of simulations in which I templated monodisperse fibers of varying geometries with even numbers of whole bilayers. All fibers geometries except fibers with a radius of 10 were templated with 2 – 10 bilayers in increments of 1. Fibers with a radius of 10 nm were templated with 2, 4, 6, 8, 10, 12, 13, 14 and 15 bilayers. The range was increased for this fiber geometry since it can support more bilayers that bud spontaneously. It should be noted that even though all bilayers except the first bud for multiple concentrations, the molar yield is variable between these points. For example, on fibers with a radius of 20 nm, all bilayers except the first bilayer bud for the first 6 nominal surface concentration points. However, the molar yield increases with increasing number of bilayers until an optimum number, which in this case is 7 bilayers. This is because as the number of bilayers is increased from 1 – 6, the first bilayer which is the only bilayer responsible for any losses in molar yield accounts for a smaller fraction of the lipid deposited on the fibers. When there are 2 bilayers, the first bilayer accounts for ~ 50% of the lipid, when there are 3 bilayers, it accounts for less than 1/3<sup>rd</sup> of the lipid since the outer bilayers have more area than the first bilayer. In fact, each additional bilayer that is added on fibers with a radius of 20 nm and a length of 2000 nm adds an incremental  $4.6 \times 10^{-19}$  moles of lipid compared to the bilayer below.

The arrows in **Figure 3.12** shows the nominal surface concentrations at which the fraction of bilayers with a negative budding energy is maximized. For  $R_f \times L_f = 10 \text{ nm} \times 4000 \text{ nm}$ , and For  $R_f \times L_f = 40 \text{ nm} \times 2000 \text{ nm}$ , the molar yield is maximized when the sites with a negative budding energy is maximized. For fibers with dimensions  $R_f \times L_f = 10 \text{ nm} \times 4000 \text{ nm}$ , the molar yield peaks at a nominal surface concentration of  $64 \text{ nmol/cm}^2$  which corresponds to 12 bilayers on all fibers. 12 bilayers is also the maximum number of bilayers that can be supported on fibers of this geometry that have a negative budding energy. Similarly, for 40 nm fibers, the yield is maximized when all fibers are coated with 2 bilayers. In fact, for this fiber geometry, coating evenly with two bilayers is the best way to maximize yields. Since all the bilayers bud only due to external energy, using a poison distribution results in wasted lipid due to over filling or under filling the sites. However, I found that on fibers with radii of 20 nm and 35 nm fibers the yield is not maximized when the fraction of sites with a negative budding energy is maximized when the bilayers evenly distributed. The 6<sup>th</sup> bilayer for 20 nm fibers and the 2<sup>nd</sup> bilayer for 35 nm fibers are the outermost bilayers that can bud spontaneously. The yield was maximized when all the fibers had one bilayer number higher, 7 bilayers on 20 nm fibers and 3 bilayers on 35 nm fibers, even though they had positive energies of budding. This is because they require a

low enough energy input that at the 20,000 k<sub>B</sub>T of external energy that I applied, 99.2% of 20 nm fibers with 7 bilayers and 99.73 of 35 nm fibers with 3 bilayers were able to bud. The small losses due to less than 1% of the sites that did not bud was offset by the gain in molar yield as a result of adding an additional bilayer as described in the previous paragraph. Thus, for these two fiber geometries, when lipid was distributed evenly, the yield was maximized when all sites had 1 bilayer more than the outermost bilayer with a negative budding energy. This is not the case when lipids were distributed using the Poisson distribution. It was also not the case for other fiber geometries with even distribution. The lowest bilayer number with a positive budding energy is the 13<sup>th</sup> bilayer for fiber that have  $R_f \times L_f = 10 \text{ nm} \times 4000 \text{ nm}$ . But with 20,000 k<sub>B</sub>T of external energy, 97.54% of all sites bud whereas when all sites have 12 bilayers, 100% of the sites bud. The losses due to 2.5% of the bilayers not budding were not offset by the addition of the 13<sup>th</sup> bilayer. Thus, I show that evenly distributing lipid brings out interesting subtleties in the budding and merging model.

The molar yield is significantly improved for fibers with lower curvature as a result of evenly distributing lipids. For fiber with a radius of 40 nm, the highest possible yield was 52% when lipid was evenly distributed, 65% higher than when lipids were distributed using a Poisson distribution which had a maximum yield of 31%. For fibers with a radius of 35 nm, the yield as a result of evenly distributing lipids increased to 70% from 41% when using a Poisson distribution. For fibers with a radius of 20 nm, the yield increased from 70% using the Poisson distribution to 80% as a result of evenly distributing lipids. The incremental difference is lowest for fibers with  $R_f \times L_f = 10 \text{ nm} \times 4000 \text{ nm}$ , that can support largest amount of bilayers with a negative energy of budding. For these fibers, the yield increased from a maximum value of 91% for Poisson distributed lipid to 97% for evenly distributed lipid. These simulation results show that the molar yield can be maximized either by altering fiber geometry to have low aspect ratios and high curvature or alternatively, if the fiber dimensions are limited to less favorable geometries, by controlling the deposition of lipid very carefully so it is as even as possible at the optimal surface concentration.

When bilayers are evenly distributed, at the optimum bilayer number, the total number of nanobuds that can be produced is optimized. This is particularly clear for the geometries with lower curvature and aspect ratios as can be seen from the difference in molar yields when lipids are evenly distributed compared to when using a Poisson distributed. When the number of nanobuds is maximized, the effect of nanobud diameter plays a larger role is more noticeable since variations in nanobud counts are not large enough to offset the sizes of the nanobuds. **Figure 3.12** b) shows the counts of the GUVs separated into 3 size classes and c) show the mean diameter of the nanobuds produced on different fiber geometries. The nanobud diameters and the counts of GUVs in the two larger size classes are closely correlated, with the counts of the vesicles being maximized for the fibers that have the largest mean diameter. The counts of the smaller vesicles were highest

for fibers with  $R_f \times L_f = 20 \text{ nm} \times 2000 \text{ nm}$  which produces nanobuds with the lowest mean diameter in the dataset. As described earlier (**Figure 3.10**), smaller nanobuds result in smaller GUVs after merging, and particularly when the nanobud counts are maximized across fiber geometries as they are in this case.

### 3.3.4. The presence of external energy increases the yields and sizes of GUVs

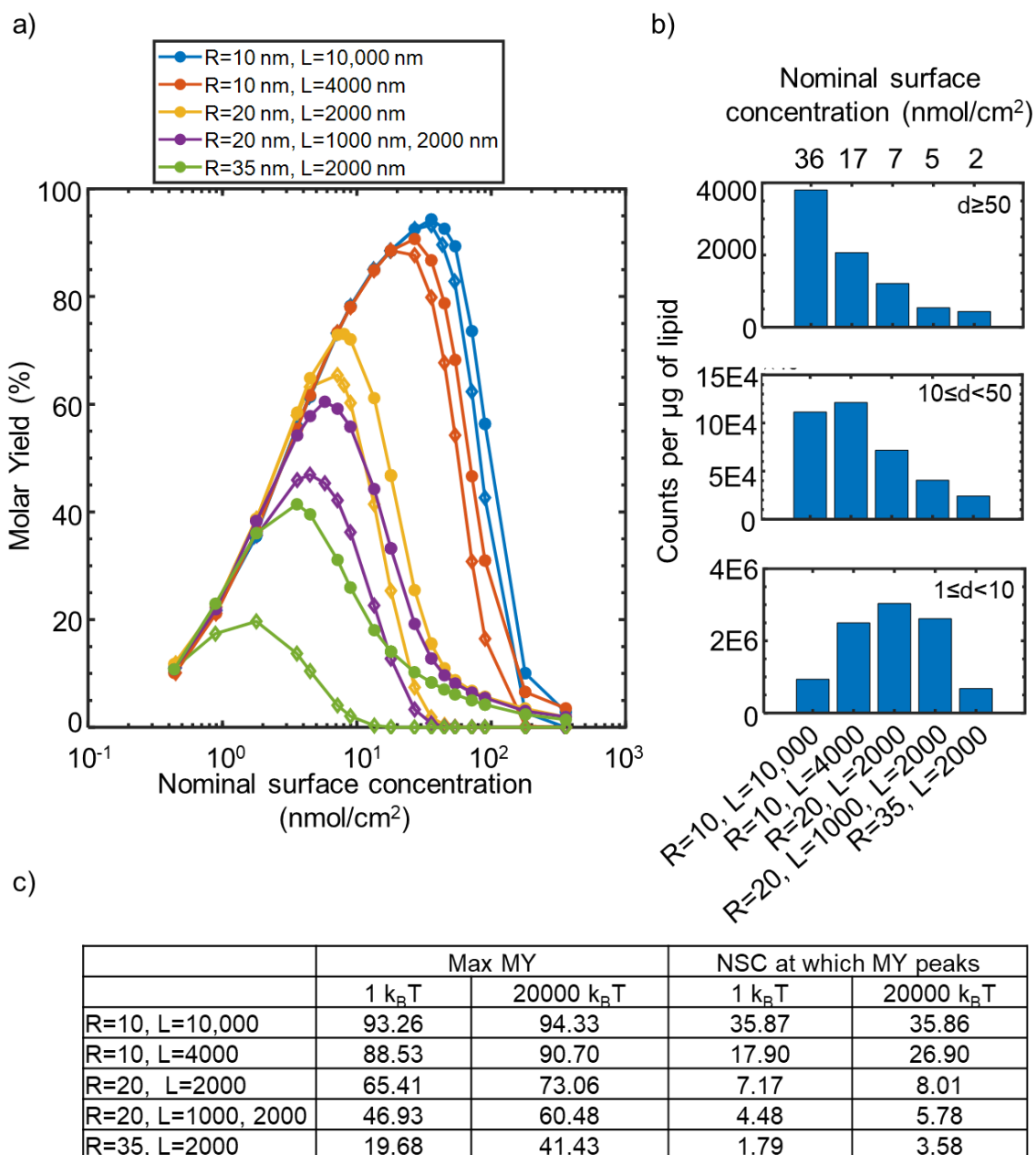


**Figure 3.13:** Yields and counts of GUVs obtained with external energy set to 1  $k_B T$ . a) Evolution of molar yields with varying surface concentrations on different fiber

geometries. The open diamonds show yields obtained with external energy set to 1 k<sub>B</sub>T and for comparison, the filled circles are the yields from **Figure 3.10** reproduced with external energy set to 20,000 k<sub>B</sub>T. The legend shows fiber dimensions with radius, R and length, L. b) Counts per microgram of lipid for the nominal concentrations at which the molar yield peaks. The x-axis at the bottom shows the fiber geometries and the x-axis at the top shows the nominal surface concentration at which the molar yield is maximized. The counts are divided into 3 size classes with diameters, d between  $1 \leq d < 10 \mu\text{m}$ ,  $10 \leq d < 50 \mu\text{m}$ ,  $d \geq 50 \mu\text{m}$ .

For all simulations, I apply 20,000 k<sub>B</sub>T of external energy, to mimic the impulse of energy delivered to the system upon pipetting the hydration solution into the growth chamber. Here I determine the effect of the magnitude of the external energy by comparing the GUV yields when using 20,000 k<sub>B</sub>T compared to the absence of external energy, by setting its value to 1 k<sub>B</sub>T. **Figure 3.13** shows the evolution of the molar yield on different fibers when the two different values of external energy are applied. The filled circles show yields with 20,000 k<sub>B</sub>T and the open diamonds show yields with 1 k<sub>B</sub>T of external energy. The difference in molar yields with external energy is more pronounced for fibers with larger radii, since they support fewer bilayers that can bud spontaneously. Thus in the absence of external energy, the yield is significantly lower. For all fibers, the molar yields decrease in the absence of external energy. For  $R_f \times L_f = 10 \text{ nm} \times 10000 \text{ nm}$ , the decrease in the maximum yield is 1.1% while for  $R_f \times L_f = 35 \text{ nm} \times 2000 \text{ nm}$ , the decrease in yield is 52%. For mixed geometries of  $R_f \times L_f = 20 \text{ nm} \times 1000 \text{ nm}$  and  $R_f \times L_f = 35 \text{ nm} \times 2000 \text{ nm}$ , the decrease in yield is 22%. I also note that for fibers with a radius of 20 nm or higher, the molar yield is zero at higher nominal surface concentrations, particularly in the absence of external energy. For example, for fibers with a radius of 35 nm, no buds are formed beyond a nominal surface concentration of 17.9 whereas in the presence of external energy, the lowest value of the molar yield is 1.4% at a concentration of 359 nmol/cm<sup>2</sup>. The nominal surface concentration at which the molar yield peaks is lowered across all fiber dimensions except  $R_f \times L_f = 10 \text{ nm} \times 10000 \text{ nm}$  as shown in the table. At higher surface concentrations, a larger number of sites do not bud, since budding can only occur via the spontaneous pathway in the absence of external energy. This is also the reason that in the absence of external energy fibers with of length 2000 nm and radii above 35 nm will have a zero molar yield at all concentration since all bilayers on these geometries require external energy to bud.

The trends in the counts per microgram of lipid in the absence of external energy are identical to the trends seen in the presence of external energy. The fiber geometries with the highest molar yields have the largest number of vesicles over 50 μm. The counts of vesicles below 50 μm affected by the balance between the number of nanobuds produced and the mean diameters of the nanobuds.

### 3.3.5. Simulations of varying surface concentrations on a flat surface also show peaked molar yields

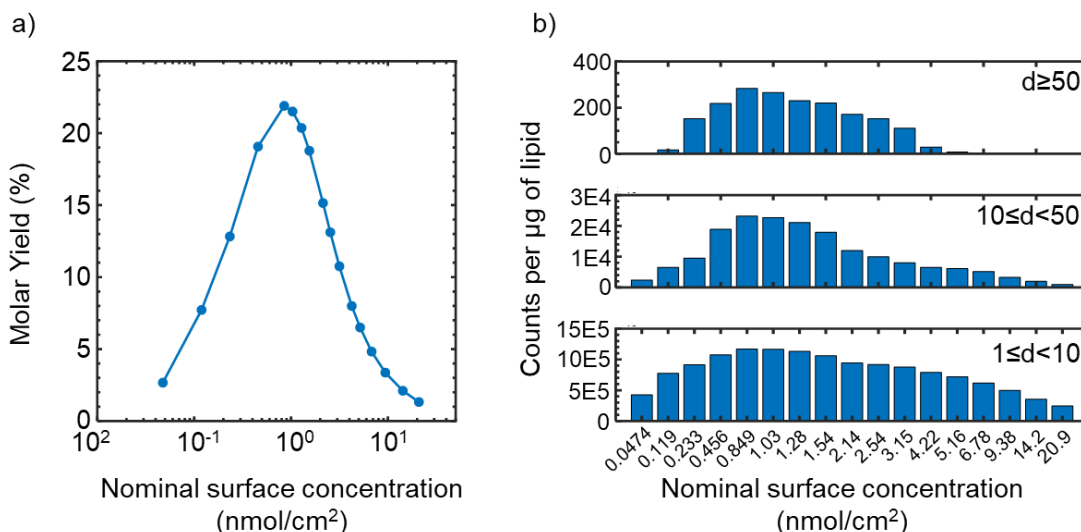


**Figure 3.14:** Simulations of varying surface concentrations on a flat substrate. a) Molar yield of GUVs obtained from the simulation at different nominal surface concentrations shows a peaked yield, similar to simulations on curved fibers. b) Counts per microgram of lipid for different nominal surface concentrations divided into 3 size classes with diameters,  $d$  between  $1 \leq d < 10 \mu\text{m}$ ,  $10 \leq d < 50 \mu\text{m}$ ,  $d \geq 50 \mu\text{m}$ . Counts for diameters larger than  $10 \mu\text{m}$  are also peaked.

Simulations carried out on flat surfaces also showed a peaked behavior. The yield and the counts per microgram of lipid were maximized at a nominal surface concentration of  $0.85 \text{ nmol/cm}^2$ . On glass, only the outermost bilayer can bud due to external energy. Therefore, sites with two bilayers have the highest molar yield. The additional of any more bilayers results in wasted lipid and decreases the molar yield.

### 3.4. Conclusion

In this chapter, I simulated the yields and sizes of GUVs assembled at varying surface concentration of zwitterionic lipid. I used a Poisson distribution with different mean values to simulate distributions of varying surface concentrations. Using the framework of the budding and merging model, I determined the number and sizes of nanobuds that form a various surface concentration. I used the concept of a merging template to then merge the nanobuds into GUVs following which I calculated the yields and sizes of the GUVs obtained. The results show that the budding and merging model replicates the peaked yield seen in experimental data for zwitterionic lipid. The counts of vesicles over

10  $\mu\text{m}$  are closely correlated with the molar yield, similar to what was seen in experiments. The simulations show that the budding and merging model is able to capture the important processes underpinning the assembly of GUVs on cylindrical fibers and reproduce the trends in yields and distributions seen in experiments.

### 3.5. Bibliography

- (1) Pazzi, J.; Subramaniam, A. B. Nanoscale Curvature Promotes High Yield Spontaneous Formation of Cell-Mimetic Giant Vesicles on Nanocellulose Paper. *ACS Appl. Mater. Interfaces* **2020**, *12*, 56549–56561.
- (2) Rideau, E.; Dimova, R.; Schwille, P.; Wurm, F. R.; Landfester, K. Liposomes and polymersomes: a comparative review towards cell mimicking. *Chem. Soc. Rev.* **2018**, *47*, 8572–8610.
- (3) Kučerka, N.; Tristram-Nagle, S.; Nagle, J. F. Structure of fully hydrated fluid phase lipid bilayers with monounsaturated chains. *J. Membr. Biol.* **2006**, *208*, 193–202.
- (4) Israelachvili, J. N. *Intermolecular and Surface Forces*, 3rd ed.; Academic Press: Waltham, MA, 2011.
- (5) Rawicz, W.; Olbrich, K. C.; McIntosh, T.; Needham, D.; Evans, E. A. Effect of chain length and unsaturation on elasticity of lipid bilayers. *Biophys. J.* **2000**, *79*, 328–339.
- (6) Sun, Y.; Lee, C. C.; Huang, H. W. Adhesion and merging of lipid bilayers: A method for measuring the free energy of adhesion and hemifusion. *Biophys. J.* **2011**, *100*, 987–995.

## Chapter 4: Shear Induced Fragmentation

### 4.1. Introduction

In Chapter 3, I show simulations based on the framework of the budding and merging model reproduces the peaked behavior seen in experiments. However, the evolution of yields of pure negatively charged lipids as well as mixtures of charged and zwitterionic lipids do not show a peaked behavior. In both these cases, the yield increases with concentration, with a reduced rate of increase at higher concentrations. We thus hypothesized that an alternate mechanism to surface budding and merging might be occurring for charged lipids. I explore the mechanism for this using high resolution confocal z-stack images. I found that for higher concentrations of charged lipids alone, a bulk  $L_\alpha$  mesophase forms, extending from the surface of the paper to anywhere between 100  $\mu\text{m}$  to 250  $\mu\text{m}$  above the surface of the paper. Upon pipetting, I show that this phase fragments to produce GUVs. The fragmentation of the mesophase is a bulk process independent of the substrate. Thus, it is a new alternative pathway that we have discovered to forming vesicles when charged lipids are present at high mol fractions and high surface concentrations.

### 4.2. Methods

**Imaging z-stacks.** To image on the surface of the paper, the lipid-coated paper was placed in a PDMS chamber (inner diameter  $\times$  height = 12  $\times$  1 mm). 150  $\mu\text{L}$  of 100 mM sucrose solution was pipetted into the chamber and a coverslip was placed over it. Confocal z-stacks were taken at regular slice intervals of 2.61  $\mu\text{m}$  starting from the surface of the substrate to 250  $\mu\text{m}$  above the surface. The images were 283.4  $\times$  283.4  $\mu\text{m}$  (1288  $\times$  1288 pixels per image). The surface of the substrate was selected in the reflected light channel by moving manually in Z and selecting the region with maximal reflected light signal. Since the microscope we used is upright, the laser light had to penetrate through the thick lipid mass which caused depth-dependent attenuation. A z-depth correction function in the Zen software was used to account for this attenuation. For images shown in **Figure 4.1**, I chose three reference slices to calibrate the laser intensity. I set the laser intensity to 10% for the slice closest to the paper ( $z=0$ ), 5% at  $z = 60 \mu\text{m}$  and 1.5% at  $z = 150 \mu\text{m}$ . For **Figure 4.4** I set the laser intensity to 3% for  $Z = 0 \mu\text{m}$  and lowered it to 1.5% at  $Z = 75 \mu\text{m}$ . For **Figure 4.7**, I set the laser intensity to 10% at  $z = 0$ , 5% at  $z = 60 \mu\text{m}$  and 1.5% at  $z = 150 \mu\text{m}$ . The laser intensities were chosen to allow visualization of features while minimizing the number of oversaturated pixels. The Zen software linearly interpolates the laser intensity between the reference z-slices.

**Measurement of the volume of the  $L_\alpha$  mesophase and the weight % of lipid.** The volume of the  $L_\alpha$  mesophase was measured using ImageJ. I used intensity thresholding to



segment the  $L_\alpha$  mesophase in the  $x$ - $z$  plane. The wand tool was used to select to calculate its area. This process was repeated for all the slices and obtained an average area which I multiplied by the  $y$ -distance of  $283.4 \mu\text{m}$  ( $x$ - $y$  image size was  $283.4 \times 283.4 \mu\text{m}$ ) to obtain the volume of the mesophase. I determine the number of moles of lipid in a single bilayer of DOPG occupying a lateral area of  $283.4 \times 283.4 \mu\text{m}$  using the value of the headgroup area shown in **Table 2.1**. We determine the number of water layers assuming that a water layer is sandwiched between two bilayers. I used a bilayer thickness of  $4 \text{ nm}$  to estimate the total volume of the lipid layer, and assign the rest of the volume to the water, thus calculate the lipid/water ratio in the mesophase.

**Z-stack imaging over 3 days.** I prepared samples for long term imaging by placing lipid coated paper in a PDMS chamber (inner diameter  $\times$  height =  $12 \times 1 \text{ mm}$ ) and hydrating in  $150 \mu\text{L}$  of  $100 \text{ mM}$  sucrose solution. I placed a coverslip over the chamber and sealed the chamber with a thick layer of Quick-set Epoxy to reduce evaporation. I took z-stack images at  $0.5$  hours,  $1$  hour,  $2$  hours,  $14$  hours,  $24$  hours,  $48$  hours and  $72$  hours.

### 4.3. Results

#### 4.3.1. Images of the surface of paper coated with DOPG show the presence of an extended lipid mass that is not present for zwitterionic DOPC.

The difference in the evolution of yield and the variations in size distributions between zwitterionic and charged lipids suggests a difference in mechanism of GUV formation. I imaged the surface of the substrate after  $1$  hour of hydration to obtain high resolution three-dimensional images using confocal microscopy. Nanocellulose is not fluorescent and was therefore visualized using confocal reflectance microscopy while the lipids were visualized using confocal fluorescence microscopy. In all the images, I defined the surface of the paper as being on the  $x$ - $y$  plane and the region normal to the surface of the paper as being on the  $z$ -axis. The upper and lower panels show representative  $x$ - $y$  slices while the middle panel shows representative  $x$ - $z$  slices. The  $x$ - $z$  images are overlays of the images of the paper surface (gray scale) and the lipid (false colored green).

**Figure 4.1** shows the surface paper coated with DOPG at nominal surface concentrations of  $18 \text{ nmol/cm}^2$ ,  $35 \text{ nmol/cm}^2$ ,  $89 \text{ nmol/cm}^2$ , and  $177 \text{ nmol/cm}^2$ . A layer of buds was present on the surface of the paper for all the nominal surface concentrations tested (lower panels). The diameters of the buds ranged from  $1 \mu\text{m}$  up to  $90 \mu\text{m}$ . For concentrations greater than  $18 \text{ nmol/cm}^2$ , I note the presence of a mass of lipid above the bud layer (b-d middle panels, solid white arrows). The  $x$ - $y$  slices of the mass in the upper panels show regions with no optically resolvable features in the regions close to the surface of the paper. In the regions further away from the paper, the mass transitioned to membranes that appeared tightly wound around a central core giving them an onion-like appearance (dashed white arrows). The mass of lipid did not fill the volume of the chamber.

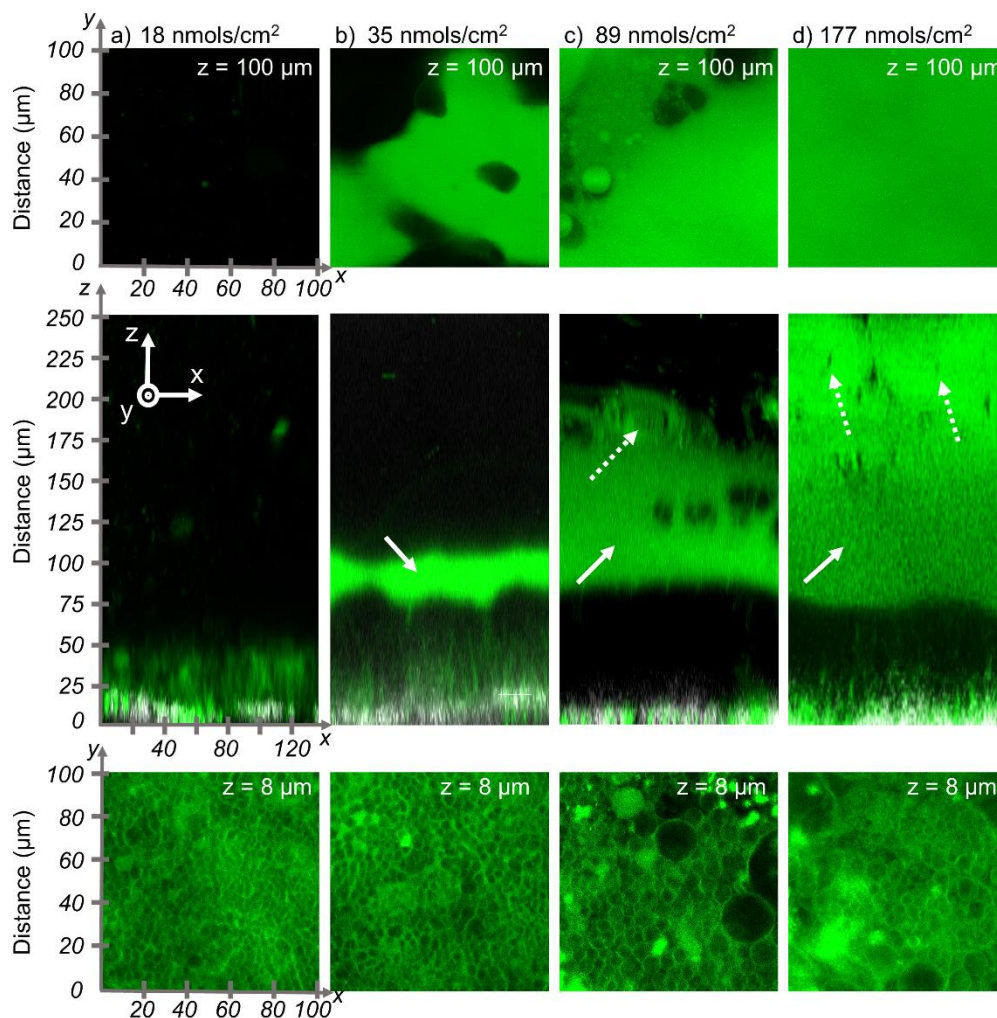


**Figure 4.1:** Slices of 3D confocal images of DOPG on the surface of nanocellulose paper. a) DOPG at  $18 \text{ nmol/cm}^2$  b) DOPG at  $35 \text{ nmol/cm}^2$ , c) DOPG at  $89 \text{ nmol/cm}^2$ , d) DOPG at  $177 \text{ nmol/cm}^2$ . The paper, (colored in gray) was imaged using reflectance contrast. The lipids (colored in green) were imaged using fluorescence contrast. Bulk water which is non-fluorescent and transparent to the laser appears black. The paper surface is in the x-y plane. The distance in the z-direction is normalized so that the surface of the paper is at  $z=0$ . Thus, the lipid covered regions which are on the surface of the paper, are on the positive z-axis. The upper panels are x-y slices at  $z=100 \mu\text{m}$  and the lower panels are x-y slices at  $z=8 \mu\text{m}$ . The white arrows point to the lipid mass that appeared uniform up to the optical resolution. The white dashed arrows point to the onion-like structures that form at the interface between the lipid mass and the excess water phase.

Interestingly, this lipid mass was not present on paper coated with zwitterionic lipid DOPC. **Figure 4.2** shows confocal images on the surface of nanopaper coated with DOPC at a surface concentration of  $18 \text{ nmol/cm}^2$  and  $180 \text{ nmol/cm}^2$ . At low concentrations

of lipid, the surface of the paper was covered with an abundant number of buds similar to  $18 \text{ nmol/cm}^2$  of DOPG with the notable difference that the GUV buds composed of DOPC were larger than those composed of DOPG. In the region of the paper shown in the figure, the layer of bud appears to extend to approximately  $60 \text{ }\mu\text{m}$  above the surface of the paper, corresponding to the diameter of the largest bud. However, for DOPC, increasing the surface concentration 10 times to  $180 \text{ nmol/cm}^2$  did not show the presence of the lipid mass seen for DOPG at a similar surface concentration ( $177 \text{ nmol/cm}^2$ ). Instead, at high surface concentrations of DOPC (**Figure 4.2 b**, lower panel) a few buds were present with the majority of the lipid layer appearing blistered. Despite the high lipid concentration however, the lipid layer did not extend beyond the surface of the paper. The images of the surface were consistent with the results in chapter 2 which showed that high nominal surface concentrations of DOPC leads to a lower molar yield of GUVs (**Figure 2.2**).

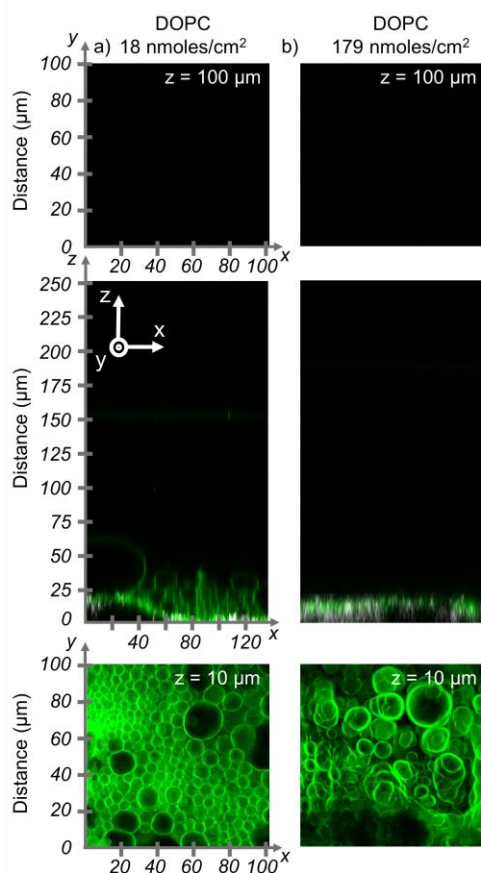


**Figure 4.2:** Slices of 3D confocal images of DOPC on the surface of nanocellulose paper. a) DOPC at  $18 \text{ nmol/cm}^2$  b) DOPC at  $180 \text{ nmol/cm}^2$ . The paper, (colored in gray) was imaged using reflectance contrast. The lipids (colored in green) were imaged using fluorescence contrast. Bulk water which is non-fluorescent and transparent to the laser appears black. The paper surface is in the x-y plane. The distance in the z-direction is normalized so that the surface of the paper is at  $z=0$ . Thus, the lipid covered regions which are on the surface of the paper, are on the positive z-axis. The upper panels are x-y slices at  $z= 100 \mu\text{m}$  and the lower panels are x-y slices at  $z= 10 \mu\text{m}$ .

#### 4.3.2. The mass of lipid is consistent with a $L\alpha$ mesophase

I calculated the volume of the mass from the confocal images and plot the data in **Figure 4.3** (details on calculations provided in section 4.2). Using linear least squares fit I demonstrate that the volume of the mass increased linearly with surface concentration. I compare the presence of this mass of lipid to phase experiments of binary mixtures of phospholipids and water in literature. Small-angle X-ray diffraction of binary mixtures of

phospholipids above their chain-melting temperatures show the formation of  $L_\alpha$  smectic mesophases for lipid/water ratios from 0.03 mol/mol to 1 mol/mol<sup>1-4</sup>. At lower lipid/water ratios, the  $L_\alpha$  smectic mesophase coexists with an excess water phase. I estimate the lipid content in the lipid mass of DOPG that forms using the volume data. The lipid/water ratios range between  $9.7 \times 10^{-5}$  to  $1.36 \times 10^{-4}$  mol/mol (0.4 – 0.6 wt% lipid). Therefore, the observed lipid mass the DOPG samples is expected to be in an  $L_\alpha$  smectic mesophase that coexists with an excess water phase.

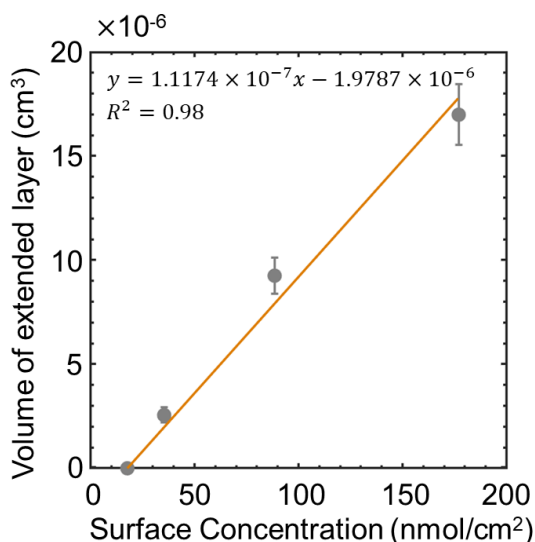


**Figure 4.3:** Plot of volume of the  $L_\alpha$  smectic mesophase versus the nominal surface concentration. The orange continuous line is a linear fit to the data

Similar images taken on DOPS and DOTAP applied on paper also show the presence of the  $L_\alpha$  mesophase that is packed into multilamellar structures (**Figure 4.4**). However, unlike in the case of DOPG in **Figure 4.1**, the mesophase is not clearly differentiated from the buds that form on the surface. Instead, pockets of buds are interspersed within the mesophase. In the middle panels showing the x-z plane, DOPS appears to have small pockets of GUV buds shown by the white arrows while DOTAP appears to have a single large pocket of buds. Close to the surface of the paper (lower panels in **Figure 4.4**), the buds can be seen intermingled with networks of featureless lipid for DOPS while for DOTAP, the buds are surrounded by featureless lipid. I also note that the mesophase extends to approximately 150  $\mu\text{m}$  over the surface of the paper for both DOPS and DOTAP while for DOPG it extended beyond 250  $\mu\text{m}$ . In the top panels in **Figure 4.4**, we see tightly packed onion-like structures for both DOPS and DOTAP. For DOTAP, these structures begin to form at just 75  $\mu\text{m}$  from the surface of the paper whereas for DOPS, we see these structures only beyond 100  $\mu\text{m}$  from the surface of the paper and for DOPG, at approximately 175  $\mu\text{m}$  from the surface of the paper.

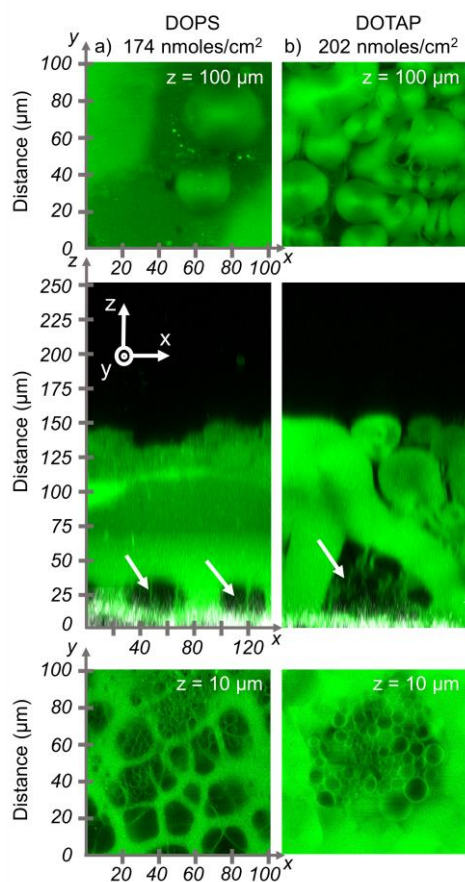


**Figure 4.4:** Slices of 3D confocal images of DOPS and on the surface of nanocellulose paper. a) Negatively charged lipid DOPS at  $174 \text{ nmol/cm}^2$  b) DOTAP at  $202 \text{ nmol/cm}^2$ . The paper, (colored in gray) was imaged using reflectance contrast. The lipids (colored in green) were imaged using fluorescence contrast. Bulk water which is non-fluorescent and transparent to the laser appears black. The paper surface is in the x-y plane. The distance in the z-direction is normalized so that the surface of the paper is at  $z=0$ . Thus, the lipid covered regions which are on the surface of the paper, are on the positive z-axis. The upper panels are x-y slices at  $z= 100 \mu\text{m}$  and the lower panels are x-y slices at  $z= 10 \mu\text{m}$ . The white arrows point to pockets of buds that are interspersed in the  $L_{\alpha}$  smectic mesophase.

#### 4.3.3. Shear-induced fragmentation of the mesophase produces free-floating GUVs

**Figure 4.5** shows representative confocal images of harvested GUVs after sedimentation in 100 mM of glucose. Although the surface images for the corresponding concentrations show the presence of the extended lamellar layer, it is not present in the harvested or sedimented samples. To further understand what happens to the mesophase, I harvested the mesophase of DOPG assembled on nanocellulose by gently pipetting all the liquid from the growth solution after 1 hour of hydration into a PDMS chamber to view using confocal

microscopy. The images in **Figure 4.6** show images of various regions of the mesophase after harvesting. The mesophase remains mostly intact, alongside free floating GUVs and shown in **Figure 4.6** a). Panels b)-d) are zoomed-in regions from panel a) showing a range of different features. A portion of the mesophase remains completely featureless as shown in **Figure 4.6** b), similar to the images on the surface of the substrate. I also note that large portions of the mesophase consists of small, dark, lumens that could indicate an increase in the interlamellar spacing. Furthermore, a significant portion of the mesophase consisted of spherical structures with diameters between 1 to 20  $\mu\text{m}$ . Since neither of these features were present in the images taken on the surface of the paper, I hypothesized that shear from pipetting and transfer of the lipid from the growth chamber induces the formation of the features that are seen.

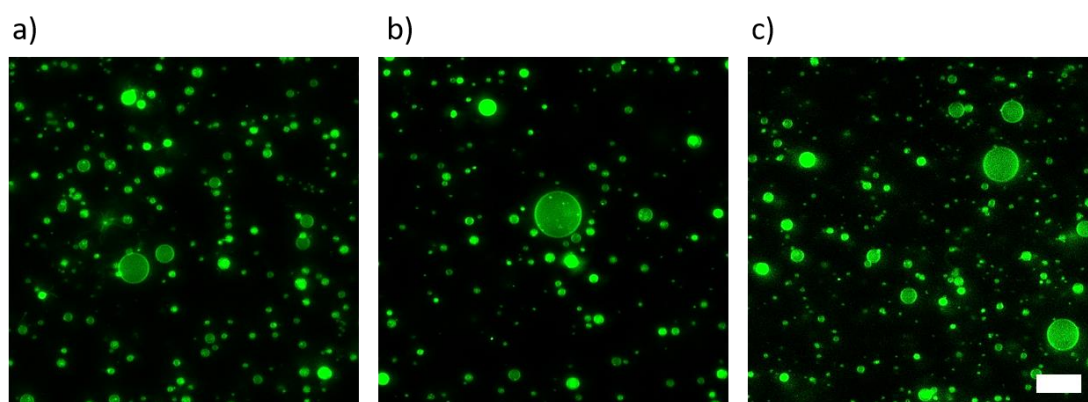


**Figure 4.5:** Images of DOPG, DOPS and DOTAP harvested after 1 hour of hydration in 100 mM sucrose solution and sedimented in 100 mM glucose for 3 hours a) 177  $\text{nmol}/\text{cm}^2$  of DOPG b) 174  $\text{nmol}/\text{cm}^2$  of DOPS and c) 202  $\text{nmol}/\text{cm}^2$  of DOTAP. Scale bar: 25  $\mu\text{m}$ .

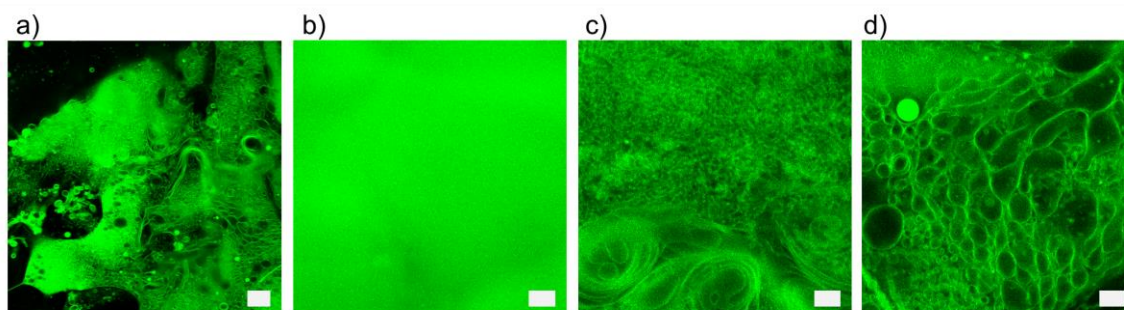


**Figure 4.6:** Confocal images of x-y slices of the mesophase after transfer to an imaging chamber. a) Portion of the largely unbroken mesophase showing a range of features. Portion of the mesophase from a) zoomed in to show b) a region that remains featureless up to the optical resolution, c) a region where interbilayer spacing increased to above the optical threshold resulting in resolvable features and d) a region that has spherical GUV-like structures. Scale bars: a) 50  $\mu\text{m}$ , b)-d) 10  $\mu\text{m}$ .

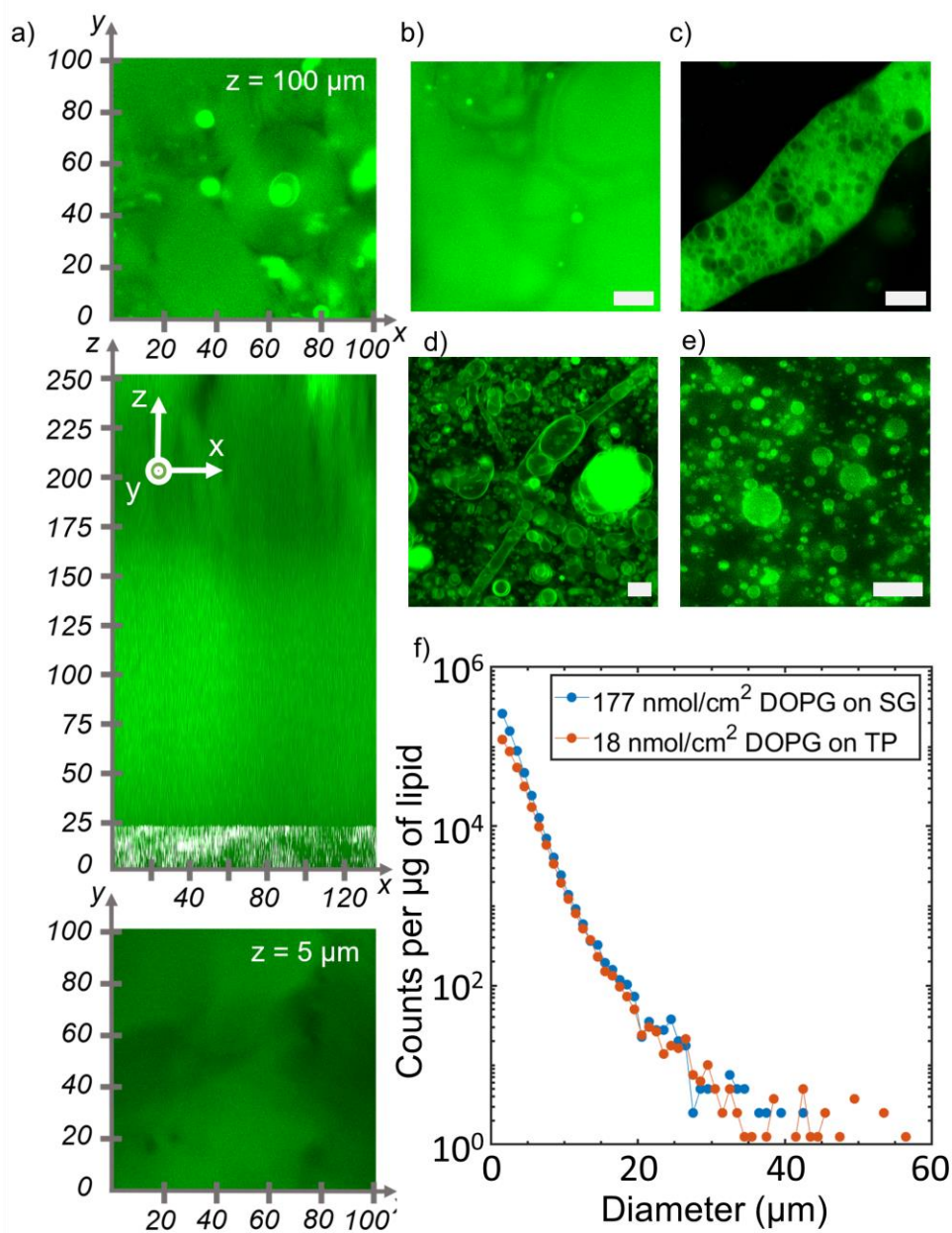


**Figure 4.7:** Experiments on silanized glass showing that the  $L_\alpha$  smectic mesophase can be sheared to produce GUVs. a) 2D slices of 3D confocal images of  $177 \text{ nmol}/\text{cm}^2$  DOPG on silanized glass. The glass (colored gray) was imaged using reflectance contrast, and the lipids (colored green) were imaged using fluorescence contrast. Bulk water which is non-fluorescent and transparent to the laser appears black. I define the glass surface to be in the  $x$ - $y$  plane. We normalize the images so that the surface of the glass is at  $z=0$ . Thus, the lipid covered regions which are on the surface of the glass, are on the positive  $z$ -axis. The upper panels are  $x$ - $y$  slices at  $z=100 \mu\text{m}$  and the lower panels are  $x$ - $y$  slices at  $z=5 \mu\text{m}$ . Example of a region within the mesophase after transfer to an imaging chamber showing b) no optically resolvable features, and c) spherical GUV-like clusters. d) Image of the



chamber after aspirating the solution with the mesophase 6 times. The chamber was filled with high concentration of GUVs, tubular and multilamellar structures and aggregates. e) Image of the solution from the chamber after it is diluted and sedimented for 3 hours in 100 mM glucose solution. f) Histogram of GUV diameters 177 nmol/cm<sup>2</sup> of DOPG (blue curve) on silanized glass for which bud formation occurs only via shear-induced fragmentation and 18 nmol/cm<sup>2</sup> of DOPG (orange curve) for which bud formation occurs only via budding and merging. Bin widths were set to 1 μm. Note the logarithmic scale on the y-axis. Scale bars 20 μm.

Since GUVs can form as a result of budding and merging of the lipid that is left behind on the surface of the paper as shown in the lower panels in **Figure 4.1**, it is difficult to determine whether the mesophase itself contributes to the formation GUVs that are present in the harvested solution. To circumvent this ambiguity, we tested the contribution of the mesophase to GUV formation using silanized glass as the substrate for growth. In previous work, Pazzi et. al determined that silanized glass does not support vesicle formation via the pathway of budding and merging<sup>5</sup>. **Figure 4.7 a)** confirms there were no buds present on the surface of the silanized glass after 1 hour of growth. As expected, the mesophase was present with similar characteristics to the mesophase produced on nanocellulose. I gently removed the solution from the growth chamber and transferred the solution to an imaging chamber. As in the nanocellulose experiment, I note that the transfer largely maintains the integrity of the mesophase. **Figure 4.7 b)** shows an example of a region where the mesophase remains featureless even after transfer to an imaging chamber while **Figure 4.7 c)** shows regions where the mesophase differentiates into a network of spherical, GUV-like structures.

The mesophase was then sheared by aspirating 6 times with a pipette with its tip cut off. After 6 rounds of aspiration, the mesophase is fragmented to produce GUVs, aggregates and other tubular structures as shown in **Figure 4.7 d)**. Since the structures were densely packed, I diluted and sedimented an aliquot of the sample which can be seen in **Figure 4.7 e)**. The sedimented samples were imaged and the yield of the GUVs were calculated to be 7%. The histogram of GUV diameters obtained from this sample was compared to the GUVs obtained from 18 nmol/cm<sup>2</sup> of DOPG assembled on nanocellulose since it has a comparable yield of  $5.3 \pm 1.1\%$ . **Figure 4.7 f)** shows this comparison. I conclude that the mesophase is sheared and fragmented during the harvesting process and contributes to the formation of GUVs and this pathway of GUV formation was labeled shear-induced fragmentation (SIF).

#### 4.3.4. The effect of salt on $L\alpha$ mesophase and GUV yields

The  $L\alpha$  mesophase formed only for lipids with a net headgroup charge. To determine the importance of electrostatic charges in the formation of the mesophase, I hydrated the lipid in 1x phosphate buffered saline (PBS) for 1 hour and over 3 days. **Figure 4.8** shows confocal z-stack images of the surface of tracing paper templated with 177 nmol/cm<sup>2</sup> of DOPG in PBS after 1 hour and 72 hours. After 1 hour of hydration, the surface contains a number of spherical and cylindrical structures that appear thick-walled and bright, indicative of multilamellar structures. The middle panel shows that there was no mesophase

present. After incubation in 100 mM sucrose solution for 72 hours, the thick-walled structures on the surface of the paper are no longer present. Instead, the lipid appeared to extend in tightly packed, multilamellar onion-like fingers up to  $\sim 125 \mu\text{m}$  above the surface of the paper. The numerous lamellae in these multilamellar structures can be seen in the top panel in b) which shows a slice in the x-y plane at a point  $100 \mu\text{m}$  above the surface of the paper. I also note that the long incubation time did not result in the formation of the featureless mesophase. The molar yield of GUVs from this sample was 4% unchanged from the yield obtained from samples incubated for 1 hr.

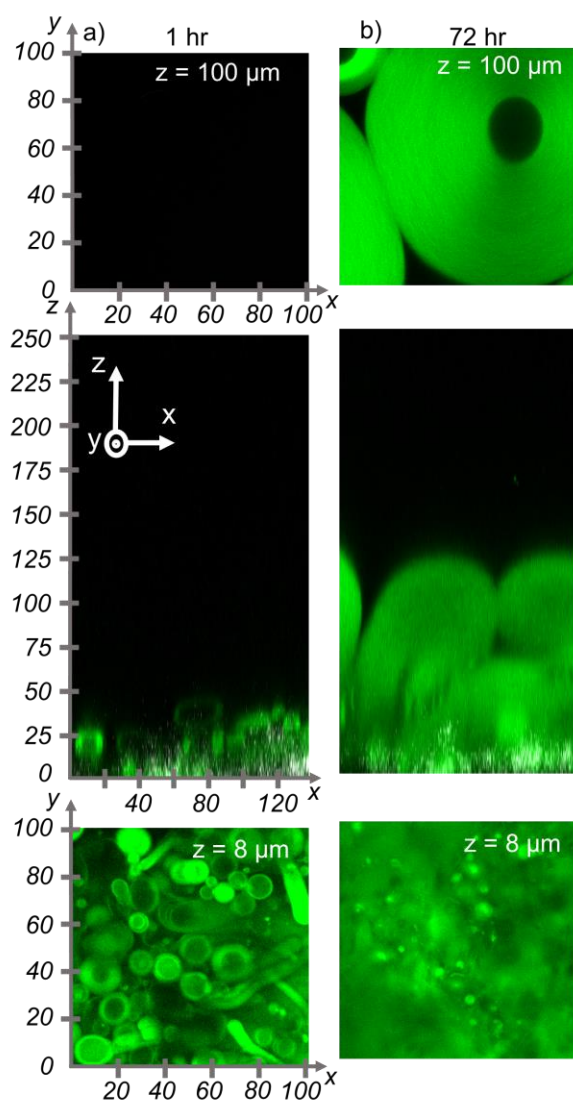


**Figure 4.8:** 3D confocal images of  $177 \text{ nmol/cm}^2$  DOPG on nanocellulose paper that is hydrated in PBS at short and long hydration times. The paper (colored in gray) was imaged using reflectance contrast. The lipids (colored in green) were imaged using fluorescence contrast. Bulk water which is non-fluorescent and transparent to the laser appears black. The paper surface to be in the x-y plane. The surface of the glass is defined to be at  $z=0$ . Thus, the lipid covered regions which are on the surface of the glass, are on the positive z-

axis. The upper panels are x-y slices at  $z=100\ \mu\text{m}$  and the lower panels are x-y slices at  $z=8\ \mu\text{m}$ . a) After 1 hour of hydration there is no  $L_\alpha$  smectic mesophase in the bulk solution. The surface is covered with bright spherical and cylindrical structures with thick walls indicative of multilamellar objects. b) After 3 days, the bright objects are no longer present on the surface. Instead, the lipid forms tightly packed onion-like fingers that extend from the surface of the paper. The fingers have diameters up to  $150\ \mu\text{m}$  and appear to consist of many hundreds of lamellar bilayers.

The Debye screening length is a parameter that determines the range of electrostatic interactions<sup>6</sup> and is a function of the concentration of ions present in the solution. The Debye screening length of 1xPBS is 0.8 nm while that in ultrapure water is 960 nm. Therefore, we would expect the charges of the headgroups of adjacent bilayers to be screened in PBS since the Debye screening length is smaller than the lamellar repeat spacing of 1.25 nm ( $d_w$  at 0.2 M of NaCl was measured to be 4.64 nm while the bilayer thickness of DOPG was measured to be 3.39 nm, resulting in an interlamellar spacing of 1.25 nm)<sup>7</sup>. This screening is likely the reason why we do not see the mesophase form in 1 x PBS. The adhesion between the bilayers is expected to be much larger at lower Debye lengths, which likely obstructs the formation of the expanded mesophase. This suggests that even after long incubation times, producing high yields of GUVs in physiological conditions is problematic. In Chapter 6, I discuss alternative methods to assembling GUVs in high salt solutions.

#### 4.3.5. Extended hydration time did not increase GUV yields

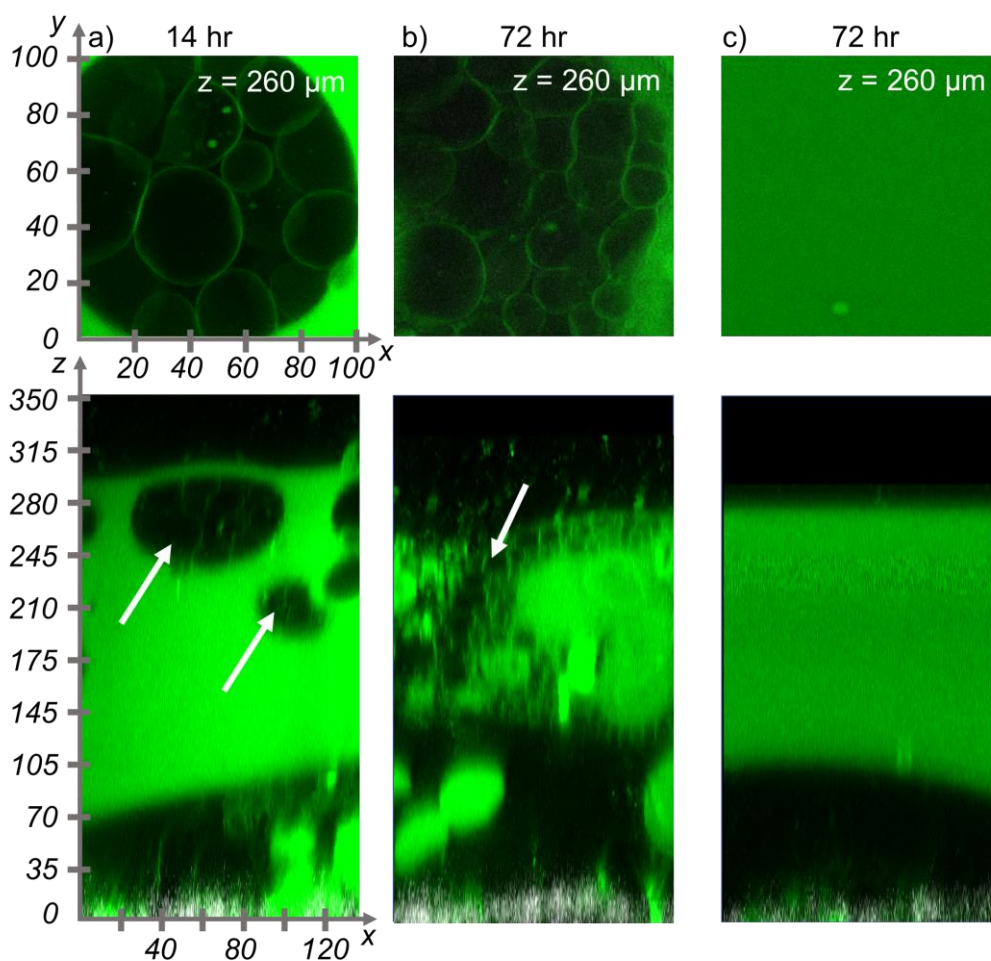
I test the effect if any of hydration time on the mesophase and the yields of GUVs produced. Long equilibration times are also consistent with procedures used to obtain GUVs through gentle hydration on glass surfaces<sup>8-10</sup>. The results show variations in behavior across the different charged lipids.

**Figure 4.9** shows the surface of nanocellulose with  $177\ \text{nmol}/\text{cm}^2$  of DOPG after hydration for 14 and 72 hours. I note that pockets of GUV-like clusters form within the mesophase at 14 hours hrs. These clusters look remarkably similar to the mesophase after it is removed from the surface of the paper and transferred to an imaging chamber in **Figure 4.7 c)**. The GUV-like clusters increase in number and size with increasing hydration time to 72 hours. However, even after 72 hours, I note that over 50% of the mesophase remains featureless at the optical limit as show in **Figure 4.9 c)**.

**Figure 4.10** shows the surface of nanocellulose with  $174\ \text{nmol}/\text{cm}^2$  of DOPS after hydration times between 1 hour and 72 hours. I noted earlier in the section that the height of the mesophase for DOPS after 1 hour of hydration is lower than that for DOPG and that the mesophase was not clearly separated from the buds that form on the surface. Here, the figures show that over time, the mesophase appears to expand over the first 14 hours to a height of approximately  $250\ \mu\text{m}$ . The images also show that the upper regions of the mesophase as well as pockets of it closer to the substrate form GUV-like structures. After 24 hours, there is a significant ‘thinning’ of the mesophase as large empty pockets of it

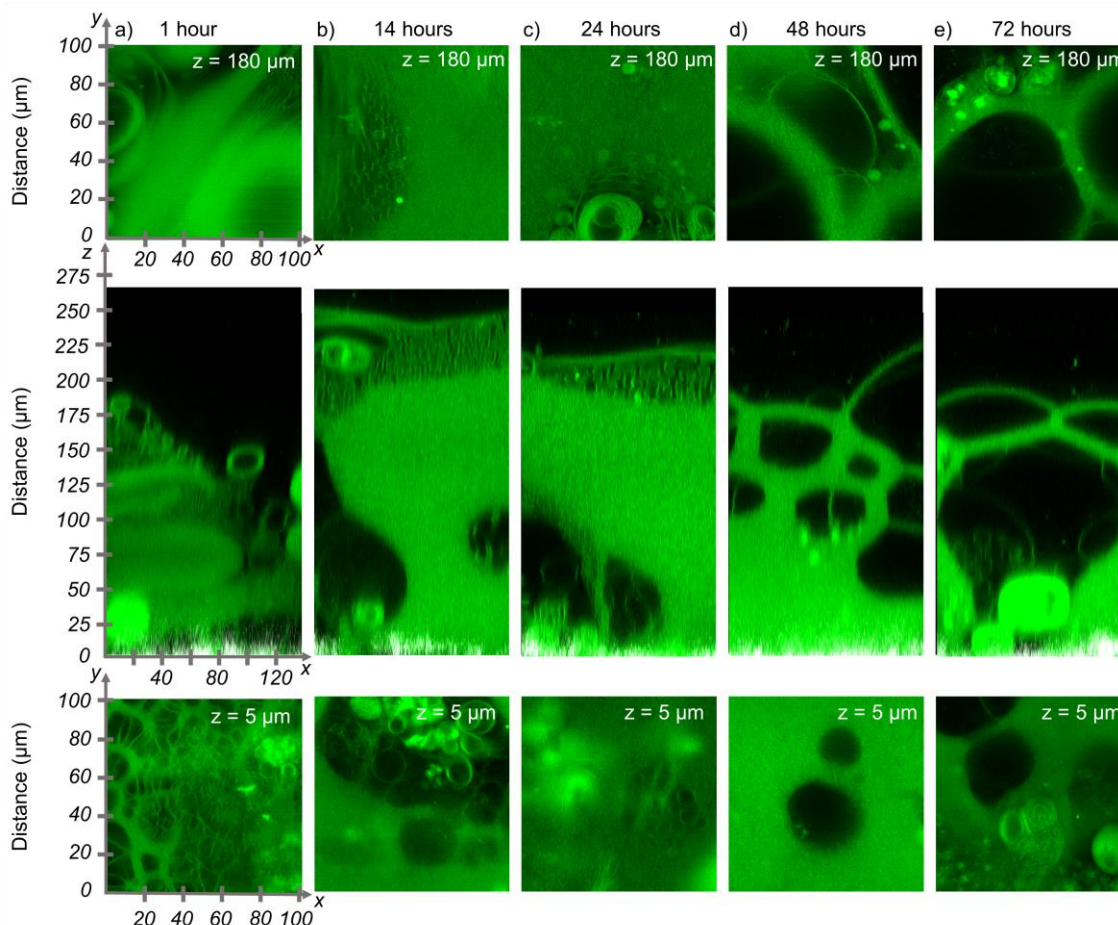
appear to form that appear to be partially filled with vesicular structures (Figure 4.10 e), middle and upper panels).

Figure 4.11 shows the surface of nanocellulose with  $202 \text{ nmol}/\text{cm}^2$  of DOTAP after hydration times between 1 hour and 72 hours. DOTAP appears to behave slightly differently from DOPG and DOPS. At 14 hours, a portion of the mesophase composed primarily of the tightly packed onion-like structures appears to detach and float to the top of the chamber, leaving behind a small amount of unstructured mesophase on the surface of the paper. After this initial evolution, the structures remain visually unchanged for the duration of the 72-hour incubation.



**Figure 4.9:** 3D confocal images of  $177 \text{ nmol}/\text{cm}^2$  DOPG on nanocellulose paper that is hydrated in 100 mM sucrose solution over long hydration periods. The paper (colored in gray) was imaged using reflectance contrast. The lipids (colored in green) was imaged using fluorescence contrast. Bulk water which is non-fluorescent and transparent to the laser appears black. The paper surface to be in the x-y plane. The surface of the glass is defined to be at  $z=0$ . Thus, the lipid covered regions which are on the surface of the glass, are on the positive z-axis. The upper panels are x-y slices at  $z=260 \mu\text{m}$ . Images were taken

after a) 14 hours of hydration and b)-c) 72 hours of hydration. The white arrows show pockets of spherical GU-like structures that appear in the mesophase after prolonged periods of hydration in a) and grow in size with increased hydration times as shown in b). Despite 72 hours of hydration, large portions of the mesophase remains featureless up to the optical resolution as shown in c).



**Figure 4.10:** 3D confocal images of  $174 \text{ nmol/cm}^2$  DOPS on nanocellulose paper that is hydrated 100 mM sucrose for 72 hours. The paper (colored in gray) was imaged using reflectance contrast. The lipids (colored in green) was imaged using fluorescence contrast. Bulk water which is non-fluorescent and transparent to the laser appears black. The paper surface to be in the x-y plane. The surface of the glass is defined to be at  $z=0$ . Thus, the lipid covered regions which are on the surface of the glass, are on the positive z-axis. The upper panels are x-y slices at  $z=180 \text{ }\mu\text{m}$  and the lower panels are x-y slices at  $z=5 \text{ }\mu\text{m}$ . Timepoints shown are a) 1 hour b) 14 hours, c) 24 hours, d) 48 hours, e) 72 hours.

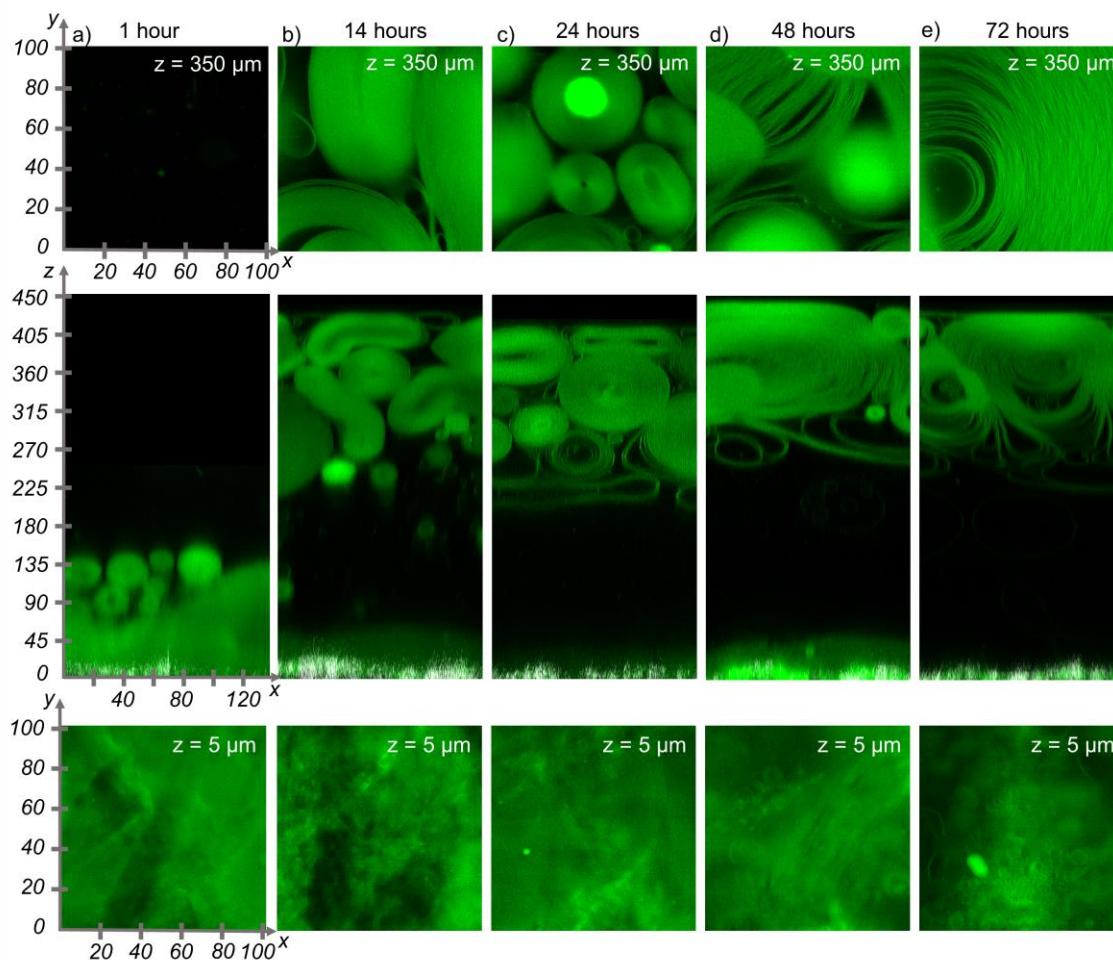


**Figure 4.11:** 3D confocal images of  $202 \text{ nmol/cm}^2$  DOTAP on nanocellulose paper that is hydrated 100 mM sucrose for 72 hours. The paper (colored in gray) was imaged using reflectance contrast. The lipids (colored in green) was imaged using fluorescence contrast. Bulk water which is non-fluorescent and transparent to the laser appears black. The paper surface to be in the x-y plane. The surface of the glass is defined to be at  $z=0$ . Thus, the lipid covered regions which are on the surface of the glass, are on the positive z-axis. The upper panels are x-y slices at  $z=350 \mu\text{m}$  and the lower panels are x-y slices at  $z=5 \mu\text{m}$ . Timepoints shown are a) 1 hour b) 14 hours, c) 24 hours, d) 48 hours, e) 72 hours

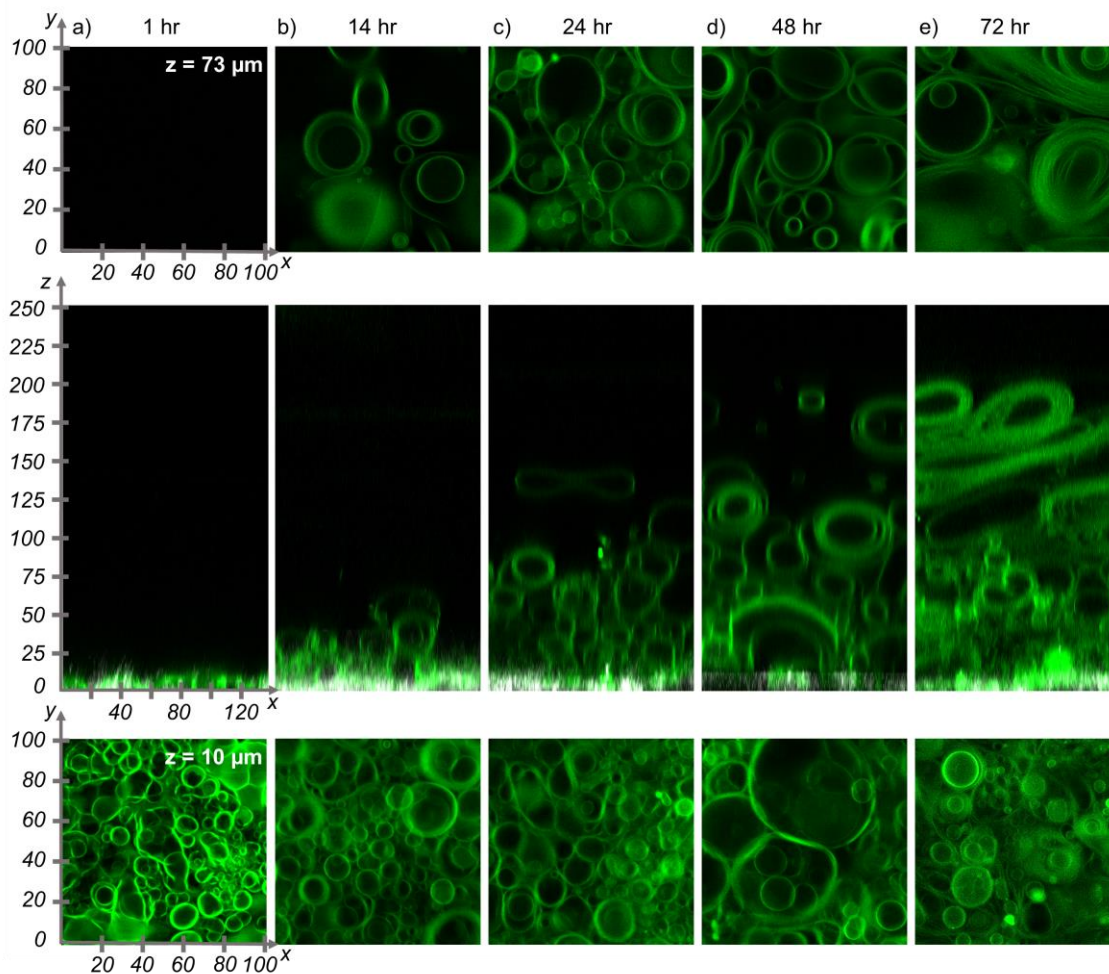


**Figure 4.12:** 3D confocal images of 180 nmol/cm<sup>2</sup> DOPC on nanocellulose paper that is hydrated 100 mM sucrose for 72 hours. The paper (colored in gray) was imaged using reflectance contrast. The lipids (colored in green) was imaged using fluorescence contrast. Bulk water which is non-fluorescent and transparent to the laser appears black. The paper surface to be in the x-y plane. The surface of the glass is defined to be at z=0. Thus, the lipid covered regions which are on the surface of the glass, are on the positive z-axis. The upper panels are x-y slices at z=73 μm and the lower panels are x-y slices at z= 10 μm. Timepoints shown are a) 1 hour b) 14 hours, c) 24 hours, d) 48 hours, e) 72 hours

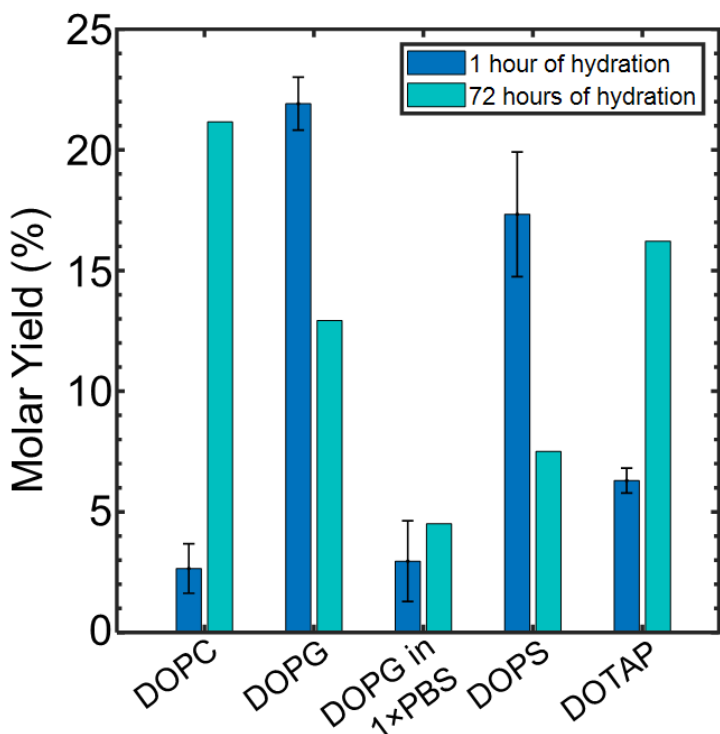


**Figure 4.13:** Bar plots comparing molar yield of GUVs obtained from different lipid types after 1 versus 72 hours of hydration.

**Figure 4.12** shows the surface of nanocellulose with  $180 \text{ nmol/cm}^2$  of DOPC for a range of hydration times between 1 hour and 72 hours. After 1 hour, I noted earlier that the surface contains mostly thick walled, blistered structures that are indicative of multilamellar structures. Furthermore, the lipids did not expand noticeably above the paper surface as can be seen in the middle panel of **Figure 4.12 a**). After 14 hours of hydration, the surface consists of a number of buds that resemble GUVs aside from multilamellar structures. This is consistent for all time points between 14 and 72 hours. A comparison of the middle panel which show slice in the transverse x-z direction across all time points shows that the lipid layer appears to extend beyond the surface of the paper, increasing in the height with increasing time. After 72 hours of hydration, the lipids appear to extend to a height of  $200 \mu\text{m}$  above the surface of the paper. However, unlike in the case of charged lipids, the lipids do not appear to form the featureless mesophase. Instead, over time, multilamellar and tubular structures along with single walled buds appear to extend above the surface of the paper. The upper panels show that the multilamellar structures appear to consist of fewer lamellae and are less densely packed than the onion-like structures that were characteristic in the upper portions of the mesophase of charged lipids. This shows that although over time, high concentrations of DOPC expand beyond the surface of the paper, the underlying behavior is different from that of charged lipids.

In all the cases, I harvested the mesophase using the usual procedure of aspirating 6 times with a pipette with its tip cut off. The yields are shown in **Figure 4.13**. The yield



of GUVs increases significantly for DOPC, from 2.7% to 21%. The yield of DOPG after 72 hours of incubation was 13 %. This yield is 7 % lower than the yield obtained by harvesting after 1 hour of incubation. The yield of DOPS was similarly lower after 72 hours of incubation at 7.5% from 17.3% after 1 hour of incubation. For DOTAP, the yields increased from 6.3% to 16.2%.

The difference in trends indicates that the process has more complexity than is apparent. For zwitterionic lipid DOPC, the images show an expansion of the lipid phase over time, and an increase in the number of GUV-like buds on the surface. The increase in yields suggest that an increase in hydration times allowed more of the zwitterionic lipid to hydrate and form single walled, GUV-like buds. Similarly, for DOTAP, it is unclear what the effect of the detached mesophase is, but a possible hypothesis is that it allows the remaining mesophase on the surface to fragment more easily. The two negatively charged lipids DOPG and DOTAP both see a drop in yields. They are also the two lipids that clearly show the evolution of the mesophase into GUV-like structures. However, the decrease in yields for these indicates that the evolution of the mesophase after 72 hours was not sufficient to improve yields. Over longer hydration periods, other factors such as oxidation<sup>11</sup> or hydrolysis<sup>12</sup> of the lipids due to prolonged incubation could also play a role in lowering yields. While losses are likely to have occurred for all lipids, DOPC and DOTAP show improvements due to longer hydration time, thus showing a net increase in molar yields whereas DOPG and DOPS may have achieved an optimum yield due to the SIF at shorter time scales and show reduced yields due to losses at longer incubation times. I conclude that longer incubation times are not practical to achieve optimal yields however, it highlights an interesting aspect of the mechanism of GUV formation in charged lipids. It appears that over time, the mesophase of charged naturally evolves into a network of GUVs. It is likely that the role of shear after 1 hour of incubation hastens this evolution, producing GUVs.

#### 4.3.6. Shear induced fragmentation as a mechanism of GUV formation

These results demonstrate that despite recreating similar assembly conditions, the mechanism of GUV formation is complex and is affected significantly by the lipid headgroup. In section 2.3.3, I showed that the number of bilayers templating the fibers is crucial in determining whether or not they are able to bud. Equation (8) shows the maximum number of bilayers that can be stacked on a fiber beyond which additional bilayers will not bud. This results in low yields for DOPC with increasing surface concentration of lipid.

Unlike for DOPC (**Figure 4.2 b** lower panel), we see the surface of paper coated with DOPG has a number of buds even at high lipid concentrations (**Figure 4.1 c**-d) lower panels). The key difference between the two lipids is the formation of the mesophase for DOPG at concentrations greater than  $> 18 \text{ nmol/cm}^2$  driven by repulsion from long range electrostatic interactions. We propose that the formation of the mesophase regulates the

amount of lipid that coats the fibers, thus removing 'excess' lipid that would otherwise hinder bud formation on the surface. This is also supported by measurements and calculations of the volume of the mesophase which increases linearly with surface concentration (**Figure 4.3**). After a certain critical concentration ( $\sim >18 \text{ nmol/cm}^2$ ), any additional lipid is incorporated into the mesophase rather than coating the fibers. Ions in salt solutions such as PBS screen the repulsion, resulting in significantly reduced swelling which prevents the formation of the  $L\text{-}\alpha$  mesophase. Therefore, all the lipids remain on the fiber, exceeding the maximum number of bilayers that can spontaneously bud. This along with the fact that adhesion also hinders budding and merging, results in low yields when assembled in salt.

I imaged the surface of the substrate templated with 5 mol% DOPG and 95 mol% DOPC at a nominal surface concentration of  $179 \text{ nmol/cm}^2$  to determine whether the  $L\alpha$  mesophase forms for lipid mixtures composed of zwitterionic and charged lipid. **Figure 4.14 a)** shows slices of the confocal z-stacks taken after 1 hour of hydration in 100 mM of sucrose solution. It appears that the electrostatic repulsion from 5 mol% of DOPG in the mixture is sufficient to form the  $L\alpha$  mesophase which appears mostly featureless up to the optical resolution and has tightly packed onion-like structures in the upper regions. Close to the surface of the substrate, I note the presence of buds, similar to what was seen for pure DOPG (**Figure 4.14**). The presence of the mesophase indicates that the increase in yields at higher concentrations likely occur as a result of fragmentation of the mesophase. Panel b) compares the histograms of GUVs obtained from mixtures with 5 mol% DOPG at a surface concentration of  $18 \text{ nmol/cm}^2$  (red) when we do not expect to see a mesophase form based on data from pure DOPG, and the  $36 \text{ nmol/cm}^2$  (green), the optimal surface concentration and one at which the extended mesophase can form. I note an increase in the number of vesicles in all diameter bins with the largest increase being for the smaller bins, between  $1 - 8 \text{ }\mu\text{m}$ . A similar plot for 25 mol% DOPG shows that the increase in concentration from  $18 \text{ nmol/cm}^2$  (red) to  $90 \text{ nmol/cm}^2$  (green) in **Figure 4.14 c)** is driven mainly by an increase in the number of vesicles in bins between  $1 - 5 \text{ }\mu\text{m}$ . Since shear-induced fragmentation of the mesophase primarily produces vesicles below  $10 \text{ }\mu\text{m}$  (and no vesicles above  $50 \text{ }\mu\text{m}$ ), the yield recovery of lipid mixtures is mainly as a result of more small vesicles with diameters below  $10 \text{ }\mu\text{m}$ . This can be seen clearly for the mixture with 25 mol% DOPG, for which bins above  $15 \text{ }\mu\text{m}$  have very minimal increases in counts at higher concentrations. For mixtures with 5 mol% DOPG, even though the increase in the number of small vesicles is more drastic, all bins have an increased number of counts. One possible reason for this could be that the formation of the mesophase optimizes the configuration of bilayers on the surface, allowing more fibers to be coated with the highest number of bilayers that can bud spontaneously. This would allow a larger number of buds to form and merge on the surface at a concentration of  $35 \text{ nmol/cm}^2$ , which could result in an increase in the number of vesicles over  $50 \text{ }\mu\text{m}$ .

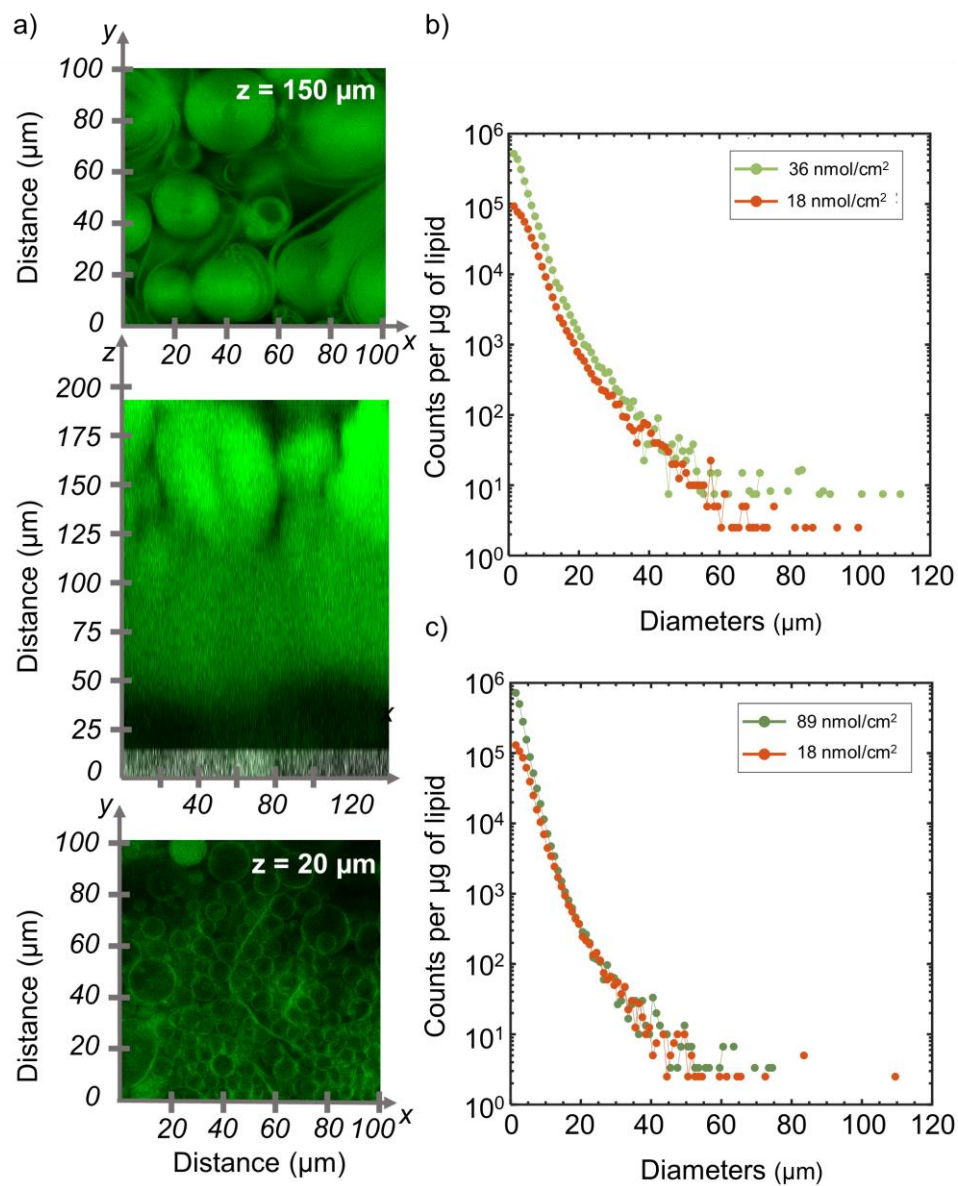


**Figure 4.14:** Slices of 3D confocal images of lipid mixtures composed of 95 mol% zwitterionic lipid DOPC and 5 mol% of charged lipid DOPG on the surface of nanocellulose paper. The nominal surface concentration of lipid on the paper is 180  $\text{nmol}/\text{cm}^2$ . The paper, (colored in gray) was imaged using reflectance contrast. The lipids (colored in green) were imaged using fluorescence contrast. Bulk water which is non-fluorescent and transparent to the laser appears black. The paper surface is in the x-y plane. The distance in the z-direction is normalized so that the surface of the paper is at  $z=0$ . Thus, the lipid covered regions which are on the surface of the paper, are on the positive z-axis. The upper panel is an x-y slice at  $z = 150 \mu\text{m}$  and the lower panel is an x-y slice at  $z = 20 \mu\text{m}$ .

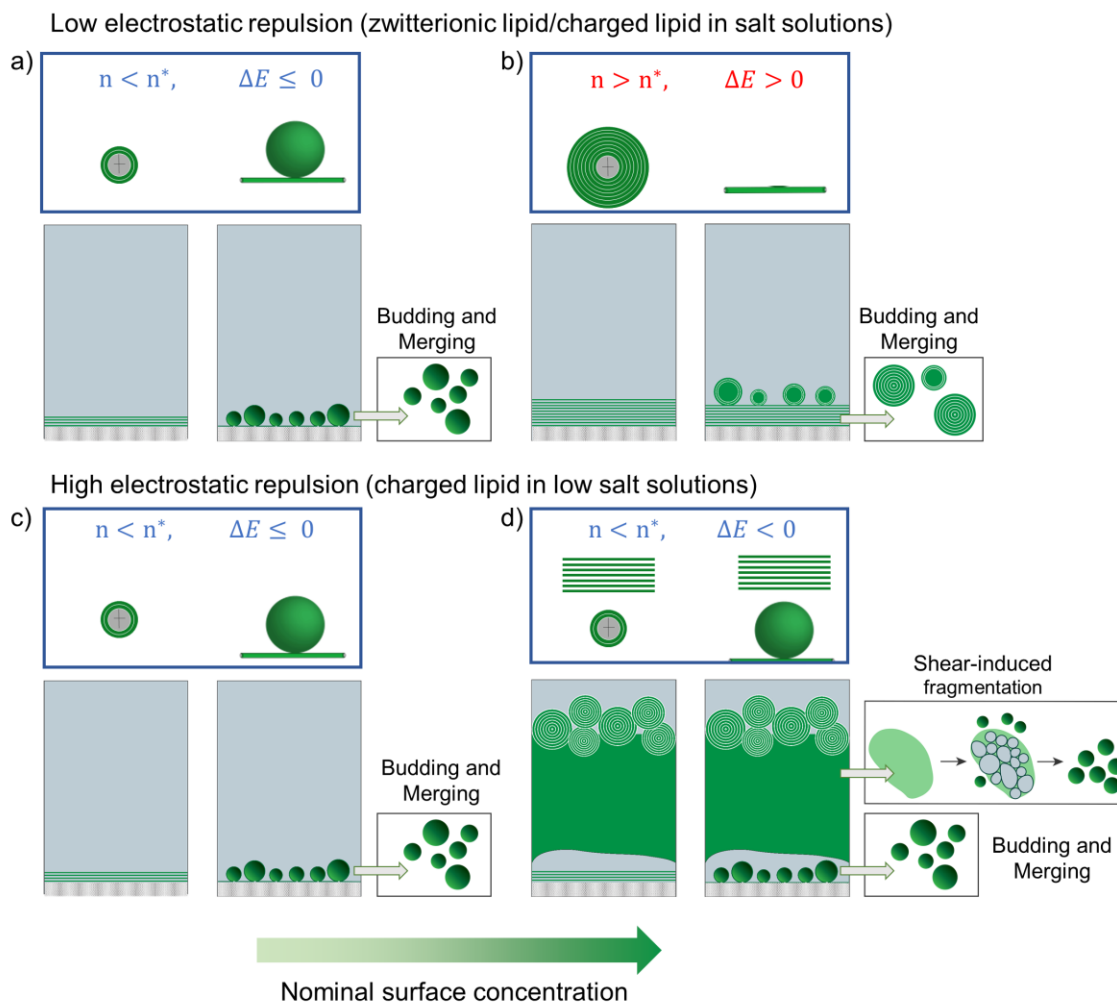


**Figure 4.15:** Schematic of the mechanism for shear-induced fragmentation. a), b) represent the low electrostatic repulsion case, which can result either when using zwitterionic lipid or charged lipids in salt solutions. Each panel depicts the configuration of lipids as seen in the confocal z-stacks. The boxes above each panel show the cross section of a fiber with bilayers templated onto it c), d) represent the high electrostatic repulsion case, which occurs when using charged lipids in low salt solutions. a) and c) represent lipid concentrations at which most of the fibers have  $n$  bilayers  $\leq$  highest bilayer number that can bud spontaneously,  $n^*$ . When  $n < n^*$ , in the presence of both low and high electrostatic repulsion, the pathway to GUV assembly occurs via budding and merging on the surface of the substrate. When  $n > n^*$  and the electrostatic repulsion is low as in b), budding cannot occur spontaneously since the budding of the outermost bilayer is endergonic. The harvested solution is composed mainly of aggregates and MLVs. When  $n > n^*$  in the presence of electrostatic repulsion as shown in d), the excess lipid lifts off the surface of the substrate and forms a mesophase. Although the initial configuration of bilayers on the fiber is not

favorable for budding, the incorporation of excess lipid into the mesophase reduces the number of bilayers below  $n^*$ , allowing the lipid on the substrate to assemble into buds that form GUVs upon harvesting. A second pathway also contributes to GUV formation. The mesophase can be fragmented using shear to form GUVs. b) represents lipid concentrations at which most sites have  $n$  bilayers  $\geq n^*$ . c) represents lipid concentrations at which most sites have  $n \leq n^*$  and can therefore bud spontaneously. d) represents lipid concentrations at which most sites have  $n > n^*$ . The excess bilayers form the mesophase composed of featureless film up to optical resolution and densely packed multilamellar structures in the upper regions.

**Figure 4.15** shows a schematic of the different conditions that affect the pathways available for GUV assembly. **Figure 4.15** a) and b) illustrate the conditions of low electrostatic repulsion, which occurs either during the assembly of zwitterionic lipids which have low net charge or for charged lipids in high salt solutions when the ions screen the electrostatic repulsion. **Figure 4.15** c) and d) illustrate the conditions of high electrostatic repulsion which occurs during the assembly of charged lipids in low salt solutions. Panels a) and c) show the scenario in which most of the fibers have the number of bilayers  $n$  below the critical value  $n^*$  which as shown in Equation (8) is the value of the largest bilayer number that can bud spontaneously. By this definition, when  $n \leq n^*$ , the energy of budding  $E$  is  $\leq 0$ , indicating that the process either requires no energy or is exergonic. We note that when  $n < n^*$ , the pathway to GUV assembly is via budding and merging on the surface of the substrate for both the low and high electrostatic repulsion cases. When most of the sites have bilayers  $n > n^*$ , the energy of budding of the outermost bilayer  $\Delta E$  is positive, requiring energy input for buds to assemble on the surface. **Figure 4.15** b) shows this scenario when there is low electrostatic repulsion. In this scenario, the surface has numerous aggregates and multilamellar structures as shown experimentally in **Figure 4.2**. **Figure 4.15** d) shows the situation when most sites have  $n$  bilayers  $> n^*$  in the presence of high electrostatic repulsion. In this scenario, the electrostatic repulsion causes the excess lipid to lift off the surface and form the mesophase. The number of bilayers left behind on the fibers after this occurs  $n$  is now less than  $n^*$  and therefore, the bilayers on the fibers can bud. Aside from this the budding and merging pathway, the application of shear to the mesophase that forms from ‘excess’ lipid fragments and produces GUVs, allowing a second bulk pathway to GUV assembly.

#### 4.4. Conclusions

In this section, I focused on the mechanism underpinning the evolution of yields of charged lipids and lipid mixtures. I introduced a previously undetermined method of GUV formation that charged lipids can undergo that was termed shear induced fragmentation (SIF). Using high resolution 3-D confocal imaging, I found that aside from a layer of buds on the surface, at high surface concentrations, charged lipids also had an expanded lamellar lipid layer extending to over 250  $\mu\text{m}$  over the surface of the paper. This layer can be fragmented using shear forces to produce GUVs. Furthermore, the use of charged lipids in literature appears contradictory – in certain cases, charged lipids appear to increase yields

while in other cases, they appear to lower them. Uncovering shear-induced fragmentation as a method of vesicle formation is a significant step in reconciling these contradictions since I show that other factors such as surface concentrations and shear input play a key role in the yields of charged GUVs.

#### 4.5. Bibliography

- (1) Ranck, J. L.; Keira, T.; Luzzati, V. A novel packing of the hydrocarbon chains in lipids the low temperature phases of dipalmitoyl phosphatidyl-glycerol. *Biochim. Biophys. Acta (BBA)/Lipids Lipid Metab.* **1977**, *488*, 432–441.
- (2) Stillwell, W. Chapter 10 - Lipid Membrane Properties. In *An Introduction to Biological Membranes*; (Second E., Ed.; Elsevier, 2016; pp 181–220.
- (3) Ulrich, A. S.; Sami, M.; Watts, A. Hydration of DOPC bilayers by differential scanning calorimetry. *BBA - Biomembr.* **1994**, *1191*, 225–230.
- (4) Cowley, A. C.; Fuller, N. L.; Rand, R. P.; Parsegian, V. A. Measurement of repulsive forces between charged phospholipid bilayers. *Biochemistry* **1978**, *17*, 3163–3168.
- (5) Pazzi, J.; Subramaniam, A. B. Nanoscale Curvature Promotes High Yield Spontaneous Formation of Cell-Mimetic Giant Vesicles on Nanocellulose Paper. *ACS Appl. Mater. Interfaces* **2020**, *12*, 56549–56561.
- (6) Israelachvili, J. N. *Intermolecular and Surface Forces: Third Edition*; 2011.
- (7) Loosley-Millman, M. E.; Rand, R. P.; Parsegian, V. A. Effects of monovalent ion binding and screening on measured electrostatic forces between charged phospholipid bilayers. *Biophys. J.* **1982**, *40*, 221–232.
- (8) Reeves, J. P.; Dowben, R. M. Formation and properties of thin-walled phospholipid vesicles. *J. Cell. Physiol.* **1969**, *73*, 49–60.
- (9) Rodriguez, N.; Pincet, F.; Cribier, S. Giant vesicles formed by gentle hydration and electroformation: A comparison by fluorescence microscopy. *Colloids Surfaces B Biointerfaces* **2005**, *42*, 125–130.
- (10) Akashi, K. I.; Miyata, H.; Itoh, H.; Kinoshita, K. Preparation of giant liposomes in physiological conditions and their characterization under an optical microscope. *Biophys. J.* **1996**, *71*, 3242–3250.
- (11) Itri, R.; Junqueira, H. C.; Mertins, O.; Baptista, M. S. Membrane changes under oxidative stress: The impact of oxidized lipids. *Biophys. Rev.* **2014**, *6*, 47–61.
- (12) Zuidam, N. J.; Crommelin, D. J. A. Chemical hydrolysis of phospholipids. *J. Pharm. Sci.* **1995**, *84*, 1113–1119.

## Chapter 5: Budding and merging with barriers to merging

### 5.1. Introduction

In Chapter 2, I showed that the molar yield of GUVs falls with increasing mole fraction of charged lipid for a given surface concentration. In Chapter 3, I described shear-induced fragmentation as an alternate pathway for GUV formation. However, in at low surface concentrations of 18 nmol/cm<sup>2</sup>, the L $\alpha$  mesophase does not form, in the absence of which, GUV assembly occurs only through the budding and merging model. With increasing surface charge of the lipid mixture, the BNM model suggests that the adhesion energy is likely to be very low (ref), making budding more favorable. Yet **Figure 2.8** shows that the molar yield decreases with increasing surface charge. Here, I show that the results can be explained by introducing barriers to merging in the BNM model. Although charged lipid mixtures may produce more nanobuds, the nanobuds are expected to repel each other, reducing instances of merging, and thus reducing the yield. I have shown that it is possible to recover the yield in these cases by increasing the surface concentration of lipids, which could result in more nanobuds crowded on a fixed substrate area, thus increasing the possibility of merging.

### 5.2. Budding and merging model with barriers explains the results

The budding and merging model describes assembly of GUVs via the formation of nanobuds from bilayers templated on the surface of a substrate followed by merging of nanobuds to form vesicles over 1  $\mu$ m in diameter. The molar yield increases due to nanobud-nanobud merging and due to nanobud-microbud merging. While microbud-microbud merging affects the size of the GUVs, it does not affect yields. The molar yield does not consider the distribution of lipid between different GUV buds, so we consider the total moles of lipids in the population of nanobuds,  $M_{NB} = N_{NB}m_{NB}$  on a fixed substrate of area. The number of buds on the surface is  $N_{NB}$  and the moles of lipids in each bud is  $m_{NB}$ . If we assume all buds are the same size, then  $m_{NB}$  is a constant.

We assume that molar yield of GUVs,  $M_{GV}$  is dependent on the fraction of nanobuds that merge,  $\phi_{merge}$

$$M_{GV} = \phi_{merge}M_{NB} \quad (22)$$

In this equation when  $\phi_{merge}$  is 1, all the buds merge to form GUVs. When  $\phi_{merge} = 0$ , none of the buds merge and the yield of GUVs is zero. We also assumed that the probability of merging depends on energy barriers to merging. In lipid mixtures with larger fractions of charged lipid, barriers to merging can arise due to increased electrostatic repulsion between the buds. The potential field around a spherical bud depends on the size of the bud and the magnitude of the repulsion energy depends on the distance between the

buds. Since the nanobuds are small, and the ionic strength is low, we expect that the Debye length to be much larger than the size of the buds.

Next, we assumed that the number of nanobuds that form was fixed across all the lipid mixture and that the probability of merging depended exponentially on the surface potential of the membrane relative to some reference potential.

$$M_{GV} = M_{NB} \exp\left(-\frac{\psi_{mem}}{\psi_{ref}}\right) \quad (23)$$

$\psi_{mem}$  is the potential of the membrane, and  $\psi_{ref}$  is a reference potential that scales the potential. I calculate  $\psi_{mem}$  from the Grahame equation shown below which describes the relationship between the surface charge and surface potential:

$$\psi_0 = \frac{2kT}{e} \sinh^{-1}\left(\frac{\sigma_{eff}}{\sqrt{8\varepsilon_0\varepsilon kT N_a C_{ions}}}\right) \quad (24)$$

In this equation,  $\psi_0$  is the potential,  $\varepsilon_0$  is the permittivity of vacuum,  $\varepsilon$  is the dielectric constant of water,  $k$  is the Boltzmann constant,  $T$  is the temperature,  $N_a$  is Avogadro's number,  $C_{ions}$  is the concentration of ions in the bulk solution and  $e$  is the elementary charge. Increasing surface charge density,  $\sigma_{eff}$  results in increasing surface potential. We calculate the surface charge density using

$$\sigma_{eff} = \sum_{i=1}^N \frac{\chi_i f_i z_i e}{A_{hg,i}} \quad (25)$$

In this equation  $\chi_i$  is the mol fraction of lipid  $i$ ,  $f_i$  is the degree of ionization of lipid  $i$ ,  $z_i$  is the net charge of the headgroup of lipid  $i$ ,  $e = 1.602 \times 10^{-19}$  C is the elementary charge, and  $A_{hg,i}$  is the headgroup area of lipid  $i$  and  $N$  is the number of lipid types present in the system. For a two-component membrane with one component being zwitterionic, with zero net charge the equation simplifies to:

$$\sigma_{eff} = \frac{f_c z_c e}{A_{hg,c}} \chi_c \quad (26)$$

For highly charged membranes in low salt solutions, measurements have shown that only 1-2 % of the lipids are dissociated<sup>1</sup>. We choose  $f_i = 0.01$ . The pH of our solution is 5.5. This is the expected pH of an unbuffered solution at equilibrium with atmospheric carbon dioxide. Thus  $C_{ions} = 3.162 \times 10^{-6} M^2$ .



Substituting these values into Equation (24) gives us Equation (27):

$$\psi_{mem} = 0.05138 \sinh^{-1}(9.5868 \chi_i) \quad (27)$$

Substituting Equation (27) into Equation (23) gives:

$$M_{GV} = M_{NB} \exp\left(\frac{0.05138 \sinh^{-1}(9.5868 \chi_i)}{\psi_{ref}}\right) \quad (28)$$

We fit this equation to our data for the molar yield of vesicles composed of DOPG and DOPS using the non-linear least squares method. The fit is good, with a SSE value of 0.0005765. **Figure 5.1** shows the fit between the experimental data and Equation (28). The experimental data has been reproduced from **Figure 2.8**.

The model shows that for a fixed surface concentration, increasing the number of nanobuds or the moles of nanobuds can increase the total yield of GUVs for a given charge fraction. The fitted value of  $N_{NB}$  is 30, and  $\psi_{ref} = 86$  mV.

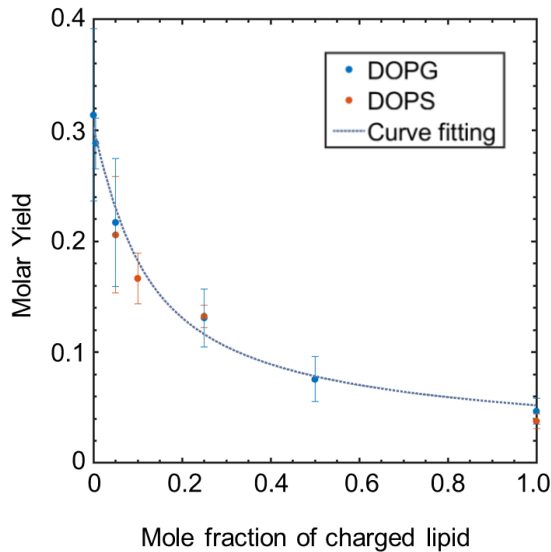


**Figure 5.1:** Data from Figure 2.8 fit to the curve generated by Equation (20). The resulting fit has a SSE value of 0.0005765, showing a good fit.

### 5.3. Conclusion

Here, I the use of the Grahame equation to describe the reduction of molar yields as a result of increasing membrane charge. We hypothesized that the increased energy cost of merging resulted in fewer nanobuds merging to form microbuds, as well as fewer microbuds merging to form larger buds. The exponential probability distribution combined with the Grahame equation is in good agreement with the experimental data. Future work in this area can include using MATLAB to simulate a barrier to merging, depending on the charge of the membrane. This can enable us to predict trends in yields and distributions as a result of varying mole fractions of charged lipids.

### 5.4. Bibliography

- (1) Gilbile, D.; Docto, D.; Kingi, D. T.; Kurniawan, J.; Monahan, D.; Tang, A.; Kuhl, T. L. How Well Can You Tailor the Charge of Lipid Vesicles? *ACS Langmuir* **2019**, *35*, 15960–15969.
- (2) Mahnke, J.; Stearnes, J.; Hayes, R. A.; Fornasiero, D.; Ralston, J. The influence of dissolved gas on the interactions between surfaces of different hydrophobicity in aqueous media. Part I. Measurement of interaction forces. *Phys. Chem. Chem. Phys.* **1999**, *1*, 2793–2798.

## Chapter 6: Model and simulations of GUV assembly in salty solutions

### 6.1. Introduction

Ions such as potassium, sodium, chloride and phosphate play crucial roles in cellular processes such as cell signaling<sup>1,2</sup>, metabolism<sup>3,4</sup>, cell proliferation<sup>5,6</sup> and apoptosis<sup>7</sup>. The plasma membrane of cells has multiple mechanisms to regulate the concentrations of each of these ions within a cell through various types of ion channels and pumps<sup>8,9</sup>. Forming GUVs in high ionic conditions is therefore a prerequisite to studying many of these cellular processes. Furthermore, in studies involving protein interactions with GUVs, many proteins require specific concentrations of certain ions to fold into their three dimensional structure<sup>10,11</sup>. For synthesis of GUVs for drug delivery related applications, 1×PBS, a solution of approximately 140 mM of a mixture of ions is used as a replacement to mimic the physiological conditions of blood or plasma<sup>12</sup>. However, the ability to assemble GUVs in solutions of high ion concentrations has been a long standing problem<sup>13,14</sup> although methods have been proposed to attempt to improve yields. The methods include incorporation of charged lipid in the membrane<sup>15</sup>, using agarose dried on glass as an alternative substrate<sup>16</sup> and increasing the voltage in the case of electroformation in order to improve yields<sup>17</sup>. While the solutions provide some improvements, there are drawbacks to many of them, ranging from the presence of polymer in the GUV membranes in the case of agarose assisted hydration<sup>18</sup> to the use of negatively charged inhibitive for GUV growth<sup>19</sup>. Furthermore, we find that while these solutions may improve yields compared to other experiments in high ionic conditions, they do not improve yields enough to match yields in low salt<sup>20</sup>.

Here, I reproduce the results previously collected by J. Pazzi on the effect of salts on the formation of GUVs that are useful to obtain a holistic picture of the impact of ions on the mechanism of GUVs assembly. The experimental results show that the molar yield of zwitterionic lipid decreases with increasing salt for GUVs assembled on both glass and tracing paper. The results<sup>20</sup> have been adapted to show the salient points in **Figure 6.1**. The scanning electron microscope images a) and b) show a difference between the flat surface of borosilicate glass and the tangled network of fibers that form nanocellulose. The evolution of molar yield with an increase in salt concentration is shown in **Figure 6.1** c). The lowest ion concentration is 0.0032 mM which has no added salt but carbon dioxide dissolved in the water which produces partially dissociated carbonic acid, resulting in a pH of 5.5<sup>21</sup>. At this lowest ion concentration, the molar yield on glass (red curve) is approximately half the molar yield on tracing paper. With increasing salt concentration, the yields on tracing paper drop sharply when the salt concentration is increased beyond 0.14 mM. The yields on glass drop gradually with increasing salt concentration up to 1.4 mM salt beyond which yields on both glass and tracing paper are very similar and evolve in tandem. The counts per microgram of lipid of GUVs assembled on glass and tracing paper at various surface concentrations are shown in d) and e). The counts of the small vesicles on glass are largely flat at a value of approximately  $8 \times 10^5$  until 1.4 mM salt

beyond which they fall, with the lowest value of  $3.8 \times 10^4$  at 1400 mM salt. Vesicles between 10 and 50  $\mu\text{m}$  fall after 0.65 mM. Large vesicles are only produced at the concentration with no additional salt, 0.0032 mM. The counts on tracing paper are higher than on glass for all size classes until 1.4 mM salt, beyond which the counts of GUVs from both substrates are very similar.

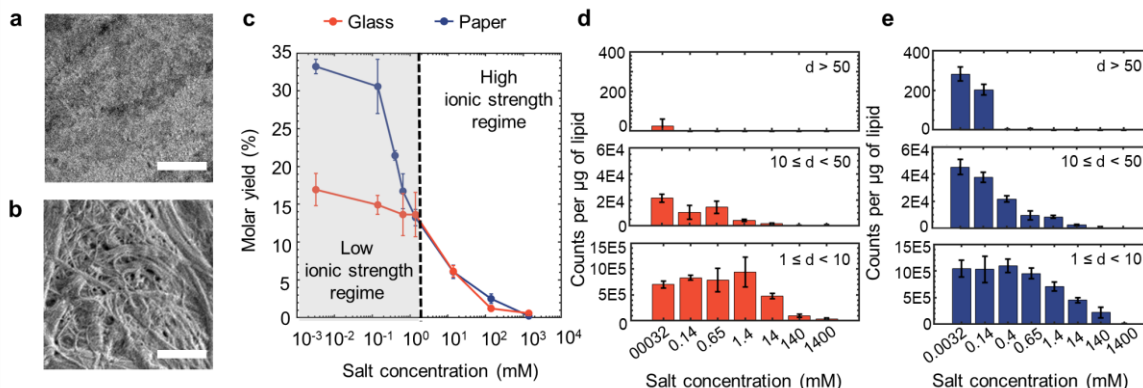


**Figure 6.1:** Experimental results of molar yields and counts of zwitterionic lipid DOPC at assembled in varying concentrations of salt Scanning electron microscopy images of a) flat surface of borosilicate glass and b) surface of nanocellulose paper composed of a network of tangled nanofibers. c) Molar yield of GUVs assembled on glass and nanopaper in varying salt concentrations. Blue curve shows the evolution of molar yield on tracing paper and the red paper shows the molar yield on glass. The counts per microgram of lipid of GUVs assembled on c) glass and d) nanocellulose. The counts are divided into 3 size classes with diameters,  $d$  between  $1 \leq d < 10 \mu\text{m}$ ,  $10 \leq d < 50 \mu\text{m}$ ,  $d \geq 50 \mu\text{m}$ . Scale bars are 2  $\mu\text{m}$ . Figures were constructed from experimental data obtained J Pazzi from the Subramaniam Lab<sup>20</sup>.

In this chapter, I use a set-up similar to the one in Chapter 3 to simulate the impact of ions on the yield and distributions of GUVs using the budding and merging model as a framework. I describe the important simulation parameters that were varied in section 6.2, and I describe the results from the simulations in section 6.3.

## 6.2. Simulation set up

The number of sites was set to 1000, and the average number of bilayers distributed on the fibers was 5 bilayers. Other than the adhesion energy, the values of all other parameters were kept constant at the values displayed in

**Table 3.1.** At higher salt concentrations, the increased screening of the charges on the counterions leads is expected to reduce the bilayer separation<sup>16,17,22</sup>, leading to higher adhesion between the bilayers. We mimicked the effect of increasing salt concentration by

increasing the adhesion energy,  $\xi$  to scale with the Debye screening length. The Debye screening length<sup>23</sup> is expressed as  $\kappa_D^{-1}$  in the following equation:

$$\kappa_D^{-1} = \sqrt{\frac{\epsilon_r \epsilon_0 k_B T}{2N_A e^2 [C]}} \quad (29)$$

Here  $\epsilon_0$  is the permittivity of free space,  $\epsilon_r$  is the dielectric constant,  $k_B$  is the Boltzmann constant,  $T$  is the absolute temperature,  $N_A$  is Avogadro's number,  $e$  is the elementary charge, and  $[C]$  is the ionic strength of the solution. The Debye screening length determines the distances over which the electrostatic effects of charges extend. All else being equal, for a fixed distance, a smaller Debye screening length is expected to increase the magnitude of the attractive van der Waals potential by screening the repulsive electrostatic potential.

The adhesion energy was varied with salt concentration using the following relationship:

$$([C]) = \frac{\xi_0}{\sqrt{[C]_0}} \sqrt{[C]} \quad (30)$$

Here,  $[C]_0 = 0.0578$  mM, sets a cutoff distance to 10 bilayer thicknesses in ultrapure water. We use  $\xi_0 = -6 \times 10^{-6}$  Jm<sup>-2</sup><sup>24</sup>. The negative sign denotes an attractive interaction.

### 6.3. Yield comparison between flat and curved surfaces

For comparison of yields on flat surfaces and curved fibers, I used the highest yielding surface concentration point to scale the model to the experiments. I divided the total area of the giant vesicles from the experimental data with the area of the average nanobud obtained from the model (0.34  $\mu\text{m}^2$  for the cylindrical surface) to obtain the nominal number of nanobuds. The simulations of the cylindrical surface predict 55 % higher nanobud counts than those observed in experiments which we attribute to the fact that in experiments, the nanocellulose paper is porous and is composed of multiple layers of nanocellulose fibers, while our simulation is of a monolayer of cylinders. Therefore, I expected a portion of the lipids to penetrate the paper resulting in lipid losses hence resulting in a lower nanobud count per mol of lipid deposited for the experimental system. I used a factor of 1.55 to scale the simulations of the cylindrical surface with experiments.

## 6.4. Results of simulations of varying salt concentration

The adhesion energy was varied between  $6 \times 10^{-6} \text{ Jm}^{-2}$  to  $9.34 \times 10^{-4} \text{ Jm}^{-2}$  to correspond to ion concentrations between 0.0032 mM to 1400 mM respectively. The adhesion energy for each concentration is shown in

**Table 6.1.**

Ion concentration (mM)	Adhesion energy $\xi$ ( $\text{Jm}^{-2}$ )
0	$6.00 \times 10^{-6}$
0.14	$9.34 \times 10^{-6}$
0.4	$1.58 \times 10^{-5}$
0.65	$2.01 \times 10^{-5}$
1.4	$2.95 \times 10^{-5}$
.14	$9.34 \times 10^{-5}$
140	$2.95 \times 10^{-4}$
1400	$9.34 \times 10^{-4}$

**Table 6.1:** Adhesion energy values for different salt concentrations calculated using Equation (30).

### 6.4.1. Effects of fiber geometry and salt concentration on the budding energy of each bilayer

The effect of varying salt concentration on the energy of budding of bilayers 2 – 11 in **Figure 6.2**. As described in section 3.3, the first bilayer is expected to adhere strongly to the substrate and is therefore not shown. The energy of budding for each bilayer is calculated using Equation (7). The energy of budding becomes progressively more positive with increasing bilayer number. The lower bilayer numbers have negative energies of budding which are shown in blue. Bilayers with positive energies of budding are shown in red. The figure also shows how the energy of budding changes depending on the fiber dimensions.

Across all fiber geometries, fewer bilayers have a negative budding energy with increasing salt concentration. When the bilayer number increases, the adhesion energy increases while the curvature of the fiber decreases (since the radius of the bilayers increase) both of which cause the process of budding to become less favorable. At high salt concentrations, the energy levels also appear to be more spread out. The total adhesion energy of a bilayer depends on the area of a bilayer – the larger the area, the larger the energy that will be required to overcome its adhesion to the bilayer below. Thus, at higher

salt concentrations when the adhesion energy is higher, the increase in area for each bilayer has a larger impact on the total adhesion energy (and the total budding energy) for each bilayer. In a), the effect of using 3 different radii of 10 nm, 20 nm or 30 nm is shown. All 3 fibers have lengths of 2000 nm. As noted in section 3.3, fibers of higher radii have a lower curvature. With increasing radius, all the energy levels are shifted to more positive values. With a radius of 10 nm, at least 1 bilayer can bud spontaneously up to and including 14 mM salt. For 20 nm fibers, none of the bilayers bud spontaneously in salt concentrations above 0.65 mM and for 30 nm fibers, beyond 0.14 mM.

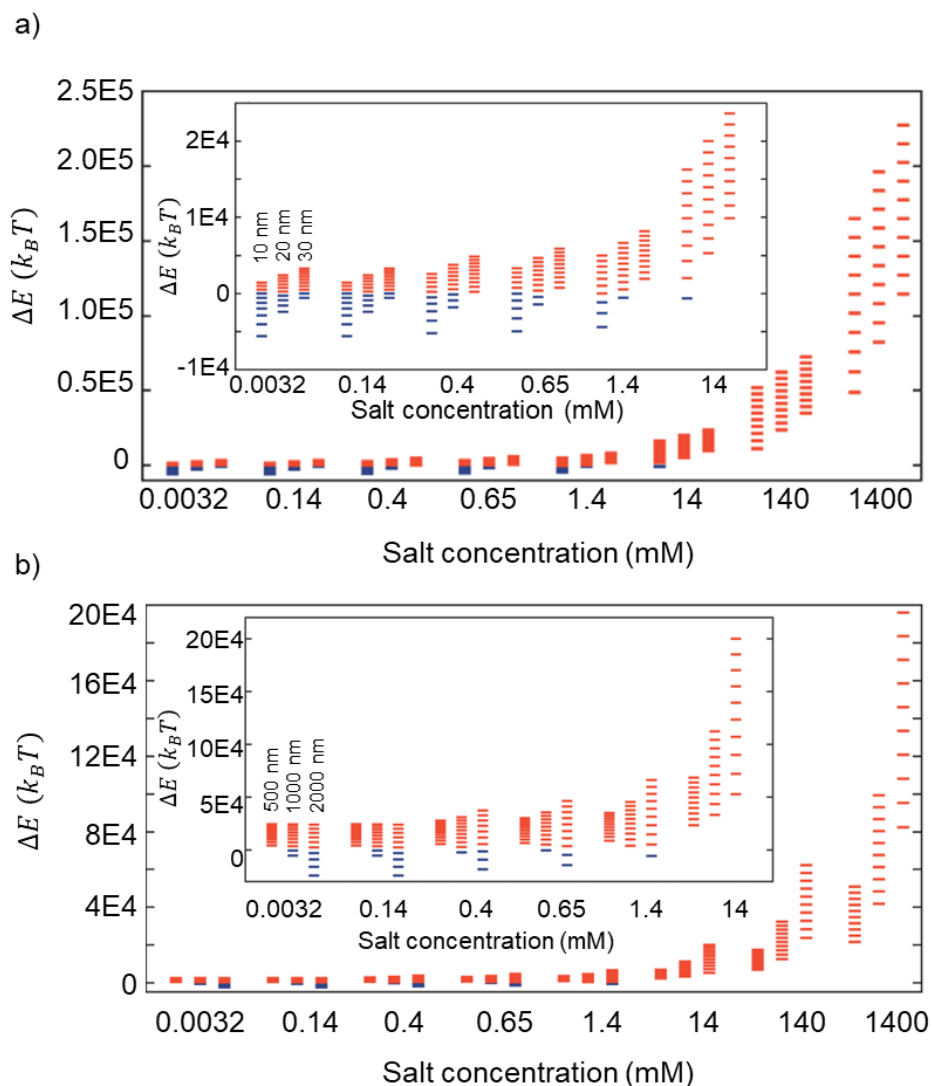


**Figure 6.2:** Energy diagrams showing how fiber dimensions affect the energy of budding. a) Energy levels for bilayers 2 – 11 on fibers of length 2000 nm and a radius of 10 nm, 20 nm or 30 nm as shown in the inset. The adhesion energy increases with increasing salt concentration. All other variables were held constant. Inset shows a zoomed-in view of the first 6 salt concentrations. The energy becomes more positive with increasing bilayer

number. Blue lines show bilayers with zero or a negative energy of budding while red shows bilayers with a positive energy of budding. b) Energy levels for bilayers 2 – 11 on fibers of radius 20 nm and lengths of 500 nm, 1000nm or 2000 nm.

In **Figure 6.2 b)** all fibers have a radius of 20 nm and the effect of 3 different fiber lengths are shown, 500 nm, 1000 nm, and 2000 nm. Longer fibers have more bilayers that can bud spontaneously for the lower salt concentrations since they have a larger aspect ratio. This results in the first term of Equation (7) being more negative and thus helps overcome the reduction in favorability due to increasing adhesion energy. Fibers with lengths of 500 nm have an aspect ratio that is too low to have any bilayers that bud spontaneously across all salt concentrations including 0.0032 mM. 1000 nm fibers have at least one bilayer that buds spontaneously until a concentration of 0.65 mM while fibers with lengths of 2000 nm have at least 1 bilayer with a negative energy of budding up to a concentration of 1.4 mM. At 0.0032 mM and 0.14 mM, longer fibers that have a larger aspect ratio have lower budding energies for the lower bilayer numbers. However, at higher bilayer numbers, the energy of budding for all fiber lengths are similar. Between 0.4 mM and 1.4 mM salt, with increasing fiber length, the lower bilayers have a more negative energy of budding while the higher bilayers have a more positive energy of budding. Beyond 1.4 mM, the trend seen at lower salt is reversed. All bilayers on all 3 fiber dimensions have a positive energy of budding but with increasing fiber length, the magnitude of the energy increases, requiring more energy input for bilayers on longer fibers to bud. This occurs for similar reasons that were discussed earlier for energy levels being further apart at higher salt concentrations. At high salt concentrations, when the adhesion between bilayers is significantly higher than in the absence of salt, the increase in fiber length results in a larger surface area that requires a higher energy input to overcome the adhesion to the bilayers below. This is also the reason that the longer fibers have larger energy intervals at all salt concentrations. Thus, to make budding more favorable in high salt conditions, designing fibers with a smaller radius rather than longer lengths is more useful.

The energy levels on glass are plotted in **Figure 6.3**. Since glass is smooth, a possible route for buds to form is by first forming a break in the bilayer coating the surface which is taken as a disk of radius  $R_d$ <sup>25</sup>. To simplify the simulation, I assume that all the disks are of the same radius and each disk is considered a site. Since all bilayers on a flat surface will have the same geometry, they will also have the same energy of budding unlike bilayers on cylindrical fibers that have different critical radii, depending on the bilayer number. Each energy level in a) is the energy of a bilayer of the disk radius of either 100 nm, 500 nm or 700 nm. From equation (17), I note that budding on glass is always endergonic and requires energy input. Thus, all energies of budding in a) are positive. For all disk sizes, an increase in salt concentration results in an increase in energy of budding. However, disks of larger radii see a far more significant increase, as with a larger surface area, a larger adhesion energy will have to be overcome to enable budding. Using a disk radius of 700 nm and 500 nm, the energy of budding increases 27 times and 20 times



respectively, from no added salt to 1400 mM salt. Compared to this, when the disk radius reduced to 100 nm, the energy of budding only increases 4 times from 0.0032 mM to 1400 mM salt. b) shows the impulse of energy that is necessary to form buds on glass. The value used in this simulation is 20,000  $k_B T$ . Bilayers that have an energy of budding that is larger than the external energy applied will not bud. In reality a number of factors can influence the disk radius. It is more likely that there is a range of radii in experiments. Factors such as variation in concentration, the smoothness of the bilayer that is templated likely affect the energy required to form breaks in the bilayer and the size of the breaks that can form.

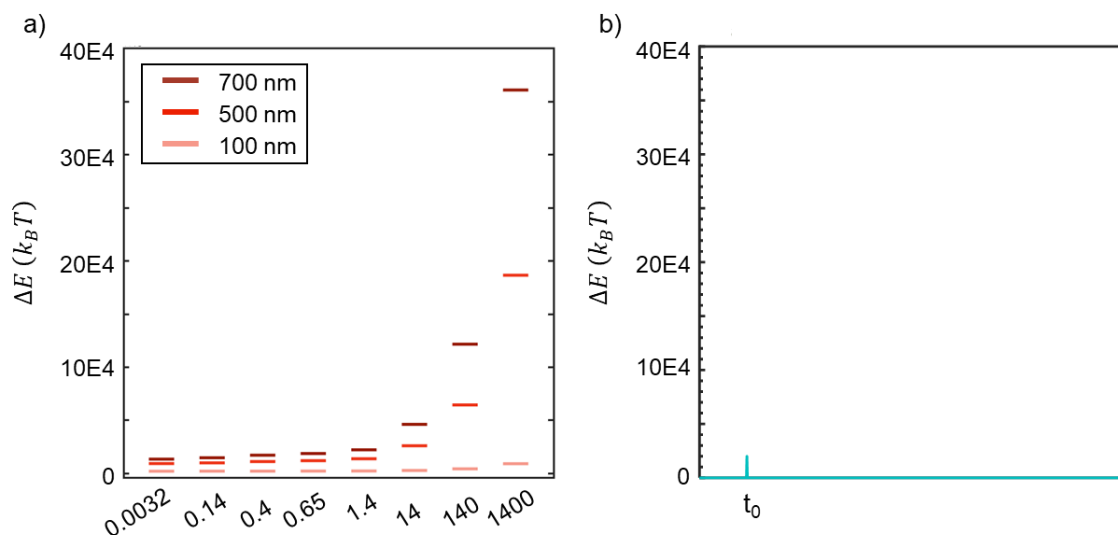


**Figure 6.3:** Variation of budding energy on glass. a) Budding energy for different starting disk radii for increasing salt concentrations. 3 different disk radii shown, 100 nm, 500 nm, and 700 nm. All bilayers on a flat surface have the same dimensions and therefore the same budding energy. Since all instances of budding on glass is endergonic, buds only form due to external energy. b) Magnitude and duration of external energy shown on a generalized time scale. The simulations use 20,000  $k_B T$  of external energy at the beginning as an impulse of energy. Any bilayers with a budding energy larger than 20,000  $k_B T$  cannot bud.

## 6.4.2. Simulation results of varying salt concentrations

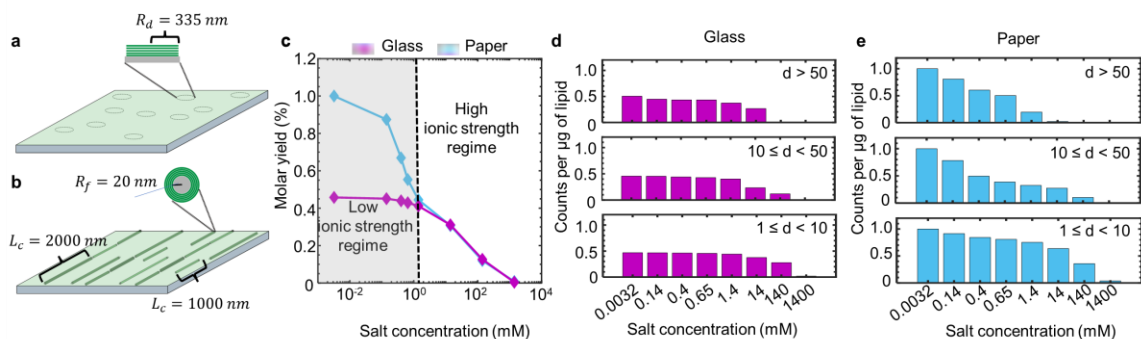


**Figure 6.4:** Results of simulation of GUV assembly on a flat surface and curved fibers at varying salt concentrations. Schematic of simulation set up shown for a) flat surface to mimic glass and b) curved fibers to mimic nanocellulose. c) Molar yields of GUVs obtained from the simulation. The magenta curve shows simulations on a flat geometry and the blue curve shows simulations on curved fibers. Counts per microgram of lipid shown obtained from the simulations for d) flat glass and e) curved nanocellulose fibers. The counts have been normalized to the highest yielding point, assembly on nanopaper at an ion concentration of 0.0032 mM. The counts are divided into 3 size classes with diameters,  $d$  between  $1 \leq d < 10 \mu\text{m}$ ,  $10 \leq d < 50 \mu\text{m}$ ,  $d \geq 50 \mu\text{m}$ .

As described in section 3.2, I keep the simulation set-up consistent with those in section 3.3 and use fiber geometries  $R_f \times L_f = 20 \text{ nm} \times 1000 \text{ nm}$  and  $R_f \times L_f = 35 \text{ nm} \times 2000 \text{ nm}$ . I compare yields between the two substrates by setting the number of sites as 1000 for both geometries and fixing the number of bilayers applied on the surface to be 5. The number of nanobuds generated were normalized with the moles of lipid prior to merging. For simulations on glass, I set each site to be a disk of radius 335 nm. The schematics of the surface set up are shown in **Figure 6.4** a) and b). The resulting molar yield obtained from the simulation is shown in c). All molar yield values on both paper and glass are normalized with the value of 31%, obtained at 0.0032 mM of ions on cylindrical fibers. The normalization showed the molar yield on flat geometry at 0.0032 mM of ions was approximately half that on cylindrical fibers and remains flat up to salt concentrations of 1.4 mM. When the salt concentration is increased beyond 1.4 mM, the initially separated yield curves on both surfaces overlap and decrease in tandem with increasing salt, similar to what was seen in experimental results (**Figure 6.1**). The counts per microgram of lipid on flat geometry is shown in d) while e) shows the counts obtained from cylindrical fibers. All counts for each size class were normalized with the counts obtained at 0.0032 mM salt on cylindrical fibers for ease of comparison. The yield on glass appears flat until 14 mM of salt for all size classes and are consistently lower than the counts obtained from simulations on cylindrical fibers. Simulation results from e) show a steady decrease in

counts across all size classes with increasing salt. The trends match those seen in experimental results, but the absolute values of the counts are higher, which is expected since the simulation is an idealized scenario of the experiments.

### **6.4.3. Budding time scales for cylindrical fibers compared to a flat geometry**

I use the simulations to understand how the process of assembly at varying time points in different salt concentrations. Since I set the assumption that buds form sequentially starting from the outermost bilayers, with the inner bilayers budding only after they are exposed, I plot the sequence of budding events on a generalized time scale in **Figure 6.5** for 3 different salt concentrations. Panel a) shows the nanobuds formed at different time points on cylindrical fibers while panel b) shows the same on a flat geometry. At 0.0032 mM of ions on cylindrical fibers, nanobuds form during 6 time intervals, the number of nanobuds being highest for the first interval and successively decreasing in number. When the salt concentration is increased to 1.4 mM, nanobuds are formed only during the first two intervals, with the number formed in the second timepoint reduced by a factor of 10 compared to the second time point at 0.0032 mM. At the highest salt concentration of 1400 mM, buds are formed only in the first time point, due to external energy and the number of buds formed is 21 times lower than for 0.0032 mM.

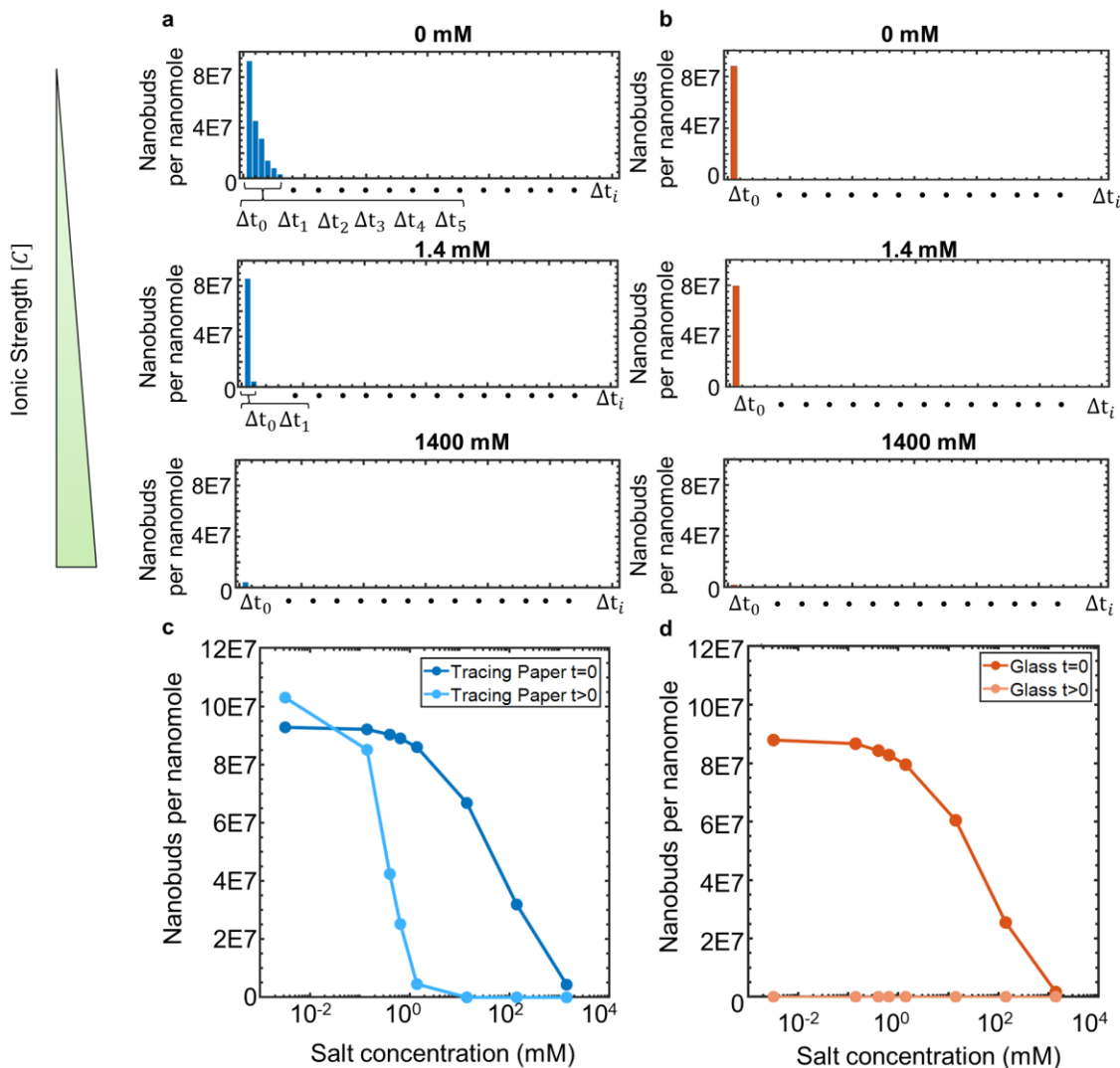


**Figure 6.5:** The budding timescales and counts are shown for different salt concentrations. Kinetic plots on a generalized time axis of the number of nanobuds that form for each  $\Delta t$  for a) assembly on cylindrical fibers and b) assembly on a flat surface in 0 mM, 1.4 mM and 1400 mM of added sodium chloride. More nanobuds form on the cylindrical fibers at all time intervals compared to the flat surface which only forms nanobuds at the first time interval. With increasing salt concentration, nanobuds only form at the earlier time intervals. The total number of nanobuds formed due to the impulse of energy (dark curves) and the nanobuds formed due to spontaneous budding (lighter curves) are shown for c) assembly on cylindrical fibers and d) flat surfaces. On flat surfaces no nanobuds form after the first time interval.

On a flat geometry, nanobuds are only formed in the first time interval for all salt concentrations, which corresponds to the only interval that has external energy applied to

the bilayers. Since no external energy is available at subsequent intervals, no buds are formed. Similar to the results on cylindrical fibers, fewer buds form at higher salt concentrations and at the highest concentration of 1400 mM salt the nanobud count 55 times lower than at 0.0032 mM.

The total number of nanobuds formed due to the impulse of energy at time point  $t = 0$  compared to the number of nanobuds that form at subsequent time points are shown for cylindrical fibers in **Figure 6.5 c)** and for a flat geometry in d). For both substrates, the variation of buds formed due to external energy at varying salt appears similar (darker colored plots). At low salt concentrations, the curves at  $t=0$  are flat up to 1.4 mM salt after which the nanobud counts begin to drop more steeply with increasing salt. The lighter curves in both c) and d) show buds formed at  $t > 0$ , which are buds that can form via the spontaneous pathway. This number is zero for a flat geometry since there is no spontaneous pathway available. On cylindrical fibers, the number of buds formed spontaneously is higher than the buds formed as a result of external energy but drops sharply above a salt concentration of 0.14 mM. Beyond 1.4 mM of salt, no buds can form spontaneously, since the high adhesion energies for all remaining bilayers results in the energy of budding becoming positive.

#### 6.4.4. Simulations of one-step modulation of salt

I have shown experimental results describing the steady decrease in yields with increasing salt concentrations and I have also shown how simulation results with increasing adhesion energy mimics the effects of salt. For biophysical studies and use in therapeutics,  $1 \times$  phosphate buffered saline which has an ionic concentration of approximately 140 mM is used as a replacement to mimic the physiological conditions of blood or plasma<sup>12</sup>. However, at this concentration of salt, experimental results shown a molar yield of 2.5%. To overcome this issue, J Pazzi from the Subramaniam lab showed a method of modulation of salt concentration can be used to overcome this issue of growth. These modifications, termed one-step modulation (OSM) involves initially assembling GUVs on tracing paper in a solution with no added salt for 10 minutes followed by an injection of a high concentration of salt solution below the nanopaper<sup>20</sup>. Since the GUV buds that are formed are connected to the surface until they are harvested, the ions diffuse into the GUVs, equalizing the osmotic pressure across the GUV membrane so that upon detachment, the GUVs are stable in an ionic solution. **Figure 6.6 a)** illustrates the experimental results conducted by J Pazzi in which the interval of low salt assembly was varied by adding salt at 0, 1, 5 and 10 minutes after incubation of the lipid coated paper in low salt. For the 0 minute timepoint, salt was added directly into the hydration solution. The upper panels show the molar yield and the lower panels show the counts per microgram of lipid. The final concentration of the GUV solution contained 140 mM of sodium chloride. The yields and counts were compared to the yields obtained in solutions with no added salt (control).

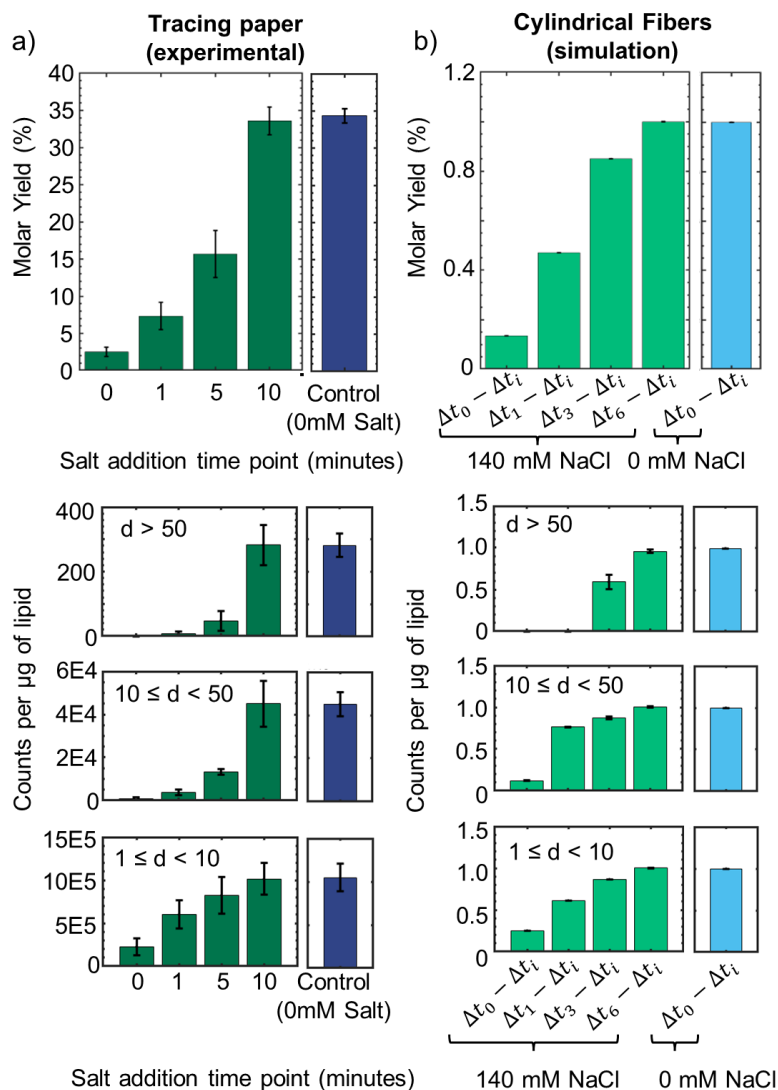


**Figure 6.6:** One-step modulation of the salt concentration produces high yields of GUVs in physiological salt solutions. Molar yield (top row) and counts of GUVs (bottom row) obtained for modulation of salt from a) experimental data and b) simulations for curved fibers. The counts are divided into 3 size classes with diameters,  $d$  between  $1 \leq d < 10 \mu\text{m}$ ,  $10 \leq d < 50 \mu\text{m}$ ,  $d \geq 50 \mu\text{m}$ . The experimental data on tracing paper was obtained from J Pazzi<sup>20</sup>.

The plots show the changes in molar yield depending on the length of time the lipid is allowed to hydrate in a low salt solution. The molar yield increases from  $2.5 \pm 0.6\%$  when the lipids are directly hydrated in a 140 mM of salt to  $7.3 \pm 1.9\%$  when salt is added after 1 minute of hydration in a low salt solution. This value increases to  $15.7 \pm 3.2\%$  when salt is injected after 5 minutes and  $33.6 \pm 1.9\%$  after 10 minutes. The counts per microgram of lipid follow a similar trend, increasing when the lipids are allowed to hydrate in a low salt solution for longer periods of time prior to adding salt. I described earlier that the

addition of salt likely increases the adhesion between the bilayers, resulting in the energy of budding becoming more positive for all bilayers and thus decreasing the number of bilayers that can bud. Longer incubation times in low salt allow a larger number of bilayers to bud via the spontaneous pathway before the addition of salt increases causes budding to become unfavorable. Note that the yields and the counts when salt is added after 10 minutes is very similar to the yields in low salt solutions. This indicates that all the bilayers that could potentially bud in low salt, do so by the 10 minute mark, beyond which addition of salt does not affect yields.

The bar plots representing the counts per microgram of lipid show that the number of medium-sized and large vesicles increase more steeply with increasing hydration times. Larger vesicles require a larger number of nanobuds to merge and therefore are closely correlated to the number of nanobuds available. When salt is injected into the solution after shorter time intervals, the total number of nanobuds produced is lower, resulting in a more significant impact on the vesicles over 10  $\mu\text{m}$  in diameter.

The simulation data in b) shows a similar trend in both molar yields and counts per microgram of lipid. The blue bars show the simulation results for growth in low salt while the green bars show results after addition of salt after varying intervals of hydration in low salt. The molar yield and counts are plotted relative to the molar in zero salt. The addition of salt is modeled by an increase in adhesion energy, which results in more bilayers becoming unfavorable to bud spontaneously.

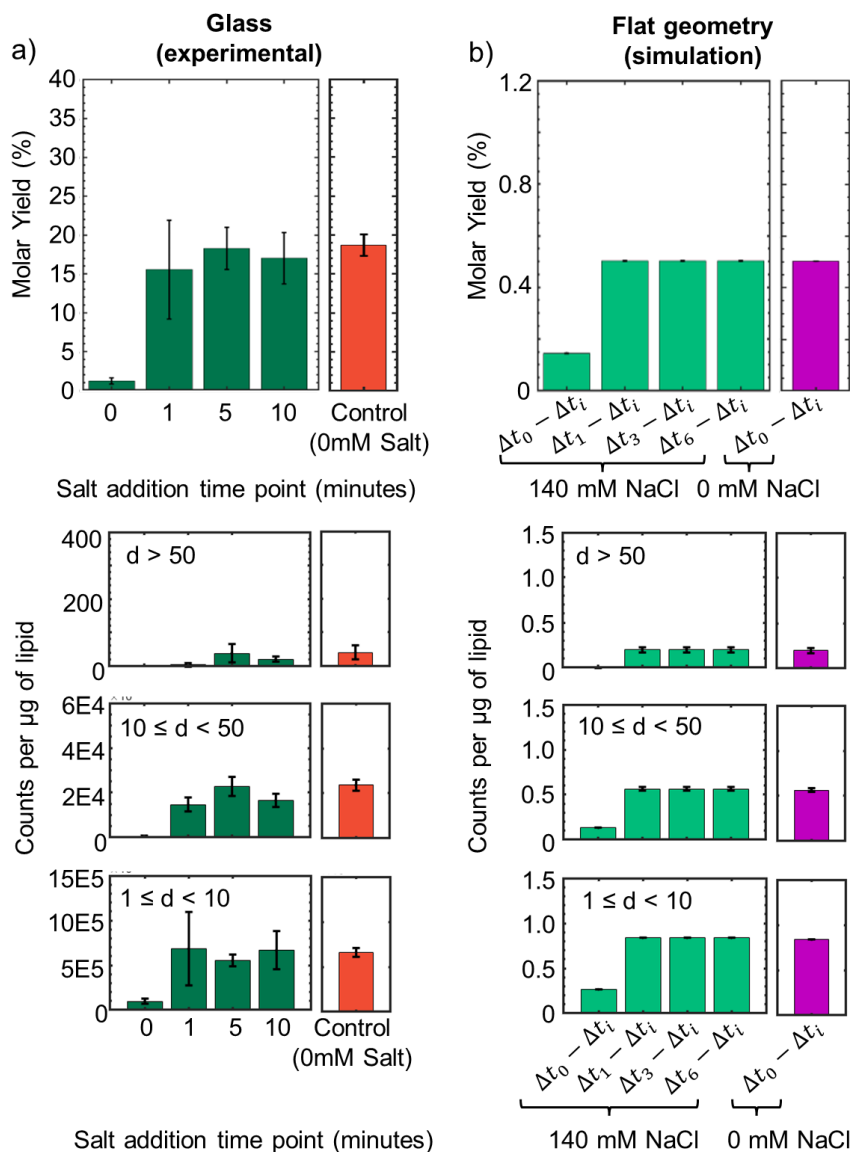


**Figure 6.7:** One-step modulation of the salt concentration produces high yields of GUVs in physiological salt solutions on glass. Molar yield (top row) and counts of GUVs (bottom row) obtained for modulation of salt from a) experimental data and b) simulations on curved fibers. The counts are divided into 3 size classes with diameters,  $d$  between  $1 \leq d < 10 \mu\text{m}$ ,  $10 \leq d < 50 \mu\text{m}$ ,  $d \geq 50 \mu\text{m}$ .

To determine the differences in behavior on a flat substrate, I carried out similar experiments on glass using one-step modulated assembly. I dosed in salt at varying time points as shown in **Figure 6.7** a) so that the final concentration of the GUV solution was 140 mM. The first time point of 0 minutes has a yield of  $1.2 \pm 0.4\%$ . Addition of salt after hydration of the lipid in low salt solution for 1 minute or longer results molar yield in the



range of  $15.5 \pm 6.3\%$  to  $18.3 \pm 2.7\%$ . Note that the overlapping errors bars indicate that the differences are not significant but arise from sample to sample variation. The counts per microgram of lipid show similar results, with no significant difference between number of GUVs for all three size classes when salt is added after 1 minute of incubation in low salt solutions. When salt is added at the 0 minute timepoint, the lipid is exposed to the effects of ions from the very beginning. This entails that the energy of budding for all bilayers is high from the very start of the hydration process due to the higher adhesion energy. On glass, all the bilayers have a positive energy of budding even in low salt solutions and therefore bud only in the presence of external energy. Since external energy is applied only at the point of hydration, all nanobuds that can bud do so at the point of hydration. Therefore, adding salt any point after this initial time point results in a similar molar yield. All budding that occurs after the instance of hydration occurs via the spontaneous pathway, which does not exist for glass. Simulations of this process in b) reflects the trends seen in the experimental results. While the relative yield is 0.27 when the adhesion energy is increased to the value of 140 mM salt, the yield increases 3 times when the adhesion energy is increased after the first timepoint. The molar yield and the counts are identical to the values in low salt when the adhesion energy is increased after the first timepoint.

#### 6.4.5. The molar yield is maximized at the salt concentration with the lowest budding energies

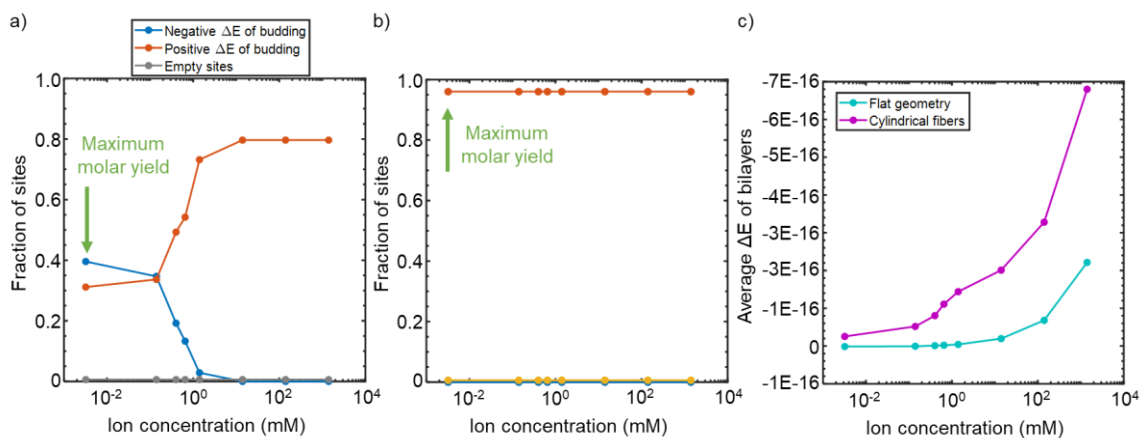


**Figure 6.8:** Variation of budding energy on curved fibers compared to flat substrates. a) Fraction of bilayers with different budding energies templated on fibers with radii of 20 nm and lengths of 1000 nm and 2000 nm distributed in a 1:1 ratio by area. Fraction of bilayers that have a positive (red) or negative (blue) energy of budding or are empty (gray) at different nominal surface concentrations. The molar yield peaks at the concentration with the highest fraction of sites that have an outer bilayer with a negative energy of budding and can bud spontaneously. b) fraction of bilayers with different budding energies

templated on a flat geometry. The fraction of bilayers with a positive energy of budding is consistent at 0.96. There are no bilayers with a negative budding energy. c) Average energy of the outermost bilayers plotted for flat geometry (magenta) and cylindrical fibers (blue) at varying salt concentrations.

In section 3.3, I showed that the molar yield is maximized when the number of sites with an outer bilayer that can bud spontaneously is maximized. In **Figure 6.8a**), I show that this is also the case when varying salt concentration on cylindrical fibers. Since adhesion energy, increases with increasing salt, the fraction of sites with a negative energy of budding is maximized at the lowest salt concentration. The fraction of sites with a positive energy of budding increase steeply beyond 1.4 mM and stabilizes at a value of  $\sim 0.8$  at 14 mM. Beyond this concentration, although the number of sites with a positive energy of budding doesn't increase since it has been maximized, the magnitude of the energy increases. This is shown in c) (blue curve). With increasing ion concentration, the average budding energy of the bilayers increases, gradually at first, and then more steeply beyond 14 mM. **Figure 6.8 b)** shows the fraction of bilayers with positive and negative budding energies on glass. There are no sites with negative budding energies. All sites are always positive, at a constant fraction of 0.96. The remainder of the sites are either empty or have a single bilayer that cannot bud. To further understand the impact of salt, the magenta curve in c) shows the magnitude of the bilayers increase with increasing salt. The rate of increase is much steeper than on tracing paper for all salt concentrations.

#### **6.4.6. Effect of varying fiber geometry on the yields and sizes of GUVs at various salt concentrations**

I showed in section 3.3 that fibers with higher curvature (smaller radius) and higher aspect ratios have high yields. Here, I determine the effect of fiber geometry at varying salt concentrations. Similar to the trends seen for varying the surface concentration of lipid, reducing the radius of the fiber increases the curvature of the fiber which results in an increase in molar yields. Fibers with a mixed geometry of lengths of 1000 nm and 2000 nm and fixed radius of 20 nm produce a maximum yield of 30% when assembled in low salt. When this is altered to monodisperse fibers of 2000 nm length and with a radius of 20 nm, the yield increases to 42%. An increase in the curvature to 10 nm and an increase in aspect ratio by increasing the length to 4000 nm increases the yield to 91%. A further increase in the aspect ratio by increasing the fiber length to 10,000 nm maintaining the radius at 10 nm does not increase the maximum yield beyond 56% but increases the yields at salt concentrations higher than 0.4 mM. Conversely, a reduction in curvature by increasing the radius from 20 nm to 40 nm keeping the length constant at 2000 nm reduces the maximum yield from 42% to 13%. All fiber lengths showed a similar evolution of molar yield with salt concentration, where the yield is maximized at the lowest salt and progressively decreased with increasing the salt concentration.

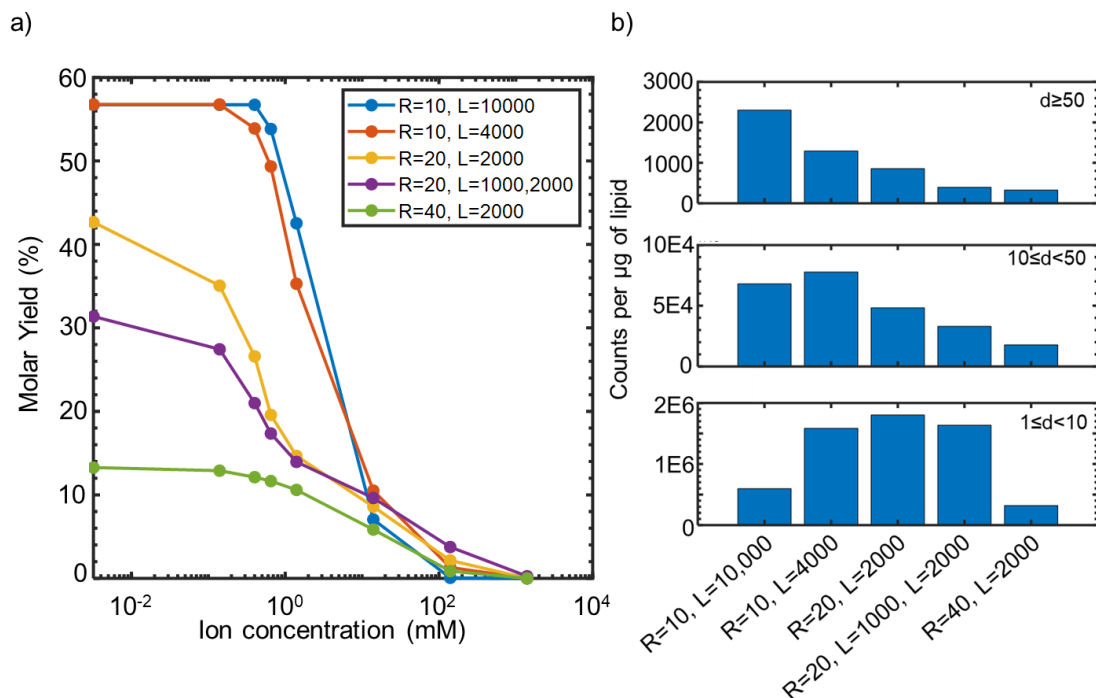


**Figure 6.9:** Yields and size distributions of GUVs assembled on fibers of varying geometries. a) Evolution of molar yields with varying salt concentrations on different fiber geometries. The legend shows fiber dimensions with radius, R and length, L. Across all fiber geometries, the yield is maximized at the lowest salt concentration. b) Counts per microgram of lipid for the nominal concentrations at which the molar yield peaks. The x-axis at the bottom shows the fiber geometries and the x-axis at the top shows the nominal surface concentration at which the molar yield is maximized. The counts are divided into 3 size classes with diameters,  $d$  between  $1 \leq d < 10 \mu\text{m}$ ,  $10 \leq d < 50 \mu\text{m}$ ,  $d \geq 50 \mu\text{m}$ .

The counts per microgram also show behavior similar to what was seen in section 3.3. Fibers with the highest curvatures and aspect ratios show the highest number of large vesicles, which decreases with decreasing curvature. The smaller vesicles do not peak at the same fiber dimensions since the fibers with higher curvatures produce nanobuds with higher mean diameters, therefore pushing the size distributions towards larger vesicle classes. Therefore, to maximize yields at higher salt concentrations altering the fibers to have higher curvature and aspect ratios can help improve yields up to a concentration of 1.4 mM. To assemble vesicles at higher salt concentrations, the OSM-PAPYRUS method remains the superior method, since it is able to match the yields obtained in low salt. A combination of fiber geometries with higher curvature and aspect ratios while using OSM-PAPYRUS method will help maximize yields.

## 6.5. Limitations and scope of the simulation set-up

In this section, I discuss the limitations of the model and the simulation set up. The first key difference between the simulations and experiments is that while nanocellulose is composed of polydisperse fiber geometries, the simulations were limited to just 2 different fiber lengths. Fibers with lower radii and longer lengths can support more bilayers that can bud spontaneously. Furthermore, each bilayer on a fiber produced a single bud in the simulations. In experiments, it is possible that bilayers templated onto fibers form multiple breaks in the membrane, resulting in multiple buds from a single bilayer. This would result in smaller nanobuds which will shift GUV distributions towards lower diameters. Similarly, on glass we set the size of each site to be a disk with a radius of 335 nm. In experiments, breaks may form due factors such as defects in the bilayer as a result of local variations in concentration, and the sites are likely to be a range of different sizes. Sites with more area will require more external energy in order to overcome adhesion energy at high salt concentrations. Nanocellulose also has pores which can result in lipid losses, leading to an overall lower yield. The application of lipid and the ability to coat fibers can also vary experimentally. We assume in simulations that each fiber is coated fully with whole bilayers. In reality, the close network of fibers can result in partial coverage of many fibers, leading to variations in the curvature experienced by some bilayers, which can change the energy of budding and the yield. In experiments, other variations in experiments can also result in fluctuations in yields. One such factor is pipetting hydration solution onto the lipid-coated substrate which is the source of external energy added into the system. Variations in pipetting can result in variations in the magnitude of the energy, which alters the number of buds that can form. Finally, in simulations, we did not set any limits on the process of merging. However, it is likely that there is a limit on the size of vesicles that can form since long incubation times do not increase the maximum diameters of the GUVs.

## 6.6. Bibliography

- (1) Levitan, I. B. Signaling protein complexes associated with neuronal ion channels. *Nat. Neurosci.* **2006**, *9*, 305–310.
- (2) Prindle, Arthur; Liu, Jintao; Asally, Munehiro; Ly, San; Garcia-Ojalvo, Jordi; Suel, G. M. Ion channels enable electrical communication in bacterial communities. *Nature* **2015**, *527*, 59–63.
- (3) Macdonald, P. E. Signal integration at the level of ion channel and exocytotic function in pancreatic  $\beta$ -cells. *Am. J. Physiol. Metab.* **2011**, *301*, 1065–1069.
- (4) Zhang, K.; Liu, X.; Wang, L.; Liu, Z.; Yi, Q.; Geng, B.; Chen, X.; Yu, D.; Xia, Y. The mechanosensory and mechanotransductive processes mediated by ion channels and the impact on bone metabolism : A systematic review. *Arch. Biochem. Biophys.* **2021**, *711*, 109020.
- (5) Serrano-novillo, C.; Capera, J.; Colomer-molera, M.; Condom, E.; Ferreres, J. C.; Felipe, A. Implication of Voltage-Gated Potassium Channels in Neoplastic Cell Proliferation. *Cancers (Basel)*. **2019**, *11*, 287.
- (6) Pérez-garcía, M. T.; Ciudad, P.; López-lópez, J. R. The secret life of ion channels : Kv1 . 3 potassium channels and proliferation. *Am. J. Cell Physiol.* **2017**, *314*, C27–C42.
- (7) Kondratskyi, A.; Kondratska, K.; Skryma, R.; Prevarskaya, N. Ion channels in the regulation of apoptosis. *BBA - Biomembr.* **2015**, *1848*, 2532–2546.
- (8) Gadsby, D. C. Ion channels versus ion pumps : the principal difference , in principle. *Nature* **2009**, *10*, 344–352.
- (9) Dubyak, G. R. Ion homeostasis , channels , and transporters : an update on cellular mechanisms. *Adv. Physiol. Educ.* **2004**, *28*, 143–154.
- (10) Castan, D.; Trigueros, T.; Millet, O.; Tadeo, X.; Lo, B. Protein Stabilization and the Hofmeister Effect : The Role of Hydrophobic Solvation. *Biophysic* **2009**, *97*, 2595–2603.
- (11) Baldwin, R. L. How Hofmeister Interactions Affect Protein Stability \*. *Biophys. J.* **1996**, *71*, 2056–2063.
- (12) Sadek, S. H.; Rubio, M.; Lima, R. Blood Particulate Analogue Fluids : A Review. *Materials (Basel)*. **2021**, *14*, 16–21.
- (13) Reeves, J. P.; Dowben, R. M. Formation and properties of thin-walled phospholipid vesicles. *J. Cell. Physiol.* **1969**, *73*, 49–60.
- (14) Angelova, M. I.; Dimitrov, D. S. Liposome Electroformation. *Faraday Discuss. Chem. Soc.* **1986**, *81*, 303–311.

- (15) Akashi, K. I.; Miyata, H.; Itoh, H.; Kinoshita, K. Preparation of giant liposomes in physiological conditions and their characterization under an optical microscope. *Biophys. J.* **1996**, *71*, 3242–3250.
- (16) Horger, K. S.; Estes, D. J.; Capone, R.; Mayer, M. Films of agarose enable rapid formation of giant liposomes in solutions of physiologic ionic strength. *J. Am. Chem. Soc.* **2009**, *131*, 1810–1819.
- (17) Li, Q.; Wang, X.; Ma, S.; Zhang, Y.; Han, X. Electroformation of giant unilamellar vesicles in saline solution. *Colloids Surfaces B Biointerfaces* **2016**, *147*, 368–375.
- (18) Lira, R. B.; Dimova, R.; Riske, K. A. Giant unilamellar vesicles formed by hybrid films of agarose and lipids display altered mechanical properties. *Biophys. J.* **2014**, *107*, 1609–1619.
- (19) Rodriguez, N.; Pincet, F.; Cribier, S. Giant vesicles formed by gentle hydration and electroformation: A comparison by fluorescence microscopy. *Colloids Surfaces B Biointerfaces* **2005**, *42*, 125–130.
- (20) Pazzi, J. E. A Comprehensive Characterization of Surface-Assembled Populations of Giant Liposomes using Novel Confocal Microscopy-Based Methods, University of California, Merced, 2021.
- (21) Mahnke, J.; Stearnes, J.; Hayes, R. A.; Fornasiero, D.; Ralston, J. The influence of dissolved gas on the interactions between surfaces of different hydrophobicity in aqueous media. Part I. Measurement of interaction forces. *Phys. Chem. Chem. Phys.* **1999**, *1*, 2793–2798.
- (22) Stein, H.; Spindler, S.; Bonakdar, N.; Wang, C.; Sandoghdar, V. Production of isolated giant unilamellar vesicles under high salt concentrations. *Front. Physiol.* **2017**, *8*, 1–16.
- (23) Israelachvili, J. N. *Intermolecular and Surface Forces: Third Edition*; 2011.
- (24) Sun, Y.; Lee, C.; Huang, H. W. Adhesion and Merging of Lipid Bilayers : A Method for Measuring the Free Energy of Adhesion and Hemifusion. *Biophysj* **2011**, *100*, 987–995.
- (25) Pazzi, J.; Subramaniam, A. B. Nanoscale Curvature Promotes High Yield Spontaneous Formation of Cell-Mimetic Giant Vesicles on Nanocellulose Paper. *ACS Appl. Mater. Interfaces* **2020**, *12*, 56549–56561.

## Appendix A: A comparison of different merging models

In Chapter 3 I described the merging model that was used in the simulations of the budding and merging model. Here, I compare the merging template to an alternative merging model that was considered. The histograms of the GUVs obtained from the simulation and the mean, median, extreme diameters and the counts were used to determine which model showed better agreement with experimental results. The set-up of the merging template is described in detail in section 3.2 of Chapter 3.

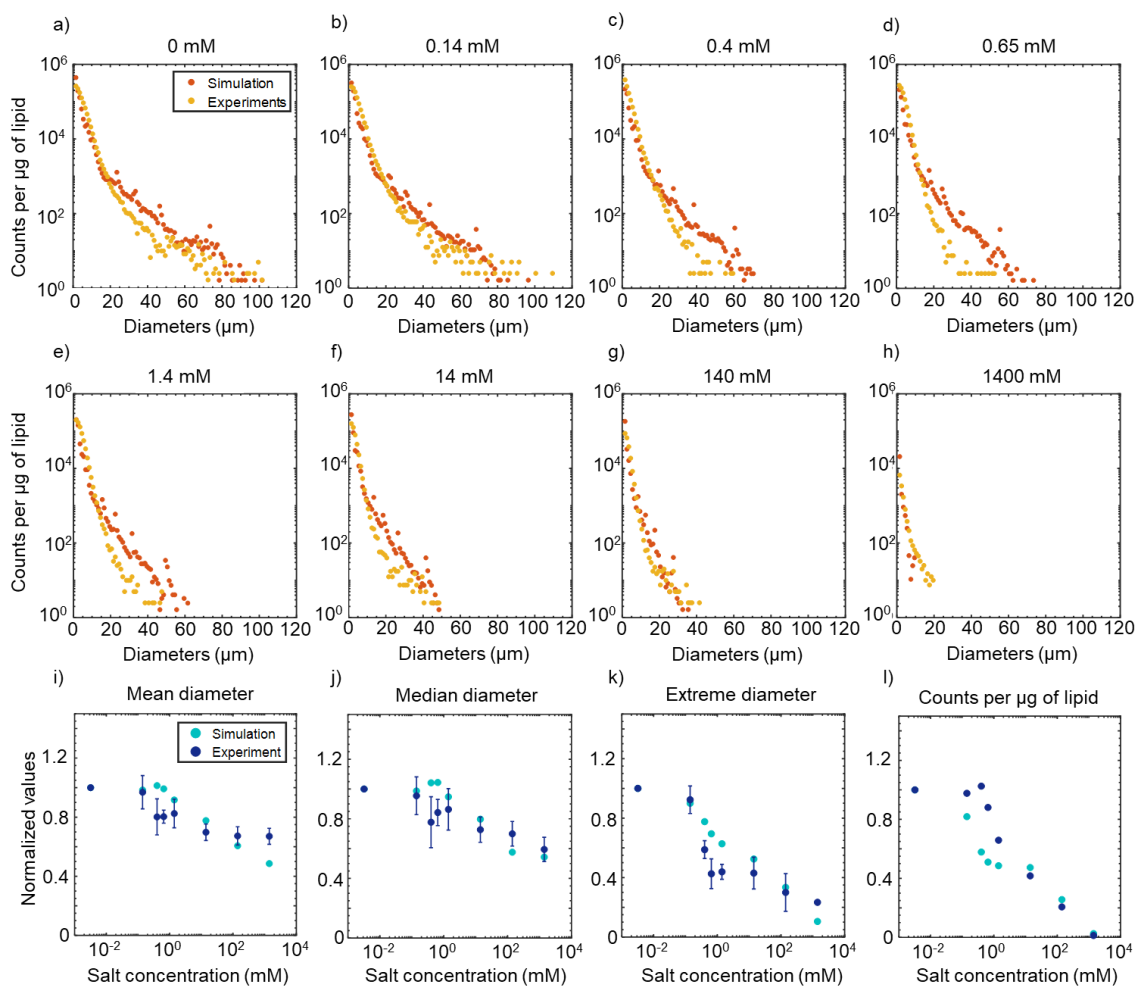


**Figure A.1:** Comparison of histograms of diameters between experimental data and simulations for curved fibers. Simulations were carried out using the concept of a merging template. a)-h) compare the distributions of diameters for a) 0 mM, b) 0.14 mM, c), 0.4 mM, d) 0.65 mM, e) 1.4 mM, f) 14 mM, g) 140 mM, and h) 1400 mM added salt. Plots i)-l) compare various parameters of the distributions obtained from the simulation and experiments. The values have been normalized with the value obtained for 0 mM salt to

compare trends between the simulations and experiments. i) Mean diameter, j) median diameter, k) extreme diameter and l) Counts per microgram of lipid.

**Figure A.1** compares the simulated and experimental distributions. In the experimental results (yellow curve) all distributions are right skewed, with significantly fewer large vesicles compared to small vesicles. Furthermore, the size distributions become consistently narrower with increasing salt concentration. The merging template reproduces both these aspects of the distributions for all the salt concentrations except for 1400 mM salt for which the nanobud distribution is narrower than the experimental results. The experimental results for 1400 mM salt have diameters up to 20  $\mu\text{m}$ , while the largest vesicles from the simulations are  $\sim 10 \mu\text{m}$ .

Merging Template 1			Merging Template 2		
Cluster size	Number of clusters	Buds selected	Cluster size	Number of clusters	Buds selected
10	10378490	1.04E+08	2000	51892	1.04E+08
50	1383798	6.92E+07	4000	17297	6.92E+07
100	461266	4.61E+07	6000	7687	4.61E+07
500	61502	3.08E+07	8000	3843	3.08E+07
1000	20500	2.05E+07	10000	2050	2.05E+07
5000	2733	1.37E+07	15000	911	1.37E+07
10000	911	9.11E+06	20000	455	9.11E+06
20000	303	6.07E+06	25000	242	6.07E+06
50000	80	4.05E+06	50000	134	4.05E+06
	<b>Selected</b>	303255649		<b>Selected</b>	303255649

**Table A.1:** Table showing two options of merging templates, 1 and 2. Template 1 results in distributions generated in **Figure A.1**. Template 2 was adjusted to match experimental



data for 1400 mM salt and then applied to other concentrations **Figure A.2** illustrates how this affects lower concentrations using the example of 0 mM salt.

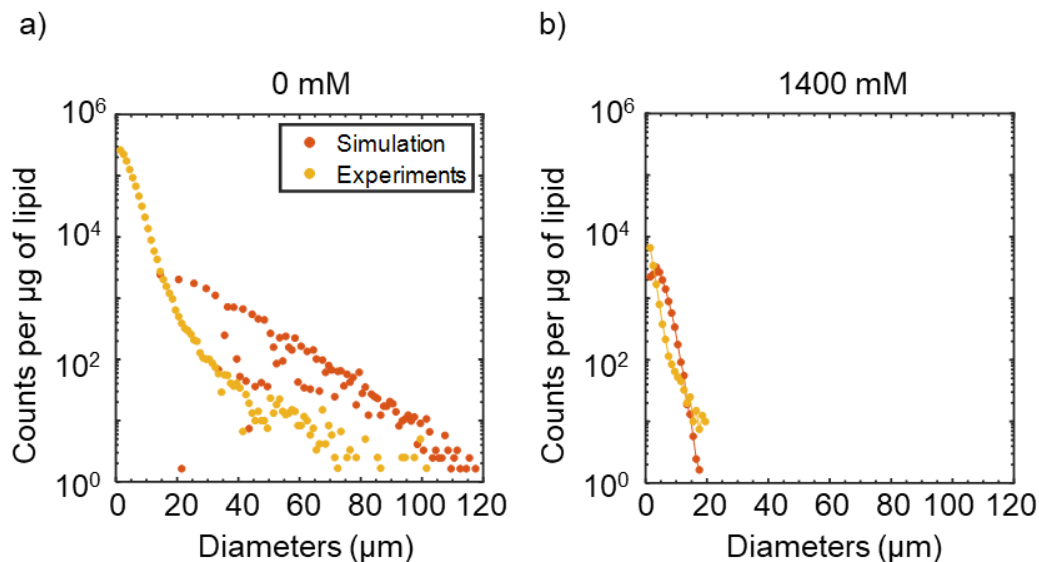


**Figure A.2:** Histograms obtained using merging template 2 at the lowest and highest salt concentrations. Merging templates with large cluster sizes broaden the distribution of diameters at 1400 mM salt but shifts the distributions away from the experimental results at 0 mM salt. a)

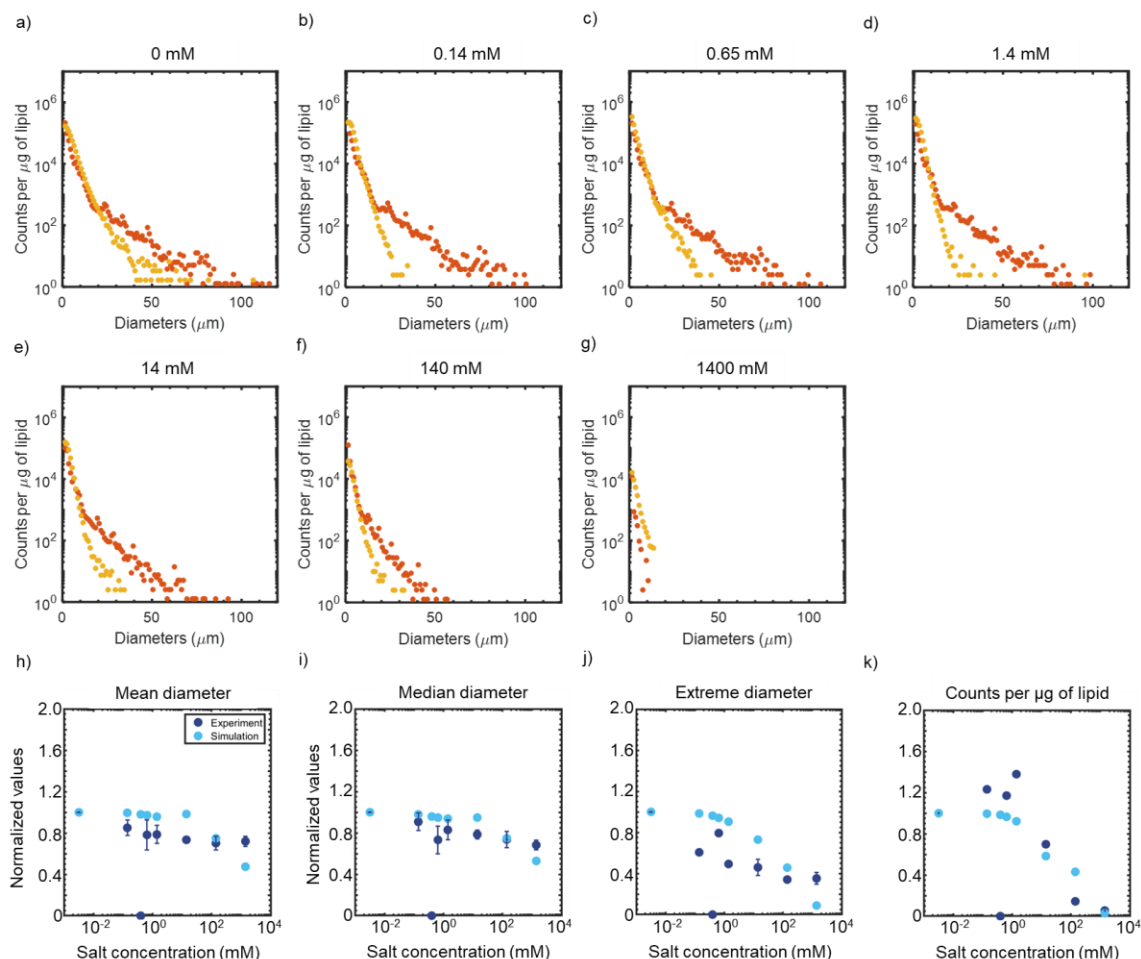
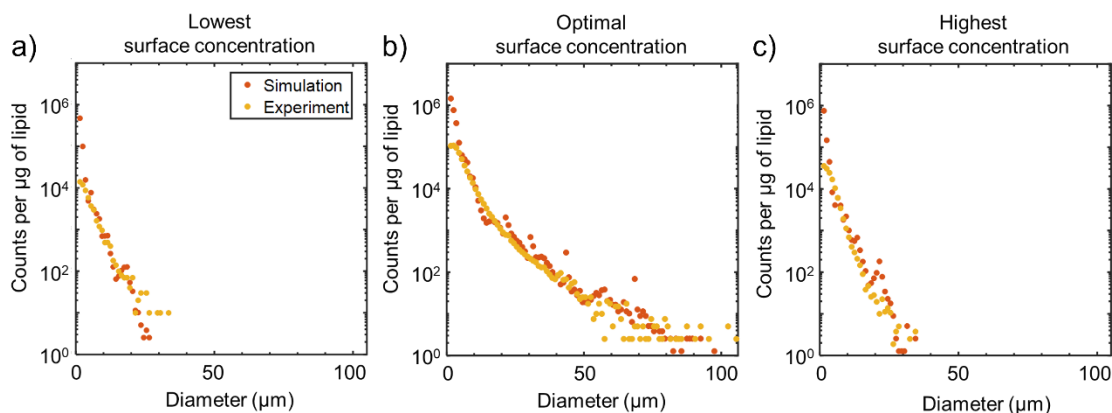


**Figure A.3:** Comparison of histograms of diameters between experimental data and simulations for a flat substrate. Simulations were carried out using the concept of a merging template. a)-h) compare the distributions of diameters for a) 0 mM, b) 0.14 mM, c) 0.65 mM, d) 1.4 mM, e) 14 mM, f) 140 mM, and g) 1400 mM added salt. Plots h)-k) compare various parameters of the distributions obtained from the simulation and experiments. The values have been normalized with the value obtained for 0 mM salt to compare trends between the simulations and experiments. h) Mean diameter, i) median diameter, j) extreme diameter and k) Counts per microgram of lipid.

I varied the merging template to determine the cluster sizes that would be required for the distribution to mimic the experimental values for 1400 mM of salt. **Table A.1** shows the merging template that would be required to achieve this. Since 1400 mM salt results in the formation of far fewer nanobuds, the starting arrangement of buds is less dense, with many more empty sites (**Figure 3.5b**). Significantly larger cluster sizes were required to increase the final size distribution of GUVs as seen in **Table A.1** shows the effect of using this merging template on the lower concentrations. While the simulated distribution of 1400 mM is closer to the experimental results, using this merging template for lower salt concentrations drastically increases the number of large vesicles and eliminates any

vesicles below 15  $\mu\text{m}$ . Therefore, merging template 1 appears to be the better choice for most of the data points.

I carry out similar simulations on flat surfaces. The maximum number of filled sites was set to be the number of nanobuds that form for 0 mM salt, the highest yielding point in the series. Recursive merging of nanobuds on flat surfaces (**Figure A.3**) deviates from experimental values. Only the extreme concentrations, 140 mM and 1400 mM appear to match the experimental values.



**A.4:** Comparison of histograms of diameters between experimental data and simulations for curved fibers. a) Comparison of low nominal surface concentration ( $0.9 \text{ nmol}/\text{cm}^2$  for experimental data) b) optimal surface concentration ( $18 \text{ nmol}/\text{cm}^2$  for experimental data) and c) highest surface concentration ( $179 \text{ nmol}/\text{cm}^2$  for experimental data). The simulation concentrations that were chosen for comparison were selected by selecting points that had the same relative reduction in molar yields compared to the optimum yield as in the experiments.

### Alternate merging schemes tested

#### Exponential distribution of nanobuds with varying mean cluster size

In this method of merging, I used a discrete exponential function to assign nanobuds into bins corresponding to clusters of nanobuds that merge. I used the following functional form to modify  $b$  for varying salt concentration:

$$b(N_{tot}) = \frac{N_{tot0}}{N_{tot}} \quad (31)$$

Here,  $b([N_{tot}])$  is the value of  $b$  for different total number of nanobuds  $N_{tot}$ ,  $N_{tot_0}$  is the nanobuds per nanomole at a reference value.  $b_0$  is the reference value. I then use Equation (32) to distribute the nanobuds into  $D_{GV} = 1 \dots 120$  bins corresponding to clusters of nanobuds that merge to form surface-attached microbuds with diameters from 1 to 120  $\mu\text{m}$ .

$$N(D_{GV}) = \frac{N_{tot,C}}{(e^{-b} - e^{-120b})} b \exp(-bD_{GV}) \quad (32)$$

Here,  $N_{tot,C}$  is the total number of nanobuds produced at a salt concentration  $C$  and  $b$  is the exponential factor. The density of the nanobuds was accounted by varying the value of the mean bin that the nanobuds occupied.  $b = 1/\mu$  where  $\mu$  is the mean bin which corresponds to the average residency of buds within the distribution. Higher values of  $\mu$  means that more buds reside in larger bins, resulting in larger cluster sizes. The assembly of giant vesicles of diameter  $D_{GV}$  from nanobuds of diameter  $D_{NB}$  requires the merging of clusters of nanobuds of cluster size,  $CS_{D_{GV}}$ , given by Equation (33):

$$CS_{D_{GV}} = \left(\frac{D_{GV}}{D_{NB}}\right)^2 \quad (33)$$

I then obtained the number of giant vesicles of a given size,  $N_{R_{GV}}$  from Equation (34):

$$N_{R_{GV}} = \frac{N(D_{GV})}{CS_{D_{GV}}} \quad (34)$$

**Figure A.5** shows plots of number of nanobuds distributed to the bins (blue dots, upper horizontal axes) and the resulting distribution of the microbuds after merging (orange dots, lower horizontal axes) from the simulation of the nanobuds obtained for varying concentration of salt. Consistent with expectations for an exponential distribution, the distribution of nanobuds appear as a straight line in the semilogarithmic plots. With the distribution rules, lower number of nanobuds leads to fewer bins with larger cluster numbers being filled. The slope of the curve also decreases with lower number of nanobuds and lower concentrations. For the higher concentrations of salt with fewer number of nanobuds, the right most bins deviate from the straight line due to not having enough nanobuds to fill the discrete bins. Interestingly, after merging, the distribution of the microbuds deviates from a straight line. The distribution did not fit any simple functional relationship such as a power law or exponential distribution.

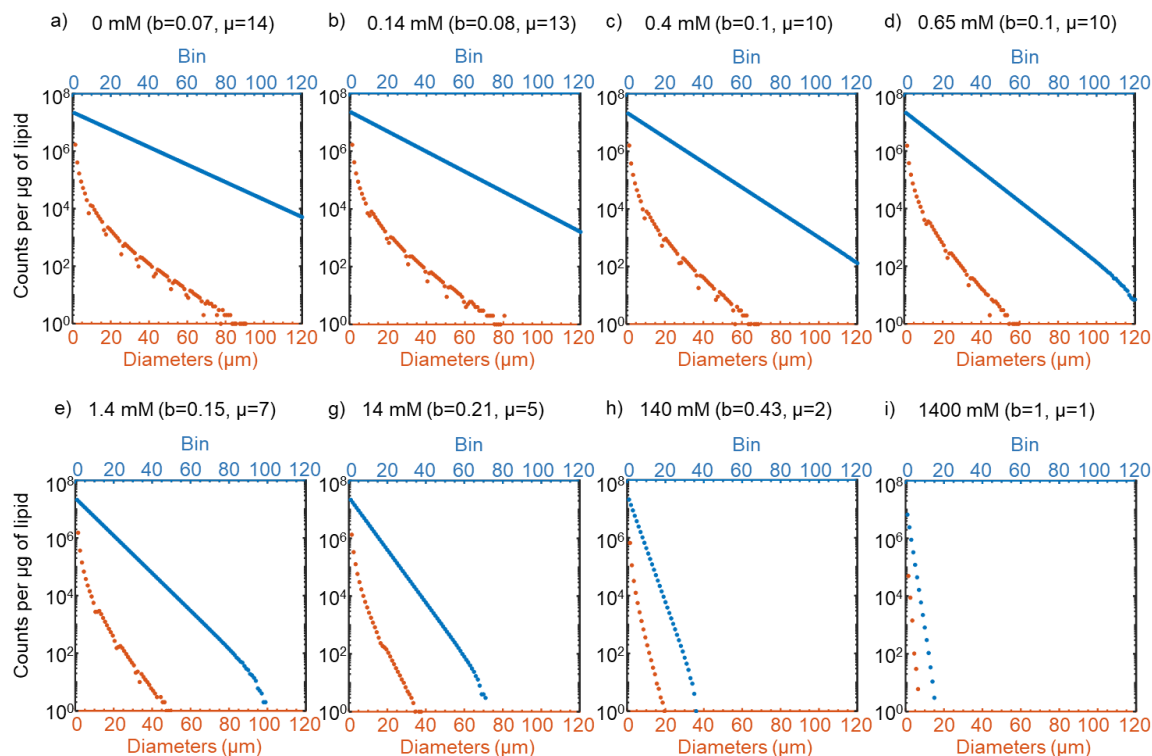


**Figure A.5:** Distributions of nanobuds and microbuds for different  $b$  values. The curves in blue show the distribution of nanobuds across 120 bins and the curves in orange show the distribution of microbuds after merging of the nanobuds. Note the logarithmic scale on the y-axis. With increasing values of the exponential factor  $b$ , the slope of the exponential function becomes steeper. Upon merging, the microbud distributions deviates from the exponential.

I compared the results of the simulation with the experimental data to determine how the choice of  $b_0$  changes the resulting distribution of  $GUV$  diameters. In the first round of simulations, I chose  $b = 0.07$  through trial and error to determine which starting value of  $b$  resulted in a histogram fit that was closest to the experimental values for 0 mM of added salt. I then used Equation (31) to determine the value of the exponential factor for all other salt concentrations. The resulting distributions are shown in **Figure A.6**. Consistent with experimental results, the distribution becomes narrower with increasing salt concentration. The distributions are similar to the experimental results for most of the concentrations. I find that the distribution is narrower than experimental values only for 140 mM and 1400 mM. The experimental distributions have vesicles up to 40  $\mu\text{m}$  and 20  $\mu\text{m}$  for 140 mM and 1400 mM respectively while the simulations have corresponding maximum values of 20  $\mu\text{m}$  and 10  $\mu\text{m}$ .

Since the higher salt concentrations, particularly 140 mM and 1400 mM deviated the most from experimental values, I determined the effect on the distributions if the exponential factor was set to the optimum value for the highest salt concentration and

adjusted proportionally for all other concentrations. At  $b = 0.3$  for 1400 mM of salt, the width of the exponential distribution matched the width of the experimental distribution. exponential factor for all other salt concentrations were adjusted using Equation (31). **Figure A.7** shows the result of this simulation. A comparison between the simulated microbud distribution and the experimental results shows that the simulated distributions are too wide and have too many large vesicles ( $> 20 \mu\text{m}$ ) for all concentrations except 1400 mM. Similar comparisons of simulations on flat surfaces compared to experiments varying salt concentrations on glass are shown in **Figure A.8**. As in the case of the merging template, I find that values for 0.14 mM, 1.4 mM and 14 mM salt concentrations deviate from the simulations.

In conclusion, merging using both the merging template as well as the exponential appears to yield similar results for varying salt concentration for simulations on curved fibers. I note more variations in both cases between simulation and experimental results on glass. However, the experimental result for glass has more variations as seen on the plots for the extreme diameter and GUV counts. Since the external energy is the only expected route to vesicle formation on glass, small variations in pipetting the hydration solution on the dried lipid stacks may result in noticeable variations in final distributions obtained compared to those obtained from assembly on curved fibers. Although both methods appear comparable, I note that the merging template matches the trends in the mean, median, extreme diameters and GUV counts more closely to the experimental results. For this reason, I chose this as the merging process for comparison and analysis in Chapters 3 and 6.

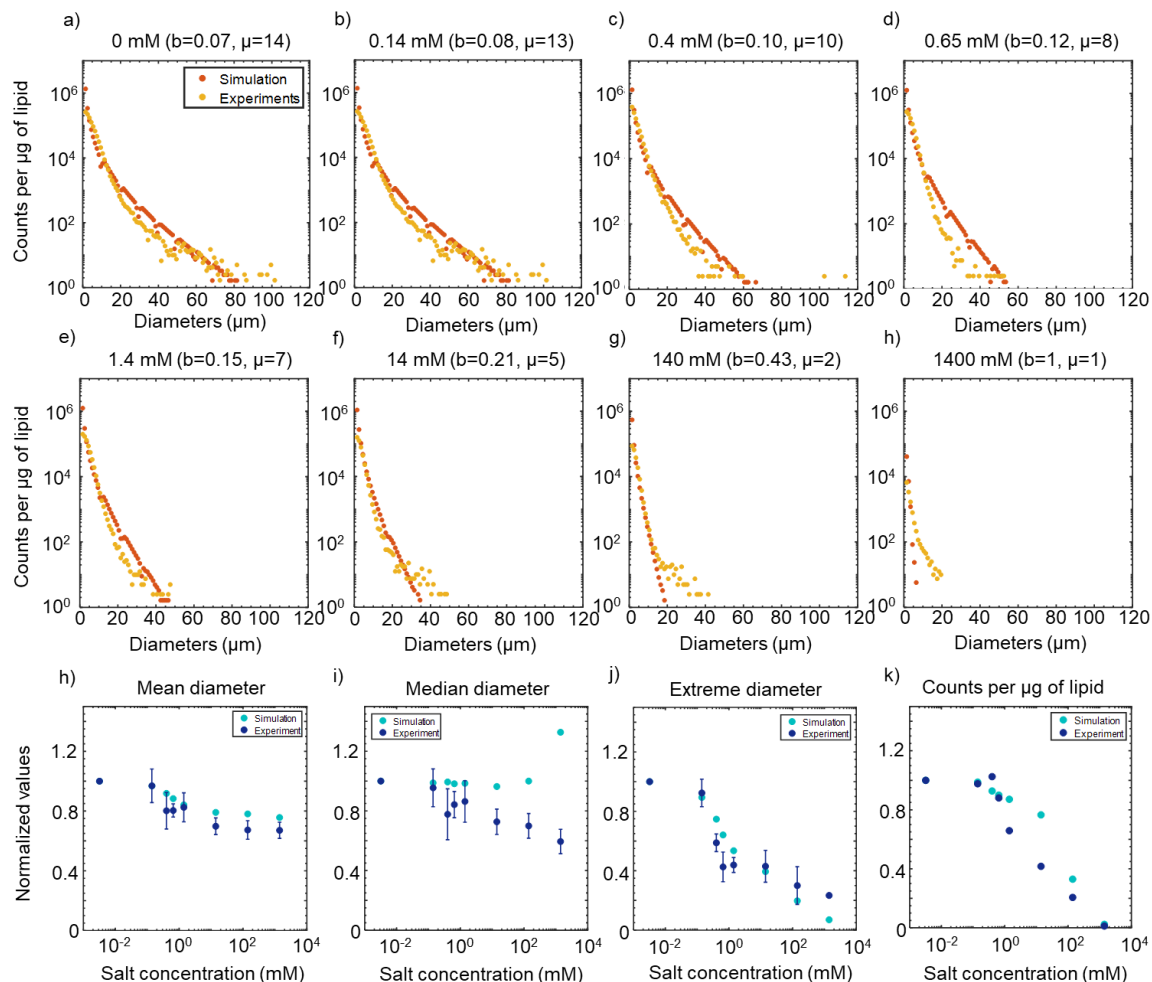


**Figure A.6:** Comparison of histograms of diameters between experimental data and simulations for curved fibers. Simulations of merging were carried out by distributing nanobuds using an exponential distribution with a varying exponential factor  $b$ . The exponential factor and the mean of the exponential distribution  $\mu$  are shown above each plot. a)-h) compare the distributions of diameters for a) 0 mM, b) 0.14 mM, c), 0.4 mM, d) 0.65 mM, e) 1.4 mM, f) 14 mM, g) 140 mM, and h) 1400 mM added salt. Plots i)-l) compare various parameters of the distributions obtained from the simulation and experiments. The values have been normalized with the value obtained for 0 mM salt to compare trends between the simulations and experiments. i) Mean diameter, j) median diameter, k) extreme diameter and l) Counts per microgram of lipid

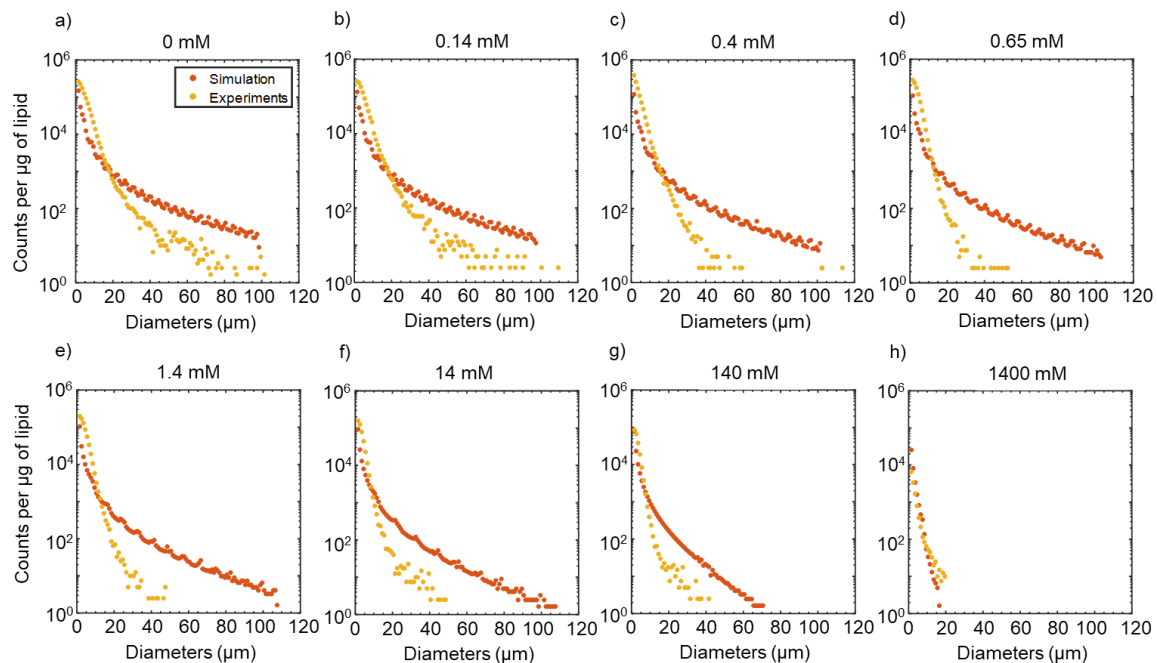


**Figure A.7:** Comparison of histograms of diameters between experimental data and simulations on curved fibers. Simulations of merging were carried out by distributing nanobuds using an exponential distribution with a varying exponential factor  $b$ . The starting value of  $b$  was set to 0.3 for 1400 mM salt and the value of  $b$  for all other salt concentrations were modified using Equation 13. a)-h) compare the distributions of diameters for a) 0 mM, b) 0.14 mM, c), 0.4 mM, d) 0.65 mM, e) 1.4 mM, f) 14 mM, g) 140 mM, and h) 1400 mM added salt. Clear deviations of the simulation results from the experimental plots can be seen for all salt concentrations except h).



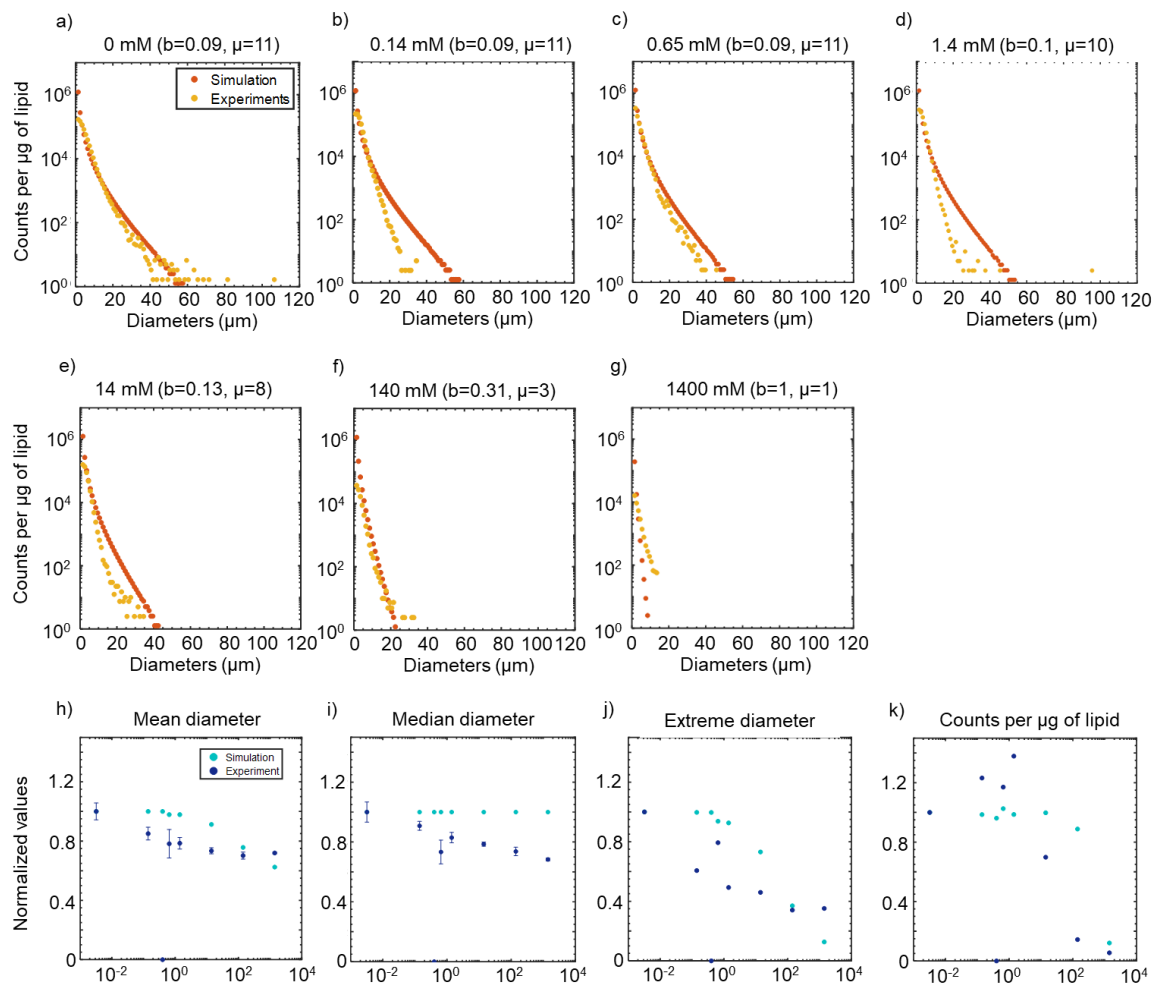


**Figure A.8:** Comparison of histograms of diameters between experimental data and simulations for a flat substrate. Simulations of merging were carried out by distributing nanobuds using an exponential distribution with a varying exponential factor  $b$ . a)-h) compare the distributions of diameters for a) 0 mM, b) 0.14 mM, c) 0.65 mM, d) 1.4 mM, e) 14 mM, f) 140 mM, and g) 1400 mM added salt. The exponential factor and the mean of the exponential distribution  $\mu$  are shown above each plot. Plots h)-k) compare various parameters of the distributions obtained from the simulation and experiments. The values have been normalized with the value obtained for 0 mM salt to compare trends between the simulations and experiments. h) Mean diameter, i) median diameter, j) extreme diameter and k) Counts per microgram of lipid.

## Appendix B: Assembly of GUVs on fabrics of diverse chemistries

### 1. Introduction

In broadening the use of thin-film hydration techniques, the substrate remains a key bottleneck to cost and versatility of use. The use of paper has key benefits over glass, which has been the traditionally used substrate, such as cost, biodegradability, and ease of use. Here, I explore the applications of the POPYRUS method to show that growth of vesicles on a wide range of fabrics, both synthetic ones such as nylon, polyester and glass fibers as well as natural fabrics such as wool, silk and rayon allows the formation of GUVs. I also show that dye molecules that are dried along with the lipid on the surface of the fabric are encapsulated within the lumen of the GUV upon hydration, demonstrating the possibility of using the GUVs as cargo delivery vehicles. These techniques allow the use of GUVs for applications such as bandages with antibiotics as encapsulants or pain relieving patches since the substrates are more durable than nanopaper. The results have been published in ACS Langmuir, titled '*Fabrics of Diverse Chemistries Promote the Formation of Giant Vesicles from Phospholipids and Amphiphilic Block Copolymers*'.

### 2. Materials and Methods

**Materials:** We purchased sucrose (BioXtra Grade, purity  $\geq 99.5\%$ ) glucose (BioXtra grade, purity  $\geq 99.5\%$ ), casein from bovine milk (BioReagent grade), and poly(ethylene glycol)-block-poly(propylene glycol)-block-poly(ethylene glycol) (PEO<sub>5</sub>PPO<sub>67</sub>PEO<sub>5</sub>, Pluronic® L121) from Sigma-Aldrich. We purchased 1,2-dioleoyl-*sn*-glycero-3-phosphocholine (DOPC), 1,2-dipalmitoyl-*sn*-glycero-3-phosphocholine (DPPC), 1,2-dioleoyl-*sn*-glycero-3-phospho-(1'-*rac*-glycerol) (DOPG), cholesterol (ovine wool), 1-palmitoyl-2-(dipyrrometheneboron difluoride)undecanoyl-*sn*-glycero-3-phosphocholine (TopFluor-PC), 1,2-dioleoyl-*sn*-glycero-3-phosphoethanolamine-N-(lissamine rhodamine B sulfonyl) (ammonium salt) (Rhod-PE), 1,2-dioleoyl-3-trimethylammonium-propane (DOTAP), and E.coli polar lipid extract from Avanti Polar Lipids, and poly(butadiene-*b*-ethylene oxide) (PBD<sub>46</sub>PEO<sub>30</sub>) (P9095-BdEO, lot# P9757) from Polymer Source Inc (Montreal, Canada). We purchased the fabrics from online vendors and from a local branch of a national fabric store Jo-Ann, LLC. The fabrics we purchased were silk (Silk Dupioni, Bright White, 100% silk), rayon (Sportswear Modal Fabric, White, 100% Rayon), nylon (Sport Nylon Fabric, White, 100 % Nylon) and polyester (Satin Tafetta, White, 100% polyester). We purchased wool fabric (100% Merino Wool Interlock – Washable) from Nature's Fabrics (naturesfabrics.com) and plain weaved fiberglass fabric (3oz Fabric Style120 E-Glass) from Fibre Glast Developments Corp. We obtained 18.2 MΩm ultrapure water from an ELGA Pure-lab Ultra water purification system (Woodridge, IL).

**Preparation of substrates:** Each piece of fabric was cut into 10 × 10 cm squares. Working in a chemical fume hood, I placed the fabric in 100 mL of neat chloroform in a 100 mL

glass media bottle. A magnetic stirrer and Teflon stir bar were used to agitate the fabric in chloroform for 30 minutes. The process was repeated twice with fresh chloroform each time. After the final chloroform wash, I removed the fabric and allowed the solvent to evaporate from the fabric. I then placed the fabric in a 1000 mL glass media bottle and alternated between soaking and rinsing the fabric in fresh batches of 1000 mL of ultrapure water over the course of 3 hours. The substrates were dried in ambient conditions and stored in a clean Petri dish for future use.

**Scanning electron microscopy:** To prepare the fabrics for imaging, we cut a small 5 mm × 5 mm pieces of the cleaned fabric and mounted them on aluminium SEM stubs using double sided copper tape. We used a field emission scanning electron microscope (GeminiSEM 500, Zeiss, Germany) to obtain images of the surfaces of the fabrics. The fabrics were exposed to a beam accelerating voltage of 1 kV, and the secondary electrons that were scattered from the surface were collected using an Everhart-Thornley detector. We collected images at a pixel resolution of 1333 nm/pixel for low magnification images and a pixel resolution of 147 nm/pixel for the high magnification images.

**Deposition of lipids and growth of DOPC GUVs for quantitative characterization of yields and size distributions:** I standardized growth conditions to allow comparison between the different substrates. I prepared a solution of 99.5:0.5 mol% of DOPC:TopFluor-PC in neat chloroform at a concentration of 2 mg/mL. Each piece of fabric was cut into 9.5 mm diameter circular disks with a pair of scissors and deposited appropriate volumes of the lipid solution to obtain 3 µg of lipid per 1 mg of the substrate. For wool I used 1.5 µg of lipid per 1 mg of substrate. After the solvent had evaporated ambiently, we placed the lipid-coated fabric in a vacuum chamber for one hour to drive-off residual solvent. The substrates were then placed into 2.0 mL Eppendorf tubes. I added 500 µL of a 100 mM solution of sucrose to hydrate the lipid-coated substrates and incubated the substrates for 60 minutes.

**Growth of GUVs with varying membrane compositions on the fabrics:** All the amphiphile-coated substrates were placed under vacuum for a minimum of one hour to drive-off residual solvent, and then incubated in an aqueous solution for 60 minutes before imaging. Growth of giant vesicles from the various amphiphiles required the use of varying growth temperatures and nominal surface concentrations. For the amphiphilic triblock Pluronic L121 polymersomes, we deposited 14 µg of 99.5:0.5 mol% Pluronic L121:TopFluor-PC per 1 mg of the substrate. Growth was performed at room temperature. For the amphiphilic diblock PBD<sub>46</sub>PEO<sub>30</sub> polymersomes we deposited 7 µg of 99.5:0.5 mol% PBD<sub>46</sub>PEO<sub>30</sub>:TopFluor-PC per 1 mg of the substrate. Growth was performed at 80 °C. For 89.5:10:0.5 mol% DOPC:DOPG:TopFluor-PC we deposited 3 µg of the lipid mixture per 1 mg of the substrate. Growth was at room temperature. For 89.5:10:0.5 mol% DOPC:DOTAP:TopFluor-PC we deposited 7 µg of the lipid mixture per 1 mg of the substrate. Growth was at room temperature. For 99.5:0.5 mol% DOPC:TopFluor-PC we deposited 3 µg of the lipid mixture per 1 mg of the substrate. Growth was at room

temperature. For 99.5:0.5 mol% DPPC we deposited 3  $\mu\text{g}$  of the lipid mixture per 1 mg of the substrate. Growth was at 65 °C. For 35.5:36:28:0.5:0.5 mol% DOPC:DPPC:Cholesterol:TopFluor-PC:Rhod-PE we deposited 8  $\mu\text{g}$  of the lipid mixture per 1 mg of the substrate. Growth was at 65 °C. For the *E. coli* membrane extract we deposited 3  $\mu\text{g}$  of the lipid mixture per 1 mg of the substrate. Growth was at 37 °C. To obtain GUVs in standard PBS, we first incubated the lipid coated fabrics in ultrapure water for 10 minutes. We then added a concentrated stock of the buffer salts (Thermo Scientific Pierce 20X Phosphate Buffered Saline, 3 M sodium chloride, 0.2 M sodium phosphate, pH 7.5). to obtain standard PBS and allowed the vesicles to grow for an additional 50 minutes before imaging.

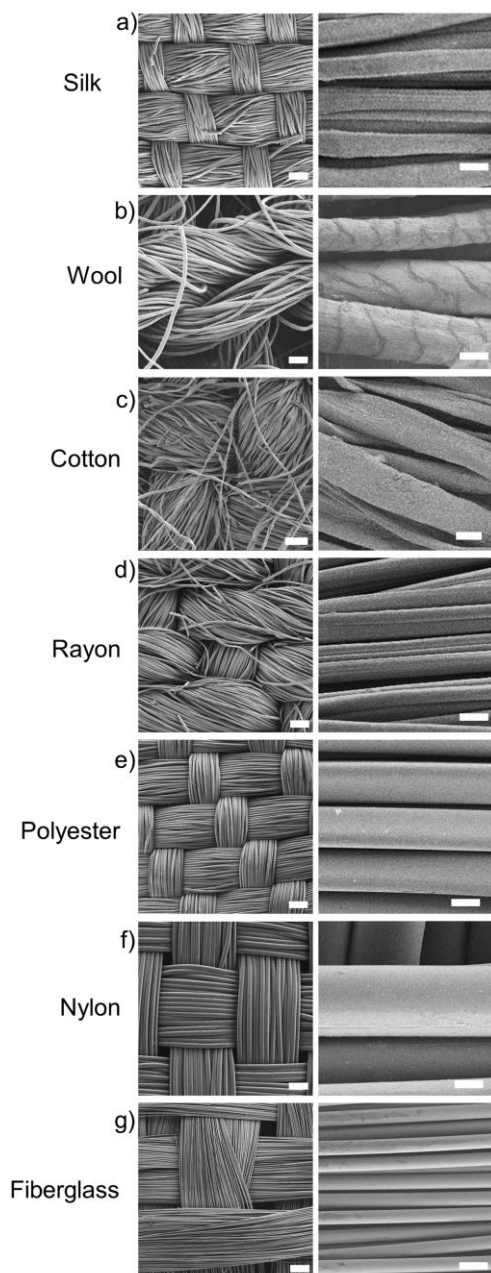
**Harvesting of the GUVs:** I placed a 100  $\mu\text{L}$  droplet of a 100 mM solution of sucrose on a clean glass coverslip. The substrates were removed from the Eppendorf tubes using forceps and quickly immersed the wet substrate into the droplet on the coverslip. I harvested the GUVs by gently aspirating the solution into a 1000  $\mu\text{L}$  pipette tip while moving the tip systematically over the surface of the fabric. The GUVs were imaged and analyzed using the procedures detailed in Chapter 2.

### 3. Results

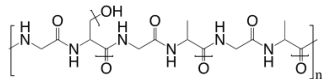
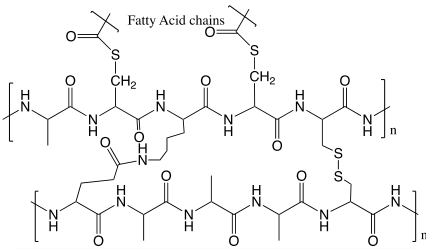
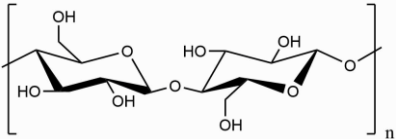
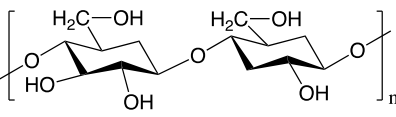
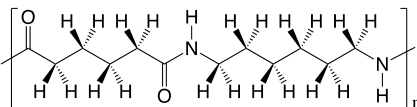
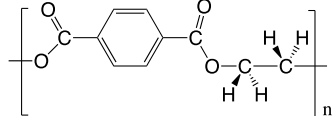
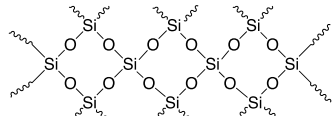
#### 3.1. Properties of the fabrics:

Silk and wool are natural protein-based fibers obtained from animals. Cocoons of the silkworm *Bombyx mori* are the primary source of commercial silk<sup>1</sup>. Silk fibers are composed of the insoluble protein fibroin<sup>1</sup>. The molecular structure of silk is rich in hydrophilic amide groups (Table 1). Silk has a moisture regain of 8.5 % indicating its hydrophilic nature<sup>1</sup>. The fleece of sheep are the primary source of commercial wool fibers<sup>1</sup>. Wool fibers are composed of the insoluble protein keratin. The molecular structure of wool is rich in hydrophilic amide groups as well as hydrophobic covalently attached fatty acids (Table 1). Wool has a moisture regain of 16 % indicating that the hydrophobic fatty acids do not inhibit the adsorption of moisture<sup>1</sup>. Wet-spinning of a cellulosic solution through a spinneret followed by chemical regeneration of the cellulose polymers results in long fibers of rayon of controlled size and crystallinity<sup>2</sup>. This process converts short cellulose fibers from woody materials into long fibers that resemble cotton or silk<sup>2</sup>. Rayon is a semisynthetic fiber since the feedstock originates from a natural source<sup>2</sup>. Natural bio-derived cellulose has a Cellulose I crystal structure. Regenerated cellulose has a Cellulose II crystal structure<sup>2</sup>. Similar to cotton, rayon is rich in hydrophilic hydroxyl groups (Table 1). Rayon has a moisture regain of 11%<sup>1</sup>. Nylon 6,6 is a synthetic fiber made by melt-spinning polyamides that result from the polycondensation of hexamethylenediamine and adipic acid<sup>2</sup>. The molecular structure of Nylon 6,6 is rich in hydrophilic amides. Nylon has a moisture regain of 4.0 - 4.5%<sup>1</sup>. Polyester fibers are melt-spun polyethylene terephthalate<sup>2</sup>. Along with hydrophilic carbonyl groups, polyester is rich with hydrophobic aromatic and methyl groups (Table 1). Polyester has a low moisture regain of 0.4 %<sup>1</sup>. The raw materials

for these synthetic fabrics originate from petroleum byproducts<sup>2</sup>. Fiberglass is solidified extruded molten glass<sup>2</sup>. Fiberglass is hydrophilic due to the presence of many surface hydroxyl group (Table 1).



**Figure B.1:** Scanning electron microscope images of the fabrics. The column on the left are lower magnification images showing the microstructure of the fabrics, while the column on the right are higher magnification images showing the surfaces of the fibers. a) Silk. b) Wool. c) Cotton. d) Rayon. e) Polyester. f) Nylon. g) Fiberglass. Scale bars a-g) left column 100  $\mu\text{m}$ , right column 10  $\mu\text{m}$ .

Fabric	Chemical Formula	Fiber diameter, $\mu\text{m}$ (mean $\pm$ sd)	Moisture Regain (%)	Fabric Weave
<b>Natural</b>				
Silk		$10.6 \pm 1.7$	11	Plain
Wool		$18.5 \pm 4.8$	16	Jersey
Cotton		$15.8 \pm 3.7$	8.5	Plain
<b>Semisynthetic</b>				
Rayon		$12.0 \pm 1.5$	11	Plain
<b>Synthetic</b>				
Nylon		$22.9 \pm 1.3$	4.0-4.5	Plain
Polyester		$12.8 \pm 1.4$	0.4	Twill
<b>Inorganic</b>				
Fiberglass (alumino-borosilicate)		$4.7 \pm 0.4$	-	Satin

**Table B.1:** Properties of the fabrics. Structural formula diagrams were obtained from the references 125 – 131<sup>3-9</sup>. Water contact angles were obtained from reference 132 – 135<sup>10-13</sup>. The fiber diameters were measured from SEM images.

### 3.2. GUVs were produced on all fabric types

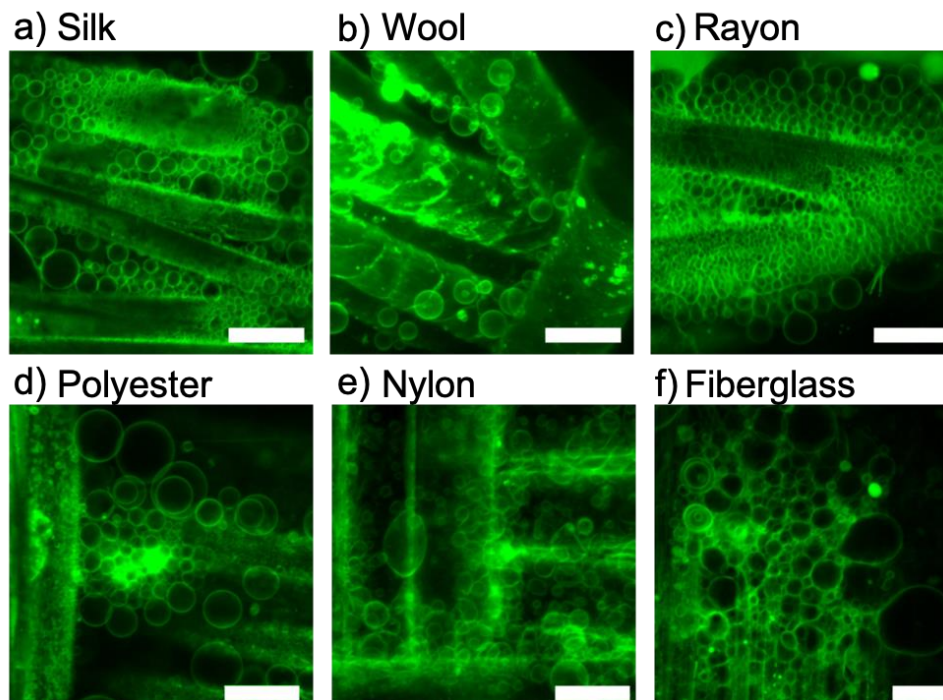


**Figure B.2:** Confocal microscope images of the surface of the hydrated fabrics after 1 hr. a) Silk. b) Wool. c) Rayon. d) Polyester. e) Nylon. f) Fiberglass. GUVs are the bright green circles with dark interiors. Although not fluorescently labeled, the fibers are visible due to the fluorescent lipid coating. a-f) Scale bars 25  $\mu\text{m}$ .

**Figure B.2** shows confocal microscope images of the lipid-coated fabrics one hour after incubation in an aqueous buffer. All the fabrics had GUVs growing from the surfaces of their fibers. These results show that the spontaneous formation of GUVs is not limited to cellulose and is general to fibers of differing surface chemistries. Silk and rayon had spherical GUVs that appeared qualitatively similar to those seen previously on cellulose paper and cotton fabric<sup>14</sup>. Wool had noticeably fewer GUVs than the other fabrics. Nylon, polyester, and fiberglass fabrics had an intermediate number of GUVs, with some regions having a higher abundance of GUVs and others having a lower abundance of GUVs. GUVs formed only from the lipid layer that coated the fibers. Multilamellar lipid structures were also seen which were more prevalent on wool, nylon, polyester, and fiberglass than on rayon, silk, or cotton. Thus, along with GUVs, other lamellar structures were present on the wool, nylon, polyester, and fiberglass fabrics.

All the fabrics promoted the growth of GUVs from both lipids as well as amphiphilic polymers. GUVs composed of lipids with long saturated alkyl chains which require growth at elevated temperatures could also be obtained since all the fibers are thermally stable to 100°C (the boiling point of water) or higher<sup>1,2</sup>. **Figure B.3** shows representative confocal images of giant polymer and lipid vesicles of various membrane

compositions growing both in low ionic strength solutions (100 mM sucrose, **Figure B.3** a-c) and high ionic strength solutions (standard PBS, **Figure B.3** d-f) on silk fibers. For growth in PBS, samples were incubated in ultrapure water for 10 minutes before a concentrated stock of the buffer salts was added to obtain standard PBS. The vesicles were allowed to continue to grow in standard PBS for a further 50 minutes before imaging. **Figure B.3** a) and b) shows polymersomes composed of the amphiphilic triblock copolymer Pluronic L121 and polymersomes composed of the amphiphilic di-block copolymer PBD<sub>46</sub>PEO<sub>30</sub>. **Figure B.3** c) shows GUVs composed of negatively charged membranes (89.5:10:0.5 mol% DOPC:DOPG:TopFluor-PC) and **Figure B.3** d) shows GUVs composed of positively charged membranes (89.5:10:0.5 mol% DOPC:DOTAP:TopFluor-PC). **Figure B.3** e) shows membranes of the zwitterionic lipid DOPC in PBS and **Figure B.3** f) shows membranes of the zwitterionic lipid DPPC in PBS grown at 65°C. DPPC has a main transition temperature of 45 °C<sup>15</sup>. Thus, DPPC is in the gel phase at room temperature. **Figure B.3** g) shows GUVs with a ternary membrane composition of 35.5:36:28:0.5:0.5 mol% DOPC:DPPC:Cholesterol:TopFluor-PC:Rhod-PE that exhibits liquid-liquid phase coexistence at room temperature<sup>15</sup>. The GUVs were grown at 65°C to ensure that the membranes were fully mixed. Upon cooling to room temperature, the membranes phase separated into liquid ordered and liquid disordered domains as evidenced by the partitioning of the Rhod-PE (false-colored red) and TopFluor-PC (false colored green) into distinct compartments in the membrane. Rhod-PE partitions strongly into the liquid disordered phase while TopFluor-PC partitions equally between the liquid disordered phase and liquid ordered phase<sup>11,47</sup>. **Figure B.3** f) shows GUVs obtained from the polar fraction of membrane extracts of the bacteria *Escherichia coli*. The membranes, composed of phosphatidylethanolamine: phosphatidylglycerol: cardiolipin 67.0: 23.2: 9.8 wt/wt% (manufacturer's specifications), are highly negatively charged.

I quantified the number and sizes of the GUVs obtained using image analysis as shown in **Figure B.4**. The number of vesicles varied from  $2.6 \times 10^5$  GUVs per  $\mu\text{g}$  of lipid for rayon and  $6.2 \times 10^4$  GUVs per  $\mu\text{g}$  of lipid for wool. Two sample T-tests were carried out that showed that only the difference in yields between rayon and wool were significant and for the most part, the number of GUVs obtained did not vary much despite the variation in the chemistries of the fabrics. Vesicles obtained using the POPYRUS method are polydisperse as was also the case with paper. Interestingly, the size distributions were very similar across the fabric types – the distribution of diameters was unimodal with a right tail, which appears to be the distribution of vesicles obtained from phospholipids in thin film hydration. In general, 98% of the vesicles across all fabrics accounted for diameters below 20  $\mu\text{m}$ . The advantages of fabrics over paper is that they are more durable and can be reused, thus opening avenues into applications across bandages and skin patches, where the vesicles grown at the point of use can be used to protect and slowly release the active ingredients over time. Furthermore, fabrics such as glass fiber and nylon are used in immunoassays as support materials or part as the conjugate pad, that supplies detection molecules into the assay. GUVs can be produced on these substrates, thus enabling their easy incorporation into existing assay devices.



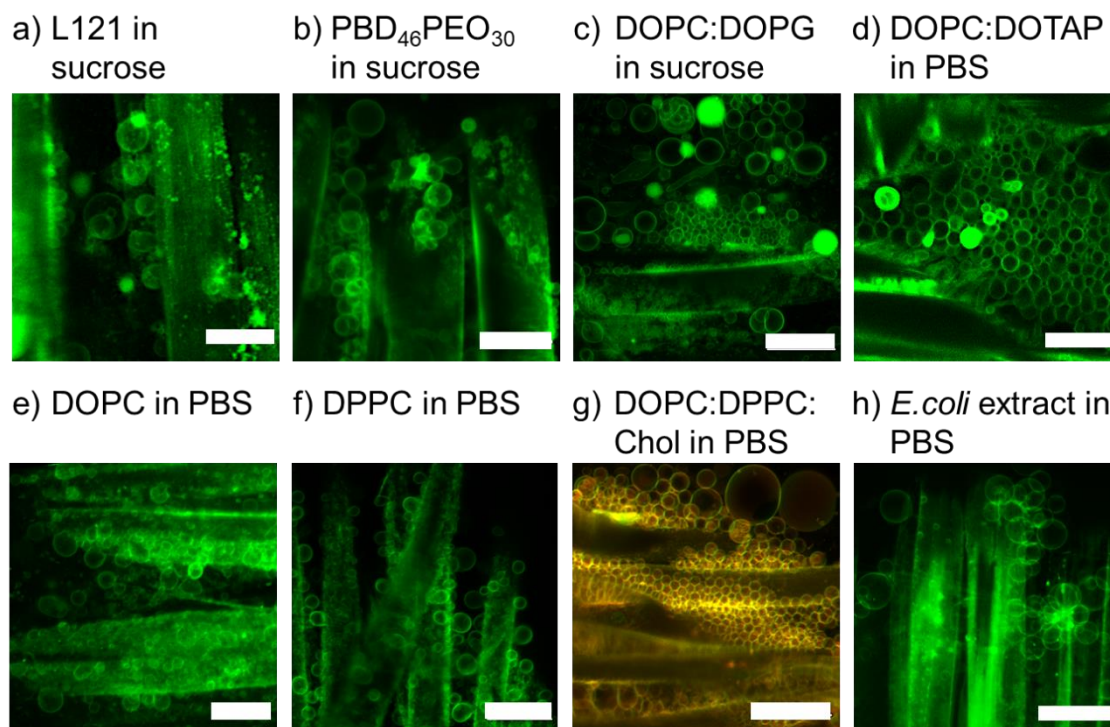


**Figure B.3:** Confocal microscope images of giant polymersomes and giant lipid vesicles on the surface of silk fibers after 1 hr in aqueous buffer. a) Giant polymersomes of the amphiphilic triblock copolymer Pluronic L121 in a solution of sucrose. b) Giant polymersomes of the amphiphilic diblock copolymer PBD<sub>46</sub>PEO<sub>30</sub> in a solution of sucrose. c) Giant vesicles with negatively charged membranes (89.5:10:0.5 mol% DOPC:DOPG:TopFluor-PC) in a solution of sucrose. d) Giant vesicles with positively charged membranes (89.5:10:0.5 mol% DOPC:DOTAP:TopFluor-PC) in standard PBS. e) Giant vesicles with zwitterionic membranes composed of two unsaturated alkyl chains (DOPC, chain melting temperature -20 °C) in standard PBS. f) Giant vesicles with zwitterionic membranes composed of saturated alkyl chains (DPPC, chain melting temperature -45 °C) in standard PBS. g) Giant vesicles with membranes exhibiting liquid-liquid phase coexistence composed of 35.5:36:28:0.5:0.5 mol% DOPC:DPPC:Cholesterol:TopFluor-PC:Rhod-PE in standard PBS. h) Giant vesicles composed of membrane extracts from *E. coli* in standard PBS. a), b), d), e) Scale bars 15  $\mu\text{m}$ . c), f), g), h) Scale bars 15  $\mu\text{m}$ .

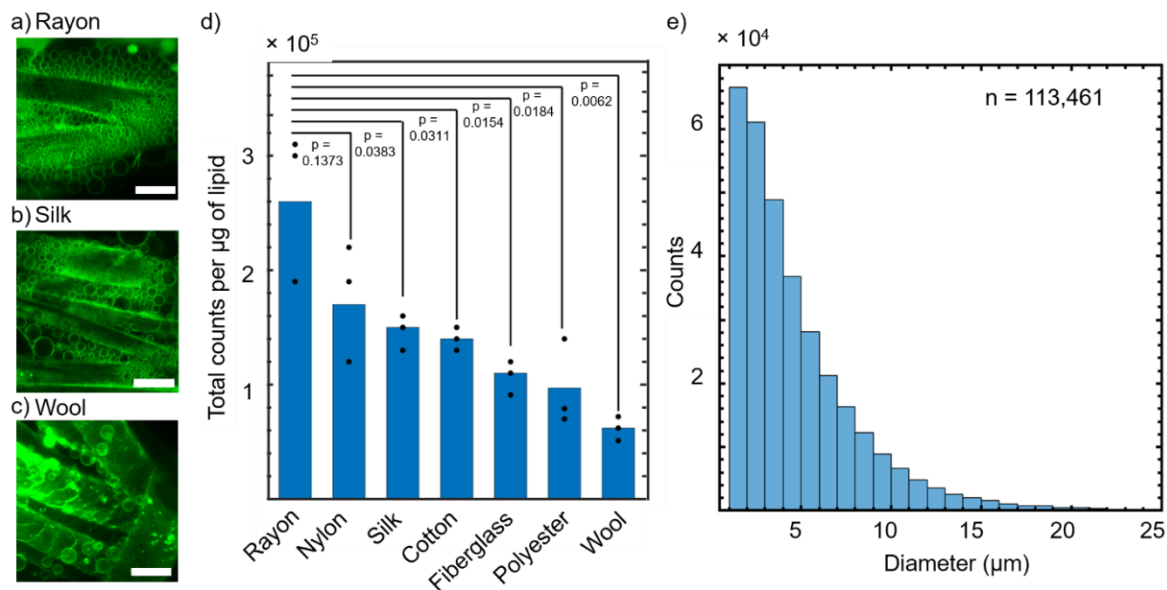


**Figure B.4:** Confocal microscope images of the surface of the hydrated fabrics after 1 h. (a) Rayon, (b) silk, (c) wool. GUVs are the bright green circles with dark interiors. Although not fluorescently labeled, the fibers are visible due to the fluorescent lipid coating. (d) Scatter and bar plot showing the number of GUVs per microgram of lipid from each of the fabrics. The black circles are the data points for the three experiments for each fabric. The blue bar is the average number of GUVs from the three experiments for each fabric. p-Values from two-sample t-tests between rayon and the other fabrics are indicated in the plot.  $p < 0.05$  is statistically significant. (e) Representative histogram of the diameters of GUVs harvested from silk. The bin widths are  $1 \mu\text{m}$ . The sample size, number of vesicles,  $n = 113,461$  (a-c) Scale bars:  $25 \mu\text{m}$ .

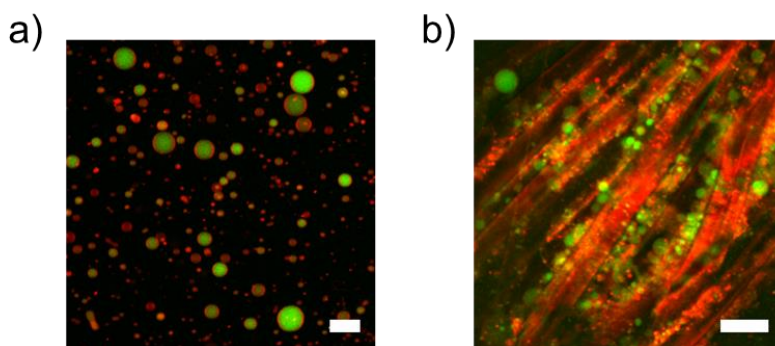


**Figure B.5:** Encapsulation of dye molecules after drying and rehydration on the substrate. a) An example of extracted DOPC vesicles grown on silk with  $0.005 \text{ mg/mL}$  fluorescein (green) in the growth solution. b) An example of silk coated with fluorescein (green) followed by lipid with rhodamine in the membrane (red). Upon hydration, the vesicles encapsulate fluorescein within the lumen. The vesicles were not extracted. Scale bars:  $25 \mu\text{m}$ .

#### 4. Conclusions

We have shown that the formation of GUVs and polymersomes from lamellar films of phospholipids and amphiphilic block copolymers is general to a surprisingly wide variety of fabrics composed of cylindrical fibers of different surface chemistries. Fabrics are widely used in various consumer and technical applications including in biomedical applications<sup>10,16–21</sup>. This demonstration that vesicles can form on a range of fabrics opens new avenues for designing smart functionalized materials. The ability to encapsulate compounds that are dried and rehydrated at the point of use also enables delivery of actives such as antibiotics and growth factors to wound sites.

#### 5. Bibliography

- (1) Cook, J. G. *Handbook of Textile Fibres: Natural Fibres*, 5th ed.; Woodhead Publishing: Cambridge, UK, 1984.
- (2) Cook, J. G. *Handbook of Textile Fibres: Man-Made Fibres*, 5th ed.; Woodhead Publishing: Cambridge, UK, 1984.
- (3) Shen, G.; Hu, X.; Guan, G.; Wang, L. Surface Modification and Characterisation of Silk Fibroin Fabric Produced by the Layer-by-Layer Self-Assembly of Multilayer Alginate/Regenerated Silk Fibroin. *PLoS One* **2015**, *10*, e0124811.
- (4) Hutchinson, S.; Evans, D.; Corino, G.; Kattenbelt, J. An evaluation of the action of thioesterases on the surface of wool. *Enzyme Microb. Technol.* **2007**, *40*, 1794–1800.
- (5) Nsor-Atindana, J.; Chen, M.; Goff, H. D.; Zhong, F.; Sharif, H. R.; Li, Y. Functionality and nutritional aspects of microcrystalline cellulose in food. *Carbohydr. Polym.* **2017**, *172*, 159–174.
- (6) Lubin, G.; Dastin, S. J. *Raw Materials - Handbook of Composites*; Lubin, G., Ed.; Springer US: Boston, MA, 1982; pp 19–272.
- (7) Ortega, R. A.; Carter, E. S.; Ortega, A. E. Nylon 6,6 Nonwoven Fabric Separates Oil Contaminates from Oil-in-Water Emulsions. *PLoS One* **2016**, *11*, e0158493.
- (8) Militky, J. 9 - The chemistry, manufacture and tensile behaviour of polyester fibers. In *Woodhead Publishing Series in Textiles*; Bunsell, A. R. B. T.-H. of T. P. of T. and T. F., Ed.; Woodhead Publishing, 2009; pp 223–314.
- (9) Cao, C.; Li, Z.-B.; Wang, X.-L.; Zhao, X.-B.; Han, W.-Q. Recent Advances in Inorganic Solid Electrolytes for Lithium Batteries. *Frontiers in Energy Research*. 2014, p 25.
- (10) Gupta, B. S. *Manufacture, types and properties of biotextiles for medical applications*; Woodhead Publishing Limited, 2013.
- (11) Le, C. V.; Ly, N. G.; Stevens, M. G. Measuring the Contact Angles of Liquid Droplets on Wool Fibers and Determining Surface Energy Components. *Text. Res.*

- J.* **1996**, *66*, 389–397.
- (12) Dutta, S.; Talukdar, B.; Bharali, R.; Rajkhowa, R.; Devi, D. Fabrication and characterization of biomaterial film from gland silk of muga and eri silkworms. *Biopolymers* **2013**, *99*, 326–333.
  - (13) Arthur W. Adamson, A. P. G. *Physical Chemistry of Surfaces*; 1997.
  - (14) Pazzi, J.; Xu, M.; Subramaniam, A. B. Size distributions and yields of giant vesicles assembled on cellulose papers and cotton fabric. *Langmuir* **2019**, *35*, 7798–7804.
  - (15) Veatch, S. L.; Keller, S. L. Separation of liquid phases in giant vesicles of ternary mixtures of phospholipids and cholesterol. *Biophys. J.* **2003**, *85*, 3074–3083.
  - (16) Kundu, B.; Kundu, S. C. Osteogenesis of human stem cells in silk biomaterial for regenerative therapy. *Prog. Polym. Sci.* **2010**, *35*, 1116–1127.
  - (17) Leal-ega, A.; Scheibel, T. Silk-based materials for biomedical applications. *Biotechnol. Appl. Biochem.* **2010**, *55*, 155–167.
  - (18) Kundu, B.; Kurland, N. E.; Bano, S.; Patra, C.; Engel, F. B.; Yadavalli, V. K.; Kundu, S. C. Silk proteins for biomedical applications: Bioengineering perspectives. *Prog. Polym. Sci.* **2014**, *39*, 251–267.
  - (19) Klemm, D.; Heublein, B.; Fink, H. P.; Bohn, A. Cellulose: Fascinating biopolymer and sustainable raw material. *Angew. Chemie - Int. Ed.* **2005**, *44*, 3358–3393.
  - (20) Maitz, M. F. Applications of synthetic polymers in clinical medicine. *Biosurface and Biotribology* **2015**, *1*, 161–176.
  - (21) Singh, C.; Wong, C.; Wang, X. Medical Textiles as Vascular Implants and Their Success to Mimic Natural Arteries. *J. Funct. Biomater.* **2015**, *6*, 500–525.

## Appendix C: Fluorescence dye has an effect on the assembly of GUVs

This section reports results of varying fractions of dye in the lipid membrane. I tested two dyes, Top-Fluor Cholesterol and Rhodamine-PE. **Figure C.1** shows the molar yield for the two dyes at different mole fractions. Top-Fluor Cholesterol is composed of the fluorescent bodipy group conjugated to a cholesterol molecule. Rhodamine-PE is composed of the fluorescent group rhodamine B sulfonyl conjugated to the 1,2-dioleoyl-*sn*-glycero-3-phosphoethanolamine (DOPE) headgroup.

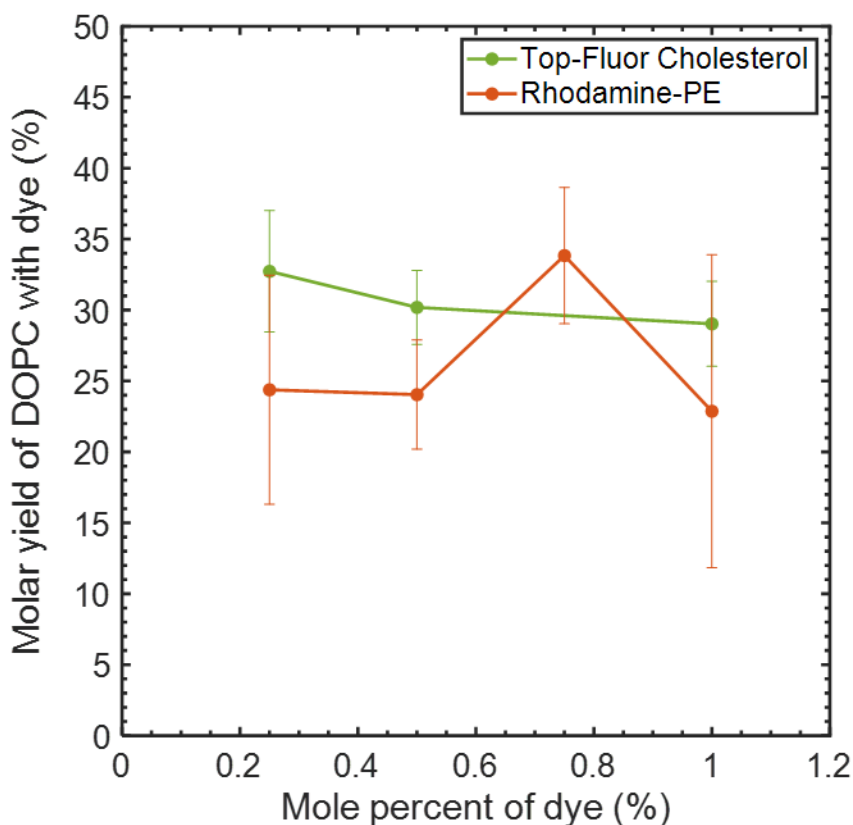


**Figure C.1:** Variation of molar yield at different mole fractions of dye. The green curve shows the variation of molar yield of DOPC vesicles doped with varying mole fractions of Top-Fluor Cholesterol while the red curve shows the variation in molar yield with Rhodamine-PE.

I note that using rhodamine resulted in larger variations in yield at different mole fractions of dye. The lowest mean yield was  $22 \pm 11$  % at 1 mole % of dye while the highest was  $33 \pm 4.8$  % at 0.75 mole % of dye. The standard deviations are also higher for DOPC mixtures with rhodamine, suggesting that the use of rhodamine might introduce more variations in the process of producing GUVs and quantifying yield. Top-fluor cholesterol on the other hand appears to show steadier yield values, varying between  $29 \pm 3.0$  % and

$32 \pm 4.3\%$ . Top-Fluor Cholesterol was chosen as the dye for all confocal imaging carried out in this dissertation because since variation of mole fractions had the lowest impact on molar yields. The standard deviations between repeat runs was less than 5%, lower than what was seen for DOPC doped with rhodamine. I used 0.5 mol % of Top-fluor Cholesterol in all lipid mixtures in this dissertation.

### Appendix D: Impact of using buffers in solutions for GUV assembly

This section reports impact of using different types of buffers on GUV assembly. All solutions had 100 mM of sucrose and the buffered solutions had 10 mM of the respective buffer. I tested the 4-(2-hydroxyethyl)-1-piperazineethanesulfonic acid (HEPES), Piperazine-1,4-bis(2-ethanesulfonic acid) dipotassium salt (PIPES), and tris(hydroxymethyl)aminomethane (Tris). The pH of the solutions prior to adding the buffers was 5.5 and the pH of all solutions after adding buffers was 7.5. All points represent a single experimental run.

**Figure D.1** shows the molar yield and the histogram of sizes obtained from GUV assembly in different types of buffers. The control with no buffer only had 100 mM of sucrose. I note that all solutions with buffers resulted in a reduction in yield from 30% to ~5% or lower. The histogram of sizes show that in the distributions narrow in the presence of buffers, resulting in fewer or no vesicles over 50  $\mu\text{m}$  in the presence of buffers. How the buffers affect the yield are unknown. A logical factor to investigate given the generality of this effect is the pH of the solution is important for yields. A citrate, acetate, or BIS-tris buffer of pH 5.5 could be used to see if yields are similar to unbuffered water. Additionally all this work was performed on cellulose paper. The effect of the substrate can also be investigated. It is important to note that modulating the addition of buffer (Section 6.4.4) eliminates this effect and we can obtain high yields GUV in any final buffer composition.

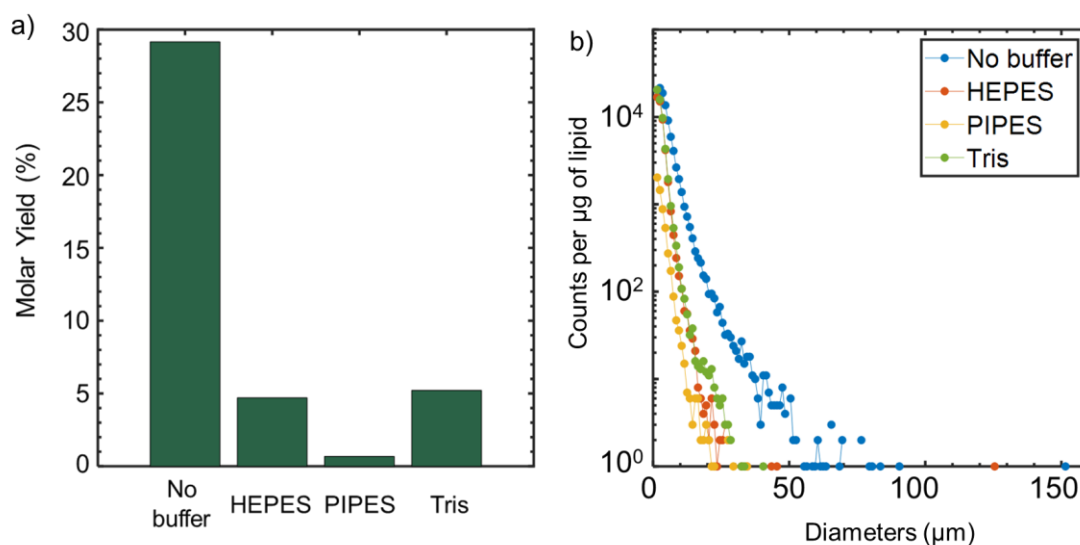


**Figure D.1:** Molar yield and histogram of sizes obtained from GUV assembly in different buffers. a) Molar yield of GUVs and b) histogram of sizes for buffers HEPES, PIPES and Tris.